

**COMPUTATIONAL FLUID DYNAMICS SIMULATION
OF A DTB CRYSTALLIZER**

Wirapong Wantha

A Thesis Submitted in Partial Fulfillment of the Requirements for the

Degree of Master of Engineering in Chemical Engineering

Suranaree University of Technology

Academic Year 2006

ISBN 974-533-579-7

การจำลองพลศาสตร์ของไหลเชิงคำนวณของเครื่องตกผลึกแบบดีทีบี

นายวีรพงษ์ วันทา

วิทยานิพนธ์นี้เป็นส่วนหนึ่งของการศึกษาตามหลักสูตรปริญญาวิศวกรรมศาสตรมหาบัณฑิต

สาขาวิชาวิศวกรรมเคมี

มหาวิทยาลัยเทคโนโลยีสุรนารี

ปีการศึกษา 2549

ISBN 974-533-579-7

**COMPUTATIONAL FLUID DYNAMICS SIMULATION
OF A DTB CRYSTALLIZER**

Suranaree University of Technology has approved this thesis submitted in partial fulfillment of the requirements for a Master's Degree.

Thesis Examining Committee



(Dr. Terasut Sookumnerd)

Chairperson



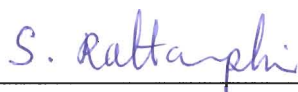
(Asst. Prof. Dr. Adrian Flood)

Member (Thesis Advisor)



(Assoc. Prof. Dr. Chaiyot Tangsathitkulchai)

Member



(Assoc. Prof. Dr. Saowanee Rattanaphani)

Vice Rector for Academic Affairs



(Assoc. Prof. Dr. Vorapot Khompis)

Dean of Institute of Engineering

วีรพงษ์ วันทา : การจำลองพลศาสตร์ของไหลเชิงคำนวณของเครื่องตกผลึกแบบดีทีบี
(COMPUTATIONAL FLUID DYNAMICS SIMULATION OF A DTB
CRYSTALLIZER) อาจารย์ที่ปรึกษา : ผู้ช่วยศาสตราจารย์ ดร.เอเดรียน ฟัดด์, 285 หน้า.
ISBN 974-533-579-7

ลักษณะการไหลของผลึกและของไหลในเครื่องตกผลึกเป็นปัจจัยสำคัญในกระบวนการตกผลึก เช่น มีผลกระทบโดยตรงต่อความสม่ำเสมอของขนาดผลึกที่ได้และพลังงานที่ต้องใช้ในการตกผลึก งานวิจัยนี้มีวัตถุประสงค์เพื่อวิเคราะห์การไหลของของไหลในเครื่องตกผลึกแบบดีทีบีที่มีการแยกเอาผลึกขนาดเล็กละเอียดออกเพื่อนำกลับเข้าสู่กระบวนการตกผลึกใหม่ โดยการจำลองเชิงตัวเลขของการไหลสองสถานะ คือการไหลของของเหลวกับไอ โดยลักษณะการไหลของผลึกถูกพิจารณาให้ไหลไปตามกระแสการไหลของของเหลว ซึ่งทำการจำลองทั้งแบบอนุกรมกึ่งที่และแบบอนุกรมไม่กึ่งที่ โดยในกรณีอนุกรมกึ่งที่ ใบพัดถูกแทนที่ด้วยแหล่งกำเนิดโมเมนตัมอย่างเดียว และในกรณีอนุกรมไม่กึ่งที่ ใบพัดถูกแทนที่ด้วยแหล่งกำเนิดโมเมนตัมและแหล่งกำเนิดความร้อน โดยการจำลองได้ใช้โปรแกรมสำเร็จรูปเชิงพาณิชย์ “ANSYS CFX-10.0” เป็นโปรแกรมหลักในการจำลองการไหลในสามมิติ โปรแกรมนี้คำนวณด้วยกรรมวิธีปริมาตรจำกัดและใช้ระบบกริดแบบไร้โครงสร้าง (Unstructured grid) ทั้งนี้ในการจำลองได้ใช้สารละลายโซเดียมคลอไรด์ 26.66% และไอน้ำ เป็นของเหลวและไอตามลำดับ ในการศึกษา

กรณีการจำลองแบบอนุกรมกึ่งที่ ไอบางส่วนเกิดขึ้นภายในเครื่องแลกเปลี่ยนความร้อนที่อยู่ภายนอกเครื่องตกผลึก ดังนั้นมีทั้งสารละลายและไอน้ำถูกส่งเข้าเครื่องตกผลึก ในกรณีนี้ได้ทำการศึกษาผลกระทบอันเนื่องมาจากการเปลี่ยนแปลงตัวแปรต่าง ๆ ได้แก่ ค่าแหล่งกำเนิดโมเมนตัม อัตราการไหลออกของผลึกขนาดเล็กละเอียด (Fines removal flow rate) ที่ไหลออกไปกับสารละลาย และอัตราการไหลออกของผลึกที่ต้องการที่ผสมอยู่กับสารละลาย (Product crystal suspension flow rate) ผลการศึกษาบ่งบอกว่าการเพิ่มค่าแหล่งกำเนิดโมเมนตัม ค่าอัตราการไหลออกของผลึกขนาดเล็กละเอียด และค่าอัตราการไหลออกของผลึกที่ต้องการ ต่างส่งผลให้ความเร็วของของเหลวสูงขึ้น แต่ค่าอัตราการไหลออกของผลึกขนาดเล็กละเอียด และค่าอัตราการไหลออกของผลึกที่ต้องการ ส่งผลกระทบน้อยกว่า และตัวแปรทั้งสามนี้มีผลกระทบต่อการเปลี่ยนแปลงความเร็วของไอเพียงเล็กน้อยเท่านั้น การเพิ่มค่าแหล่งกำเนิดโมเมนตัม และอัตราการไหลออกของผลึกขนาดเล็กละเอียด ส่งผลให้ขนาดของผลึกเล็กละเอียดที่แยกออกไป (Fines removal cut-size) ใหญ่ขึ้น ในขณะที่การเพิ่มค่าอัตราการไหลออกของผลึกที่ต้องการ ส่งผลให้ขนาดของผลึกเล็กละเอียดที่แยกออกไปเล็กลง ซึ่งจะมีผลต่อการกระจายตัวของขนาดผลึกที่ได้

นอกจากนี้ยังพบว่าที่ค่าแหล่งกำเนิดโมเมนต์ $25,000 \text{ kg/m}^2/\text{s}^2$ ขึ้นไป การไหลของของเหลวในตัวเครื่องตกผลึก (Main body crystallizer) มีความสม่ำเสมอ ซึ่งจะมีผลทำให้ได้ผลึกที่มีขนาดสม่ำเสมอ

กรณีการจำลองแบบอนุกรมไม่คงที่ ไอเกิดขึ้นภายในเครื่องตกผลึกโดยได้รับความร้อนจากเครื่องแลกเปลี่ยนความร้อนที่อยู่ภายในเครื่องตกผลึก ในกรณีนี้ได้ทำการศึกษาผลกระทบอันเนื่องมาจากการเปลี่ยนแปลงค่าแหล่งกำเนิดความร้อน ผลการศึกษาบ่งบอกว่าการเพิ่มค่าแหล่งกำเนิดความร้อนมีผลกระทบต่อการเปลี่ยนแปลงความเร็วของของเหลวและไอเพียงเล็กน้อยเท่านั้น และส่งผลให้ปริมาณไอที่เกิดขึ้นในเครื่องตกผลึกมีปริมาณเพิ่มขึ้นเป็นสัดส่วน โดยตรงกับค่าแหล่งกำเนิดความร้อนที่เพิ่มขึ้น

การเปรียบเทียบผลการจำลองที่ได้กับทฤษฎีและงานวิจัยในอดีต ผลที่ได้นั้นสอดคล้องกัน ดังนั้นวิธีการจำลองพลศาสตร์ของไหลเชิงคำนวณสามารถนำมาใช้ในการออกแบบและหาสภาวะที่เหมาะสมของเครื่องตกผลึกแบบคิทีบีเชิงพาณิชย์ได้

WIRAPONG WANTHA : COMPUTATIONAL FLUID DYNAMICS

SIMULATION OF A DTB CRYSTALLIZER. THESIS ADVISOR : ASST.

PROF. ADRIAN FLOOD, Ph.D. 285 PP. ISBN 974-533-579-7

COMPUTATIONAL FLUID DYNAMICS/ SIMULATION/ TWO-PHASE FLOW/
DTB CRYSTALLIZER

The characteristics of solids and fluid flows in crystallizers are key factors for crystallization processes. For example, they directly influence the crystal size distributions and energy requirements for the crystallizer. The purpose of this research is to numerically simulate the two-phase (liquid and vapor) flow in a Draft Tube Baffle (DTB) crystallizer with fines removal streams: once the fluid phase flows have been determined, general characteristics of the flow of the crystals can be ascertained. In order to reduce the execution time of the simulation, the impeller was modeled using a momentum source for the isothermal simulation, and both a momentum source (for the impeller) and heat source (for the internal heat exchanger) for the non-isothermal simulation, a method shown to be effective in previous research. The commercial software ANSYS CFX-10.0 was employed to perform 3D simulation using the finite volume method with an unstructured mesh topology. Water solutions with 26.66 % NaCl and water-vapor are the fluids used in the simulation.

For the isothermal simulation, the simulation assumed that the vapor formed in an external heat exchanger before the fluid was fed to the crystallizer for crystal nucleation and growth, and the simulations were performed with various momentum

source values, fines removal flow rate values, and product crystal suspension flow rate values. The results show that the overall magnitude of the liquid velocity within the crystallizer can be strongly increased by the increasing the axial momentum source but only slightly increased by the product crystal suspension and fines removal flow rates, and the vapor velocity can be slightly influenced by these variables. The fines removal cut-size can be increased with increasing momentum source and fines removal flow rate, and decreased with increasing product crystal suspension flow rate. This will strongly affect the product crystal size distribution. Furthermore, the liquid flow is found to be fully uniform in the main body of the crystallizer for momentum sources larger than or equal to $25,000 \text{ kg/m}^2/\text{s}^2$; uniform flow assists in producing a narrow crystal size distribution.

For the non-isothermal simulation, the simulation assumed that the vapor formed in the crystallizer by use of an internal heat exchanger, and the simulations were performed with various heat source values. The results show that the overall velocity for both phases (liquid and vapor) can be slightly influenced by the heat source, and the amount of vapor formed in the crystallizer can be increased linearly with increasing heat source values.

A comparison of the results has been made between CFD predictions and original theory and the literature. The results support that the CFD methodology can be used for the optimization of commercial-scale DTB crystallizer designs.

School of Chemical Engineering

Academic Year 2006

Student's Signature _____

Advisor's Signature _____



ACKNOWLEDGEMENTS

I would like to express my appreciation to my thesis examining committee for their wonderful questions and guidance. I am most grateful to my thesis advisor, Asst. Prof. Dr. Adrian Flood for his supporting information and invaluable advice and encouragement that have helped me pass through my difficult times.

I would like to thank all of the lecturers at the School of Chemical Engineering, Suranaree University of Technology (SUT) for their good attitude and advice. I would also like to thank all of my friends who are graduate students in the School of Chemical Engineering and the School of Mechanical Engineering, who shared the experience of graduate student life, and CFX at the SUT, and who have made this experience very joyous and memorable.

I would like to express my honest gratefulness to everyone in my family, especially my parents for their love and care.

Finally, I gratefully acknowledge the invaluable help of everyone I may have forgotten to mention here. I am also grateful to SUT for the full scholarship throughout my study, and the financial support from SUT research fund.

Wirapong Wantha

TABLE OF CONTENTS

	PAGE
ABSTRACT (THAI).....	I
ABSTRACT (ENGLISH).....	III
ACKNOWLEDGEMENTS	V
TABLE OF CONTENTS.....	VI
LIST OF TABLES.....	XIV
LIST OF FIGURES.....	XV
SYMBOLS AND ABBREVIATIONS.....	XXXI
CHAPTER	
I INTRODUCTION.....	1
1.1 Background and Significance.....	1
1.2 Objectives.....	6
1.3 Scope and Assumptions of Work.....	7
1.3.1 Overall scope and assumptions.....	7
1.3.2 Specific scope and assumptions of the isothermal simulation.....	8
1.3.3 Specific scope and assumptions of the non-isothermal simulation.....	8
1.4 Outcomes of the Research.....	9

TABLE OF CONTENTS (CONTINUED)

	PAGE
II THEORY AND LITERATURE REVIEW	10
2.1 Crystallization from Solution.....	10
2.1.1 Continuous, steady-state crystallizers.....	11
2.1.2 Batch crystallizer.....	12
2.1.3 Seeded crystallizer.....	12
2.1.4 Cooling crystallization.....	13
2.1.5 Evaporative crystallization.....	14
2.1.6 Vacuum crystallization.....	14
2.1.7 Non-solvent (drowning-out) crystallization.....	14
2.1.8 Pressure crystallization.....	15
2.1.9 Reaction crystallization (precipitation).....	15
2.1.10 Purge streams.....	16
2.1.11 Recycle streams.....	16
2.2 Industrial Crystallizers.....	16
2.2.1 Industrial crystallization apparatus.....	16
2.2.2 Draft tube baffle (DTB) crystallizers.....	22
2.3 The Effect of Hydrodynamics in Crystallizers.....	25
2.3.1 Introduction to crystallization mechanisms.....	26
2.3.2 Introduction to mixing in crystallization processes.....	28
2.3.3 Mixing effects on nucleation.....	31

TABLE OF CONTENTS (CONTINUED)

	PAGE
2.3.4	Mixing effects on growth.....32
2.3.5	Particle settling.....33
2.3.6	Previous fluid dynamic studies relating to crystallizers.....36
2.4	CFD Modeling of Crystallizers.....42
2.4.1	Introduction to CFD.....42
2.4.2	CFD modeling of crystallizers.....44
2.5	Conclusions.....53
III	MATHEMATICAL MODELS54
3.1	Introduction.....54
3.2	Mathematical Models.....56
3.2.1	Isothermal simulation57
3.2.1.1	The continuity equation.....57
3.2.1.2	The momentum equation.....58
3.2.1.3	The volume conservation equation59
3.2.1.4	The pressure constraint.....60
3.2.1.5	Momentum sources60
3.2.1.6	The interphase momentum transfer model...62
3.2.1.7	Turbulence models.....67

TABLE OF CONTENTS (CONTINUED)

	PAGE
3.2.2 Non-isothermal simulation	74
3.2.2.1 The continuity equation.....	74
3.2.2.2 The momentum equation	75
3.2.2.3 The energy equation.....	76
3.2.2.4 The volume conservation equation	78
3.2.2.5 The pressure constraint.....	78
3.2.2.6 The interphase momentum transfer model....	78
3.2.2.7 Inhomogeneous interphase heat transfer models	78
3.2.2.8 Interphase mass transfer.....	80
3.2.2.9 The thermal phase change model.....	82
3.2.2.10 Turbulence models.....	84
3.2.2.11 Momentum sources.....	86
3.2.2.12 Heat sources.....	87
3.3 Conclusions.....	87
IV APPARATUS AND METHODS	89
4.1 Apparatus	89
4.2 Study Methods.....	90
4.2.1 Isothermal simulation.....	90

TABLE OF CONTENTS (CONTINUED)

	PAGE
4.2.1.1 Study into the general characteristics of flow fields and classification of crystals in a DTB crystallizer.....	90
4.2.1.2 Study into the effect of the momentum source strength on the flow characteristics and the classification of crystals.....	94
4.2.1.3 Study into the effect of the fines removal flow rate on the flow characteristics and the classification of crystals.....	94
4.2.1.4 Study into the effect of the product crystal suspension flow rate on the flow characteristics and the classification of crystals.....	95
4.2.2 Non-isothermal simulation.....	95
4.2.2.1 The validation of the degassing condition at the liquid surface.....	96
4.2.2.2 Study into the effect of heat and mass transfer via the evaporation on the flow characteristics and classification of crystals	96
4.3 Simulation Methods.....	97

TABLE OF CONTENTS (CONTINUED)

	PAGE
4.3.1 Geometry.....	97
4.3.2 Mesh.....	99
4.3.2.1 Mesh generation.....	100
4.3.2.2 Procedures of the optimum mesh generation.....	103
4.3.3 Physical definition	119
4.3.3.1 Fluid properties	119
4.3.3.2 Flow conditions.....	119
4.3.3.3 Initial and boundary conditions.....	124
4.3.3.4 Mesh adaptation and solver control	129
4.3.4 Solver	130
4.3.5 Post-processing.....	131
4.4 Conclusions.....	131
V RESULTS AND DISCUSSION	133
5.1 Isothermal Simulation.....	133
5.1.1 General characteristics of flow fields and classification of crystals in a DTB crystallizer.....	133
5.1.2 Effect of the momentum source.....	145
5.1.3 Effect of the fines removal flow rate.....	170
5.1.4 Effect of the product crystal suspension flow rate.....	187

TABLE OF CONTENTS (CONTINUED)

	PAGE
5.2 Non-isothermal Simulation	203
5.2.1 Validation of the degassing condition at the free surface.....	203
5.2.2 Effect of the heat source.....	209
5.3 Conclusions.....	225
VI CONCLUSIONS AND RECOMMENDATIONS.....	227
6.1 Conclusions.....	227
6.1.1 Isothermal simulation.....	227
6.1.2 Non-isothermal simulation.....	229
6.2 Recommendations.....	230
REFERENCES.....	231
APPENDICES	
APPENDIX A SUMMARY OF THE AGREEMENT BETWEEN EXPERIMENT RESULTS AND CFD MODELING IN PREVIOUS STUDIES.....	240
APPENDIX B MATHEMATICAL NOTATIONS AND FUNCTIONS.....	246
B.1 The Vector Operator ∇ and $\nabla \bullet$	247
B.2 The Dyadic Product.....	248
B.3 Matrix Transposition.....	249

TABLE OF CONTENTS (CONTINUED)

	PAGE
B.4 Mathematical Functions Used in the Study.....	249
APPENDIX C THE NUMBER OF NODES AND ELEMENTS OF EACH CASE STUDY.....	250
APPENDIX D SIMULATION RESULTS.....	253
D.1 Isothermal Simulation Results.....	254
D.2 Non-isothermal Simulation Results.....	265
APPENDIX E EXAMPLE OF SOURCE CODES.....	268
BIOGRAPHY.....	285

LIST OF TABLES

TABLE	PAGE
2.1 Hydrodynamic regimes for settling particles.....	35
4.1 Case studies for the isothermal simulations.....	91
4.2 Case studies for the non-isothermal simulations.....	96
4.3 Mesh sizes of each run; used to find the optimum mesh.....	105
4.4 Mesh sizes of each run with fine mesh around draft tube.....	112
4.5 Physical properties of vapor and liquid.....	120
5.1 Values of the power transmitted by the impeller	146
A.1 Summary of the agreement between experiment results and CFD modeling in previous studies.....	241
C.1 The number of nodes and elements of each case study.....	251

LIST OF FIGURES

FIGURE	PAGE
2.1 Solubility of a general solution.....	11
2.2 General schematic of a crystallization process.....	12
2.3 Solubility curves for several anhydrates.....	13
2.4 Solubility of some solutions.....	16
2.5 Typical industrial crystallizers.....	17
2.6 Industrial crystallization apparatus: (a) cooling crystallizer; (b) evaporative crystallizer; (c) vacuum crystallizer; (d) continuously operated vacuum crystallizer with a circulating device; (e) vacuum crystallizer with a circulating device in a tube; (f) horizontal five-stage vacuum crystallizer; (g) prilling tower for production calcium nitrate.....	19
2.7 Swenson DTB crystallizer.....	23
2.8 DTB crystallizer.....	25
2.9 The metastable regions on a phase diagram.....	28
2.10 Pitched blade turbine.....	30
2.11 CFD modeling procedures.....	43
2.12 CFD results for vacuum pan: (a) with steam jiggers; (b) without steam jiggers.....	50
2.13 Vector of flow field inside an evaporator vessel.....	51

LIST OF FIGURES (CONTINUED)

FIGURE	PAGE
2.14 CFD results for FCC at different configurations: (a) surface deformation; (b) two phase velocity field.....	52
3.1 Momentum source subdomain.....	61
3.2 Flow regions for describing turbulent flow near a wall.....	73
4.1 DTB crystallizer geometry and dimensions. Dimensions are given in meters: (a) side view; (b) top view	98
4.2 3D geometry of DTB crystallizer.....	99
4.3 Composite 2D regions.....	101
4.4 Fine mesh in the specified regions.....	102
4.5 Line positions used to measure the liquid velocity. The positions are given in the form (X,Y,Z).....	106
4.6 Liquid velocity profiles at line 1.....	107
4.7 Liquid velocity profiles at line 2.....	107
4.8 Liquid velocity profiles at line 3.....	108
4.9 Liquid velocity profiles at line 4.....	108
4.10 Liquid velocity profiles at line 5.....	109
4.11 Liquid velocity profiles at line 6.....	109
4.12 Liquid velocity profiles at line 7.....	110
4.13 Liquid velocity profiles at line 8.....	110
4.14 Fine mesh around draft tube.....	111

LIST OF FIGURES (CONTINUED)

FIGURE	PAGE
4.15 Liquid velocity profiles at line 1 with fine mesh around draft tube.....	113
4.16 Liquid velocity profiles at line 2 with fine mesh around draft tube.....	113
4.17 Liquid velocity profiles at line 3 with fine mesh around draft tube.....	114
4.18 Liquid velocity profiles at line 4 with fine mesh around draft tube.....	114
4.19 Liquid velocity profiles at line 5 with fine mesh around draft tube.....	115
4.20 Liquid velocity profiles at line 6 with fine mesh around draft tube.....	115
4.21 Liquid velocity profiles at line 7 with fine mesh around draft tube.....	116
4.22 Liquid velocity profiles at line 8 with fine mesh around draft tube.....	116
4.23 Computational mesh of Run14: (a) before mesh adaptation; (b) after mesh adaptation.....	117
4.24 Examples of computational mesh of a DTB crystallizer for non-isothermal simulation part: (a) before mesh adaptation; (b) after mesh adaptation.....	118
4.25 Liquid velocity vectors for the simulation results from the viscosity values of (a) 0.00152 kg/s/m; (b) 0.00052 kg/s/m.....	120
4.26 Liquid velocity profiles comparing the results from the viscosity values of 0.00152 and 0.00052 kg/s/m.....	121
4.27 Locations of impeller subdomain	122
4.28 The boundary conditions of the DTB crystallizer for isothermal simulation.....	125

LIST OF FIGURES (CONTINUED)

FIGURE	PAGE
4.29 The boundary conditions of the DTB crystallizer for non-isothermal simulation	126
4.30 Initial conditions: (a) pressure; (b) volume fraction.....	129
5.1 The volume defined to calculate the average liquid velocity above the top center of the impeller	134
5.2 Streamlines of liquid flow inside and outside of the draft tube: Case 5.....	136
5.3 Contours of volume fraction of vapor in the vertical center plane: Case 5: (a) overall fraction; (b) magnified scale to enable visualization in the draft tube.....	136
5.4 Contours of absolute pressure in the vertical center plane: Case 5.....	137
5.5 Liquid and vapor velocity at the vertical center plane: Case 5; (a) liquid velocity vectors; (b) contours of liquid velocity; (c) vapor velocity vectors; (d) contours of vapor velocity.....	139
5.6 Liquid velocity vectors around top of draft tube in the vertical center plane: Case 5.....	140
5.7 Vapor velocity vectors at the vapor-liquid interface in the horizontal plane: Case 5; at the height of (a) 2.11 m; (b) 2.12 m.....	140
5.8 Liquid velocity vectors in the horizontal plane: Case 5; at the height of (a) 0.05 m; (b) 0.075 m; (c) 0.0875 m; (d) 0.1 m (the base of the draft tube); (e) 1.9 m; (f) 2 m (the top of the draft tube).....	142

LIST OF FIGURES (CONTINUED)

FIGURE	PAGE
5.9 Liquid velocity vectors at the tank bottom: Case 5.....	143
5.10 The volume defined to calculate the average velocity in the annular settling zone.....	144
5.11 Bubble Reynolds number in the draft tube for case studies 1 to 8 as a function of power transmitted by the impeller	146
5.12 Liquid Reynolds number inside and outside the draft tube, and in the settling zone for case studies 1 to 8 as a function of power transmitted by the impeller	147
5.13 Contours of vapor volume fraction in the vertical center plane for no momentum source addition ($0 \text{ kg/m}^2/\text{s}^2$); (a) overall fraction; (b) magnified scale to enable visualization in the draft tube.....	149
5.14 Contours of vapor volume fraction in the vertical center plane for momentum source addition of $1,000 \text{ kg/m}^2/\text{s}^2$; (a) overall fraction; (b) magnified scale to enable visualization in the draft tube.....	149
5.15 Contours of vapor volume fraction in the vertical center plane for momentum source addition of $4,000 \text{ kg/m}^2/\text{s}^2$; (a) overall fraction; (b) magnified scale to enable visualization in the draft tube	150
5.16 Contours of vapor volume fraction in the vertical center plane for momentum source addition of $7,000 \text{ kg/m}^2/\text{s}^2$; (a) overall fraction; (b) magnified scale to enable visualization in the draft tube	150

LIST OF FIGURES (CONTINUED)

FIGURE	PAGE
5.17 Contours of vapor volume fraction in the vertical center plane for momentum source addition of $10,000 \text{ kg/m}^2/\text{s}^2$; (a) overall fraction; (b) magnified scale to enable visualization in the draft tube	151
5.18 Contours of vapor volume fraction in the vertical center plane for momentum source addition of $15,000 \text{ kg/m}^2/\text{s}^2$; (a) overall fraction; (b) magnified scale to enable visualization in the draft tube	151
5.19 Contours of vapor volume fraction in the vertical center plane for momentum source addition of $25,000 \text{ kg/m}^2/\text{s}^2$; (a) overall fraction; (b) magnified scale to enable visualization in the draft tube.....	152
5.20 Contours of vapor volume fraction in the vertical center plane for momentum source addition of $30,000 \text{ kg/m}^2/\text{s}^2$; (a) overall fraction; (b) magnified scale to enable visualization in the draft tube	152
5.21 Velocity vectors, contours, and streamlines of liquid (a) and vapor (b) in the vertical center plane for momentum source of $0 \text{ kg/m}^2/\text{s}^2$	156
5.22 Velocity vectors, contours, and streamlines of liquid (a) and vapor (b) in the vertical center plane for momentum source of $1,000 \text{ kg/m}^2/\text{s}^2$	157
5.23 Velocity vectors, contours, and streamlines of liquid (a) and vapor (b) in the vertical center plane for momentum source of $4,000 \text{ kg/m}^2/\text{s}^2$	158
5.24 Velocity vectors, contours and streamlines of liquid (a) and vapor (b) in the vertical center plane for momentum source of $7,000 \text{ kg/m}^2/\text{s}^2$	159

LIST OF FIGURES (CONTINUED)

FIGURE	PAGE
5.25 Velocity vectors, contours, and streamlines of liquid (a) and vapor (b) in the vertical center plane for momentum source of 10,000 kg/m ² /s ²	160
5.26 Velocity vectors, contours, and streamlines of liquid (a) and vapor (b) in the vertical center plane for momentum source of 15,000 kg/m ² /s ²	161
5.27 Velocity vectors, contours, and streamlines of liquid (a) and vapor (b) in the vertical center plane for momentum source of 25,000 kg/m ² /s ²	162
5.28 Velocity vectors, contours, and streamlines of liquid (a) and vapor (b) in the vertical center plane for momentum source of 30,000 kg/m ² /s ²	163
5.29 Vapor velocity vectors in the horizontal plane at the vapor-liquid interface for momentum source additions of (a) 4,000 kg/m ² /s ² (at the height of 2.11 m); (b) 7,000 kg/m ² /s ² (at the height of 2.11 m); (c) 10,000 kg/m ² /s ² (at the height of 2.11 m); (d) 15,000 kg/m ² /s ² (at the height of 2.118 m); (e) 25,000 kg/m ² /s ² (at the height of 2.132 m); (f) 30,000 kg/m ² /s ² (at the height of 2.138 m)	165
5.30 Contours of the absolute pressure in the vertical center plane for momentum source additions of (a) 4,000 kg/m ² /s ² ; (b) 7,000 kg/m ² /s ² ; (c) 10,000 kg/m ² /s ² ; (d) 15,000 kg/m ² /s ² ; (e) 25,000 kg/m ² /s ² ; (f) 30,000 kg/m ² /s ²	168
5.31 Terminal velocity for case studies 3 to 8 as a function of fines removal cut-size	169

LIST OF FIGURES (CONTINUED)

FIGURE	PAGE
5.32 Terminal velocity and particle Reynolds number for case studies 3 to 8 as a function of power transmitted by the impeller	169
5.33 Bubble Reynolds number inside the draft tube for case studies 9 to 13 as a function of fines removal flow	170
5.34 Liquid Reynolds number inside and outside the draft tube, and in the settling zone for case studies 9 to 13 as a function of fines removal flow.....	171
5.35 Contours of vapor volume fraction in the vertical center plane for fines removal flow of 0.4672 kg/s; (a) overall fraction; (b) magnified scale to enable visualization in the draft tube	172
5.36 Contours of vapor volume fraction in the vertical center plane for fines removal flow of 1.0063 kg/s; (a) overall fraction; (b) magnified scale to enable visualization in the draft tube	172
5.37 Contours of vapor volume fraction in the vertical center plane for fines removal flow of 1.5454 kg/s; (a) overall fraction; (b) magnified scale to enable visualization in the draft tube ...	173
5.38 Contours of vapor volume fraction in the vertical center plane for fines removal flow of 2.3002 kg/s; (a) overall fraction; (b) magnified scale to enable visualization in the draft tube ...	173

LIST OF FIGURES (CONTINUED)

FIGURE	PAGE
5.39 Contours of vapor volume fraction in the vertical center plane for fines removal flow of 3.594 kg/s; (a) overall fraction; (b) magnified scale to enable visualization in the draft tube	174
5.40 Velocity vectors, contours, and streamlines of liquid (a) and vapor (b) in the vertical center plane for fines removal flow of 0.4672 kg/s	176
5.41 Velocity vectors, contours, and streamlines of liquid (a) and vapor (b) in the vertical center plane for fines removal flow of 1.0063 kg/s.....	177
5.42 Velocity vectors, contours, and streamlines of liquid (a) and vapor (b) in the vertical center plane for fines removal flow of 1.5454 kg/s	178
5.43 Velocity vectors, contours, and streamlines of liquid (a) and vapor (b) in the vertical center plane for fines removal flow of 2.3002 kg/s	179
5.44 Velocity vectors, contours, and streamlines of liquid (a) and vapor (b) in the vertical center plane for fines removal flow of 3.594 kg/s	180
5.45 Vapor velocity vectors in the horizontal plane at the vapor-liquid interface for fines removal flows of (a) 0.4672 kg/s (at the height of 2.128 m); (b) 1.0063 kg/s (at the height of 2.11 m); (c) 1.5454 kg/s (at the height of 2.11 m); (d) 2.3002 kg/s (at the height of 2.11 m); (e) 3.594 kg/s (at the height of 2.11 m).....	182

LIST OF FIGURES (CONTINUED)

FIGURE	PAGE
5.46 Contours of the absolute pressure in the vertical center plane for fines removal flows of (a) 0.4672 kg/s; (b) 1.0063 kg/s; (c) 1.5454 kg/s; (d) 2.3002 kg/s; (e) 3.594 kg/s.....	184
5.47 Terminal velocity for case studies 9 to 13 as a function of fines removal cut-size	186
5.48 Terminal velocity and particle Reynolds number for case studies 9 to 13 as a function of fines removal flow.....	186
5.49 Bubble Reynolds number inside the draft tube for case studies 14 to 18 as a function of product crystal suspension flow rate	187
5.50 Liquid Reynolds number inside and outside the draft tube, and in the settling zone for case studies 14 to 18 as a function of product crystal suspension flow rate	188
5.51 Contours of vapor volume fraction in the vertical center plane for product crystal suspension flow of 0.0599 kg/s; (a) overall fraction; (b) magnified scale to enable visualization in the draft tube.....	189
5.52 Contours of vapor volume fraction in the vertical center plane for product crystal suspension flow of 0.1198 kg/s; (a) overall fraction; (b) magnified scale to enable visualization in the draft tube.....	189

LIST OF FIGURES (CONTINUED)

FIGURE	PAGE
5.53 Contours of vapor volume fraction in the vertical center plane for product crystal suspension flow of 0.1797 kg/s; (a) overall fraction; (b) magnified scale to enable visualization in the draft tube.....	190
5.54 Contours of vapor volume fraction in the vertical center plane for product crystal suspension flow of 0.2636 kg/s; (a) overall fraction; (b) magnified scale to enable visualization in the draft tube.....	190
5.55 Contours of vapor volume fraction in the vertical center plane for product crystal suspension flow of 0.4672 kg/s; (a) overall fraction; (b) magnified scale to enable visualization in the draft tube.....	191
5.56 Velocity vectors, contours, and streamlines of liquid (a) and vapor (b) in the vertical center plane for product crystal suspension flow of 0.0599 kg/s.....	193
5.57 Velocity vectors, contours, and streamlines of liquid (a) and vapor (b) in the vertical center plane for product crystal suspension flow of 0.1198 kg/s.....	194
5.58 Velocity vectors, contours, and streamlines of liquid (a) and vapor (b) in the vertical center plane for product crystal suspension flow of 0.1797 kg/s.....	195

LIST OF FIGURES (CONTINUED)

FIGURE	PAGE
5.59 Velocity vectors, contours, and streamlines of liquid (a) and vapor (b) in the vertical center plane for product crystal suspension flow of 0.2636 kg/s	196
5.60 Velocity vectors, contours, and streamlines of liquid (a) and vapor (b) in the vertical center plane for product crystal suspension flow of 0.4672 kg/s	197
5.61 Vapor velocity vectors in the horizontal plane at the height of 2.11 m (initial height of vapor-liquid interface) for product crystal suspension flows of (a) 0.0599 kg/s; (b) 0.1198 kg/s; (c) 0.1797 kg/s; (d) 0.2636; (e) 0.4672 kg/s	198
5.62 Contours of the absolute pressure in the vertical center plane for product crystal suspension flows of (a) 0.0599 kg/s; (b) 0.1198 kg/s; (c) 0.1797 kg/s; (d) 0.2636 kg/s; (e) 0.4672 kg/s	201
5.63 Terminal velocity for case studies 14 to 18 as a function of fines removal cut-size	202
5.64 Terminal velocity and particle Reynolds number for case studies 14 to 18 as a function of product crystal suspension flow	202
5.65 Liquid velocity vectors of isothermal simulation (case study 5) for (a) free surface flow model; (b) degassing condition at the liquid surface	204

LIST OF FIGURES (CONTINUED)

FIGURE	PAGE
5.66 (a) liquid velocity at the center of draft tube; (b) percent error of liquid velocity of degassing condition from free surface flow model.....	205
5.67 (a) liquid velocity at X= -0.03 m; (b) percent error of liquid velocity of degassing condition from free surface flow model.....	205
5.68 (a) liquid velocity at X = -0.08 m; (b) percent error of liquid velocity of degassing condition from free surface flow model.....	206
5.69 (a) liquid velocity at Y = 0.09 m; (b) percent error of liquid velocity of degassing condition from free surface flow model.....	206
5.70 (a) liquid velocity at Y = 0.3 m; (b) percent error of liquid velocity of degassing condition from free surface flow model.....	207
5.71 (a) liquid velocity at Y = 1.0 m; (b) percent error of liquid velocity of degassing condition from free surface flow model.....	207
5.72 (a) liquid velocity at Y = 1.9 m; (b) percent error of liquid velocity of degassing condition from free surface flow model.....	208
5.73 (a) liquid velocity at Y = 2.0 m; (b) percent error of liquid velocity of degassing condition from free surface flow model.....	208
5.74 (a) liquid velocity at Y = 2.05 m; (b) percent error of liquid velocity of degassing condition from free surface flow model	209
5.75 Evaporation rate for case studies 19 to 22 as a function of heat input.....	210
5.76 Energy balance of a continuously operated crystallizer.....	211

LIST OF FIGURES (CONTINUED)

FIGURE	PAGE
5.77 Contours of liquid temperature for heat source additions of (a) 11,000 kW/m ³ ; (b) 12,000 kW/m ³ ; (c) 13,000 kW/m ³ ; (d) 13,500 kW/m ³	215
5.78 Contours of vapor volume fraction for heat source additions of (a) 11,000 kW/m ³ ; (b) 12,000 kW/m ³ ; (c) 13,000 kW/m ³ ; (d) 13,500 kW/m ³	216
5.79 Contours of absolute pressure for heat source additions of (a) 11,000 kW/m ³ ; (b) 12,000 kW/m ³ ; (c) 13,000 kW/m ³ ; (d) 13,500 kW/m ³	217
5.80 Velocity vectors, contours, and streamlines of liquid (a) and vapor (b) in the vertical center plane for a heat source of 11,000 kW/m ³	220
5.81 Velocity vectors, contours, and streamlines of liquid (a) and vapor (b) in the vertical center plane for a heat source of 12,000 kW/m ³	221
5.82 Velocity vectors, contours, and streamlines of liquid (a) and vapor (b) in the vertical center plane for a heat source of 13,000 kW/m ³	222
5.83 Velocity vectors, contours, and streamlines of liquid (a) and vapor (b) in the vertical center plane for a heat source of 13,500 kW/m ³	223
5.84 Liquid and vapor velocity vector at the top of draft tube for heat source additions of (a) 11,000 kW/m ³ ; (b) 12,000 kW/m ³ ; (c) 13,000 kW/m ³ ; (d) 13,500 kW/m ³	224

LIST OF FIGURES (CONTINUED)

FIGURE	PAGE
D.1 3D streamlines of liquid velocity in DTB crystallizer for momentum source additions of (a) 0 kg/m ² /s ² ; (b) 1,000 kg/m ² /s ² ; (c) 4,000 kg/m ² /s ² ; (d) 7,000 kg/m ² /s ² ; (e) 10,000 kg/m ² /s ² ; (f) 15,000 kg/m ² /s ² ; (g) 25,000 kg/m ² /s ² ; (h) 30,000 kg/m ² /s ²	254
D.2 3D streamlines of liquid velocity in DTB crystallizer for fines removal flows of (a) 0.46722 kg/s; (b) 1.00632 kg/s; (c) 1.54542 kg/s; (d) 2.30016 kg/s; (e) 3.594 kg/s.....	255
D.3 3D streamlines of liquid velocity in DTB crystallizer for product crystal suspension flows of (a) 0.0599 kg/s; (b) 0.1198 kg/s; (c) 0.1797 kg/s; (d) 0.26356 kg/s; (e) 0.46722 kg/s.....	256
D.4 3D streamlines of vapor velocity in DTB crystallizer for momentum source additions of (a) 0 kg/m ² /s ² ; (b) 1,000 kg/m ² /s ² ; (c) 4,000 kg/m ² /s ² ; (d) 7,000 kg/m ² /s ² ; (e) 10,000 kg/m ² /s ² ; (f) 15,000 kg/m ² /s ² ; (g) 25,000 kg/m ² /s ² ; (h) 30,000 kg/m ² /s ²	257
D.5 3D streamlines of vapor velocity in DTB crystallizer for fines removal flows of (a) 0.4672 kg/s; (b) 1.0063 kg/s; (c) 1.5454 kg/s; (d) 2.3002 kg/s; (e) 3.594 kg/s.....	258
D.6 3D streamlines of vapor velocity in DTB crystallizer for product crystal suspension flows of (a) 0.0599 kg/s; (b) 0.1198 kg/s; (c) 0.1797 kg/s; (d) 0.2636 kg/s; (e) .4672 kg/s.....	259

LIST OF FIGURES (CONTINUED)

FIGURE	PAGE
D.7 Liquid velocity vectors at the tank bottom for momentum source additions of (a) 4,000 kg/m ² /s ² ; (b) 7,000 kg/m ² /s ² ; (c) 10,000 kg/m ² /s ² ; (d) 15,000 kg/m ² /s ² ; (e) 25,000 kg/m ² /s ² ; (f) 30,000 kg/m ² /s ² ; (e) 25,000 kg/m ² /s ² ; (f) 30,000 kg/m ² /s ²	260
D.8 Liquid velocity vectors at the tank bottom for fines removal flows of (a) 0.4672 kg/s; (b) 1.0063 kg/s; (c) 1.5454 kg/s; (d) 2.3002 kg/s; (e) 3.594 kg/s.....	261
D.9 Liquid velocity vectors at the tank bottom for product crystal suspension flows of (a) 0.0599 kg/s; (b) 0.1198 kg/s; (c) 0.1797 kg/s; (d) 0.2636 kg/s; (e) 0.4672 kg/s.....	263
D.10 3D streamlines of liquid velocity in DTB crystallizer for heat source additions of (a) 11,000 kW/m ³ ; (b) 12,000 kW/m ³ ; (c) 13,000 kW/m ³ ; (d) 13,500 kW/m ³	265
D.11 3D streamlines of vapor velocity in DTB crystallizer for heat source additions of (a) 11,000 kW/m ³ ; (b) 12,000 kW/m ³ ; (c) 13,000 kW/m ³ ; (d) 13,500 kW/m ³	266
D.12 Liquid velocity vectors at the tank bottom for heat source additions of (a) 11,000 kW/m ³ ; (b) 12,000 kW/m ³ ; (c) 13,000 kW/m ³ ; (d) 13,500 kW/m ³	267

SYMBOLS AND ABBREVIATIONS

A	=	Cross-sectional area or projected area in the direction of flow, [m ²]
	=	Interfacial area per unit volume, [m ⁻¹]
C_D	=	Drag coefficient, [-]
$C_{\varepsilon 1}$	=	$k - \varepsilon$ Turbulent model constant, [1.44]
$C_{\varepsilon 2}$	=	$k - \varepsilon$ Turbulent model constant, [1.92]
C_{μ}	=	$k - \varepsilon$ Turbulent model constant, [0.09]
$C_{\mu b}$	=	Model constant bubble induced turbulence, [0.6]
c	=	Concentration, [kg anhydrous solute/kg solution]
$c^{(d)}$	=	Intephase drag term, [kg/m ³ /s]
c_p	=	Specific constant pressure heat capacity, [kJ/kg/K]
D	=	Drag force, [kg/m ² /s ²]
	=	Impeller diameter or diameter of draft tube, [m]
d	=	Mean diameter, [m] and [microns]
E	=	Specific energy, [kJ/kg]
E_0	=	Eotvos number, [-]
F	=	Force, [kg · m/s ²]
g	=	Gravity magnitude, [m/s ²]
\mathbf{g}	=	Gravity vector, [m/s ²]

SYMBOLS AND ABBREVIATIONS (CONTINUED)

g^*	=	Classification function defined by average population density in the crystallizer divided by the population density in the product, [-]
H	=	Interfacial enthalpy or enthalpy, [kJ/kg]
h	=	Heat transfer coefficient, [kJ/m ² /K]
	=	Specific enthalpy, [kJ/kg]
h^*	=	Classification function defined by average population density in the product divided by the population density in the crystallizer, [-]
h_{tot}	=	Specific total enthalpy, [kJ/kg]
k	=	Turbulent kinetic energy, [m ² /s ²]
L	=	Particle size, [m]
	=	Latent heat, [kJ/kg]
	=	Length scale, [m]
\mathbf{M}	=	Interphase momentum transfer, [kg/m ² /s ²]
m	=	Mass, [kg]
\dot{m}	=	Mass flux, [kg/m ² /s]
	=	Mass flow rate, [kg/s]
N	=	Impeller speed, [rpm]
N_p	=	Number of phase, [#]
Nu	=	Nusselt number, [-]
n	=	Population density, [#m ⁻⁴]
\bar{n}_j	=	Average population density, [#m ⁻⁴]

SYMBOLS AND ABBREVIATIONS (CONTINUED)

n_p	=	Number of bubble per unit volume, [#/ m^3]
P	=	Power, [W] or [kW]
	=	Pressure, [Pa]
Pr	=	Prandtl number, [-]
P_k	=	Shear production of turbulent, [$kg/m/s^3$]
Pr_t	=	Turbulent Prandtl number, [-]
p'	=	Modified pressure, [Pa]
Q	=	Interphase heat transfer, [kW/m^3]
\dot{Q}	=	Heat rate, [kW]
q	=	Heat flux, [kW/m^2]
Re	=	Reynolds number, [-]
r	=	Volume fraction, [-]
	=	Radius of draft tube, [m]
Sc_t	=	Turbulent Schmidt number, [-]
S_E	=	Heat source, [kW/m^3]
S_{MS}	=	Mass source, [$kg/m^3/s$]
S_M	=	Momentum source, [$kg/m^2/s^2$]
S_{spec}	=	Specified momentum source, [$kg/m^2/s^2$]
s	=	Relative supersaturation, [-]
T	=	Temperature, [K]
	=	Time scale, [s]

SYMBOLS AND ABBREVIATIONS (CONTINUED)

t	=	Time, [s]
U	=	Velocity magnitude, [m/s]
\mathbf{U}	=	Vector of velocity, [m/s]
\bar{U}	=	Mean velocity, [m/s]
U_t	=	Terminal velocity, [m/s]
	=	Tangent velocity, [m/s]
U_{ts}	=	Hindered settling velocity, [m/s]
\mathbf{u}	=	Fluctuating velocity component in the turbulent flow, [m/s]
u^+	=	The logarithmic relation for the near wall velocity, [-]
u_τ	=	Friction velocity, [m/s]
V	=	Volume, [m ³]
\dot{W}	=	Work, [kW]
X,Y,Z	=	Cartesian coordinates
Z	=	Spatial variable to express the location in the crystallizer
Z_0	=	Spatial variable to express the location of product removal
y^+	=	Dimensionless distance from the wall, [-]

SYMBOLS AND ABBREVIATIONS (CONTINUED)

Greek Symbols

δ	=	The identity matrix, [-]
ε	=	Turbulence eddy dissipation, [m^2/s^3]
Γ	=	Interphase mass transfer, [$\text{kg}/\text{m}^3/\text{s}$]
Γ_t	=	Turbulent diffusivity, [$\text{kg}/\text{m}/\text{s}$]
κ	=	Von Karman constant, [0.41]
λ	=	Thermal conductivity, [$\text{W}/\text{m}/\text{K}$]
ρ	=	Density, [kg/m^3]
μ	=	Dynamic viscosity, [$\text{kg}/\text{s}/\text{m}$]
μ_{eff}	=	Effective viscosity, [$\text{kg}/\text{m}/\text{s}$]
μ_t	=	Turbulent viscosity, [$\text{kg}/\text{m}/\text{s}$]
μ_{tb}	=	Particle induced eddy viscosity, [$\text{kg}/\text{m}/\text{s}$]
π	=	Constant, [3.14159...]
ϕ	=	Transported variables, [-]
χ	=	Volume fraction of solid in the suspension, [-]
σ	=	Surface tension coefficient, [kg/s^2]
σ_ε	=	$k - \varepsilon$ Turbulent model constant, [1.3]
σ_k	=	Turbulent model constant for the k equation, [1.0]
τ_ω	=	Wall shear stress, [$\text{kg}/\text{m}/\text{s}^2$]

SYMBOLS AND ABBREVIATIONS (CONTINUED)

Superscripts

D	=	Drag
L	=	Lift force
LUB	=	Wall lubrication force
TD	=	Turbulent dispersion force
T	=	Matrix transpose
sat,sol	=	Saturated solution
sat,vap	=	Saturated vapor
VM	=	Virtual mass force
$+$	=	Positive value

Subscripts

c	=	Continuous phase (Liquid)
d	=	Dispersed phase (Vapor)
F	=	Feed
Fines	=	Fines
p	=	Particle, droplet, and bubble
	=	Product
s	=	Interfacial
sat	=	Saturation
to	=	Input

SYMBOLS AND ABBREVIATIONS (CONTINUED)

v = Vapor

$\alpha\beta$ = From phase β to phase α

α = Phase index

β = Phase index

CHAPTER I

INTRODUCTION

1.1 Background and Significance

Crystallization is a separation and purification process, which is a phase transition process of one or more substances from an amorphous solid, liquid or gaseous state to a crystalline state. In crystallization from solution a species crystallizes from a liquid mixture, which will occur only if the solute concentration exceeds its solubility. This type of solution is said to be supersaturated. Supersaturation can be obtained by many methods such as cooling, evaporation, vacuum, pressure, and reaction, or a combination of these processes. Evaporative crystallization is one of the most common processes used in industrial crystallizers. It is a process in which the mixture requires heating to achieve a supersaturated state.

Crystallization is used in the production of a wide range of materials from bulk commodity chemicals to specialty chemicals and pharmaceuticals. Continuous crystallizers are the most common used for production of industrial chemicals, due to their efficiency of operation. The common configurations of the continuous units include the forced circulation (FC), draft-tube-baffle (DTB), and fluidized-suspension (FS) units. They are normally operated with evaporating or cooling, and mixed-suspension, mixed-product removal (MSMPR) modes. The evaporating or cooling modes can be achieved either adiabatically or isothermally by means of indirect heat input via a heat exchanger (Genck, 2004). In the MSMPR mode (also called

circulating magma crystallizers), the liquid phase and the solid phase in the crystallizer are perfectly mixed, and the particle size distribution of the product crystals is the same as the distribution in the crystallizer (Randolph and Larson, 1988). Many mixed suspension crystallizers are designed to modify the crystal size distribution (CSD) by the systems of fines destruction, and clear liquid advance (deliberate removal of mother liquor) to change the slurry density and/or product classification.

Many industrial crystallizers are of the DTB crystallizer type. The DTB crystallizer is a combination of the MSMPR crystallizer (crystallization zone) and a classifier. The classifier is employed to remove particles of a given size from the crystallizer vessel. The DTB crystallizer produces larger crystals, and narrows their size distribution. “It has been studied well both by its creators and by academia. While it suffers the disadvantage of not being easily reproduced in small scale, the design parameters are easy to define and control accurately. As a result, its understanding is based on well-proven theoretical work, and this makes the DTB easy to apply to new crystallization systems, troubleshoot, and optimize” (Fakatselis, 2006).

The design and scale-up of industrial crystallizers is one of the most complex tasks in process engineering and there are many factors to consider, such as yield, selectivity, purity, and particle size distribution. The ease of the separation process increases with an increase in particle size so the prediction of the PSD is an important part of the crystallizer design. The particle size distribution is commonly modeled by population balance equations, as a function of process conditions, crystallizer layout, and type of crystallization process. This equation is used to describe the crystal population distribution dynamics. It can be influenced through settling, attrition,

agglomeration, and local flow conditions. These factors, which are important factors in the design of crystallizers, are based on parameters directly linked to the concept of mixing, such as power input per unit volume (impeller speed), suspension, shear, and heat transfer.

In practice, much of the retained mother liquid in the crystal product is separated by filtration or centrifuging, and the balance is removed by washing with fresh solvent. The effectiveness of these purification steps depends on the size and uniformity of the crystals. It is clear that the important objectives in crystallization are good yield, high purity, and the appearance and size range of a crystalline product. If the crystals are used in other processes, suitable size and size uniformity are desirable for filtering, washing, reacting with other chemicals, transporting, and storing the crystals. "If the crystals are to be marketable as a final product, customers need individual crystals that must be strong nonaggregated, uniform in size, and noncaking in the package" (McCabe, Smith, and Harriott, 2001). For these reasons the PSD must be under control.

Uniformity of crystals (a narrow CSD) is an important factor in manufacturing processes and the market. Poor CSD causes problems in manufacturing processes, such as filtration of the crystals if the crystals are too small, causing clogging of filter media, increased pressure drip, and damage to the filter media. Too large crystal size results in the crystals settling to the bottom of the tank and then agglomerating. A wide range of crystal sizes results in the costs to separate the crystals being increased. Wide CSD also causes marketing problems, such as when the crystal sizes are not in the desirable range, resulting in a low quality product, which reduces the sale price or requires additional post processing to separate and classify.

There are several factors that impact crystal size and uniformity of crystals and the following are samples of these factors (Tangtongsakulwong, 2003):

1. Flow characteristic and mixing of solution in crystallizer.
 2. Crystallization temperature.
 3. Concentration of feed solution.
 4. Saturation level of solution.
- etc.

The flow characteristic, mixing, temperature, and density distributions in the crystallizer are important effects in determining the crystal size and uniformity of the crystals. Good mixing supports the uniformity of the crystals, and hence it is important to study these effects in industrial crystallizers.

In this thesis, a DTB crystallizer (or continuous operating vacuum crystallizer with a circulating device, draft tube, and settling space) was used to study the flow characteristics of liquid (mother liquor) and vapor.

There are three methods to study engineering processes: these are experimental, analytical, and numerical methods. Experimental methods are typically high cost methods because of the need to construct a real crystallizer, so it is difficult to study the effects of some parameters that are difficult to change, and it is not possible to control some external conditions or some circumstances in the crystallizer. For analytical methods, the difficulties are based on construction of the mathematical equations and producing reasonable assumptions that result in a system of equations that has an analytical solution. The complexity of the geometry of industrial crystallizer makes analytical solutions impossible to achieve.

Numerical methods are computer aided calculation techniques to find solutions to complex problems. Currently, simulations are conducted to analyze problems and design process equipment or processes in engineering work. In the fluid dynamics field, computers can analyze problems to find velocity, temperature, pressure, and other physical thermodynamic parameters, and this field is called computational fluid dynamics (CFD). This method is a body of knowledge and techniques to solve mathematical models of fluid dynamics on digital computers. Analysis of the different quantities in the process, and graphical solutions can be made by this method. This allows researchers to understand the flow phenomena, and to develop or alter design in the computer until a desirable solution is obtained before constructing a real system or model. This method reduces cost and time, there is no waste and no risk, it consumes less energy and is safer, etc. when compared to the experimental method.

CFD uses a range of space and time discretization methods in order to enable a numerical solution to be calculated. The finite volume technique is the most common method to discretize the volume in commercial CFD code. Firstly, the volume being investigated is discretized into small tetrahedral elements with nodes at each corner of the element. The information relating to the simulation is stored in the nodes of the elements, and equations of flow can then be applied to each finite volume in the simulation. The last pieces of information that are required by the software are the boundary conditions for each of the boundaries of the total volume (flow rate at the inlet, conditions at the outlets, etc,...), the physical properties of the fluid(s) and particles in the system, and the physical model that are required for the system.

Due to the advantages of the CFD technique, this work is conducted using the commercial CFD software “ANSYS CFX-10.0” to perform 3D (three dimension) simulation with the finite volume method using an unstructured mesh to study the two-phase (vapor-liquid) flow and heat transfer behavior of turbulent steady-state-flow in the DTB crystallizer.

1.2 Objectives

The objectives of this thesis are discussed in the following points:

1.2.1 To study the two-phase (vapor and liquid) flow characteristics in the DTB crystallizer. Note that the impact of solids on the flow field is negligible because the particles are mostly sufficiently small to be considered to follow the liquid flow, and that the particle suspension is reasonably dilute.

1.2.2 To study the effect of the product crystal suspension flow rate and fines removal flow rate on the flow characteristics and the classification of crystals.

1.2.3 To study the effect of the momentum source strength (this is the representation of the impeller speed) on the flow characteristics and the classification of crystals.

1.2.4 To study the effect of heat and mass transfer via the evaporation of liquid on the flow characteristics and the classification of crystals.

1.3 Scope and Assumptions of Work

1.3.1 Overall scope and assumptions

1.3.1.1 The work is divided into two parts; modeling the DTB crystallizer using an isothermal simulation and modeling the DTB crystallizer using a non-isothermal simulation.

1.3.1.2 The flow in the crystallizer was modeled with two phases (vapor and liquid).

1.3.1.3 A water solution with 26.66 % NaCl is the liquid phase in the crystallizer, and water-vapor is the vapor phase. The physical properties of these materials are constant.

1.3.1.4 The impeller was modeled as an axial momentum source term (Pericleous and Patel, 1987) that has been added at the base of the draft tube, at the position and size of the true impeller. This model can reduce the computation time and model complexity of the real impeller. It is not necessary to model a radial momentum source because it does not create a significance difference in the fluid flow profile for baffled crystallizers (this is proposed by Tangtongkulwong, 2003).

1.3.1.5 Steady state flow is assumed throughout because the industrial crystallizer is mostly operated as a steady-state continuous process.

1.3.1.6 Turbulent flow is assumed throughout because the mixing process in the crystallizer normally produces turbulent flow.

1.3.1.7 The DTB crystallizer was studied using the CFD modeling software ANSYS CFX-10.0. A 3D geometry was used to account for the strong 3D flow.

1.3.2 Specific scope and assumptions of the isothermal simulation

1.3.2.1 A DTB crystallizer with an external heat exchanger was modeled.

1.3.2.2 The effect of the temperature was not considered because the vapor is assumed to form in an external heat exchanger before being fed into the crystallizer, which leads to the temperature rise in the circulated magma caused by the impeller and heat of crystallization to be a low value (in the order of 1 - 2 °C) (Genck, 2004).

1.3.2.3 Both liquid and vapor was fed to the crystallizer.

1.3.3 Specific scope and assumptions of the non-isothermal simulation

1.3.3.1 A DTB crystallizer with both external and internal heat exchangers was modeled.

1.3.3.2 This simulation considers the effect of temperature variation due to heat and mass transfer.

1.3.3.3 Only liquid was fed to the crystallizer.

1.3.3.4 Mass and heat transfer via the evaporation of liquid was modeled.

1.3.3.5 The internal heat exchanger could be modeled as a heat source from a solid object (such as a heat exchanger pipe). However, for convenience the bulk heat source can be specified directly at the impeller domain, which is an acceptable approach considering the temperature rise in the crystallizer caused by the heat exchanger is a low value (in the order of 1 - 2 °C) to reach the boiling temperature, and normally the heat exchanger is located near the impeller. This method can reduce the computation time and model complexity of the solid heat source.

1.3.3.6 The saturation temperature (with respect to vapor-liquid equilibrium) of the liquid is constant.

1.4 Outcomes of the Research

The outcomes of this thesis are following:

1.4.1 Better understanding of flow phenomena in DTB crystallizers has been achieved, which has led to a better description of the effects of feed flow, fines removal flow, product crystal suspension flow, momentum source (or impeller speed), and heat and mass transfer via the evaporation of liquid to the flow characteristics and product crystal size.

1.4.2 This study will help to improve the design and upgrade of crystallizers and their operations.

1.4.3 To facilitate and develop the CFD knowledge for the chemical process industries and other industries.

1.4.4 To strengthen and set up engineering knowledge and work experience through the experience of research methodology in the CFD field.

CHAPTER II

THEORY AND LITERATURE REVIEW

The Theory and Literature Review section will focus on crystallization from solution, industrial crystallizers, the effect of hydrodynamics in crystallizers, CFD modeling of crystallizers and summations of the published literature.

2.1 Crystallization from Solution

Crystallization may be defined as a phase change in which a crystalline product is obtained from solution (Myerson, 2002). A solution is a homogeneous single phase that is formed by the mixing of two or more species. Solutions are normally liquid, however solutions may include solids and even gases. Typically the term solution means a liquid solution, consisting of a solvent, which is a liquid as a pure species at the conditions, (T, P) , of the solution, and a solute, which is a solid as a pure species at the conditions of interest. The term melt means a material that is solid at ambient conditions and is heated until it becomes a molten liquid. Melts may be pure material or they may be mixtures of materials.

Crystallization from solution occurs when the solute concentration in a solvent exceeds its solubility (Randolph and Larson, 1988). This type of solution is said to be supersaturated. Figure 2.1 shows the solubility of a general solution, where c_s is the saturation concentration and relative supersaturation is defined as

$$s = (c - c_s) / c_s \quad (2.1)$$

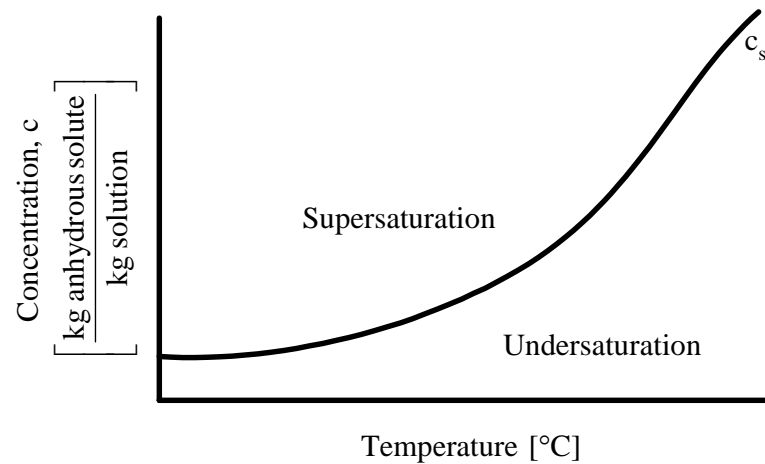


Figure 2.1 Solubility of a general solution.

Crystallization at different supersaturations causes different crystal sizes and shapes. Therefore, a good CSD will occur by having the supersaturation uniform throughout the crystallizer; good mixing in the crystallizer supports this purpose.

Industrial crystallization from solution is carried out in a wide range of processing equipment, but we can draw a general schematic, as in Figure 2.2. If looking at the general period of operation the streams shown may be present, or absent from a particular type of operation. The following terms are typically used to distinguish particular modes of operation:

2.1.1 Continuous, steady-state crystallizers

The mass flow rates of the inflow stream equal the outflow stream. There is (essentially) no time variation in any of the crystal or fluid properties in the unit. The unit will not operate at equilibrium conditions at any time.

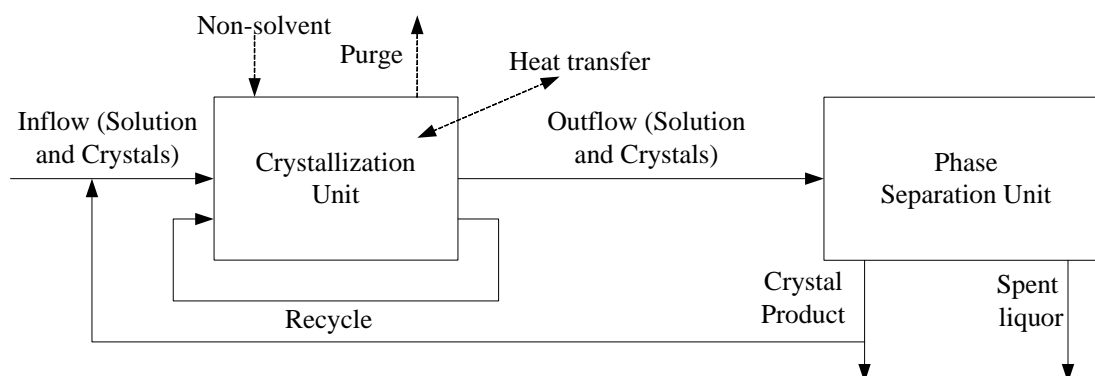


Figure 2.2 General schematic of a crystallization process. (Flood, 2003)

2.1.2 Batch crystallizer

There are no inflow and outflow streams (batch mode) or one of the inflow or outflow streams (semi-batch mode) is not present in these types of crystallizers. The fluid and physical properties in the vessel will vary with time (unsteady-state) during the batch. The contents of the vessel may be allowed enough time to reach a state very close to the equilibrium condition, or the batch may be completed before this time. This crystallizer is not common for large scale operations since batch crystallizers usually require larger operating and equipment cost. The main advantages of batch crystallizers are that they can produce a narrow range of product crystal sizes, can sometimes produce slightly more pure products, and are very flexible for plants that produce small quantities of a wide range of products.

2.1.3 Seeded crystallizer

In seeded crystallizers, solute crystals are added to the feed of the crystallizer to initiate crystallization. The purposes of this operation are to remove the requirement to operate at driving forces high enough to produce nuclei (since crystals

already exist in the liquor the nucleation step is not required), or to promote the formation of low numbers of nuclei at low driving forces. Seeding may be performed in both batch and continuous crystallizers.

2.1.4 Cooling crystallization

The process of cooling crystallization can be used when the solubility of solute greatly increases as the temperature increases; NaNO_3 , NH_4CO_3 , NaClO_3 , KNO_3 , etc. are examples of this type of solubility (see Figures 2.3). The simplest type of this process is where the solution is evaporated at high temperature, where the solubility is high (the solution is undersaturated) before being fed to the crystallizer. This feed solution is cooled via either an external jacket or a cooler inside the crystallizer until the crystallizing species becomes supersaturated (while the amount of solute is constant), and thus crystal is produced.

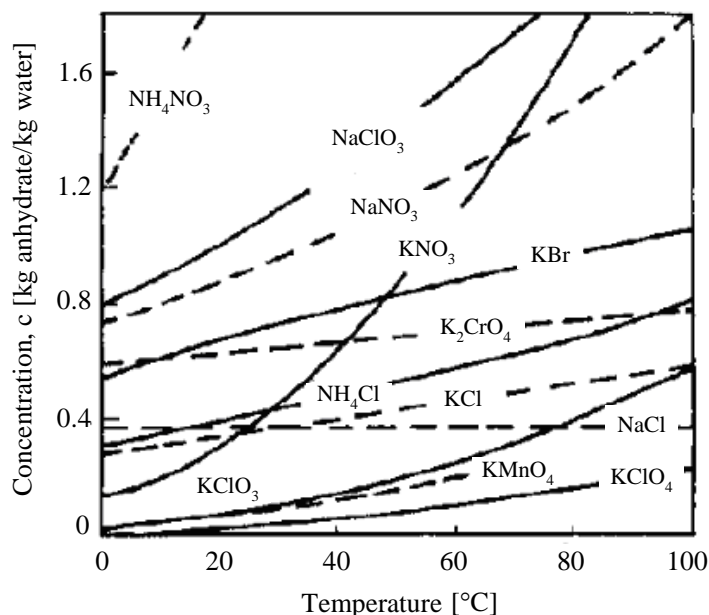


Figure 2.3 Solubility curves for several anhydrites. (Mersmann, 2001)

2.1.5 Evaporative crystallization

The process of evaporative crystallization can be used when the solubility of the solute increases only slightly, remains almost constant, or even decreases with temperature; NaCl is an example of this solubility (see Figure 2.3). The concepts of this mode are that the undersaturated solution is fed into the crystallizer, and then this feed solution is heated to the boiling point of the solution so that the solvent evaporates. The boiling point of the solution is usually a function of pressure so boiling tends to take place at the surface of the liquid, which can lead to a high level of supersaturation. On the other hand, in crystallizers where there are heat transfer tubes in the bulk solution and weak mixing (i.e. sugar crystallization) the hottest point is near the tubes, and boiling occurs there despite the pressure differential.

2.1.6 Vacuum crystallization

In vacuum crystallization, the solution is evaporated and cooled simultaneously by decreasing the temperature and pressure. The vacuum is often created above the liquid level and maintained by steam jet compressors. When the evaporation occurs, the solution loses the energy required to evaporate the solvent (heat of evaporation) causing the solution to cool and become supersaturated (in addition to the supersaturation caused by solvent loss), and thus partially crystallize.

2.1.7 Non-solvent (drowning-out) crystallization

If the supersaturation required for the crystallization is achieved through the addition of a solvent designed to reduce the solubility of the solute, the process is known as a non-solvent (or anti-solvent) crystallization. The addition of other solutes (other crystallizable species; species not considered as solvents) designed to reduce

solubility is known as drowning-out crystallization. Drowning-out crystallization may offer the advantage over other processes of reducing energy consumption. As the enthalpy of evaporation of drowning-out agents is usually considerably smaller than that for solvent the drowning-out agent can be recovered easily by distillation. This process can be combined with other processes that enable energy to be saved.

2.1.8 Pressure crystallization

Pressure crystallization is a process used when the solubility increases with temperature until it reaches a maximum, after which the solubility decreases as the temperature increases, see Figure 2.4 (Mersmann, 2001). This applies to salt solution, such as Na_2SO_4 and Na_2SO_3 . This method occurs when aqueous solutions of these salts are held under pressure to avoid evaporation of solvent, and are heated above the temperature of their maximum solubility; at this point nuclei form and grow due to supersaturation. In these systems, the compression of the liquid solution and the high pressure in the crystallizer involve additional costs, but the solvent does not need to be evaporated. Encrustation can be reduced since nucleation takes place in the bulk of the solution.

2.1.9 Reaction crystallization (precipitation)

Reaction crystallization is where supersaturation is achieved by adding individual reagents to the crystallization vessel. The reaction product forms at a concentration higher than its solubility. One or more reactants react with one or more components in the liquid phase for homogeneous reaction crystallization, and a reactant is often added in the gas or vapor form for heterogeneous reaction crystallization.

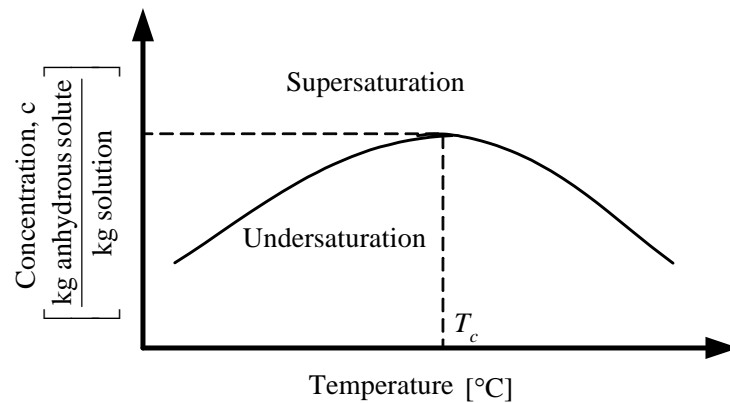


Figure 2.4 Solubility of some solutions.

2.1.10 Purge streams

A purge stream may also be necessary to remove a particular fraction of the crystalline content of the vessel in order to improve the particle size distribution of the product.

2.1.11 Recycle streams

A recycle stream may also be necessary to recycle either the crystal or the solution phase. For example, the smallest crystals that are present in the suspension might be removed from the vessel, destroyed by heating, and the fluid passed back to the suspension so that the remaining solute can be redeposited onto the larger crystals.

2.2 Industrial Crystallizers

2.2.1 Industrial crystallization apparatus

In industrial crystallization from solution, where crystals are generated out of a solution in a crystallizer, the suspension must be mixed, and deposition onto

the equipment must be avoided. This leads to the entire suspension, including coarse crystals, needing to be circulated by a circulating device (stirrer or axial/radial pump). In the former case, relatively strong attrition occurs, especially of large crystals. Figure 2.5 shows typical industrial crystallizers. The fluidized bed (FB) crystallizer differs from other crystallizers by the fact that a suspension flow containing only small crystals (e.g. under $100\ \mu\text{m}$) is conducted by the circulation device (pump). This is since the larger crystals are heavier than the smaller crystals so the small size crystals flow up by the pump and create a fluidized bed, and the large size crystals settle at the bottom tank by the gravitational force and flow out to be the products. Therefore, FB crystallizers generally produce a coarser product than stirred vessel (STR) and forced-circulation (FC) crystallizers. The advantage of the FC and the FB over the STR is that the ratio of the heat exchanger surface to the crystallizer volume can be maintained when scaling up the crystallizers due to the external heat exchanger.

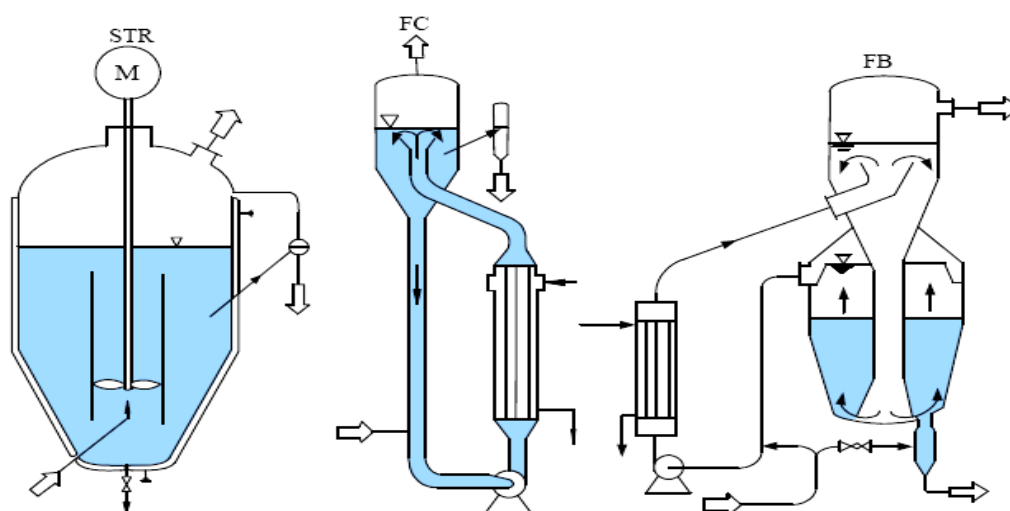


Figure 2.5 Typical industrial crystallizers. (Mersmann, 2001)

The FB crystallizer is illustrated in Figure 2.6 (a) and 2.6 (b); this type of crystallizer is a classifying crystallizer to attain spatial separation of supersaturation and growth by external circulation of the solution. “The solution is supersaturated in a virtually crystal-free zone, whereas the supersaturation in the growth zone is given over the crystallizer” (Mersmann, 2001). A fluidized bed is created by the upward flow, since the growth zone is designed in this way.

Figure 2.6 (a) shows a cooling crystallizer with an external heat exchanger. A small flow of warm, concentrated inlet solution is added directly to the much larger circulating flow upstream of the heat exchanger. The supersaturated solution in the heat exchanger enters the crystallization chamber at bottom of the crystallizer and suspends the crystals. Despite the minimal temperature difference allowed (usually under 2 °C) between the circulated solution and solvent, high heat flux densities can be obtained. The solid is separated by enlarging the flow cross-section. The growing crystals sink to lower levels by their rate of sedimentation until they finally reach the product outlet.

Figure 2.6 (b) shows an evaporative crystallizer with an external boiler, it looks similar to the cooling crystallizer but has a different method of reaching supersaturation (evaporation rather than cooling). The evaporation unit and crystallizer are joined directly to each other. The crystallization vessel is connected to the heat exchanger by a circulation pump and the fresh solution is fed into the circulation flow.

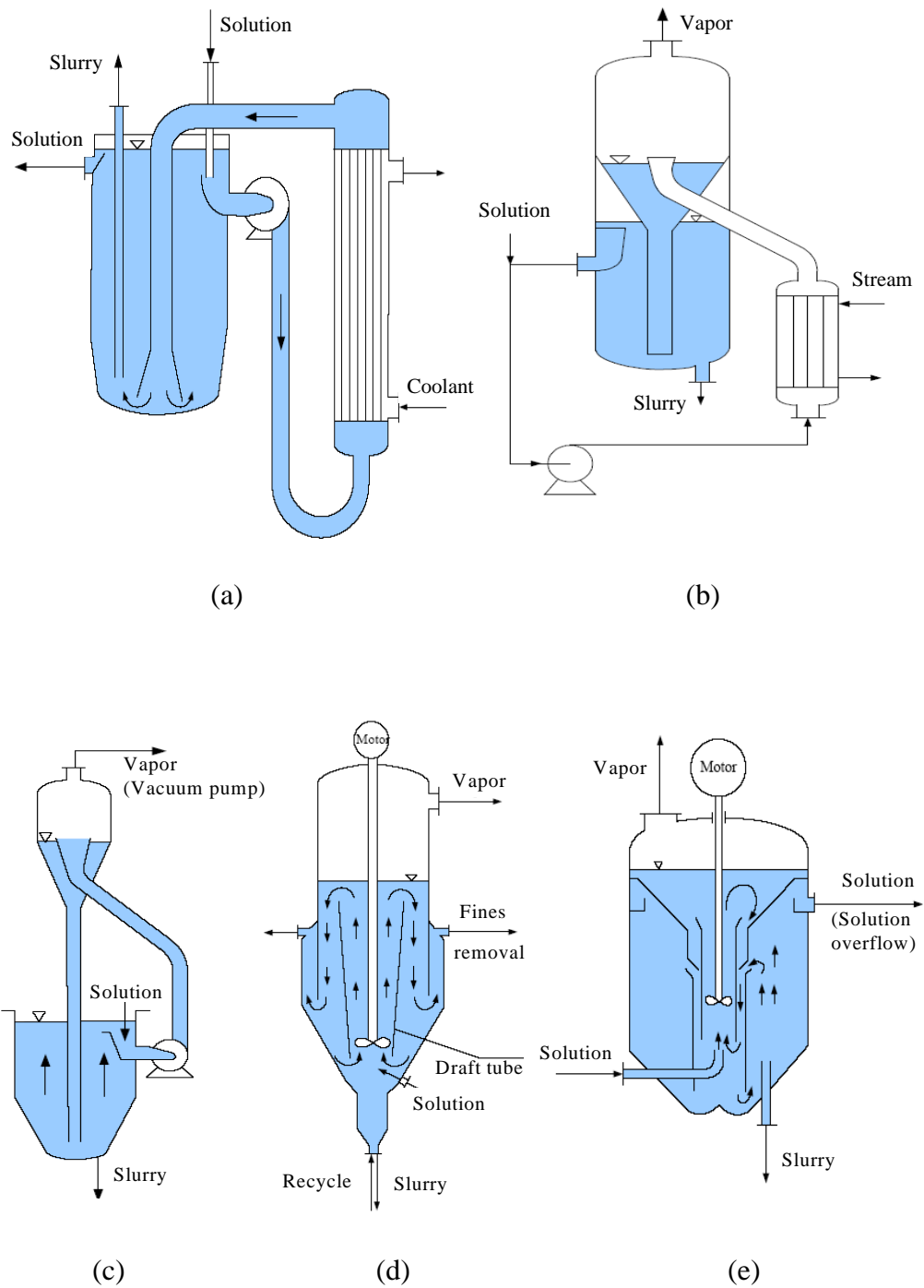


Figure 2.6 Industrial crystallization apparatus: (a) cooling crystallizer; (b) evaporative crystallizer; (c) vacuum crystallizer; (d) continuously operated vacuum crystallizer with a circulating device; (e) vacuum crystallizer with a circulating device in a tube; *(continued)*

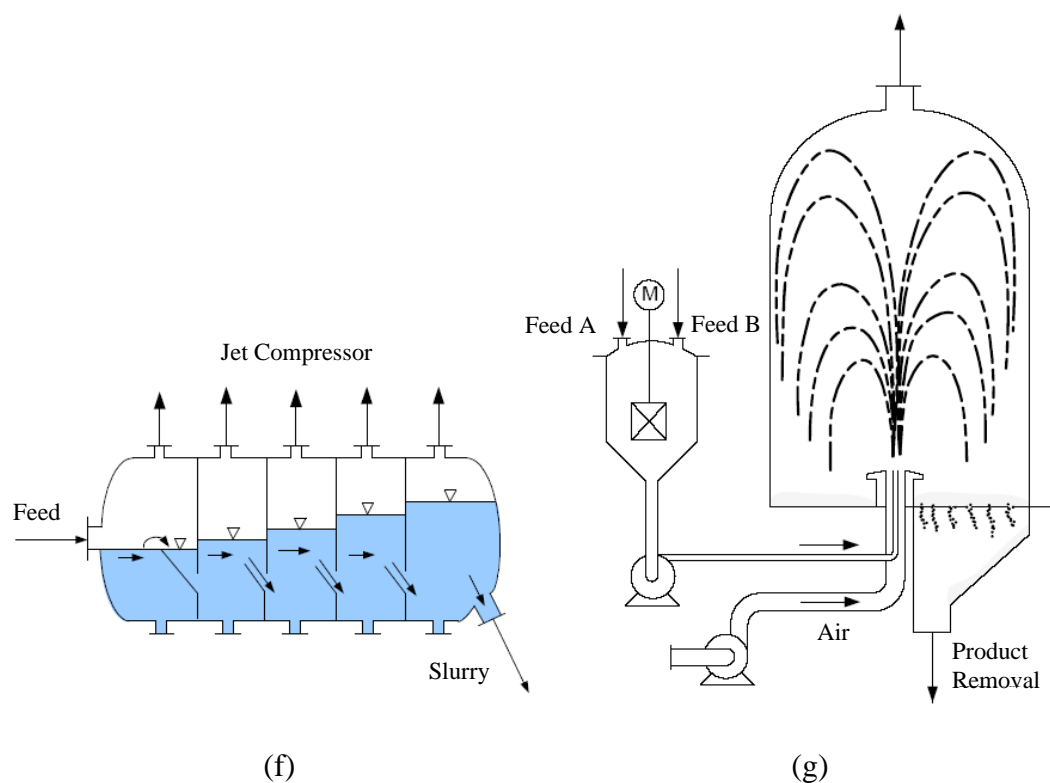


Figure 2.6 (continued) (f) horizontal five-stage vacuum crystallizer; (g) prilling tower for production calcium nitrate. (Mersmann, 2001)

Figure 2.6 (c) shows a vacuum cooling crystallizer with separate crystallization and evaporation chambers. This does not have a heat exchanger in the crystallizer, and uses an open vessel under atmospheric pressure as the crystallization vessel. Hot saturated feed enters at the suction pump, and mixes with the mother liquor passing through pump, and is then cooled back to the crystallizer temperature by evaporation in the evaporation chamber (Strickland-Constable, 1968). The difference in pressure relative to the vacuum part is compensated by the hydrostatic pressure of the liquid.

Figure 2.6 (d) shows a vacuum crystallizer with upward flow in the tube and agitator baffles. This crystallizer type produces a coarse crystal product. The circulating device is built into the lower part of the draft tube. Fresh solution is fed directly into the tube. The crystals enter the vicinity of the vaporizing surface, where supersaturation is largest. Fines can be removed by an overflow in the ring chamber. The coarse part of the narrow crystal size distribution is separated by a screening tube at the lower end of the crystallizer.

Figure 2.6 (e) shows a two suspension circulation flow in a fluidized-bed crystallizer, which has two concentric tubes, a bottom tube with a circulating device and an external ejection tube and continuous gap around the crystallizer. A fine product exists primarily in the inner circulation loop, which has a fast upward flow in the inner tube and a high supersaturation value at the evaporation surface. In the external chamber, a classifying fluidized bed is formed and coarse crystals exist; fine crystals are carried away and drawn into the inner circulation via the ejector gap. The overflow above the classifying zone influences the crystal content. Fresh solution is fed directly into the tube. The product is withdrawn from the classifying zone.

Figure 2.6 (f) shows a multistage crystallizer in a horizontal position without moving parts. It is suitable for vacuum-cooling crystallization. The evaporation chambers are separated from each other by several partitions. Fresh solution is fed in at the first stage and is cooled continuously from stage to stage. The product is withdrawn from the last stage, which has the lowest pressure. Steam jets maintain the various low pressures. In many cases, the liquid is brought into motion in the individual stage by bubbling gas (air) through the stage.

The final crystallizer is shown in Figure 2.6 (g). In this crystallizer an air flow cools the solution and causes the solvent to evaporate. The solid crystals drop to the floor of the prilling tower, from where they are mechanically transported to a cooling drum.

2.2.2 Draft tube baffle (DTB) crystallizers

The DTB crystallizer is shown in Figure 2.7 (which is similar to Figure 2.6 (d)). This is a vacuum crystallizer with upward flow in the tube and agitator baffles, and consists of a body which has growing crystals and circulation from the lower portion to the boiling surface. The mechanical circulation has a significant impact on the level of nucleation in the crystallizer. For this reason, low speed impellers in the draft tube are sometimes incorporated into the body to reduce the shear force seen by the circulating pump. Surrounding the suspended magma of growing crystals is an annular settling zone; in this zone a stream of mother liquor can be removed and fine crystals follow this stream. The fine crystals separate from the growing suspension of crystals by gravitational settling in the annular baffle zone.

In the case of evaporative-DTB crystallizers, fine crystals in the mother liquor leaving the baffle zone are sent to a settler and heat exchanger. The fines are destroyed by heating, mixed with dilute feed, or water, and the warm or heated mother liquor is returned to the suction of the propeller circulator. Incoming feed is also mixed at the eye of the propeller. In this evaporative crystallizer, the temperature rise in the circulated magma caused by the mixing of the feed or heated mother liquor is in the order of 1-2 °C. This low temperature rise can be achieved at very low power consumption because of the small head loss in the circulated liquid-solid circulation path.

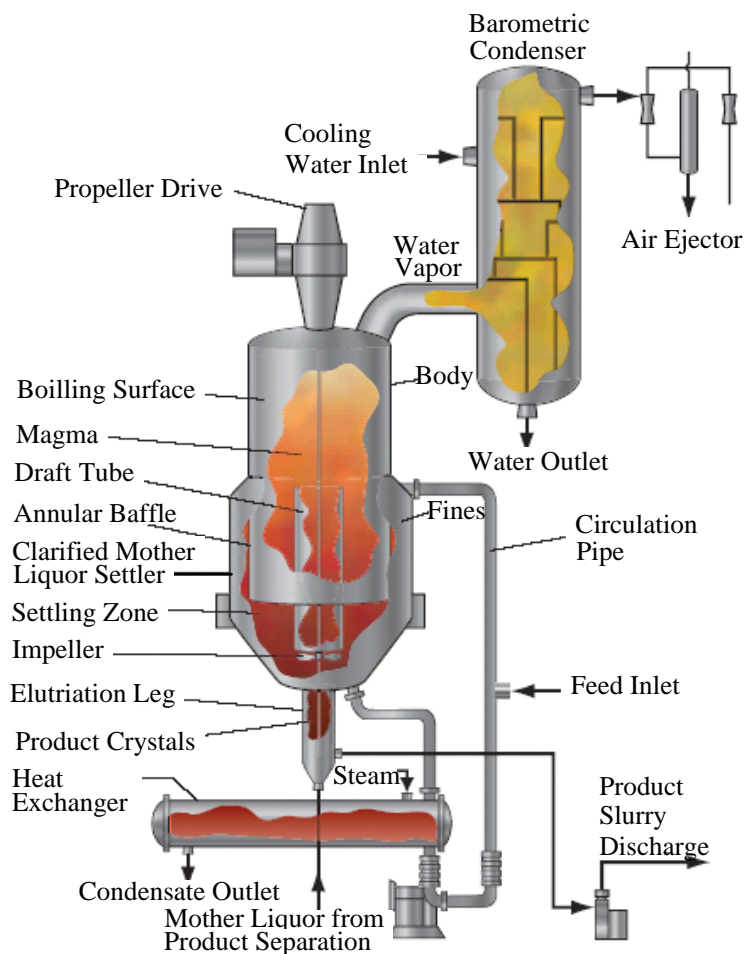


Figure 2.7 Swenson DTB crystallizer. (Genck, 2004)

The amount of temperature change as the slurry is pumped through the boiling surface limits the amount of supersaturation created per pass to about 1 °C and thereby limits the nucleation rate to very low values. The boiling action is concentrated mostly in the center of the vessel and is well distributed across the surface by the vertical inlet. The active volume of a DTB (including areas inside and outside the draft tube and excluding areas behind the baffle) typically contains a solids loading equal to 25-50 % of the apparent settled volume. Decreasing crystallization buildup on the wall of the crystallizer and extending the operating

cycle can be achieved by lowering the temperature drop at the boiling surface, and creating a uniform distribution of boiling created by the circulation pattern.

In the fines removal process, the residence time for the fines is less than the residence time for the product. The baffles can be segmented to one or more settling sections and these are utilized to separate fine crystalline material from coarse crystals. Changing either the flow rate in the active baffle area or the amount of baffle area is used to control the CSD in the body of the crystallizer via the vertical velocity of the slurry in the baffle area, and the maximum crystal size that will be removed and dissolved.

Increasing the solids content of the slurry within the crystallizer body is sometime done by withdrawing a stream of mother liquor from the baffle zone, which increases the thickness of the slurry in the body. High slurry densities tend to reduce the efficiency of baffle performance. To improve performance, one may add a lamella plate in the main body to direct the flow vertically at the baffle entrance, or install alternating donut baffles in the settling zone behind the regular baffles. These donuts dissipate large liquid eddies that can trap and carry out undesirable larger crystals.

All techniques used in this crystallizer are employed to produce a larger product crystal size with a narrow size distribution. This type of crystallizer is used primarily in production of a variety of large-size crystalline material such as Ammonium Sulfate, Potassium Chloride and Diammonium Phosphate for the fertilizer industry.

An example of this crystallizer is shown in Figure 2.7. It is equipped with an external heat exchanger; generally, this type of crystallizer can be equipped with an internal heat exchanger, where the heat exchanger is directly attached to the

draft tube. For the evaporation mode the saturated solution is directly fed to the crystallizer. Another configuration of this crystallizer is shown in Figure 2.8, where the shape of the tank bottom is rounded and there is a center peak under the agitator.

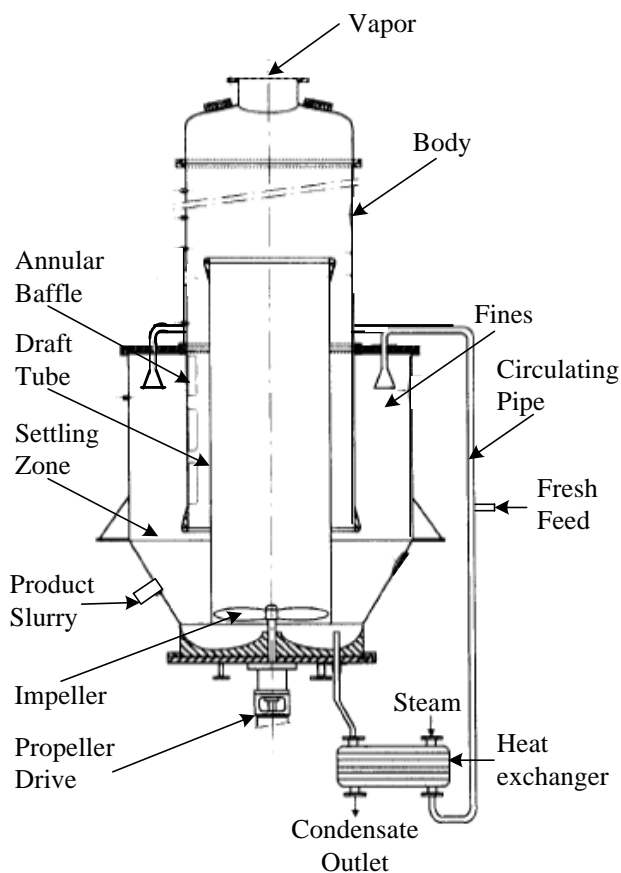


Figure 2.8 DTB crystallizer. (Kramer *et al.*, 1996)

2.3 The Effect of Hydrodynamics in Crystallizers

The role of hydrodynamics is one of the key aspects in the dynamic behavior of a crystallization process. On a macroscopic scale the hydrodynamic conditions control the crystal residence time and the circulation time in the crystallizer (which control the solid suspension in the crystallizer). On a microscopic scale, the smallest

scale flow determines the crystal collisions (a source of secondary nucleation and agglomeration) and mass transfer for crystal growth. This research investigates the hydrodynamic conditions where fluid-particle flow and mixing are concerned.

2.3.1 Introduction to crystallization mechanisms

Crystal growth involves phase change thermodynamics, solution chemistry, mass transfer, fluid dynamics, and heat transfer. In solution, crystal growth occurs by increasing the solute concentration. This may be done by evaporation (known as vapor diffusion) or liquid-liquid diffusion to remove solvent. In a vapor diffusion system, evaporation takes place at the free surface of the solution, heat is transferred by convection when the difference between the surface temperature of the heating surface and that of the liquid is small; this is known as *convective boiling* (Mersmann, 2001). When a specific temperature difference is exceeded, more and more vapor bubbles are formed, leading to enhanced *nucleate boiling*. When the temperature difference is even greater, the bubbles formed on the heating surface may be so close to one another that they grow together to form a film of vapor; this is known as *film boiling*. A liquid-liquid diffusion system consists of a solution surrounded by another immiscible liquid that is permeable to the solvent (Sadhal and Trinh, 2002).

Nucleation is the birth of new crystals. Nucleation is classified into primary and secondary nucleation. Primary nucleation is divided into homogeneous mechanisms and heterogeneous mechanisms. In homogeneous nucleation, there are no external nucleation sites available (as could be caused by the walls of the vessel, dust particles, crystals or solids of other solute, etc.). Heterogeneous nucleation occurs when the presence of such foreign surfaces is required to obtain primary nuclei.

Secondary nucleation is far more significant than primary nucleation in most industrial crystallization units because the vessel is run continuously having solute crystals inside. There are five principle mechanisms of secondary nucleation, as shown below (Randolph and Larson, 1988):

1. Contact nuclei are formed from crystal-crystal, crystal-vessel wall, and crystal-impeller contacts that result in the removal of an adsorbed layer from a growing crystal. If the amount of adsorbed layer removed is above the size of the critical nucleus, it forms a nucleus.
2. Shear nucleation is a similar mechanism where the adsorbed layer is removed by fluid shear.
3. Fracture nucleation is caused by breakage of crystals due to collisions similar to those in (1).
4. Attrition nuclei are attrition fragments of layer crystals.
5. Needle breeding results from the removal of dendritic fragments from a larger crystal.

It is generally considered that (for many species), there is a region on the phase diagram where crystal growth occurs, but nucleation does not. Nucleation events may occur in their own region at higher concentrations. Growth can occur in any supersaturated solution. The supersaturated region where nucleation does not occur is known as the metastable region: it is larger for primary nucleation than for secondary nucleation, and is highest for homogeneous nucleation (see Figure 2.9).

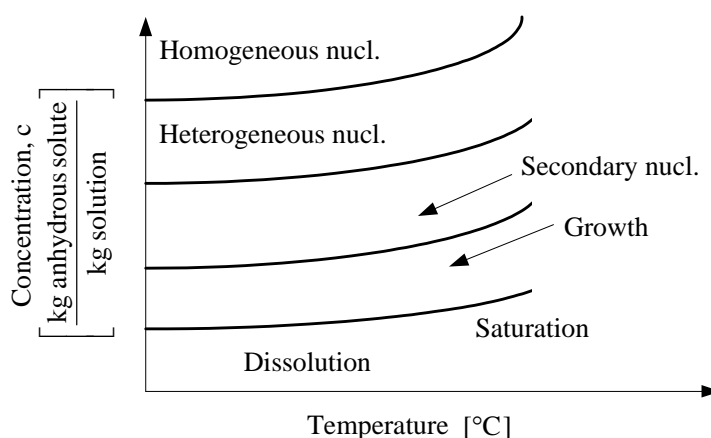


Figure 2.9 The metastable regions on a phase diagram.

2.3.2 Introduction to mixing in crystallization processes

Crystallization is usually carried out in a suspension, so knowledge of mixing is important to study the crystallization process. Both mixing between fluid and particles, and particles and particles affect the crystallization process. The mixing effect is mainly considered on two scales of mixing. One is macromixing, i.e. residence time distribution, which defines retention time of the elementary volumes, and the other is micromixing, which describes communication between elementary volumes (Sha and Palosaari, 2000a).

Successful operations depend on identifying the mixing parameters for the most critical aspects of the process and then evaluating whether those parameters will be satisfactory for the other aspects. The crystallizers normally employed in the fine chemical and pharmaceutical industries are multipurpose vessels with various impellers, baffles, and draft tube configurations. The pitched blade turbine is an axial flow impeller and can create good circulation at relatively low shear. These attributes help reduce secondary nucleation and crystal breakage while achieving good

suspension and circulation. The flat-blade turbine is less applicable because of high shear and less overall circulation. Baffles are required to prevent poor mixing due to swirling as well as entrainment of vapor that can provide nucleation sites. A draft tube is usually installed centrally within the vessel. An axial flow impeller located inside the draft tube is used to provide an efficient top-to-bottom circulation pattern, which is important for flow controlled process (Paul, Atiemo-Obeng, and Kresta, 2004).

A pitched blade turbine (see Figure 2.10) is the most commonly used agitator in DTB crystallizers. It is an axial flow impeller and consists of a hub with an even number of blades bolted and tack-welded on it. It is heavier than a propeller of the same diameter. The blades can have an angle between 10 and 90° from the horizontal, but the most common blade angle is 45°. The flow discharge from a pitched blade impeller has components of both axial and radial flow velocity in low to medium viscosity liquids and is considered to be a mixed-flow impeller with 50% axial flow and 50% radial flow.

The location and design of inlets and outlets are based on the process, type of feed, and sensitivity of the process result to the rate of feed dispersion. For slow batch processes, the feed inlet can be from the top. It should be pointed at an active surface away from the tank wall and the impeller shaft. For processes requiring quick dispersion of feed, the inlet nozzle should be located in a highly turbulent region such as the suction or discharge of the impeller. The inlet nozzle should be sized to prevent backmixing of the tank contents into the inlet pipe, where lack of mixing may cause poor process results.

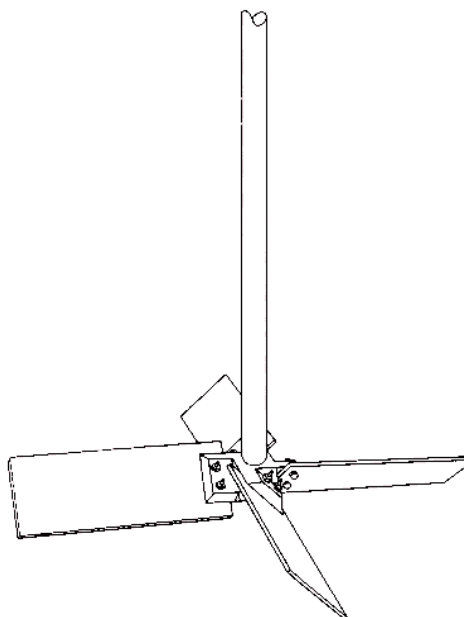


Figure 2.10 Pitched blade turbine. (Perry and Green, 1997)

Air feeds can affect the power required for the impeller to operate the mixing tank reactor, with different inlet air velocity conditions resulting in different amounts of impeller power (when air is located under the impeller) as discussed by Kleinstreuer (2003). This research shows that less power is required by the impeller to mix the two phases when more air is injected into the mixing tank. This discussion can be related to other mixing processes, such as liquid feeds, but the feed must be located under the impeller.

The outlet is generally located on the side near the tank bottom or in the bottom head if the vessel needs to be drained completely. When solids are present, this bottom outlet can get plugged and can cause poor contacting of liquid and solids unless fitted with a flush-bottomed valve. A small impeller, installed very close to the tank bottom, also helps to eliminate this problem and provides mixing at low liquid

levels. In continuously operated agitated tanks, the outlet must be located far from the inlet to minimize short-circuiting of the feed.

2.3.3 Mixing effects on nucleation

Mixing can effect both primary nucleation and secondary nucleation. In industrial crystallization the mixing effects on secondary nucleation become important. Secondary nucleation is mixing dependent as follows (Paul *et al.*, (2004):

1. Crystal-crystal impact: a function of both the local micromixing environment and the overall macromixing circulation.
2. Crystal-impeller and crystal-wall impact: these are functions of the impeller speed, shape of blade, and material of construction.
3. Adsorbed layer thickness: the thickness of the adsorbed layer is decreased by increased mixing.

These factors affect the rate of nucleation, which determines the number of nuclei formed and their size. Final crystal product size is a function of the number of nuclei generated. The number of nuclei generated by the several forms of nucleation, including agitation, has an exponential effect, as expected from this purely geometrical relationship, on the ultimate size that can be achieved by growth subsequent to nucleation.

The effects of agitation on secondary nucleation are discussed by Mullin (2001). This discussion highlights the complex nature and unpredictability of these interactions. The critical mixing factors are impeller speed and type and their influence on local turbulence and overall circulation. These factors are the key factors in causing difficulty in scale-up of nucleation dominated crystallization process, even with small quantities of seed. Since the localized turbulence distribution or the overall

circulation time can not realistically be maintained constant on scale-up, the extent to which changes in the crystallizing environment will affect nucleation are extremely difficult to predict. To the mixing issues must be added the uncertainties caused by soluble and insoluble impurities that may be present in sufficiently different concentration from batch to batch to cause variation in nucleation rate.

It is important to remember that low-level impurities can also have significant impact on crystal growth, usually by blocking growth sites on the growth surface, reemphasizing the importance of controlling reaction conditions with suitable local mixing. However, impurities can more easily disturb a molecular cluster trying to arrange itself into a critical sized nucleate than they can an already formed growing surface, so the effect is clearly more pronounced in nucleation.

2.3.4 Mixing effects on growth

Paul *et al.* (2004) has shown that mixing can effect crystal growth in several ways, as summarized below:

1. Mass transfer rate in the diffusion film around the growing crystal.
2. Bulk turnover rate and its affect on minimizing differences in the supersaturation ratio throughout the vessel.
3. Heat transfer rate and wall thickness.
4. The effect of shear on crystal breakage.
5. Dispersion of an antisolvent or reagent.
6. Growth rate dispersion
7. Uniformity of crystal suspension.
8. Minimizing impurity concentration at the crystal surface.
9. Avoidance of settling.

Minimizing the supersaturation gradient in the film around a growing crystal by maintaining a high mass transfer rate is one of the primary functions of mixing in a crystallization operation. As in other types of mass transfer operation, the mass transfer coefficient increases with increased mixing, although at high Reynolds numbers, this increase becomes less significant to the crystallization, because the process becomes controlled by the rate of integration of species into the surface of the crystal. The other functions that improve with increased mixing are the effects mentioned above. However, these requirements must be balanced against the possibility of the negative results of over-mixing, which can result in crystal breakage and/or shedding of nuclei as well as increased secondary nucleation. Increased mixing results in increased growth of large crystals (assuming that the growth rate is mass transfer dependent), but has little effect on small crystals ($< 10 \mu\text{m}$) since these crystals are smaller than the turbulent eddies and have little relative movement. The last effect may be a contributing factor in the increase in the mean of the size distribution that is common on scale-up.

For the reasons discussed above, it is necessary to choose a mixing condition (impeller speed, type, etc.), which may actually not be the optimum of any aspect of crystallization, but is optimal for the process as a whole. In many cases, one end result, such as PSD, bulk density, uniformity of suspension, and approach to equilibrium solubility may dictate the choice of mixing conditions.

2.3.5 Particle settling

Particles heavier than the suspending fluid may be removed from a gas or liquid in a large settling box or tank, in which the fluid velocity is low and the particles have ample time to settle out (McCabe *et al.*, 2001). A device that separates

the solids into two fractions is called a *classifier* and most classifiers in chemical processes separate particles on the basis of size. The annular settling zone of the DTB crystallizer shown in Figures 2.7 and 2.8 is an example. If the upward velocity of the liquid is smaller than the terminal settling velocity of acceptable large crystals, the large crystals are separated (settled); this device carries unwanted fine crystals back to the crystallizing zone for the further growth, or alternatively is used to destroy fine crystals by removing them and dissolving them.

A dense solid particle placed in a quiescent fluid will accelerate to a steady state settling velocity (free or terminal settling velocity). This velocity occurs when the drag force balances the buoyancy and gravitational force of the fluid on the particle.

Correlations for the terminal settling velocity have been derived for spherical particles. In newtonian fluids, the terminal settling velocity, U_t , is calculated by expression (McCabe *et al.*, 2001).

$$U_t = \sqrt{\frac{4g(\rho_p - \rho)d_p}{3C_D\rho}} \quad (2.2)$$

where g is the gravitational constant (9.81 m/s^2), ρ is the liquid density, ρ_p is the particle density, d_p is the particle diameter, μ is viscosity of liquid, and C_D is the drag coefficient. The corresponding ranges for Re_p ($Re_p = \rho U_t d_p / \mu$) and the correlating expression for C_D are shown in Table 2.1 for three hydrodynamic regimes.

When the expressions for C_D are substituted in equation (2.2), the resulting expressions for free settling velocity, U_t are:

For the Stokes' law (laminar, $Re_p < 0.2$) regime:

$$U_t = \frac{gd_p^2(\rho_p - \rho)}{18\mu} \quad (2.3)$$

For the Newton's law (turbulent) regime, $Re_p > 500$:

$$U_t = 1.75 \sqrt{\frac{gd_p(\rho_p - \rho)}{\rho}} \quad (2.4)$$

Table 2.1 Hydrodynamic regimes for settling particles.

Regime	Reynolds Number	C_D Expression
Stokes' law (laminar) ¹	$Re_p < 0.2$	$C_D = 24/Re_p$
Intermediate law ²	$0.2 < Re_p < 500$	$C_D = 18.5/Re_p^{3/5}$
Newton's law (turbulent) ¹	$500 < Re_p < 3.5 \times 10^5$	$C_D = 0.44$

Sources: ¹Yang (2003); ²Paul *et. al.* (2004)

The above expression of settling velocity is based on the hydrodynamics of a single particle. If other particles are present in the system the settling velocity is lower due to a mechanism called *hindered settling*. Hindered settling occurs because of (1) the interactions with surrounding particles, (2) interactions with the upward flow of fluid created by the downward settling of particles, and (3) increases in the

apparent suspension viscosity and density (Paul *et al.*, 2004). An empirical correlation for hindered settling in monodispersed suspensions is reported by Maude (1958) as

$$U_{ts} = U_t (1 - \chi)^n \quad (2.5)$$

where U_{ts} is the hindered settling velocity, χ the volume fraction of solids in the suspension, and n is a function of the particle Reynolds number as follows: $n = 4.65$ for $Re_p < 0.2$, $n = 4.375 Re_p^{-0.0875}$ for $0.2 < Re_p < 500$, and $n = 2.33$ for $Re_p > 500$.

2.3.6 Previous fluid dynamic studies relating to crystallizers

Experiments to study the mixing effects in crystallizers and related systems (e.g. stirrer vessel, reactor. etc.) have been investigated by many researchers, and the main results are discussed in the following sections.

The mixing effects on the solid suspension in an agitated vessel were studied by researchers such as Barresi and Baldi (1987), Shamlou and Koutsakos (1989), Nasr-El-Din, Mac Taggart, and Masliyah (1996), Guiraud, Costes, and Bertrand (1997), and Angst and Kraume (2005). The results showed that the impeller speed had an important effect on the uniformity of the particle suspension; the uniformity increased when the impeller speed increased.

The results of Shamlou and Koutsakos (1987), and Nasr-El-Din *et al.* (1996) showed that the variation of solid concentrations increased with the particle mean size and the impeller speed. Moreover, the particle size distribution in the outlet tube was not the same as in the vessel and the particles in the system had different residence times.

The results of Barresi and Baldi (1987) showed that the particle free zone at the top of the vessel increased when the impeller speed decreased. The height from the bottom of vessel to the location of the maximum solid concentration rose with increasing impeller speed.

The results of Guiraud *et al.* (1997) showed that in the presence of particles, the particles lagged behind the liquid phase in the upward parts of the field, but were ahead in some downward parts. The root-mean-square axial velocities of the particles were always greater than the continuous phase. Larger particles (970 μm) were more difficult to fluidize than smaller particles (250 μm) and had a lower mean axial velocity in the upward flow.

The same attributes were studied by Drewer, Ahmed, and Jameson (2000). They found that the capacity of existing plants can be increased by raising the solids concentration, thus maximizing the individual vessel or reactor productivity. It was also found that increasing solids concentration increased the power required for solid suspension. All suspensions had an optimum concentration where the specific power was at a minimum. Operating at high solids concentrations should result in reduced capital and running costs.

Research similar to the above studies, but focusing on the air-water system was performed by Chen and Chen (2000). This study on the air-water system should be considered because the system is quite similar to the work in this thesis (a vapor-liquid system, in which solids are neglected). In this study, the author found that the decrease in the power input due to gassing for the concave blade impeller was decreased with an increase in the blade curvature. Under the same gassed power level and gas flow rate, the use of the concave blade impellers generally resulted in a small

but definite increase in the mass transfer coefficient compared to the Rushton impeller. The maximum mass transfer coefficient varied with the blade curvature, and depended on the impeller speed.

All of the studies mentioned above focus on stirred vessels. Studies in crystallizers are described below:

Sha and Palosaari (2000b) studied a continuous crystallizer (similar to a mixing tank). The results showed that when the suspension density was higher near the bottom of the crystallizer where the product removal is, this resulted in many particles being removed. Most crystals removed were large crystals because they stayed near the bottom, whereas small crystals were circulated in the crystallizer. The suspension density in the product line was lower than the suspension density at the removal location in the crystallizer; this is a condition of imperfect suspension in the continuous crystallizer. With increasing mixing intensity, the suspension density distribution along a height of the crystallizer tended to become more uniform. For a fixed product removal location, when the mixing intensity was strong, the supersaturation density for each size of crystal tended to be uniform, the classification became smaller, and the crystal size distribution of the product became narrow. The residence time of particles was longer than the solution, and the residence time of large-size particles was longer than that of small particles. In this imperfectly mixed suspension crystallizer, supersaturation not only depended on residence time, but also on mixing intensity and product removal location, since the supersaturation level was decreased with increasing values of average suspension density. For the reasons mentioned above, the crystal growth rate and nucleation rate increased with an

increase in supersaturation, so crystal growth rates decreased with increasing values of average suspension density too, or increasing values of mixing intensity.

The study by Sha and Palosaari (2000a) defined the classification function as:

$$g^*(Z_0, f(N, D), L_j) = \frac{\overline{n_j}}{n_{pj}} \quad (2.6)$$

or

$$h^*(Z_0, f(N, D), L_j) = \frac{n_{pj}}{\overline{n_j}} \quad (2.7)$$

where $\overline{n_j}$ = average population density in the crystallizer

n_{pj} = population density in the product

These factors were discussed based on the theory of crystallization processes in imperfectly mixed suspension continuous crystallizers. The results showed that the product classification depended on the crystal size, product removal location, and mixing intensity. The classification decreased with increased mixing intensity for the same sized particle. Different product removal location gave different types of classification function. The relationship between the particle size and degree of classification depended on where the product removal location was. The difference between the value of the classification parameter and unity increased with increasing

particle size. The size dependent classification function can be correlated with the specific power input (due to mixing intensity) and particle size in an empirical model.

Many researchers have studied the effect of mixing in precipitation systems, and these are represented by the following:

Agglomeration in a stirred tank (batch reactor) was studied by van Leeuwen, Bruinsma, van Rosmalen, Hounslow, and Seckler (2000). Their results showed that the agglomeration rate constant was directly proportional to the growth rate, and was related to the power input in the reactor system. It was clearly indicated that agglomeration can be strongly influenced by local conditions in the reactor.

A continuous precipitation system was studied by Farkas, Blickle, Ulbert, and Nasznos-Nezdei (1996). In this work, they determined a method of characterizing the mixing of precipitated suspensions by applying a function of mean residence time and particle size distribution. They found that this function was suited to describe the residence time as a function of particle size. With increasing rotation speed the standard deviation of the functions approaches zero, which was the state of perfect mixing expected for producing highly uniform crystals.

For semi-batch precipitation systems, there are many studies such as Åslund and Rasmuson (1992), Philips, Rohani, and Baldyga (2000), Torbacke and Rasmuson (2001), and Mandare and Pangarkar (2003). The results of Philips *et al.*, and Torbacke and Rasmuson showed that the product mean size increased with increasing circulation rate in the loop, and with increasing feed point mixing intensity. An increase in the feed addition time (slower feed rate) increased the size of the particles for the same stirrer speed. This was because increasing the feed addition time increased the time available for the particle growth. Feed near the impeller resulted in

larger particles, because at this location a high and sudden dilution occurs, resulting in a reduction in the supersaturation.

The results of Philips *et al.* (2000) showed that, at low initial concentration, the growth rate of NaCl increases more than the nucleation rate. At large initial concentration, the order of nucleation changed from 1.775 to 15, thereby producing smaller particles. An increase in the volume ratio decreased the size of the particles as predicted by different feed positions due to an increase in the local supersaturation (and therefore a higher nucleation rate).

The results of Åslund and Rasmuson (1992) showed that the product weight mean size initially increased with increasing local energy dissipation rate, reached a maximum, and then decreased again. At the feed point, the solubility was much lower than the reactant solution concentrations, and the reaction was very fast. Hence the local supersaturation at the feed point became very high, leading to rapid nucleation and crystal growth. From the very high value at the feed point, the supersaturation decayed when the solution was conveyed into the bulk. Mixing in the stirred tank reactor brought reactants together on the one hand, but may also act to dilute local concentrations. Macroscopic circulation brought supersaturation and crystals back to the feed point. Small nuclei generated at the feed point were conveyed by macro-mixing into the bulk and many dissolve due to Ostwald ripening. The maximum product supersaturation was gradually reduced and the size distribution of the suspension changed over the process time. A similar system was studied by Torbacke and Rasmuson (2001), and they found similar results. Moreover, they found that the product mean size increased with decreasing feed pipe diameter.

The study of Mandare and Pangarkar (2003) gave similar results to the other studies, except that secondary nucleation played a dominant role in deciding the final crystal size. The data of average crystal size was correlated with power consumption per unit mass and solid loading.

All previous studies described above generally agree with each other for researchers who discuss the same point. Namely, the uniformity increased when the impeller speed increased for the study into the mixing effects on the solid suspension in an agitated vessel that were studied by Barresi and Baldi (1987), Shamlou and Koutsakos (1989), Nasr-El-Din *et al.* (1996), Guiraud *et al.* (1997), and Angst and Kraume (2005). For semi-batch precipitation systems, which were studied by Philips *et al.* (2000), and Torbacke and Rasmuson (2001), the results showed that the product mean size increased with increasing circulation rate in the loop, and with increasing feed point mixing intensity. An increase in the feed addition time (slower feed rate) increased the size of the particles for the same stirrer speed. The confirmations by CFD of some results of the studies in this section are discussed in the next section.

2.4 CFD Modeling of Crystallizers

2.4.1 Introduction to CFD

Computational Fluid Dynamics (CFD) is a computer-based tool for simulating the behavior of systems involving fluid flow, heat transfer, and other related physical processes. It works by solving the equations of fluid flow (in a special form) and the equation for heat transfer over a region of interest, with specified (known) conditions on the boundary of that region.

CFD is used to predict a system's performance in various areas, which can potentially be used to improve the efficiency of existing systems as well as the design of new systems. It can help to shorten product and process development cycles, optimize processes to improve energy efficiency and environmental performance, and solve problems as they arise in plant operations. There are many potential applications of CFD in chemical processes where predicting the characteristics of fluid flow are important, such as mixers, chemical reactors, packed beds, crystallizers, dissolving equipment, pneumatic conveyers and classifiers, sprayers, etc. (Thompson and Kontomaris, 1999).

The process of performing a single CFD simulation is split into four components:

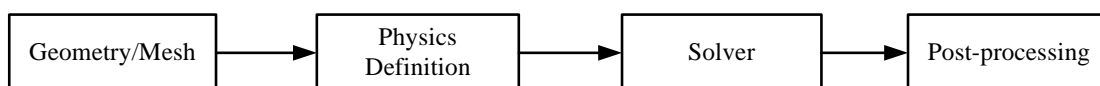


Figure 2.11 CFD modeling procedures.

Geometry/Mesh: This process is the first pre-processing stage. The objective is to produce a mesh for input to the physics pre-processor. Before a mesh can be produced, a closed geometric solid is required.

Physics definition: This interactive process is the second pre-processing stage and is used to create the input required by the solver. The physical models which are to be included in the simulation are selected. Fluid properties and boundary conditions are specified in the physics definition.

The solver: The component which solves the CFD problem is called the solver. It produces the required results in a non-interactive/batch process. The CFD problem is solved as follows:

1. The partial differential equations are integrated over all the control volumes in the region of interest. This is equivalent to applying a basic conservation law (e.g. for mass or momentum) to each control volume.
2. These integral equations are converted to a system of algebraic equations by generating a set of approximations for the terms in the integral equations.
3. The algebraic equations are solved iteratively.

The solver produces a results file which is then passed to the post-processor.

The post-processor: The post-processor is the component used to analyze, visualize and present the results interactively. Post-processing includes anything from obtaining point values to complex animated sequences.

2.4.2 CFD modeling of crystallizers

The characteristics of fluid and solids flow in crystallizers are one of the applications of CFD. In these systems, CFD is used to simulate the hydrodynamics or mixing processes by evaluating the flow patterns and local variables, such as the velocity, turbulent kinetic energy, volume fraction of solid, liquid or gas, temperature, mass transfer by evaporation, mixing rate, liquid free surface, etc. It can be used to scale-up and optimize processes. There is much research on the mixing effects on this system and related systems (e.g. stirred vessel, reactor, etc.) by CFD modeling, as discussed in the following paragraphs.

Many researchers have used CFD modeling in solid suspension systems (e.g. stirred tank, mixing reactor), such as Bakker, Fasano, and Myers (1998), Maggioris, Goulas, Alexopoulos, Chatzi, and Kiparissides (1998), Sha, Palosaari, Oinas, and Ogawa (2001), Oshinowo and Bakker (2002), Brucato, Micale, Montante, and Scuzzarella (2002), and Wang, F., Wang, W., Wang, Y., and Mao, Z. (2003). All of these studies considered turbulent flow.

The studies of Bakker *et al.* (1998) and Maggioris *et al.* (1998) modeled the liquid phase only and the solids were considered to follow the liquid flow. The results of Bakker *et al.* showed that when the impeller diameter and/or impeller-bottom clearance were too large, the flow direction at the bottom reversed, and two circulation loops occurred. These results hampered solids suspensions: solids settled and agglomerated at the bottom of the tank. Adding a second impeller did not decrease the just-suspended speed. A second impeller did increase the homogeneity of the suspension, provided that the spacing between the impellers was not too large. The results of Maggioris *et al.* showed that breakage and agglomeration are a function of energy dissipation rate and the physical geometry of tank. In the area of high energy dissipation loss, high breakage rates occurred. In this area a circulation loop occurred and then the collision between particle fragments occurred. This effect results in a reduction of product quality.

The works of Sha *et al.* (2001), Oshinowo and Bakker (2002), and Wang *et al.* (2003) used CFD to model two-phase (solid-liquid) flow in the stirred tank. Their results showed that the axial velocities of the solid phase were always below those of the liquid due to the fact that the solid particles were heavier than the liquid. The maximum solid concentration occurred on the centre of the tank bottom, and the

solids concentration gradually decreased from the bottom to the free liquid surface. The distribution of the solid phase was more homogeneous for high impeller speeds. The uniformity of the solid distribution decreased with increasing particle size.

The results of Oshinowo and Bakker (2002) showed that the velocity distribution and cloud height predicted by CFD were in good agreement with the experiment study of Guiraud *et al.* (1997), as discussed on page 37.

Sha *et al.* (2001) showed that a low solid fraction can be found at the top of the tank and below the propeller. The particles settled in the centre and the corners of the bottom of the vessel, revealing clearly the dead zone of the mixed tank. The particle free zone and the height from the bottom of vessel to the location of the maximum solid concentration were in good agreement with experimental study of Barresi and Baldi (1987), as discussed on page 37.

The work of Brucato *et al.* (2002) studied the thickness of a clear liquid layer of the stirred solid-liquid dense system by both CFD modeling and experiment. The results showed good agreement between the experimental results and the CFD simulation. The clear liquid layer thickness reduced when the agitation speed increased.

There is much research using CFD to model flow in continuous crystallizers (such as MSMPR crystallizers) and the studies are discussed below:

Sha, Oinas, Louhi-Kultanen, Yang, and Palosaari (2001) simulated the suspension crystallizer in term of factors affecting size-dependent classification. This work investigated the experiment of Sha and Palosaari (2000a) using CFD, as discussed on page 39. It was found that tanks of different geometries had different classifications. The same type of system was studied by Rielly and Marquis (2001).

Their results confirmed a non-ideal MSMR or imperfectly mixed suspension crystallizer. These results are in good agreement with the experiments of Sha and Palosaari (2000b), as discussed on page 38.

A crystallizer with a draft tube was studied by Synowiec, Bigda, and Wójcik (2002). The calculations were carried out using a CFD package for homogeneous liquid in conditions of turbulent flow. They found that systems without a draft tube and having a flat bottom used a power input higher than those with a draft tube and an elliptic bottom, so that the draft tube helped to reduce the cost. Increasing stirrer diameter decreased power input. These results agreed well with Franke and Mersmann (1995).

The experimental results of Mandae and Pangarkar (2003) showed that secondary nucleation was the main effect determining the final product quality. The influence of crystal-impeller and crystal-bottom (impeller-bottom distance) collisions on secondary nucleation were studied by Liiri, Koironen, and Aittamaa (2002) by CFD modeling. These two parameters had a strong effect on the growth and breakage of the crystals.

CFD simulations of batch cooling crystallization were studied by Yang, Louhi-Kultanen, and Kallas (2002), and Lung-Somarrriba, Moscosa-Santillan, Porte, and Delacroix (2002). The results of Yang *et al.* showed that the values of temperature were the lowest at the upper region near the wall, which can be explained by the effect of less turbulent flow in this part of the tank and also by the cooling due to the wall temperature on the boundary. The supersaturation distribution was mainly determined by the temperature distribution, while at the same time, it was also affected by the concentration distribution of the mother liquor and the particle size

distribution of the crystals. However, the supersaturation distribution affected the local concentration and local crystal size in return through the local crystal growth rate. The results of Lung-Somarriba *et al.* showed the best impeller and operation conditions for glycerin crystallization.

CFD simulations of precipitation processes were studied for both continuous and batch operations. Continuous operations were studied by van Leeuwen, Bruinsma, and van Rosmalen (1996), and Jaworski and Nienow (2003). The results of van Leeuwen, Bruinsma, and van Rosmalen showed that the mean particle size depended on residence time; this result agreed well with the experiment of Farkas *et al.* (1996), as discussed on page 40. Moreover, the mean crystal size slowly increased with increasing impeller speed. Jaworski and Nienow studied both experimented and CFD methods. Their results showed that the simulated flow pattern was in good agreement with the experiments. The simulations predicted the influence of the inlet velocity ratio on the area mean particle size, the coefficient of variation of the CSD and the degree of conversion very well.

A semibatch crystallizer was studied by Wei, Zhou, and Garside (2001). Their results agreed well with the experiment of Philips *et al.* (2000), and showed that mean crystal size depended on impeller speed, operating time, and feed location, and it increased linearly with operating time, and resulted in a large crystal size when the feed location is in a poor mixing area. Reactive precipitation only occurred in an effective zone (such as near the feed point).

Another study on semibatch systems was performed by Zauner and Jones (2002). This work used a segregated feed model (SFM), compartment model, and CFD modeling. Their results showed that the overall nucleation rate strongly

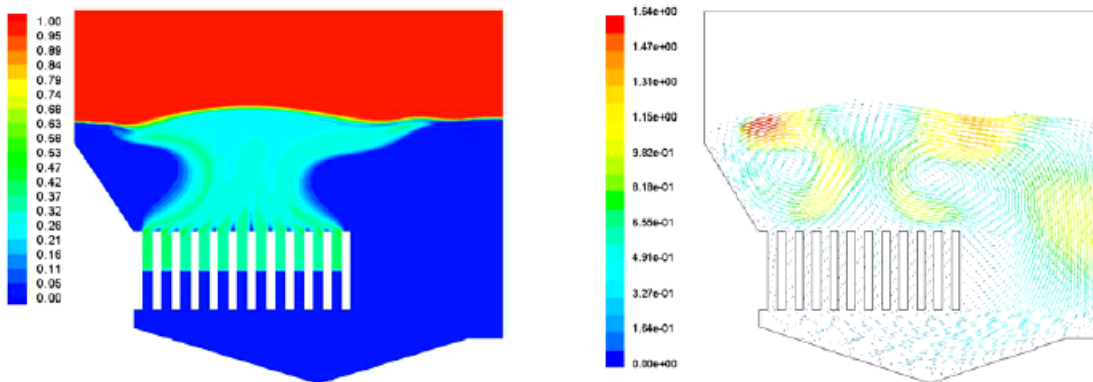
depended on mixing conditions, as it depended on the level of supersaturation. The SFM model also provides explanations for effects that are usually observed in precipitation processes. It can account for the influence on the particle size distribution of the feed point position, feed rate, feed tube diameter, average and local dissipation rate, and impeller type and speed. This work was in good agreement with the experiments of Åslund and Rasmuson (1992), as discussed on page 41.

CFD modeling of evaporative crystallizations have been performed in many types of crystallizers, such as vacuum pan crystallizers, forced-circulation crystallizers (FCC), etc., and are discussed in the following section:

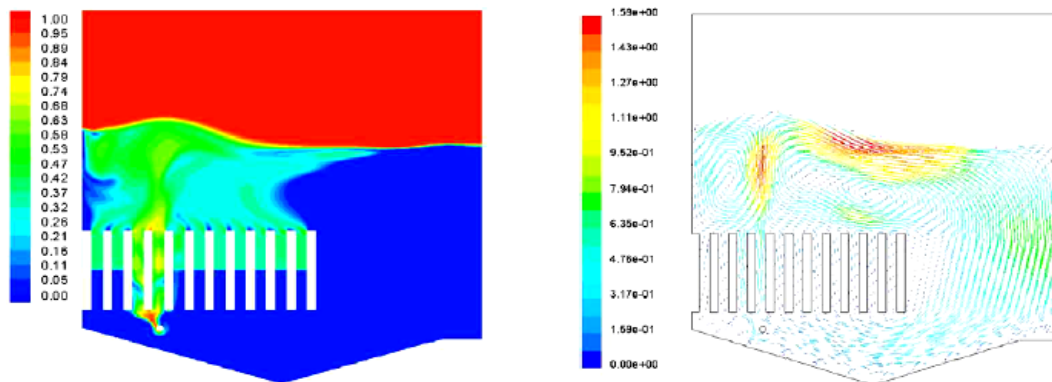
CFD modeling of vacuum pans was studied by Rein, Echeverri and Acharya (2004). In this work, CFD was used to model the two-phase (massecuite-vapor) flow inside a vacuum pan. The temperature field was assumed isothermal, and it was assumed that the evaporation took place across the calandria. Example results are shown in Figure 2.12. This figure shows that the steam injected below the calandria increased substantially the circulation in the pan, vorticity over the top tube plate, and the average circulation.

Systems similar to this work were studied by Pennisi, Liow, and Schneider (2003), and Dixon, Mann, Hobson, Plaza, Pennisi, and Steindl (2003); both studies focused on a sugar mill evaporator, and did not model the area above the calandria, or the free surface in the region above the calandria was modeled with a rigid boundary with free slip. Figure 2.13 shows a typical prediction of the velocity field within the body of the evaporator. Other results of Pennisi *et al.* showed reasonable agreement when compared with measurements taken from the actual vessel. The predictions showed that the design of the juice distribution system at the

inlet to the vessel had a major influence on the flow field in the remainder of the vessel. A large amount of mixing was found to occur at the inlet resulting in the calandria region being exposed to juice with properties close to the properties of the outlet stream, which was detrimental to performance.



(a)



(b)

Figure 2.12 CFD results for vacuum pan: (a) with steam jiggers; (b) without steam jiggers. (Rein *et al.*, 2004)

Note The left pictures are the contours volume fraction of vapor (%) and the right pictures are the massecuite velocity vectors.

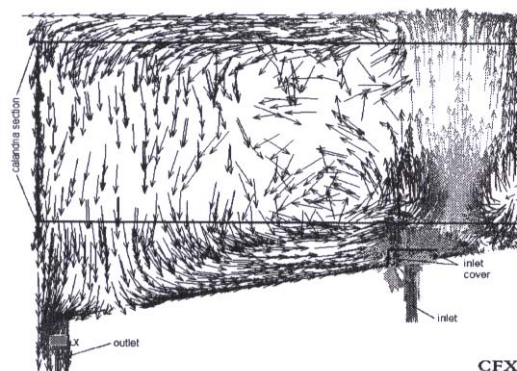


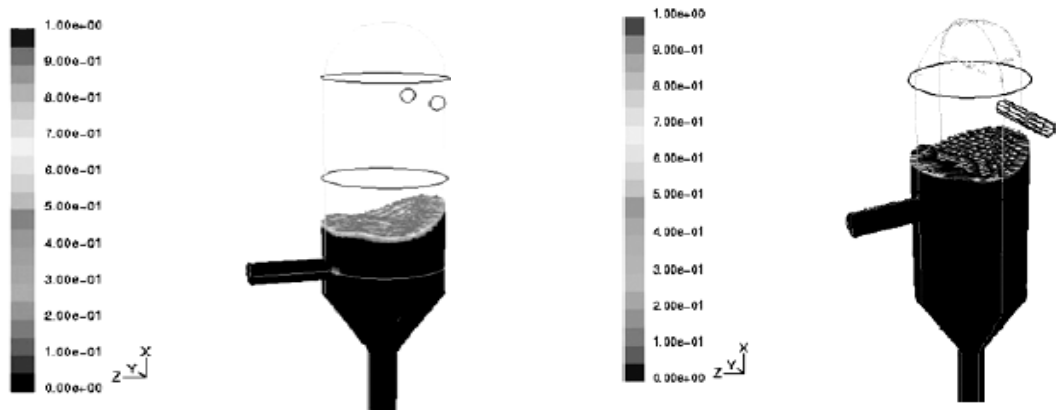
Figure 2.13 Vector of flow field inside an evaporator vessel. (Dixon *et al.*, 2003)

CFD modeling on FCC crystallizers was studied by Kramer, Dijkstra, Verheijen, and van Rosmalen (2000), and Essemiani, Traversay, and Gallot (2004). Their work assumed the crystallizers were isothermal systems and hence considered only the hydrodynamic effects. Kramer *et al.* modeled only the part below the free surface by a single phase model (liquid only). Their results showed that the flow in an industrial crystallizer was not uniform. This result indicated that the MSMR assumption can not be used to analyze the parameters in the crystallizer. They suggested that the reasonable analysis should analyze parameters at each location in the crystallizer.

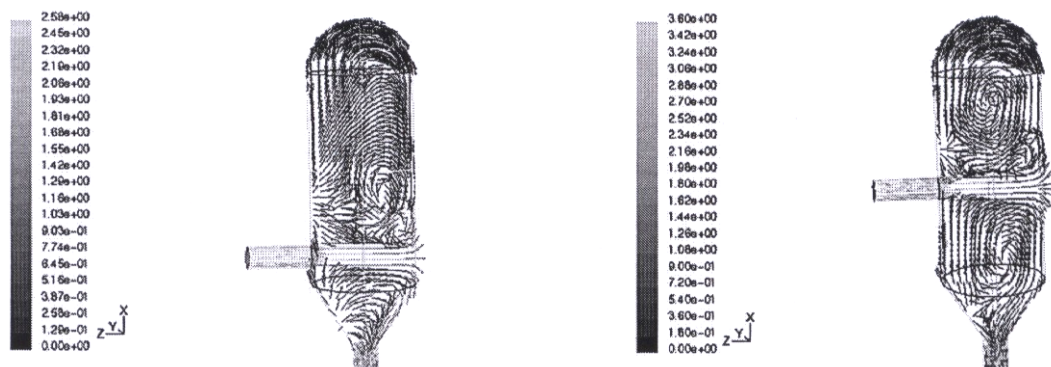
Essemiani *et al.* (2004) modeled a whole tank with two-phase (liquid-vapor) flow. Their results showed that the system was not perfectly mixed and the feed rate and crystallizer geometry affected the flow characteristics (see Figure 2.14).

All previous CFD studies described above generally agree with each other for researchers who discuss the same point and agree with the experiments that

are discussed in previous section. The agreement between experiments and CFD modeling are summarized in appendix A (Table A.1).



(a)



(b)

Figure 2.14 CFD results for FCC at different configurations: (a) surface deformation; (b) two phase velocity field. (Essemiani *et al.*, 2004)

2.5 Conclusions

From the previous studies for both experiment and CFD modeling, which are discussed in the sections 2.3.6 and 2.4.2, we can conclude that there is good agreement between experiments and CFD modeling, and these are shown in Table A.1 in appendix A. Table A.1 clearly shows that the CFD tools can be used to design and upgrade industrial mixing systems and industrial crystallizers. From previous studies and this table we can clearly see that no research has used CFD to model two-phase (vapor-liquid) flow in a DTB crystallizer. Therefore, this work will model the vapor-liquid in the DTB crystallizer using the CFD modeling software ANSYS CFX-10.0.

CHAPTER III

MATHEMATICAL MODELS

In the DTB crystallizer there are three phases: liquid (mother liquor); gas (water vapor); and solid (crystal). However, for convenience the crystallizer can be analyzed as a two-phase flow (liquid and vapor) system, which is an acceptable approach considering the particles are mostly sufficiently small to be considered to follow the liquid flow, and that the particle suspension is reasonably dilute so that the impact of solids on the flow field is negligible. If a more exact description of particle flowlines is required it is possible to do this using the two phase simulation results or using a Lagrangian model for the particles. The DTB crystallizer was studied using the CFD modeling software ANSYS CFX-10.0. 3D geometry was used to account for the strong 3D flow.

The aim of this chapter is to show the mathematical models describing the physical phenomena that occur as fluids flow in this system.

3.1 Introduction

Multiphase flow refers to the situation where more than one fluid is present. In this work the Eulerian-Eulerian multiphase model was used to simulate the vapor-liquid flow in the DTB crystallizer.

The Eulerian-Eulerian multiphase model is designed for two or more immiscible fluids (fluids that can not be uniformly mixed or blended with the other fluid and are separated by a distinct resolvable interface) and two or more interpenetrating fluids (fluids that can be uniformly mixed or blended with the other fluid). The different phases are treated mathematically as interpenetrating continua. The concept of phase volume fraction is introduced because the volume occupied by a phase can not be occupied by any other phase. The share of the flow domain each phase occupies is given by the phase volume fraction. The volume fractions of the phases are tracked, with the condition that the sum of the volume fractions for all phases is equal to 1 at all times in all control volumes. Conservation equations for each phase are derived to obtain a set of equations that have a similar structure for all phases. Within the Eulerian-Eulerian model, the interphase transfer terms can be modeled using the particle model, the mixture model or the homogeneous model.

Because the liquid and vapor in this system are separated by a distinct interface, the particle model and free surface flow model (this is used to track the liquid free surface) should be used together to model the vapor-liquid two-phase flow (gas bubbles in the bulk liquid). In the Eulerian-Eulerian multiphase flow model, the flow can be separated to homogeneous, inhomogeneous, and multicomponent flow.

The homogeneous flow model is a limiting case of multiphase flow where all fluids share the same velocity fields and other relevant field such as temperature, turbulence, etc. The pressure field is shared by all fluids.

The inhomogeneous flow model can be used to allow the two phases to separate. This will be required if entrainment of one phase within another occurs and it is desired to allow the phases to separate again. In this model, separate velocity

fields and other relevant fields exist for each fluid. The pressure field is shared by all fluids. The fluids interact via an interphase transfer term.

The multicomponent flow is the flow which more than one fluid is present, and each such fluid may be a mixture of chemical species mixed at molecular length scales.

In this work, an inhomogeneous model was considered. In this model, liquid is a continuous phase and vapor is a dispersed phase or dispersed fluid, which is a fluid which is present in discrete regions which are not connected.

There are two parts of study in this work: these are modeling of the DTB crystallizer with the inhomogeneous two-phase flow model (particle model) together with the free surface flow model using isothermal simulation, and modeling of the DTB crystallizer with the inhomogeneous two-phase flow using non-isothermal simulation (this part contains no model of the area above the liquid free surface, and the liquid free surface is considered to be flat and frictionless).

3.2 Mathematical Models

In this section, the governing equations of fluid flow and heat transfer, and the turbulence model are described. The governing equations of fluid flow and the turbulence model were used in the isothermal simulation part and all sets of governing equations were used in the non-isothermal simulations. Note that all equations presented here are written in the form used by the ANSYS CFX program: see ANSYS CFX-10.0 Manual, ANSYS Canada Ltd. (2005). The vector and tensor notations which are used throughout this chapter are described in appendix B.

3.2.1 Isothermal simulation

3.2.1.1 The continuity equation

The full form of this equation is shown in concise form below

$$\frac{\partial(r_\alpha \rho_\alpha)}{\partial t} + (\nabla \cdot r_\alpha \rho_\alpha \mathbf{U}_\alpha) = S_{MS,\alpha} + \sum_{\beta=1}^{N_p} \Gamma_{\alpha\beta} \quad (3.1)$$

where

- $S_{MS,\alpha}$ describes user specified mass sources.
- $\Gamma_{\alpha\beta}$ is the mass flow rate per unit volume from phase β to phase α . This term only occurs if interface mass transfer occurs.
- N_p is total number of phases. In this work $N_p = 2$, and we denote the liquid phase by 1 and vapor phase by 2.

In the isothermal part, the system is at steady state, with no mass source and no phase change, so that equation (3.1) becomes

$$(\nabla \cdot r_\alpha \rho_\alpha \mathbf{U}_\alpha) = 0 \quad (3.2)$$

where r_α , ρ_α , \mathbf{U}_α , respectively represent the volume fraction, phase density, and cartesian velocity component of phase α . So the equation of continuity of each phase can be written as shown below:

For the vapor phase (dispersed phase):

$$(\nabla \bullet r_d \rho_d \mathbf{U}_d) = 0 \quad (3.3)$$

For the liquid phase (continuous phase):

$$(\nabla \bullet r_c \rho_c \mathbf{U}_c) = 0 \quad (3.4)$$

3.2.1.2 The momentum equation

The full form of this equation is shown in concise form below

$$\begin{aligned} \frac{\partial}{\partial t} (r_\alpha \rho_\alpha \mathbf{U}_\alpha) + \nabla \bullet (r_\alpha \rho_\alpha \mathbf{U}_\alpha \mathbf{U}_\alpha) = & -r_\alpha \nabla p_\alpha + r_\alpha \rho_\alpha \mathbf{g} \\ + \nabla \bullet r_\alpha \mu_\alpha (\nabla \mathbf{U}_\alpha + (\nabla \mathbf{U}_\alpha)^T) + \sum_{\beta=1}^{N_p} (\Gamma_{\alpha\beta}^+ \mathbf{U}_\beta - \Gamma_{\beta\alpha}^+ \mathbf{U}_\alpha) + \mathbf{S}_{M,\alpha} + \sum_{\beta=1}^{N_p} \mathbf{M}_{\alpha\beta} \end{aligned} \quad (3.5)$$

where

- $\mathbf{S}_{M,\alpha}$ describes user defined momentum sources, see momentum sources (p. 60).
- $\mathbf{M}_{\alpha\beta}$ describes the interfacial forces acting on phase α due to the interaction with another phase β . See interphase momentum transfer model (p. 62).
- The term $\Gamma_{\alpha\beta}^+ \mathbf{U}_\beta - \Gamma_{\beta\alpha}^+ \mathbf{U}_\alpha$ represents momentum transfer induced by interphase mass transfer.

In the isothermal part, the system is at steady state and there is no phase change, so that equation (3.5) becomes

$$\begin{aligned} \nabla \bullet (r_\alpha \rho_\alpha \mathbf{U}_\alpha \mathbf{U}_\alpha) &= -r_\alpha \nabla p_\alpha + r_\alpha \rho_\alpha \mathbf{g} + \nabla \bullet r_\alpha \mu_\alpha (\nabla \mathbf{U}_\alpha + (\nabla \mathbf{U}_\alpha)^T) \\ &+ \mathbf{S}_{M,\alpha} + \sum_{\beta=1}^{N_p} \mathbf{M}_{\alpha\beta} \end{aligned} \quad (3.6)$$

So the momentum equation of each phase can be written as shown below:

For the vapor phase:

$$\begin{aligned} \nabla \bullet (r_d \rho_d \mathbf{U}_d \mathbf{U}_d) &= -r_d \nabla p_d + r_d \rho_d \mathbf{g} + \nabla \bullet r_d \mu_d (\nabla \mathbf{U}_d + (\nabla \mathbf{U}_d)^T) \\ &+ \mathbf{S}_{M,d} + \mathbf{M}_{dc} \end{aligned} \quad (3.7)$$

For the liquid phase:

$$\begin{aligned} \nabla \bullet (r_c \rho_c \mathbf{U}_c \mathbf{U}_c) &= -r_c \nabla p_c + r_c \rho_c \mathbf{g} + \nabla \bullet r_c \mu_c (\nabla \mathbf{U}_c + (\nabla \mathbf{U}_c)^T) \\ &+ \mathbf{S}_{M,c} + \mathbf{M}_{cd} \end{aligned} \quad (3.8)$$

Note that \mathbf{M}_{dd} and \mathbf{M}_{cc} are equal to zero, since there is no need for transfer terms into phase the originated from.

3.2.1.3 The volume conservation equation

This is simply the constraint that the volume fractions sum to unity:

$$\sum_{\alpha=1}^{N_p=2} r_{\alpha} = 1 \quad (3.9)$$

In this work two phases are present, so that

$$r_d + r_c = 1 \quad (3.10)$$

3.2.1.4 The pressure constraint

All phases share the same pressures field:

$$p_d = p_c \quad (3.11)$$

3.2.1.5 Momentum sources

Sources are optional terms which may be attached to most equations, so as to model additional or specialized physical processes. In this work, the volume defined by a subdomain is represented as the impeller and this creates a momentum source in the y-direction only.

In the ANSYS CFX program, the user must specify momentum addition directly in terms of a momentum source value per unit volume of subdomain in a specified direction. A source can be specified for y-direction as follows:

$$\mathbf{S}_{M,y} = S_{spec,y} \mathbf{j} \quad (3.12)$$

where the $S_{spec,y}$ is the specified momentum component, as shown below:

$$S_{spec,y} = \frac{F_{net,y}}{V} = \frac{P_{net,y}}{U_{net,y}V} \quad (3.13)$$

where P is the power. This momentum source has dimensions of $ML^{-2}T^{-2}$ (e.g. $kg/m^2/s^2$). Considering Figure 3.1, the relationship between force and fluid velocity can be written as:

$$F_{net,y} = \rho AU^2 \quad (3.14)$$

where V and A respectively represent the volume of subdomain and cross-sectional area normal to the flow.

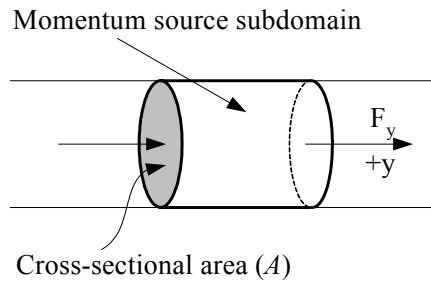


Figure 3.1 Momentum source subdomain.

The momentum source of each phase can be specified directly and written below

For the vapor phase:

$$\mathbf{S}_{M,d} = \mathbf{S}_{M,dy} = S_{specy,d} \mathbf{j} \quad (3.15)$$

For the liquid phase:

$$\mathbf{S}_{M,c} = \mathbf{S}_{M,cy} = S_{specy,c} \mathbf{j} \quad (3.16)$$

3.2.1.6 The interphase momentum transfer model

Interphase momentum transfer, $\mathbf{M}_{\alpha\beta}$, occurs due to interfacial forces acting on each phase due to interaction with another phase β . The total force on phase α due to interaction with another phase is given by:

$$\mathbf{M}_{\alpha} = \sum_{\beta \neq \alpha} \mathbf{M}_{\alpha\beta} \quad (3.17)$$

Note that interfacial forces between two phases are equal and opposite, so the net interfacial forces sum to zero:

$$(\mathbf{M}_{\alpha\beta} = -\mathbf{M}_{\beta\alpha}) \Rightarrow \sum_{\alpha} \mathbf{M}_{\alpha} = 0 \quad (3.18)$$

The total interfacial force acting between two phases may arise from several independent physical effects:

$$\mathbf{M}_{\alpha\beta} = \mathbf{M}_{\alpha\beta}^D + \mathbf{M}_{\alpha\beta}^L + \mathbf{M}_{\alpha\beta}^{LUB} + \mathbf{M}_{\alpha\beta}^{VM} + \mathbf{M}_{\alpha\beta}^{TD} + \mathbf{M}_S + \dots \quad (3.19)$$

The forces indicated above represent respectively the interphase drag force, lift force, wall lubrication force, virtual mass force, turbulence dispersion force, and solid pressure force. In this work, the tank diameter (draft tube diameter) is not comparable to the diameter of the bubbles (a very small diameter) so the lift force can be neglected, the flow is mostly axial flow (parallel with the wall) so the wall lubrication force can be neglected, the work is in a steady state system so the virtual mass force can be neglected, and there are negligible solids in this system so the solid dispersion force can be neglected. This indicates that the interphase drag and turbulence dispersion force only need to be considered in this work, and then equation (3.19) becomes

$$\mathbf{M}_{\alpha\beta} = \mathbf{M}_{\alpha\beta}^D + \mathbf{M}_{\alpha\beta}^{TD} \quad (3.20)$$

In the particle drag model, calculation of the interphase drag term is based on calculating the drag exerted on an immersed body in a moving fluid. The drag arises from two mechanisms, the first is the *skin friction* due to the viscous surface shear stress and the second is the *form drag* due to the pressure distribution around the body (Maqableh, Simmons, Hibberd, Power, and Young, 2003). The total drag force is expressed in terms of a non-dimensional drag coefficient:

$$C_D = \frac{D}{\frac{1}{2}\rho_\alpha(U_\alpha - U_\beta)^2 A} \quad (3.21)$$

where D is the magnitude of the drag force, $(U_\alpha - U_\beta)$ is the relative speed, and A is the projected area of the body in the direction of the flow. We denote the continuous phase by α and the dispersed phase by β . Thus, the drag exerted by a single droplet on a continuous phase can be written using equation (3.21) as:

$$\mathbf{D}_p = \frac{1}{2} C_D \rho_c A_d |\mathbf{U}_d - \mathbf{U}_c| (\mathbf{U}_d - \mathbf{U}_c) \quad (3.22)$$

For spherical bubbles, the area of a single bubble projected in the flow direction, A_p , and the volume of a single bubble V_p are given by: $A_p = \pi d^2 / 4$ and $V_p = \pi d^3 / 6$ where d is the mean diameter. The number of bubbles per unit volume, n_p , is given by:

$$n_p = \frac{r_d}{V_p} = \frac{6r_d}{\pi d^3} \quad (3.23)$$

The total drag exerted by the dispersed phase on the continuous phase per unit volume is:

$$\mathbf{M}_{cd}^D = n_p \mathbf{D}_p = \mathbf{D}_{cd} = \frac{3}{4} \frac{C_D}{d} r_d \rho_c |\mathbf{U}_d - \mathbf{U}_c| (\mathbf{U}_d - \mathbf{U}_c) \quad (3.24)$$

or written in the terms of interface drag term ($c_{cd}^{(d)}$), the total drag is given by:

$$\mathbf{M}_{cd}^D = \mathbf{D}_{cd} = c_{cd}^{(d)} (\mathbf{U}_d - \mathbf{U}_c) \quad (3.25)$$

The interface drag term $c_{cd}^{(d)}$ is thus defined as:

$$c_{cd}^{(d)} = \frac{3}{4} \frac{C_D}{d} r_d \rho_c |\mathbf{U}_d - \mathbf{U}_c| \quad (3.26)$$

Empirical correlations are available for the drag coefficient, C_D , which generally decreases monotonically with Reynolds number (Maqableh *et al.*, 2003).

At sufficiently small particle Reynolds numbers (the viscous regime), fluid particles behave in the same manner as solid spherical particles. Hence the drag coefficient is well approximated by the Schiller and Naumann (1933) correlation shown in equation 3.27:

$$C_D = \frac{24}{\text{Re}} (1 + 0.15 \text{Re}^{0.687}) \quad (3.27)$$

At larger particle Reynolds numbers, the inertial or distorted particle regime, surface tension effects become important. At first, fluid particles become approximately ellipsoidal in shape, and finally, spherical cap shaped. One of the correlations used in this regime is that of Ishii and Zuber (1979):

$$C_D(\text{ellipse}) = \frac{2}{3} E_0^{1/2} \quad (3.28)$$

In this case, ANSYS CFX automatically takes into account the spherical particle and spherical cap limits by setting:

$$C_D = \max[C_D(\text{sphere}), C_D(\text{dist})] \quad (3.29)$$

where

$$C_D(\text{dist}) = \min[C_D(\text{ellipse}), C_D(\text{cap})] \quad (3.30)$$

$$C_D(\text{sphere}) = \max\left[\frac{24}{\text{Re}}(1 + 0.15 \text{Re}^{0.687}), 0.44\right] \quad (3.31)$$

$$C_D(\text{cap}) = \frac{8}{3} \quad (3.32)$$

Note that $C_D(\text{cap})$ is the drag coefficient in the spherical cap regime.

$\text{Re}_{cd} = \rho_c |U_d - U_c| d / \mu_c$. E_0 is the *Eotvos number*, which measures the ratio between gravitational and surface tension forces:

$$E_0 = \frac{g \Delta \rho d_p^2}{\sigma} \quad (3.33)$$

where $\Delta \rho$ is the density difference between phases, and σ is the surface tension coefficient.

For the turbulent dispersion force, \mathbf{M}_{cd}^{TD} is given by Lopez de Bertodano (1991), and is shown below:

$$\mathbf{M}_{cd}^{TD} = -\mathbf{M}_{dc}^{TD} = -C_{TD}\rho_c k_c \nabla r_c \quad (3.34)$$

where C_{TD} values of 0.1-0.5 should be used in this work, since the bubble diameter is in the order of a few millimeters.

3.2.1.7 Turbulence models

Turbulence models seek to solve a modified set of transport equations by the introduction of averaged and fluctuating components. A velocity \mathbf{U} may be divided into an average component, $\overline{\mathbf{U}}$, and a time varying component, \mathbf{u} .

$$\mathbf{U} = \overline{\mathbf{U}} + \mathbf{u} \quad (3.35)$$

The averaged component is given by:

$$\overline{\mathbf{U}} = \frac{1}{\Delta t} \int_t^{t+\Delta t} \mathbf{U} dt \quad (3.36)$$

where dt is a time scale that is large relative to the turbulent fluctuations, but small relative to the time scale to which the equations are solved. Substituting the time averaged quantities into the original transport equations (equations 3.3, 3.4, 3.7, and 3.8) results in the Reynolds-averaged equations given below. Note that the continuity equations (equations 3.3 and 3.4) have not been altered.

The momentum equation for vapor phase is:

$$\begin{aligned} \nabla \cdot (r_d \rho_d \mathbf{U}_d \mathbf{U}_d) &= -r_d \nabla p_d + r_d \rho_d \mathbf{g} \\ + \nabla \cdot r_d \left[\left(\mu_d (\nabla \mathbf{U}_d + (\nabla \mathbf{U}_d)^T) \right) - \rho_d \overline{\mathbf{u}_d \mathbf{u}_d} \right] &+ \mathbf{S}_{M,d} + \mathbf{M}_{dc} \end{aligned} \quad (3.37)$$

The momentum equation for liquid phase is:

$$\begin{aligned} \nabla \cdot (r_c \rho_c \mathbf{U}_c \mathbf{U}_c) &= -r_c \nabla p_c + r_c \rho_c \mathbf{g} \\ + \nabla \cdot r_c \left[\left(\mu_c (\nabla \mathbf{U}_c + (\nabla \mathbf{U}_c)^T) \right) - \rho_c \overline{\mathbf{u}_c \mathbf{u}_c} \right] &+ \mathbf{S}_{M,c} + \mathbf{M}_{cd} \end{aligned} \quad (3.38)$$

where $-\rho_d \overline{\mathbf{u}_d \mathbf{u}_d}$ and $-\rho_c \overline{\mathbf{u}_c \mathbf{u}_c}$ are the Reynolds stresses for vapor and liquid phase, respectively.

In inhomogeneous multiphase flow, the bulk turbulence equations which are solved are the same as the single phase equations; this means that a single turbulence field is solved using a single turbulence model. In this work, the turbulence was treated using the $k-\varepsilon$ model where both phases share the same values for k and ε (Micale and Montante, 1999). In this model, the Reynolds stresses is given by (Chung, 2002)

$$-\rho \overline{\mathbf{u} \mathbf{u}} = -\frac{2}{3} \rho k \delta + \mu_t (\nabla \mathbf{U} + (\nabla \mathbf{U})^T) \quad (3.39)$$

where μ_t is the eddy viscosity or turbulent viscosity. Equations (3.37) and (3.38) become

$$\begin{aligned} \nabla \cdot (r_d \rho_d \mathbf{U}_d \mathbf{U}_d) &= -r_d \nabla p'_d + r_d \rho_d \mathbf{g} + \nabla \cdot r_d \mu_{eff,d} (\nabla \mathbf{U}_d + (\nabla \mathbf{U}_d)^T) \\ &+ \mathbf{S}_{M,d} + \mathbf{M}_{dc} \end{aligned} \quad (3.40)$$

and

$$\begin{aligned} \nabla \cdot (r_c \rho_c \mathbf{U}_c \mathbf{U}_c) &= -r_c \nabla p'_c + r_c \rho_c \mathbf{g} + \nabla \cdot r_c \mu_{eff,c} (\nabla \mathbf{U}_c + (\nabla \mathbf{U}_c)^T) \\ &+ \mathbf{S}_{M,c} + \mathbf{M}_{cd} \end{aligned} \quad (3.41)$$

where μ_{eff} is the effective viscosity accounting for turbulence given by

$$\mu_{eff,c} = \mu_c + \mu_t = \mu_c + \mu_{t,c} + \mu_{t,b} \quad (3.42)$$

The turbulent viscosity of the liquid phase is based on the $k-\varepsilon$ model and formulated as follows:

$$\mu_{t,c} = C_\mu \rho_c \frac{k^2}{\varepsilon} \quad (3.43)$$

where $C_\mu = 0.09$. The term $\mu_{t,b}$ is particle induced eddy viscosity. There are several models available to take account of this viscosity. In this work the model proposed by Sato and Sekoguchi (1975) was used:

$$\mu_{t,b} = C_{\mu,b} \rho_c r_d d |U_d - U_c| \quad (3.44)$$

with $C_{\mu,b}$ a model constant which equals 0.6 (Deen, Solberg, and Hjertager, 2002).

The effective vapor viscosity is calculated from the effective liquid viscosity as follows:

$$\mu_{eff,d} = \frac{\rho_d}{\rho_c} \mu_{eff,c} \quad (3.45)$$

as was proposed by Jakobsen, Sannaes, Grevskott, and Svendsen (1997). The term p' is the modified pressure given by

$$p'_d = p_d + \frac{2}{3} \rho_d k \quad \text{and} \quad p'_c = p_c + \frac{2}{3} \rho_c k \quad (3.46)$$

The values of k and ε come directly from the differential transport equation for the turbulence kinetic energy and turbulent dissipation rate, as shown below:

The transport equation of the turbulent kinetic energy, k is:

$$\frac{\partial(\rho k)}{\partial t} + \nabla \cdot (\rho \mathbf{U} k) = \nabla \cdot \left[\left(\mu + \frac{\mu_t}{\sigma_k} \right) \nabla k \right] + P_k - \rho \varepsilon \quad (3.47)$$

where $\sigma_k = 1.0$, $\rho = r_d \rho_d + r_c \rho_c$, $\mu = r_d \mu_d + r_c \mu_c$, $\mathbf{U} = (r_d \rho_d \mathbf{U}_d + r_c \rho_c \mathbf{U}_c) / \rho$,

$\mu_t = C_{\mu} \rho k^2 / \varepsilon$, k is the turbulent kinetic energy, and is defined as the variance of the fluctuation in velocity, and has dimensions of $L^2 T^{-2}$ (e.g. m^2/s^2). ε is the turbulent eddy dissipation (the rate at which the velocity fluctuations dissipate) and has

dimensions of L^2T^{-3} (e.g. m^2/s^3). P_k is the turbulence production due to viscous and buoyancy forces, which is modeled using:

$$P_k = \mu_t \nabla \mathbf{U} \cdot (\nabla \mathbf{U} + (\nabla \mathbf{U})^T) + P_{kb} \quad (3.48)$$

If the full buoyancy model is being used, the buoyancy production term P_{kb} is modeled as:

$$P_{kb} = -\frac{\mu_t}{\rho \text{Pr}_t} \mathbf{g} \cdot \nabla \rho \quad (3.49)$$

where Pr_t is the Turbulent Prandtl number, defined as: $c_p \mu / \lambda_t$. μ , c_p and λ_t respectively represent the viscosity, specific heat capacity at constant pressure and thermal conductivity for the liquid phase.

The transport equation of the dissipation rate of the turbulence kinetic energy, ε is:

$$\frac{\partial(\rho\varepsilon)}{\partial t} + \nabla \cdot (\rho \mathbf{U} \varepsilon) = \nabla \cdot \left[\left(\mu + \frac{\mu_t}{\sigma_\varepsilon} \right) \nabla \varepsilon \right] + \frac{\varepsilon}{k} (C_{\varepsilon 1} P_k - C_{\varepsilon 2} \rho \varepsilon) \quad (3.50)$$

where $\sigma_\varepsilon = 1.3$, $C_{\varepsilon 1} = 1.44$, and $C_{\varepsilon 2} = 1.92$.

In the ANSYS CFX program, a production term is also included in the ε equation if set to Production and Dissipation expert parameter is set and if the value of P_{kb} is positive:

$$P_{\varepsilon b} = C_3 \bullet \max(0, P_{kb}) \quad (3.51)$$

If the directional option is enabled, then $P_{\varepsilon b}$ is modified by a factor accounting for the angle α between the velocity and the gravity vectors:

$$P_{\varepsilon b} = C_3 \bullet \max(0, P_{kb}) \bullet \sin \alpha \quad (3.52)$$

where the default model constants are given by: $Sc_t = 1$ (full buoyancy model) and $C_3 = 1$.

Special consideration is required for flow near a no-slip wall, where there are strong gradients in the dependent variables. The near-wall region can be subdivided into two layers. In the layer very near the wall, called the “laminar (viscous) sublayer”, the molecular viscosity plays a dominant role in momentum and heat transfer. Further away from the wall, in the “logarithmic layer”, turbulence dominates the mixing process. Moreover, between the viscous sublayer and logarithmic layer, there is the “buffer layer”, where the effect of molecular viscosity and turbulence are of equal importance. Figure 3.2 shows these subdivisions of near-wall region.

A logarithmic profile is a reasonable assumption for the velocity distribution near the wall; this provides a means to numerically compute the fluid

shear stress as a function of the velocity at a given distance from the wall. This is known as a “wall function” and the logarithmic nature gives rise to the well known “log law of the wall”.

In this work the scalable wall function is conducted to model the flow near the wall, this function was developed by ANSYS CFX.

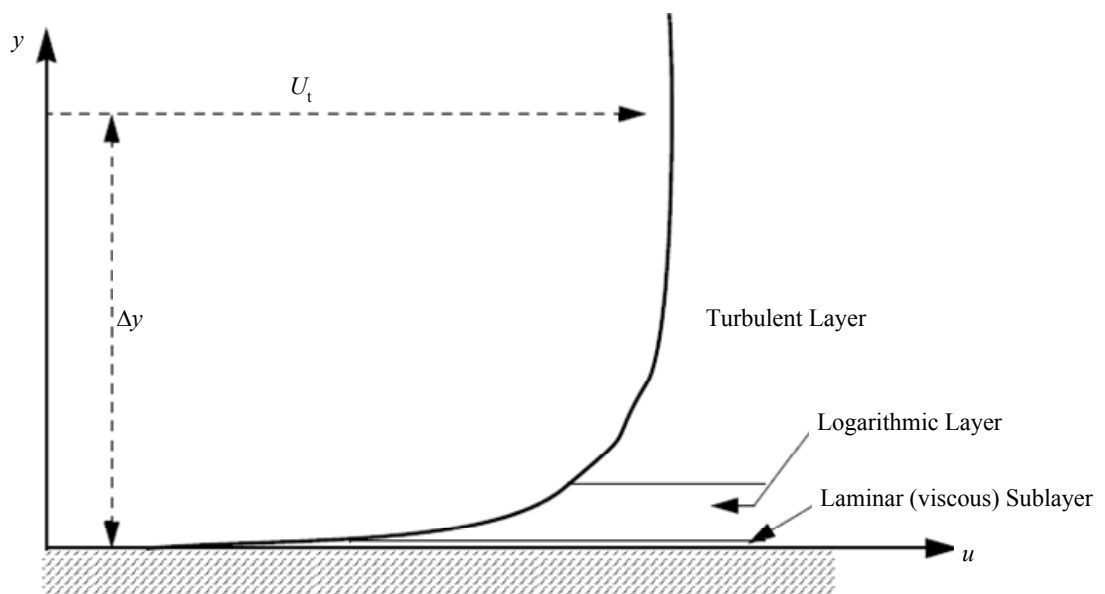


Figure 3.2 Flow regions for describing turbulent flow near a wall. (ANSYS Canada Ltd., 2005)

The logarithmic relation for the near wall velocity is given by:

$$u^+ = C_{\mu}^{1/4} k^{1/2} \quad (3.53)$$

The friction velocity is given by:

$$u_\tau = \frac{U_t}{\frac{1}{\kappa} \ln(y^+) + C} \quad (3.54)$$

The absolute value of the wall shear stress is then obtained from:

$$\tau_w = \rho u^+ u_\tau \quad (3.55)$$

where U_t is the known velocity tangent to the wall at a distance of Δy , $\kappa = 0.41$ (von Karman constant or kappa coefficient), $C = 5.2$, and $y^+ = (\rho u^+ \Delta y) / \mu$ (dimensionless distance from the wall). Note that the minimum y^+ is 11.06, this value is the intersection between logarithmic and the linear near wall profile. The computed y^+ is therefore not allowed to fall below this limit.

3.2.2 Non-isothermal simulation

3.2.2.1 The continuity equation

The full form of this equation is shown in equation (3.1). In this part, the system is at steady state and there is no mass source, so equation (3.1) becomes

$$\nabla \cdot (r_\alpha \rho_\alpha \mathbf{U}_\alpha) = \sum_{\beta=1}^{N_p=2} \Gamma_{\alpha\beta} \quad (3.56)$$

where $\Gamma_{\alpha\beta}$ is the mass flow rate per unit volume from phase β to phase α . See interphase mass transfer (p. 80). The continuity equation of each phase can be written below:

For the vapor phase:

$$\nabla \cdot (r_d \rho_d \mathbf{U}_d) = \Gamma_{dc} \quad (3.57)$$

For the liquid phase:

$$\nabla \cdot (r_c \rho_c \mathbf{U}_c) = \Gamma_{cd} \quad (3.58)$$

Note that Γ_{dd} and Γ_{cc} are both equal to zero, since there is no need for transfer terms into the phase the material originated from.

3.2.2.2 The momentum equation

The full form of this equation is shown in equation (3.5). In this part, the system is at steady state, so that equation (3.5) becomes

$$\begin{aligned} \nabla \cdot (r_\alpha \rho_\alpha \mathbf{U}_\alpha \mathbf{U}_\alpha) = & -r_\alpha \nabla p_\alpha + r_\alpha \rho_\alpha \mathbf{g} + \nabla \cdot r_\alpha \boldsymbol{\mu}_\alpha (\nabla \mathbf{U}_\alpha + (\nabla \mathbf{U}_\alpha)^T) \\ & + \sum_{\beta=1}^{N_p} (\Gamma_{\alpha\beta}^+ \mathbf{U}_\beta - \Gamma_{\beta\alpha}^+ \mathbf{U}_\alpha) + \mathbf{S}_{M,\alpha} + \sum_{\beta=1}^{N_p} \mathbf{M}_{\alpha\beta} \end{aligned} \quad (3.59)$$

where the term $(\Gamma_{\alpha\beta}^+ \mathbf{U}_\beta - \Gamma_{\beta\alpha}^+ \mathbf{U}_\alpha)$ represents momentum transfer induced by interphase mass transfer (see interphase mass transfer [p. 80]). The momentum equation of each phase can be written below:

For the vapor phase:

$$\begin{aligned} \nabla \bullet (r_d \rho_d \mathbf{U}_d \mathbf{U}_d) &= -r_d \nabla p_d + r_d \rho_d \mathbf{g} + \nabla \bullet r_d \mu_d (\nabla \mathbf{U}_d + (\nabla \mathbf{U}_d)^T) \\ &+ (\Gamma_{dc}^+ \mathbf{U}_c - \Gamma_{cd}^+ \mathbf{U}_d) + \mathbf{S}_{M,d} + \mathbf{M}_{dc} \end{aligned} \quad (3.60)$$

For the liquid phase:

$$\begin{aligned} \nabla \bullet (r_c \rho_c \mathbf{U}_c \mathbf{U}_c) &= -r_c \nabla p_c + r_c \rho_c \mathbf{g} + \nabla \bullet r_c \mu_c (\nabla \mathbf{U}_c + (\nabla \mathbf{U}_c)^T) \\ &+ (\Gamma_{cd}^+ \mathbf{U}_d - \Gamma_{dc}^+ \mathbf{U}_c) + \mathbf{S}_{M,c} + \mathbf{M}_{cd} \end{aligned} \quad (3.61)$$

Note that Γ_{dd}^+ , Γ_{cc}^+ , \mathbf{M}_{dd} , and \mathbf{M}_{cc} are both equal to zero, since there is no need for transfer terms into the phase the material originated from.

3.2.2.3 The energy equation

The full form of this equation is given in concise form below

$$\begin{aligned} \frac{\partial}{\partial t} (r_\alpha \rho_\alpha h_{tot,\alpha}) - r_\alpha \frac{\partial p}{\partial t} + \nabla \bullet (r_\alpha \rho_\alpha \mathbf{U}_\alpha h_{tot,\alpha} - r_\alpha \lambda_\alpha \nabla T_\alpha) \\ - \nabla \bullet (r_\alpha \mu_\alpha [\nabla \mathbf{U}_\alpha + (\nabla \mathbf{U}_\alpha)^T] \mathbf{U}_\alpha) = \sum_{\beta=1}^{N_p} (\Gamma_{\alpha\beta}^+ h_{tot,\beta} - \Gamma_{\beta\alpha}^+ h_{tot,\alpha}) \\ + \rho_\alpha r_\alpha (\mathbf{U}_\alpha \bullet \mathbf{g}) + S_{E,\alpha} + \sum_{\beta=1}^{N_p} Q_{\alpha\beta} \end{aligned} \quad (3.62)$$

In this part, the system is at steady state, so that equation (3.62) becomes

$$\begin{aligned} & \nabla \cdot (r_\alpha \rho_\alpha \mathbf{U}_\alpha h_{tot,\alpha} - r_\alpha \lambda_\alpha \nabla T_\alpha) - \nabla \cdot (r_\alpha \mu_\alpha [\nabla \mathbf{U}_\alpha + (\nabla \mathbf{U}_\alpha)^T] \mathbf{U}_\alpha) \\ &= \sum_{\beta=1}^{N_p} (\Gamma_{\alpha\beta}^+ h_{tot,\beta} - \Gamma_{\beta\alpha}^+ h_{tot,\alpha}) + \rho_\alpha r_\alpha (\mathbf{U}_\alpha \cdot \mathbf{g}) + S_{E,\alpha} + \sum_{\beta=1}^{N_p} Q_{\alpha\beta} \end{aligned} \quad (3.63)$$

where

- $h_{tot,\alpha}$, T_α , λ_α denote the total static enthalpy, the temperature, and the thermal conductivity of phase α .
- S_E denote external heat source, see heat source (p. 87).
- $Q_{\alpha\beta}$ denote interphase heat transfer to phase α across interfaces with other phases. See inhomogeneous interphase heat transfer model (p. 78).
- The term: $(\Gamma_{\alpha\beta}^+ h_{tot,\beta} - \Gamma_{\beta\alpha}^+ h_{tot,\alpha})$ represents heat transfer induced by interphase mass transfer. See interphase mass transfer (p. 80).

The energy equation of each phase can be written below

For the vapor phase:

$$\begin{aligned} & \nabla \cdot (r_d \rho_d \mathbf{U}_d h_{tot,d} - r_d \lambda_d \nabla T_d) - \nabla \cdot (r_d \mu_d [\nabla \mathbf{U}_d + (\nabla \mathbf{U}_d)^T] \mathbf{U}_d) \\ &= (\Gamma_{dc}^+ h_{tot,c} - \Gamma_{cd}^+ h_{tot,d}) + \rho_d r_d (\mathbf{U}_d \cdot \mathbf{g}) + S_{E,d} + Q_{dc} \end{aligned} \quad (3.64)$$

For the liquid phase:

$$\begin{aligned} & \nabla \cdot (r_c \rho_c \mathbf{U}_c h_{tot,c} - r_c \lambda_c \nabla T_c) - \nabla \cdot (r_c \mu_c [\nabla \mathbf{U}_c + (\nabla \mathbf{U}_c)^T] \mathbf{U}_c) \\ &= (\Gamma_{cd}^+ h_{tot,d} - \Gamma_{dc}^+ h_{tot,c}) + \rho_c r_c (\mathbf{U}_c \cdot \mathbf{g}) + S_{E,c} + Q_{cd} \end{aligned} \quad (3.65)$$

Note that Q_{dd} and Q_{cc} are both equal to zero, since there is no need for transfer terms into the phase the material originated from.

3.2.2.4 The volume conservation equation

This equation is the same as equation (3.9).

3.2.2.5 The pressure constraint

This equation is the same as equation (3.11).

3.2.2.6 The interphase momentum transfer model

This model is the same as the section 3.2.1.6. See the section on the interphase momentum transfer model (p. 62).

3.2.2.7 Inhomogeneous interphase heat transfer models

Interphase heat transfer occurs due to a state of thermal non-equilibrium across phase interfaces. The total heat per unit volume transferred to phase α due to interaction with another phase is denoted Q_α , and is given by:

$$Q_\alpha = \sum_{\beta \neq \alpha} Q_{\alpha\beta} \quad (3.66)$$

$$Q_{\alpha\beta} = -Q_{\beta\alpha} \Rightarrow \sum_{\alpha} Q_\alpha = 0 \quad (3.67)$$

In this work, the Two Resistance model for interphase heat transfer must be used in conjunction with the thermal phase change model. This model considers separate heat transfer processes either side of the phase interface. This is achieved by using two heat transfer coefficients defined on each phase interface.

Defining the sensible heat flux to the vapor phase from the interface as:

$$q_d = h_d(T_s - T_d) \quad (3.68)$$

and the sensible heat flux to the liquid phase from the interface as:

$$q_c = h_c(T_s - T_c) \quad (3.69)$$

where h_d and h_c are the vapor phase and liquid phase heat transfer coefficients respectively. T_s is the interface temperature, and it is assumed to be the same for both phases. Ignoring effects of surface tension on pressure, we assume $T_s = T_{sat}$. The liquid phase heat transfer coefficient is calculated via the fluid-specific Nusselt number ($Nu_\alpha = h_\alpha d_{\alpha\beta} / \lambda_\alpha$). In this work, the Hughmark (1967) correlation is used to find the heat transfer coefficient of the continuous phase and thus the Nusselt number is defined as:

$$Nu_c = \begin{cases} 2 + 0.6 Re_d^{0.5} Pr_c^{0.33} & 0 \leq Re_d < 776.06 & 0 \leq Pr_c < 250 \\ 2 + 0.27 Re_d^{0.62} Pr_c^{0.33} & 776.06 \leq Re_d & 0 \leq Pr_c < 250 \end{cases} \quad (3.70)$$

The Prandtl number is taken as $Pr_c = \mu_c C_{pc} / \lambda_c$. In the disperse phase side we select Zero Resistance, which is equivalent to an infinite fluid specific heat transfer

coefficient, $h_d \rightarrow \infty$. The effect of this is to force the interfacial temperature to be the same as the dispersed phase temperature, $T_s = T_d$, so that equation (3.68) becomes

$$q_d = 0 \quad (3.71)$$

and equation (3.69) becomes

$$q_c = h_c(T_d - T_c) \quad (3.72)$$

More detail of the theory used in this section is in the “thermal phase change model” section (p. 82).

3.2.2.8 Interphase mass transfer

Interphase mass transfer is a process where amounts of a chemical species is carried from one phase into another phase.

Γ_α is the mass source per unit volume into phase α due to interphase mass transfer. This is expressed as follows:

$$\Gamma_\alpha = \sum_{\beta=1}^{N_p-2} \Gamma_{\alpha\beta} \quad (3.73)$$

where $\Gamma_{\alpha\beta}$ is the mass flow rate per unit volume from phase β to phase α . So we get:

$$\Gamma_{\alpha\beta} = -\Gamma_{\beta\alpha} \Rightarrow \sum_{\alpha=1}^{N_p-2} \Gamma_\alpha = 0 \quad (3.74)$$

It is convenient to express $\Gamma_{\alpha\beta}$ in the direction of mass transfer processes, as follows:

$$\Gamma_{\alpha\beta} = \Gamma_{\alpha\beta}^+ - \Gamma_{\beta\alpha}^+ \quad (3.75)$$

The term $\Gamma_{\alpha\beta}^+ > 0$ is the positive flow rate per unit volume from phase β to phase α .

For the mass transfer processes across a phase interphase, it is useful to express the volumetric mass sources in term of density between the phases.

$$\Gamma_{\alpha\beta} = \dot{m}_{\alpha\beta} A_{\alpha\beta} \quad (3.76)$$

where $\dot{m}_{\alpha\beta}$ is the mass flow rate per unit volume interfacial area from phase β to phase α , and $A_{\alpha\beta}$ is the interfacial area per unit volume between the phases. For the dispersed phase it is assumed that the disperse phase is a spherical particle, $A_{\alpha\beta} = 6r_{\beta} / d_{\beta}$. See more details in the thermal phase change model (p. 82).

The default form of the secondary source terms for a transported variable ϕ_{α} is:

$$S_{m\alpha} = \sum_{\beta=1}^{N_p-2} (\Gamma_{\alpha\beta}^+ \phi_{\beta} - \Gamma_{\beta\alpha}^+ \phi_{\alpha}) \quad (3.77)$$

This means that the mass transfer from a phase β into a phase α carries the bulk conserved quantity ϕ_{β} into phase α . It is referred to as an upwind formulation, as the upwind value is carried out from the outgoing phase, and into the incoming phase.

This default formulation is modified in certain circumstances, in order to take account of discontinuities in the transported variable at the phase interface, for this work, velocity and enthalpy are considered.

3.2.2.9 The thermal phase change model

This is the model of phase change induced by interphase heat transfer in the interior of the flow. In this work, the saturation temperature is constant so that the vapor phase temperature should remain fixed at saturation conditions. It is possible to run the vapor phase as isothermal, with a reference temperature set equal to the vapor saturation temperature. For the liquid phase, the total energy model was used to model the heat transfer process.

In the case of mass transfer, the interphase mass transfer is determined from the total heat balance, as follows:

Total heat flux to liquid phase from the interface:

$$Q_{cd} = q_c + \dot{m}_{cd} H_{s,c} \quad (3.78)$$

Total heat flux to vapor phase from the interface:

$$Q_{dc} = q_d - \dot{m}_{cd} H_{s,d} \quad (3.79)$$

Substitution of equation (3.71) into (3.79), gives

$$Q_{dc} = -\dot{m}_{cd} H_{s,d} \quad (3.80)$$

where $H_{s,c}$ and $H_{s,d}$ represent interfacial values of enthalpy of liquid and vapor, respectively, which are carried into and out of the phases due to phase change.

The total heat balance $Q_c + Q_d = 0$ now determines the interphase mass flux:

$$\dot{m}_{cd} = \frac{q_c}{H_{s,d} - H_{s,c}} \quad (3.81)$$

The discontinuity in static enthalpy due to latent heat between the two phases must be taken into account by the secondary heat flux term, which is achieved using a modification of the upwind formulation (equation 3.77). In this formulation, the bulk fluid enthalpy is carried out of the outgoing phase, as in the default upwind formulation. However, the saturation enthalpy is carried into the incoming phase. Thus:

$$\dot{m}_{cd} > 0 \Rightarrow H_{s,c} = H_{sat,c}, \quad H_{s,d} = H_d \quad (3.82)$$

$$\dot{m}_{cd} < 0 \Rightarrow H_{s,c} = H_c, \quad H_{s,d} = H_{sat,d}$$

This leads to a formulation which is stable both physically and numerically. It implies that the denominator (equation 3.81) is non-zero. Being greater than or equal to the latent heat transfer:

$$L = H_{sat,d} - H_{sat,c} \quad (3.83)$$

In this work, the effects of surface tension on pressure are ignored so $T_s = T_{sat}$.

Equation (3.81) becomes

$$\dot{m}_{cd} = \frac{h_c(T_{sat} - T_c)}{L} \quad (3.84)$$

3.2.2.10 Turbulence models

The momentum equations are considered the same way as for the isothermal simulation. So that the equations

$$\begin{aligned} \nabla \cdot (r_d \rho_d \mathbf{U}_d \mathbf{U}_d) &= -r_d \nabla p'_d + r_d \rho_d \mathbf{g} + \nabla \cdot r_d \mu_{eff,d} (\nabla \mathbf{U}_d + (\nabla \mathbf{U}_d)^T) \\ &+ (\Gamma_{dc}^+ \mathbf{U}_c - \Gamma_{cd}^+ \mathbf{U}_d) + \mathbf{S}_{M,d} + \mathbf{M}_{dc} \end{aligned} \quad (3.85)$$

and

$$\begin{aligned} \nabla \cdot (r_c \rho_c \mathbf{U}_c \mathbf{U}_c) &= -r_c \nabla p'_c + r_c \rho_c \mathbf{g} + \nabla \cdot r_c \mu_{eff,c} (\nabla \mathbf{U}_c + (\nabla \mathbf{U}_c)^T) \\ &+ (\Gamma_{cd}^+ \mathbf{U}_d - \Gamma_{dc}^+ \mathbf{U}_c) + \mathbf{S}_{M,c} + \mathbf{M}_{cd} \end{aligned} \quad (3.86)$$

for the vapor and liquid phase, respectively, are used. For the liquid phase, the $k - \varepsilon$ turbulent model was employed. Most equations in this model are the same as the isothermal part, except the velocity and other transport properties in the k and ε equations are from the liquid properties. For the vapor phase, the Dispersed Phase Zero Equation model was employed. In this model, the $\mu_{t,d} = \rho_d \mu_{t,c} / \rho_c \sigma$ so that the effective vapor viscosity is

$$\mu_{eff,d} = \mu_d + \frac{\rho_d}{\rho_c} \frac{\mu_{t,c}}{\sigma} \quad (3.87)$$

The parameter σ is a turbulent Prandtl number relating the dispersed phase kinetic eddy viscosity to the continuous phase kinetic eddy viscosity ($\sigma = \nu_{t,d} \nu_{t,c}$). In this work the default value of 1.0 is used.

Convective transport due to turbulent velocity fluctuations will act to enhance mixing over and above that caused by thermal fluctuations at the molecular level. At high Reynolds numbers, the mean free path of thermal fluctuations is smaller than the turbulent velocity fluctuations occur over a length scale, so that the turbulent fluxes are much larger than the molecular fluxes (this means that the term of $\nabla \cdot (r_\alpha \mu_\alpha (\nabla \mathbf{U}_\alpha + (\nabla \mathbf{U}_\alpha)^T) \mathbf{U}_\alpha)$ in the energy equation for both phase are canceled). So that the Reynolds-averaged energy equations are:

For the vapor phase:

$$\begin{aligned} & \nabla \cdot (r_d \rho_d \mathbf{U}_d h_{tot,d} - r_d \lambda_d \nabla T_d + \rho_d \overline{\mathbf{u}_d h_{tot,d}}) \\ & = (\Gamma_{dc}^+ h_{tot,c} - \Gamma_{cd}^+ h_{tot,d}) + \rho_d r_d (\mathbf{U}_d \cdot \mathbf{g}) + S_{E,d} + Q_{dc} \end{aligned} \quad (3.88)$$

For the liquid phase:

$$\begin{aligned} & \nabla \cdot (r_c \rho_c \mathbf{U}_c h_{tot,c} - r_c \lambda_c \nabla T_c + \rho_c \overline{\mathbf{u}_c h_{tot,c}}) \\ & = (\Gamma_{cd}^+ h_{tot,d} - \Gamma_{dc}^+ h_{tot,c}) + \rho_c r_c (\mathbf{U}_c \cdot \mathbf{g}) + S_{E,c} + Q_{cd} \end{aligned} \quad (3.89)$$

where $-\rho_d \overline{\mathbf{u}_d h_{tot,d}}$ and $-\rho_c \overline{\mathbf{u}_c h_{tot,c}}$ are the Reynolds fluxes of enthalpy for vapor and liquid, respectively. The Reynolds fluxes of enthalpy is given by

$$-\rho \overline{\mathbf{u}h} = \Gamma_t \nabla h \quad (3.90)$$

where Γ_t is the eddy diffusivity and given by $\Gamma_t = \mu_t / \text{Pr}_t$. So the Reynolds averaged energy equations become:

For the vapor phase:

$$\begin{aligned} \nabla \cdot \left(r_d \rho_d \mathbf{U}_d h_{tot,d} - r_d \lambda_d \nabla T_d + \frac{\mu_t}{\text{Pr}_t} \nabla h_{tot,d} \right) &= (\Gamma_{dc}^+ h_{tot,c} - \Gamma_{cd}^+ h_{tot,d}) \\ + \rho_d r_d (\mathbf{U}_d \cdot \mathbf{g}) + S_{E,d} + Q_{dc} \end{aligned} \quad (3.91)$$

For the liquid phase:

$$\begin{aligned} \nabla \cdot \left(r_c \rho_c \mathbf{U}_c h_{tot,c} - r_c \lambda_c \nabla T_c + \frac{\mu_t}{\text{Pr}_t} \nabla h_{tot,c} \right) &= (\Gamma_{cd}^+ h_{tot,d} - \Gamma_{dc}^+ h_{tot,c}) \\ + \rho_c r_c (\mathbf{U}_c \cdot \mathbf{g}) + S_{E,c} + Q_{cd} \end{aligned} \quad (3.92)$$

The eddy viscosity, μ_t , is related to k and ε , which their differential equations are the same as section 3.2.1.7.

3.2.2.11 Momentum sources

The source is the same as described in section 3.2.1.5.

3.2.2.12 Heat sources

The heat exchanger is represented as specifying bulk heat source term and can be specifying directly at the heat exchanger subdomain. However, for convenience the bulk heat source can be specified directly at the impeller subdomain, which is an acceptable approach considering the temperature rise in the crystallizer caused by the heat exchanger is a low value (in the order of 1 - 2 °C) to reach the boiling temperature, and normally the heat exchanger is located near the impeller. This method can reduce the computation time and model complexity of the solid heat source.

$$S_{E,c} = \frac{\dot{Q}}{V} = \frac{\text{heat quantity}}{\text{volume of source}} \quad \left[\frac{\text{W}}{\text{m}^3} \right] \quad (3.93)$$

3.3 Conclusions

The complete set of steady state governing equations of fluid flow and heat transfer for Newtonian two-phase flow (Eulerian-Eulerian multiphase model) are given. In the isothermal part, the homogeneous $k - \varepsilon$ turbulence model was employed where both phases share the same values for k and ε . And in the non-isothermal part, the $k - \varepsilon$ turbulence model was employed in the liquid phase, and the Dispersed Phase Zero Equation model was employed in the vapor phase. So that the main transport equations for isothermal simulation are equations 3.3, 3.4, 3.40, 3.41, 3.42, 3.45, 3.47, and 3.50 and for non-isothermal simulation are equations 3.42, 3.47, 3.50, 3.57, 3.58, 3.85, 3.86, 3.87, 3.91, and 3.92. These equations do not have analytical solutions for most systems, but CFD uses a range of space and time

discretization method in order to enable a numerical solution to be calculated. In this thesis, the commercial CFD software ANSYS CFX-10.0 with the finite volume method using an unstructured mesh was used to discretize the volume and find the solution of these equations.

CHAPTER IV

APPARATUS AND METHODS

The aim of this chapter is to describe the apparatus used in this work, the study methods to approach each objective shown in chapter 1, and the simulation methods to obtain the results. The simulation methods will focus on the processes of the ANSYS CFX-10.0 simulation, which are split into five components: geometry creation (ANSYS Workbench 10.0), mesh creation (CFX-Mesh), physical definitions (CFX-Pre), solver (CFX-Solver), and post-processing (CFX-Post).

4.1 Apparatus

In this thesis, the following apparatus were used:

1. A Pentium IV 3.0GHz processor with 512 MB of RAM and a AMD Athlon(tm) XP 2500+ 1.84 GHz processor with 384 MB of RAM.
2. An operating system of Microsoft Windows XP Professional Version 2002 Service Pack 1.
3. The commercial software ANSYS CFX-10.0, ANSYS Workbench 10.0, Microsoft Office Professional Edition 2003, and Microsoft Visio Professional 2002 [English].

4.2 Study Methods

The methods to achieve each objective of this study are described below.

4.2.1 Isothermal simulation

In this section, the vapor is assumed to form in an external heat exchanger before being fed into the crystallizer. The temperature rise in the crystallizer, which is caused by heat produced by the impeller and heat of crystallization, is not more than 2 °C (Genck, 2004). Therefore, the crystallizer can be assumed to be an isothermal process without significant error. This indicates that the DTB crystallizer with an external heat exchanger can be adequately modeled by an isothermal process in order to reduce the computation time and model complexity.

4.2.1.1 Study into the general characteristics of flow fields and classification of crystals in a DTB crystallizer

It is necessary to understand the general characteristics of the flow fields in a DTB crystallizer before study into the effect of the different operating parameters. The case study number 5 in Table 4.1 is the general case that was selected to achieve this purpose.

Other case studies are also presented in Table 4.1; values of the parameters chosen were based on values used in an experimental and theoretical paper on the same crystallizer at Delft University of Technology (Eek, Dijkstra, and van Rosmalen, 1995).

Table 4.1 Case studies for the isothermal simulations.

Case Study Number	Variable					
	Solution Inlet ¹		Total Fines Flow ^{2,3} (kg/s)	Vapor Out Flow (kg/s)	Product Out ³ Flow (kg/s)	Momentum Source (kg/m ² /s ²)
	Liquid Flow (kg/s)	Vapor Flow (kg/s)				
1	1.1860	0.0000649	1.0063	0.0000649	0.1797	0
2	1.1860	0.0000649	1.0063	0.0000649	0.1797	1,000
3	1.1860	0.0000649	1.0063	0.0000649	0.1797	4,000
4	1.1860	0.0000649	1.0063	0.0000649	0.1797	7,000
5	1.1860	0.0000649	1.0063	0.0000649	0.1797	10,000

¹Solution inlet = Fines + Fresh feed solution.

²Fines Removal1 flow = Fines Removal2 flow = Total Fines flow ÷ 2

³Fines and Product streams are assumed to have the properties of liquids for convenience.

Table 4.1 (Continued)

Case Study Number	Variable					
	Solution Inlet		Total Fines Flow (kg/s)	Vapor Out Flow (kg/s)	Product Out Flow (kg/s)	Momentum Source (kg/m ² /s ²)
	Liquid Flow (kg/s)	Vapor Flow (kg/s)				
6	1.1860	0.0000649	1.0063	0.0000649	0.1797	15,000
7	1.1860	0.0000649	1.0063	0.0000649	0.1797	25,000
8	1.1860	0.0000649	1.0063	0.0000649	0.1797	30,000
9	0.6469	0.0000354	0.4672	0.0000354	0.1797	10,000
10	1.1860	0.0000649	1.0063	0.0000649	0.1797	10,000
11	1.7251	0.0000944	1.5454	0.0000944	0.1797	10,000
12	2.4799	0.0001357	2.3002	0.0001357	0.1797	10,000

Table 4.1 (Continued)

Case Study Number	Variable					
	Solution Inlet		Total Fines Flow (kg/s)	Vapor Out Flow (kg/s)	Product Out Flow (kg/s)	Momentum Source (kg/m ² /s ²)
	Liquid Flow (kg/s)	Vapor Flow (kg/s)				
13	3.7737	0.0002065	3.5940	0.0002065	0.1797	10,000
14	1.0662	0.0000583	1.0063	0.0000583	0.0599	10,000
15	1.1261	0.0000616	1.0063	0.0000616	0.1198	10,000
16	1.1860	0.0000649	1.0063	0.0000649	0.1797	10,000
17	1.2699	0.0000695	1.0063	0.0000695	0.2636	10,000
18	1.4735	0.0000806	1.0063	0.0000806	0.4672	10,000

4.2.1.2 Study into the effect of the momentum source strength on the flow characteristics and the classification of crystals

A momentum source is used to represent the impeller in order to reduce the computation time and model complexity. This is based on studies of Pericleous and Patel (1987) who showed that this is an effective way to model an impeller in CFD modeling of mixing vessels. Therefore, it is important to study the effect of the momentum source strength, which is equivalent to a study of the effect of impeller speed.

In this study, the flow characteristics and the classification of crystals obtained from different amounts of the momentum source were compared under the same solution inlet flow rate, fines removal flow rate, and product crystal suspension flow rate. The momentum source values are 0, 1,000, 4,000, 7,000, 10,000, 15,000, 25,000, and 30,000 $\text{kg/m}^2/\text{s}^2$, as indicated in case studies 1 to 8 in Table 4.1.

4.2.1.3 Study into the effect of the fines removal flow rate on the flow characteristics and the classification of crystals

The fine crystals in the mother liquor are separated out from the crystallizer in an annular zone outside the main body of the crystallizer (the settling zone). In this zone, fines removed from the annulus must flow upward to obtain crystal segregation based on differences in settling velocity. Normally a higher fines removal flow will result in a fines removal cut-size larger than for a lower fines removal flow, because higher flows create larger upflow velocities in the settling zone, and thus larger particles are drawn upwards and removed.

In this study, the flow characteristics and the classification of crystals obtained from different values of the fines removal flow rate were compared under the same solution inlet flow rate, amount of momentum source, and product crystal suspension flow rate. The fines removal flows were varied at 0.4672, 1.0063, 1.5454, 2.3002, and 3.594 kg/s, as shown in case studies 9 to 13 of Table 4.1. To achieve the material balance, increasing the fines removal flow necessitated increasing the feed solution (because the product flow is maintained constant).

4.2.1.4 Study into the effect of the product crystal suspension flow rate on the flow characteristics and the classification of crystals

In this study, the flow characteristics and the classification of crystals obtained from different values of the product crystal suspension flow rate were compared under the same solution inlet flow rate, amount of momentum source, and product crystal suspension flow rate. For a feed solution flow of approximately 1 kg/s, product crystal suspension flows were varied at 0.0599, 0.1198, 0.1797, 0.2636, and 0.4672 kg/s, as shown case studies 14 to 18 of Table 4.1. To achieve the material balance, increasing the product crystal suspension flow necessitated increasing the feed solution (because the fines removal flow is maintained constant).

4.2.2 Non-isothermal simulation

In this section, the feed solution is heated by an external heat exchanger to a temperature about 1-2 °C below the boiling point. The vapor is formed in the crystallizer, due to the temperature rising to the boiling point due to the internal heat exchanger. For this reason, the area above the liquid surface was not modeled and the liquid surface is considered to be flat and frictionless in order to reduce the model complexity.

4.2.2.1 The validation of the degassing condition at the liquid surface

It is necessary to validate this condition because the non-isothermal study models only the area below the liquid surface and the free surface flow model with heat and mass transfer is difficult to do. In this section the flow fields of case study number 5 were simulated to validate between the free surface flow model and the degassing condition at the liquid surface.

4.2.2.2 Study into the effect of heat and mass transfer via the evaporation on the flow characteristics and classification of crystals

The flow characteristics and classification of crystals obtained from crystallizers with varying heat source strengths were compared under the same solution inlet flow rate, amount of momentum source, fines removal flow rate, and product crystal suspension flow rate. The details in each case study of these studies are shown in Table 4.2.

Table 4.2 Case studies for the non-isothermal simulations.

Case Study Number	Liquid Solution Inlet (kg/s)	Product Out Flow (kg/s)	Momentum Source (kg/m ² /s ²)	Heat Source (kW/m ³)
19	1.1860	0.1797	10,000	11,000
20	1.1860	0.1797	10,000	12,000
21	1.1860	0.1797	20,000	13,000
22	1.1860	0.1797	30,000	13,500

The heat source values used are substantially lower than used in the experimental work of Eek *et al.* (1995). The values used produce approximately the correct amount of vapor (about 10% vapor) in the crystallizer. Presumably the crystallizer used in the experimental work had very high values of heat loss, meaning that more heat input was required. At high value of heat addition vapor production was high and the simulation could not converge.

4.3 Simulation Methods

To obtain the results of each study listed in Tables 4.1 and 4.2, simulation by ANSYS CFX-10.0 was conducted to determine flow fields (and temperature profiles for non-isothermal runs) in the DTB crystallizer.

The processes of the ANSYS CFX-10.0 simulation are split into five components. These are geometry creation, mesh creation, physical definitions (physics of the problem, physical parameter constants, among other considerations), equation solver, and post-processing. Each component is described below:

4.3.1 Geometry

In this work the DTB crystallizer geometry was created by the program DesignModeler in ANSYS Workbench v.10.0.

The crystallizer used for numerical simulation in this work is a pilot scale 1,050 L DTB crystallizer. The crystallizer dimensions and 3D geometry are given in Figures 4.1 and 4.2, respectively. The operating parameters and performance of this crystallizer are discussed in chapter 2 (section 2.2.2).

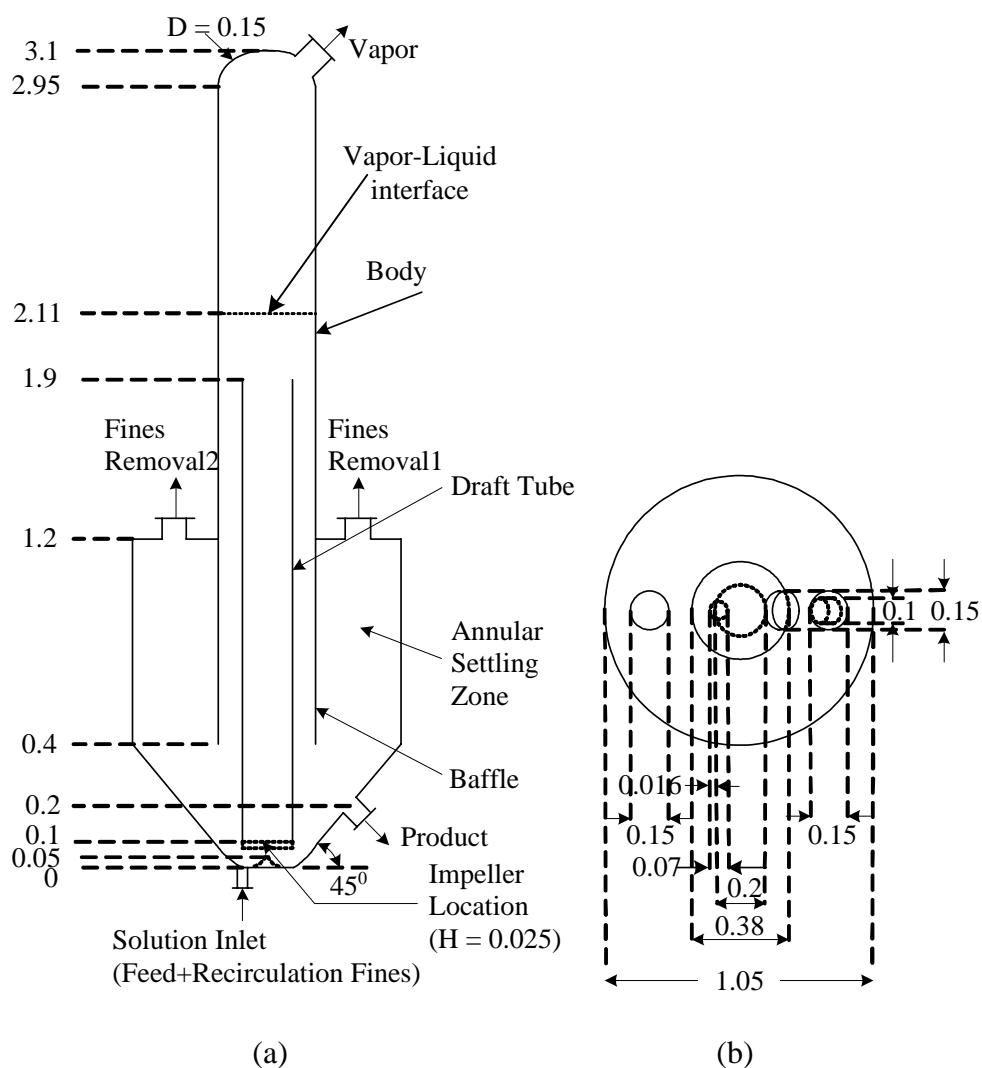


Figure 4.1 DTB crystallizer geometry and dimensions. Dimensions are given in meters: (a) side view; (b) top view.

For convenience in the simulation, the wall of the solution inlet tube, product outlet tube, fines removal tube, vapor outlet tube, draft tube, baffle, and tank are described using a thin surface material. The impeller (in this crystallizer the impeller is considered to be a turbine of diameter: height 8:1, with a 45° pitched blade) is represented as a momentum source term in the vertical direction (upward

flow) only. In the real impeller there are also radial components of the momentum addition, however they are effectively damped out by baffles placed in the normal direction to the tank walls. Since the radial components of the momentum addition are damped out in this design, we have not attempted to model them here to reduce the model complexity. A momentum source term has been added at the base of the draft tube, at the position and size of the true impeller (see Figure 4.1).

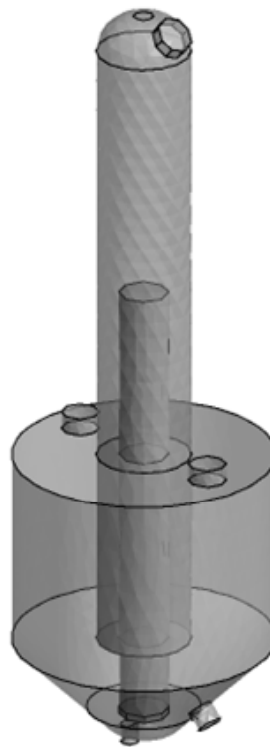


Figure 4.2 3D geometry of DTB crystallizer.

4.3.2 Mesh

In this work the mesh was created by the program CFX-Mesh in ANSYS Workbench v.10.0.

The first step in mesh creation is to create composite 2D regions to specify locations in CFX-Mesh and define boundary conditions in CFX-Pre. These regions include the solution inlet, product outlet, fines removal, vapor outlet, draft tube, baffle, and tank walls (the remaining outside walls) (see Figure 4.3).

The final step before the physics definition is to create the mesh, which was created by the program CFX-Mesh in ANSYS Workbench v.10.0. ANSYS CFX-10.0 uses the finite volume solution technique with an unstructured mesh. Initially the program creates a 2D mesh on the boundaries of the crystallizer geometry, and then this mesh is extrapolated into the body of the geometry. The volume of the crystallizer tank is broken into a set of discrete subdomains, computational cells, or control volumes using a grid, or mesh. The mesh can contain elements of many shapes and size. The points of intersection of the lines that make up the sides of the elements are referred to as nodes. In CFX-Mesh, 3-D elements are usually tetrahedral (with four sides), prisms (with five sides), pyramids (with five sides), and hexahedra (with six sides).

4.3.2.1 Mesh generation

Generally, the density of cells in a computational mesh needs to be fine enough to capture the flow detail, but not so fine that the overall number of cells in the domain is excessively large, since problems described by large numbers of cells require more time to solve (Paul *et al.*, 2004). Non-uniform meshes of any topology can be used to give higher mesh density in regions where it is needed and to allow for lower mesh densities in other regions.

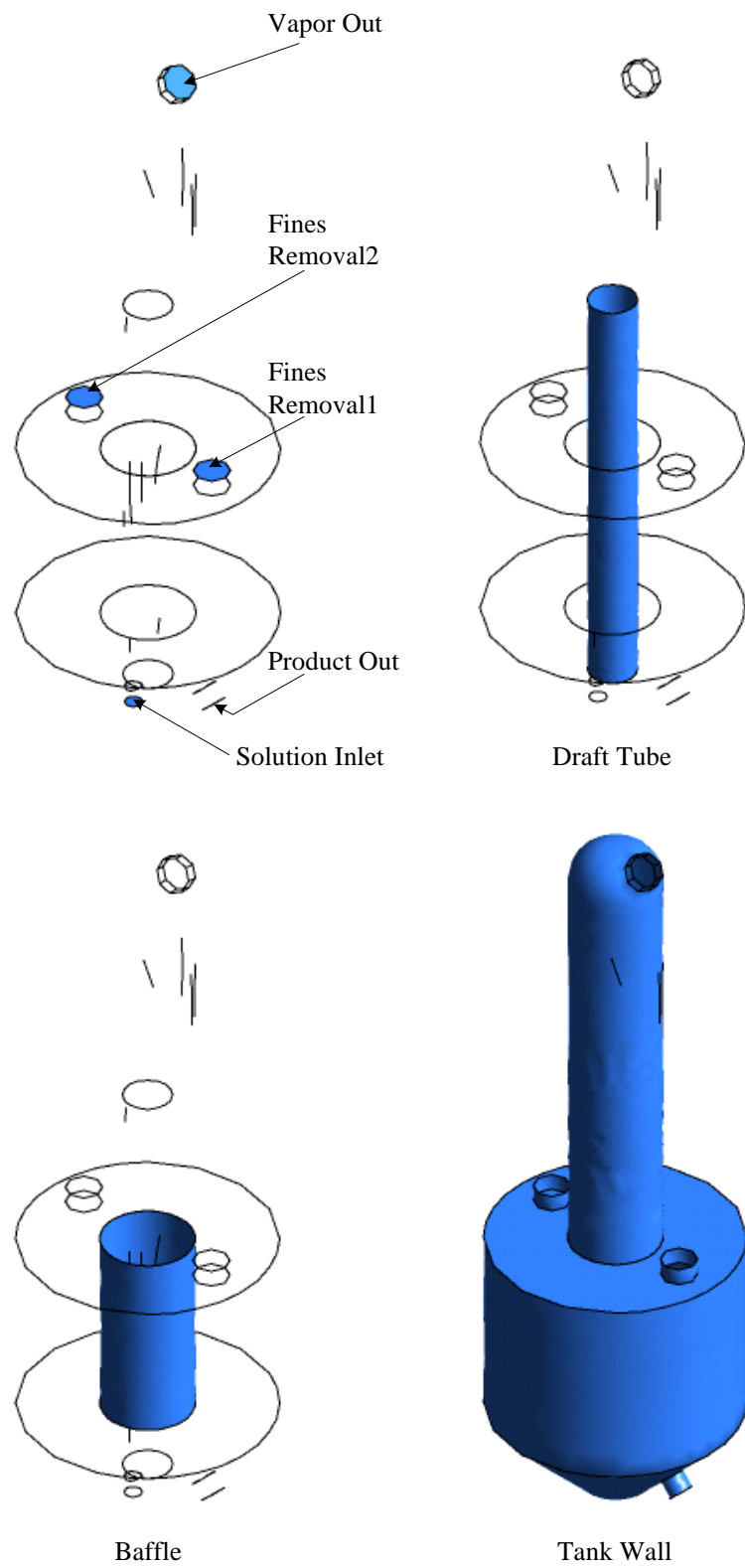


Figure 4.3 Composite 2D regions.

In this work, the mesh near the solution inlet boundary, product outlet boundary, the region under the draft tube, the region around the draft tube, and the region around the upper edge of draft tube should be refined to have a reasonably fine mesh and allow the solution to capture the flow details (especially, the velocity, since it changes rapidly in these regions). An example of the fine mesh of the above boundaries and regions is shown in Figure 4.4.

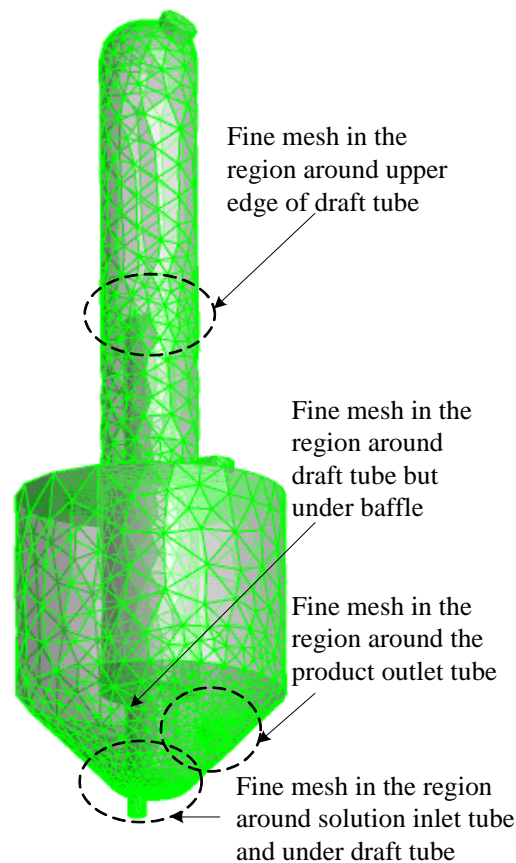


Figure 4.4 Fine mesh in the specified regions.

After defining and setting the conditions of the mesh and the region where a fine mesh is required, the surface mesh will be generated prior to the

volume mesh generation. However, it is often helpful to explicitly generate at least part of the surface mesh before volume meshing, to view it and ensure that the chosen scales and controls will have the desired effect.

4.3.2.2 Procedures of the optimum mesh generation

The mesh generation is important to the numerical solutions. If the mesh is not suitable (particularly if the mesh spacing is too large), the numerical results diverge or produce incorrect results. The method which was used to find the optimum mesh is separated to four steps, as described below:

1st step: Firstly, the maximum spacing was set (this is the maximum element size which will be used when creating triangles on the faces of the body and tetrahedral element in the volume of the body); the initial setting is set automatically by the program to around 5% (0.17 m) of the maximum extent of the model. Then the maximum edge length (this is set equal to the maximum spacing) and the minimum edge length were set. Finally, the mesh was created and then loaded into CFX-Pre to specify the model conditions, fluid properties, flow conditions, initial conditions, and boundary conditions. Note that these conditions will be the same for all runs.

2nd step: The second step of the mesh creation is variable based mesh adaptation. In this work, this technique is used to increase the mesh density in the region of a liquid-vapor interface. CFX-Pre has a mesh adaptation mode where once or more during a run, the mesh is selectively refined in areas which depend on the adaptation criteria specified. This means that as the solution is calculated, the mesh density can automatically be increased or decreased in locations where solution variables change rapidly, in order to resolve the features of the flow in these regions.

In this work, the vapor volume fraction was selected as the adaptation variable, because it is an important variable that changes rapidly in the region of the liquid-vapor interface. The number of adaptation steps was set to 2, and the maximum iterations per step to 200: (if the maximum iterations is set to 300, this results in a total maximum number of iterations of 600 [$200 \times 2 + 300 = 700$]). Note that this step uses the same parameters for all runs.

3rd step: Solve the problem using CFX-Solver. Calculate and record the liquid velocity (and other variables) at the measured positions (see Figure 4.5).

4th step: Decrease the maximum spacing, maximum edge length, and minimum edge length and then repeat the 2nd and 3rd steps. The liquid velocity of each run was compared; if the values are different, these parameter values must be adjusted continuously until the change in the values of the simulated variables is small or zero. Meshes that give no change in values of the simulated variables (mesh independent results) are the optimum meshes, but a mesh that has the maximum mesh scale to reduce the calculation times or the average calculation size should be selected for computational efficiency. All mesh scales in each run used to determine mesh independent results are summarized in Table 4.3. The liquid velocities of each run are compared in Figures 4.6 to 4.13.

Table 4.3 Mesh sizes of each run; used to find the optimum mesh.

Run	Maximum Edge Length ¹ (m)	Minimum Edge Length (m)	Number of Nodes		Number of Elements	
			Before mesh adaptation	After mesh adaptation	Before mesh adaptation	After mesh adaptation
1	0.17	0.0085	8,421	41,485	41,068	207,461
2	0.1	0.007	8,634	42,248	41,961	210,960
3	0.1	0.001	9,460	46,557	46,606	233,682
4	0.09	0.001	9,899	47,735	48,503	238,977
5	0.08	0.001	10,257	49,461	50,341	247,376
6	0.07	0.001	11,782	55,971	57,398	279,436
7	0.06	0.001	13,330	63,997	65,475	319,291

¹Maximum edge length is set equal to the maximum spacing.

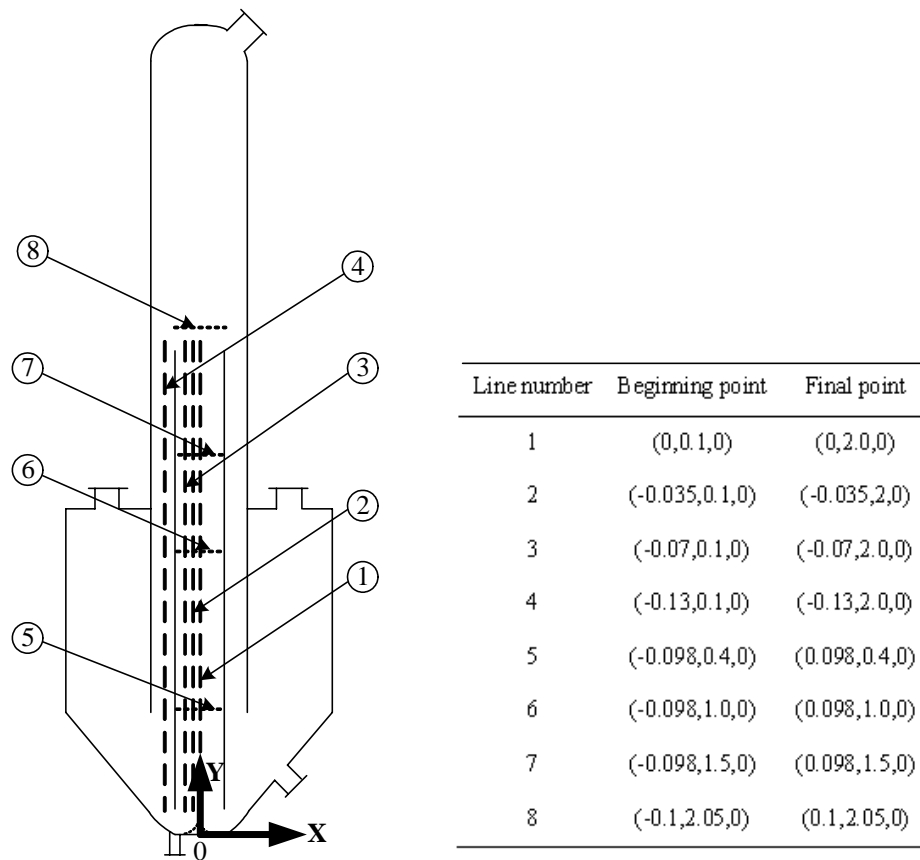


Figure 4.5 Line positions used to measure the liquid velocity. The positions are given in the form (X,Y,Z).

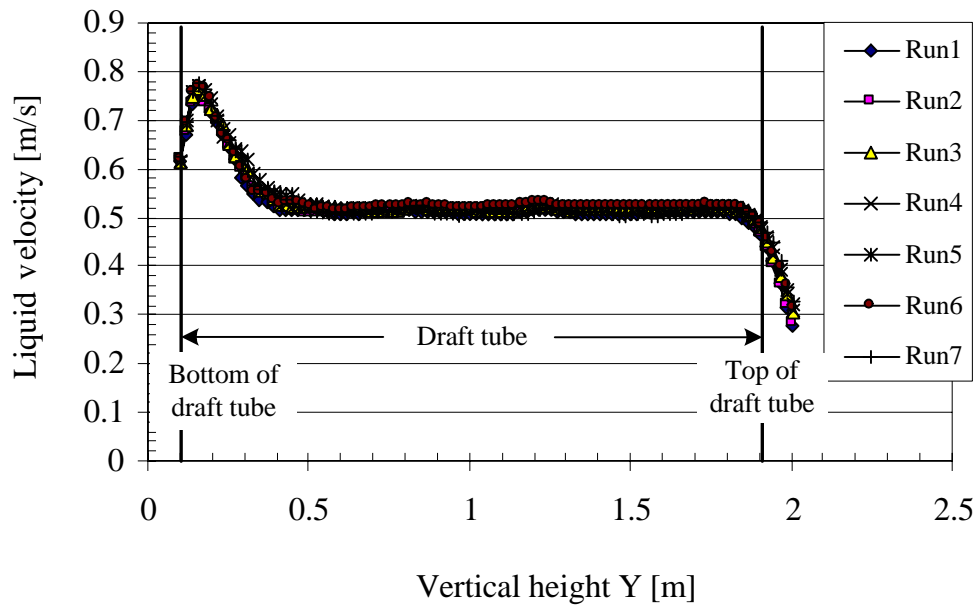


Figure 4.6 Liquid velocity profiles at line 1.

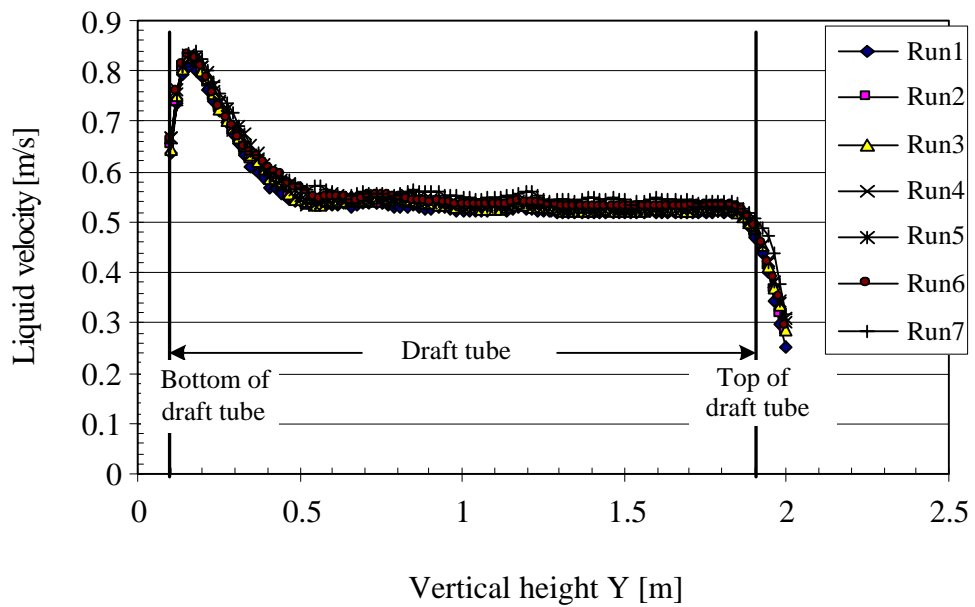


Figure 4.7 Liquid velocity profiles at line 2.

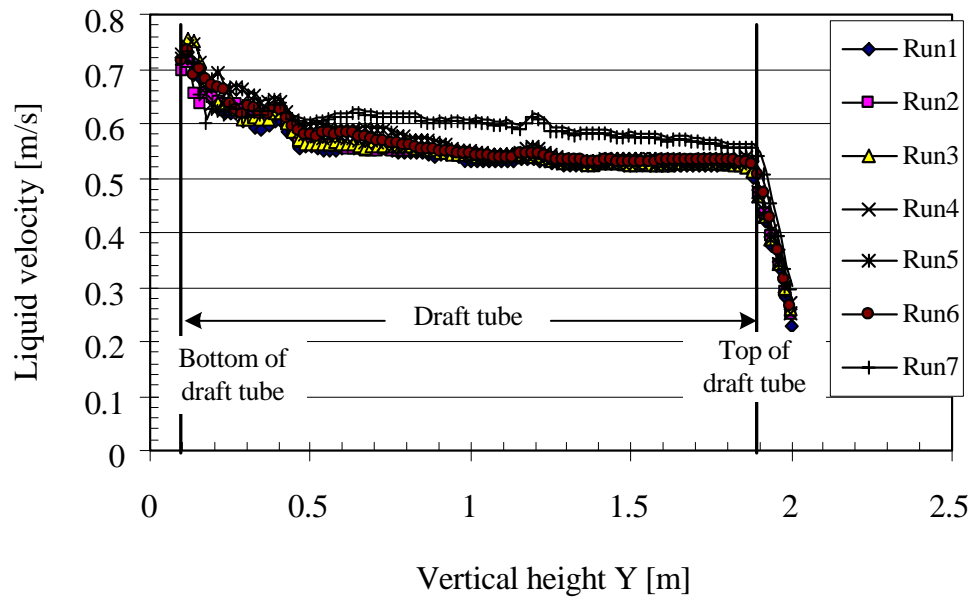


Figure 4.8 Liquid velocity profiles at line 3.

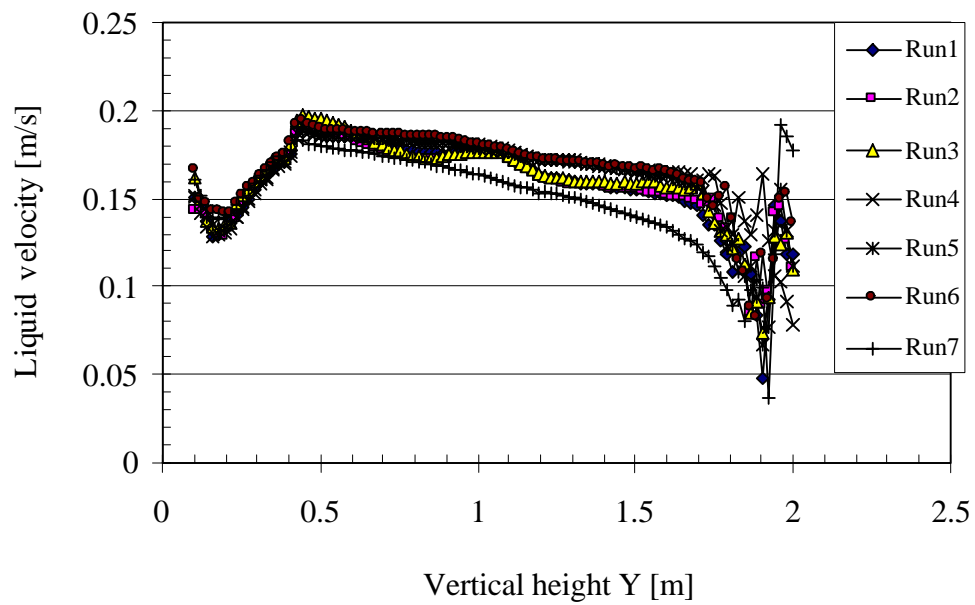


Figure 4.9 Liquid velocity profiles at line 4.

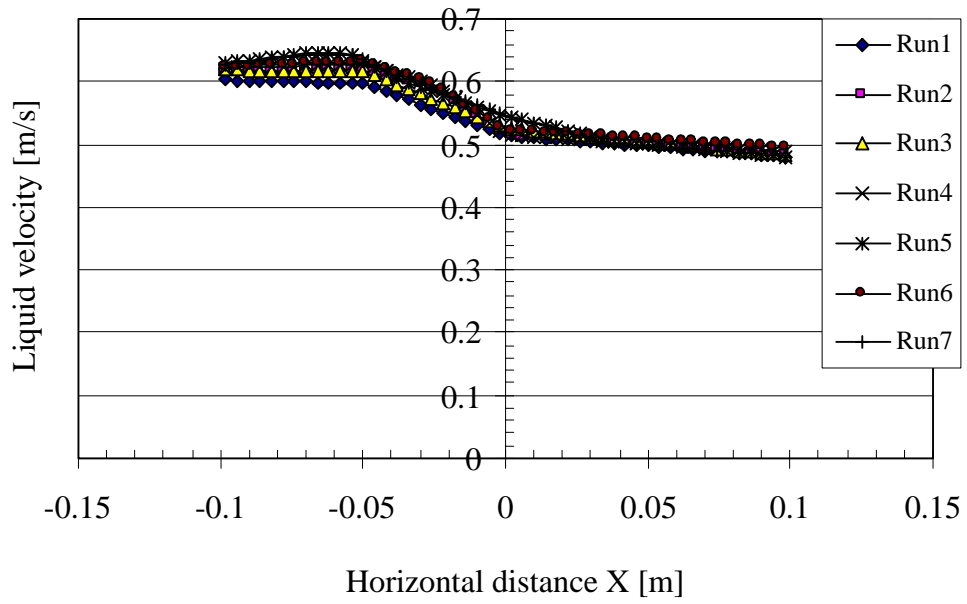


Figure 4.10 Liquid velocity profiles at line 5.

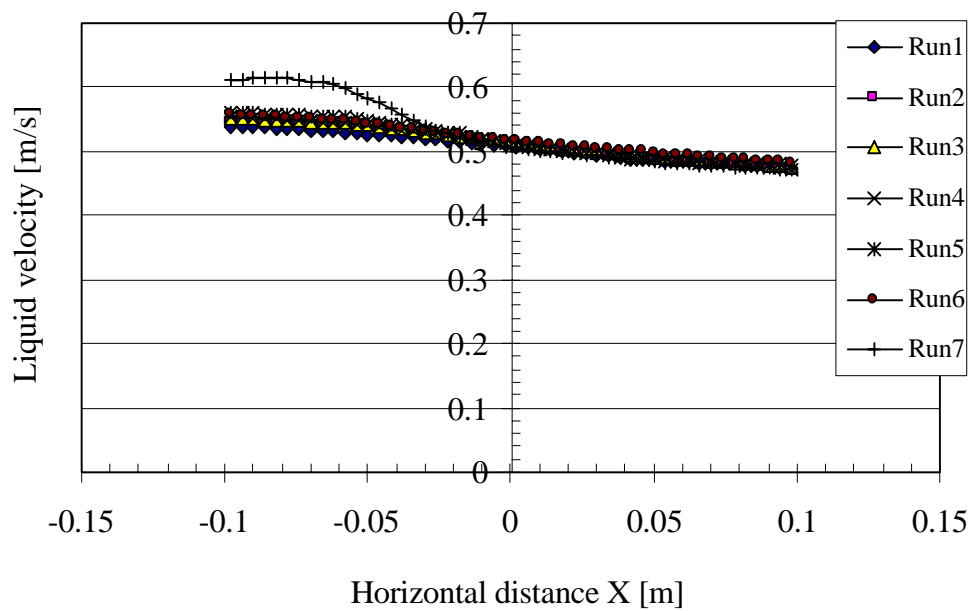


Figure 4.11 Liquid velocity profiles at line 6.

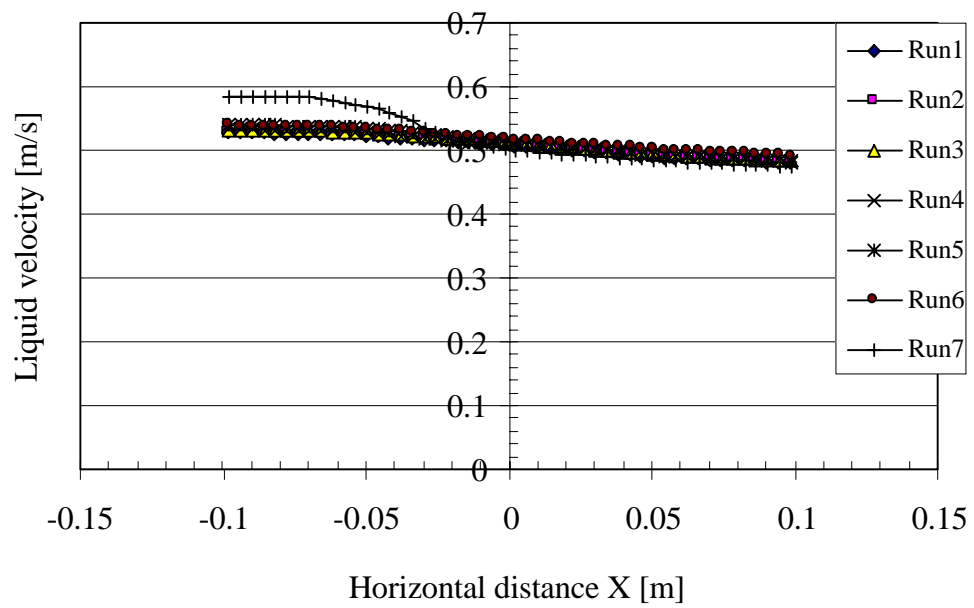


Figure 4.12 Liquid velocity profiles at line 7.

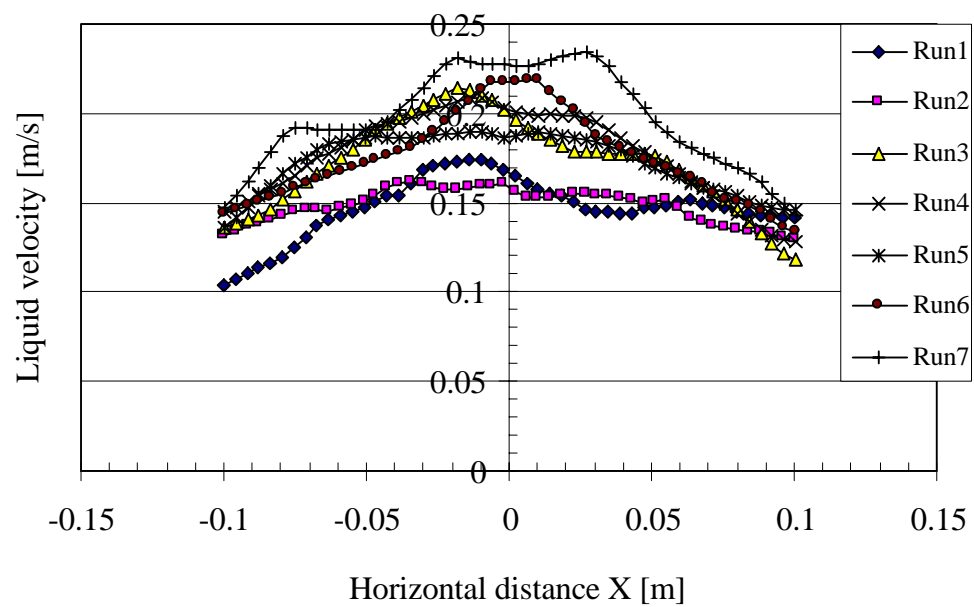


Figure 4.13 Liquid velocity profiles at line 8.

Figures 4.6 to 4.13 show that the liquid velocity profiles at line 1, 2, and 5 of all runs are not different or have only small differences, but at line 3, 4, 6, 7, and 8 liquid velocity profiles of run number 7 (the smallest mesh size) is different from the other runs. It can be seen that the different velocity of run number 7 occurs near the draft tube wall so that a fine mesh size in this region should be considered. This mesh is shown in Figure 4.14 and new runs with this mesh are shown in Table 4.4: liquid velocity profiles for each line are shown in Figure 4.15 to 4.22.

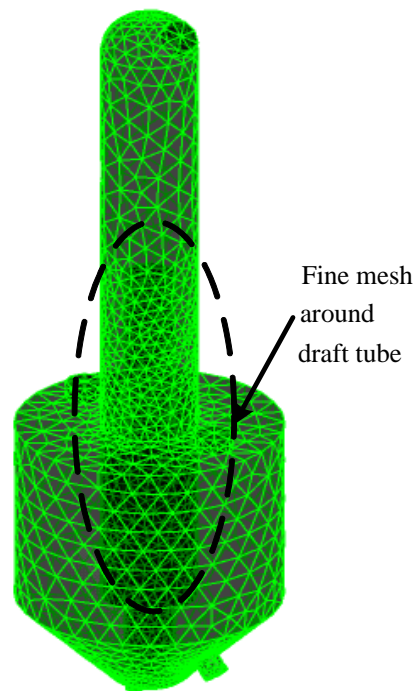


Figure 4.14 Fine mesh around draft tube.

Table 4.4 Mesh sizes of each run with fine mesh around draft tube.

Run	Maximum Edge Length (m)	Minimum Edge Length (m)	Number of Nodes		Number of Elements	
			Before mesh adaptation	After mesh adaptation	Before mesh adaptation	After mesh adaptation
8	0.17	0.0085	15,012	71,841	73,672	358,549
9	0.1	0.001	15,630	75,547	77,144	378,233
10	0.09	0.001	15,952	76,619	78,663	383,757
11	0.08	0.001	15,986	77,226	78,726	386,259
12	0.07	0.001	16,962	82,341	83,136	411,021
13	0.06	0.001	17,870	87,467	88,061	437,243
14 ¹	0.1	0.001	16,058	77,867	79,460	389,739

¹This run, the overall edge lengths are the same as run number 9, but the maximum edge length around draft tube is 0.07 m.

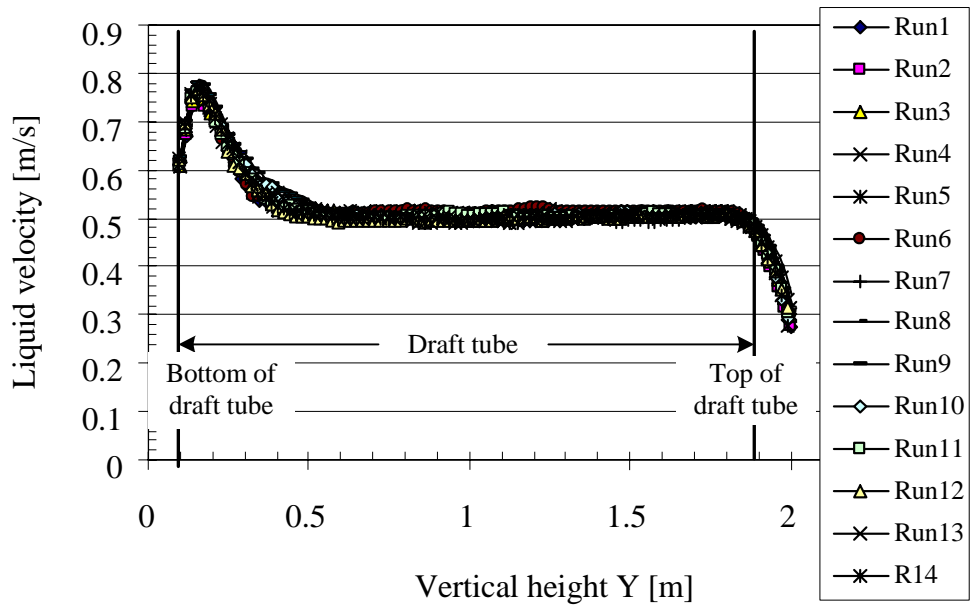


Figure 4.15 Liquid velocity profiles at line 1 with fine mesh around draft tube.

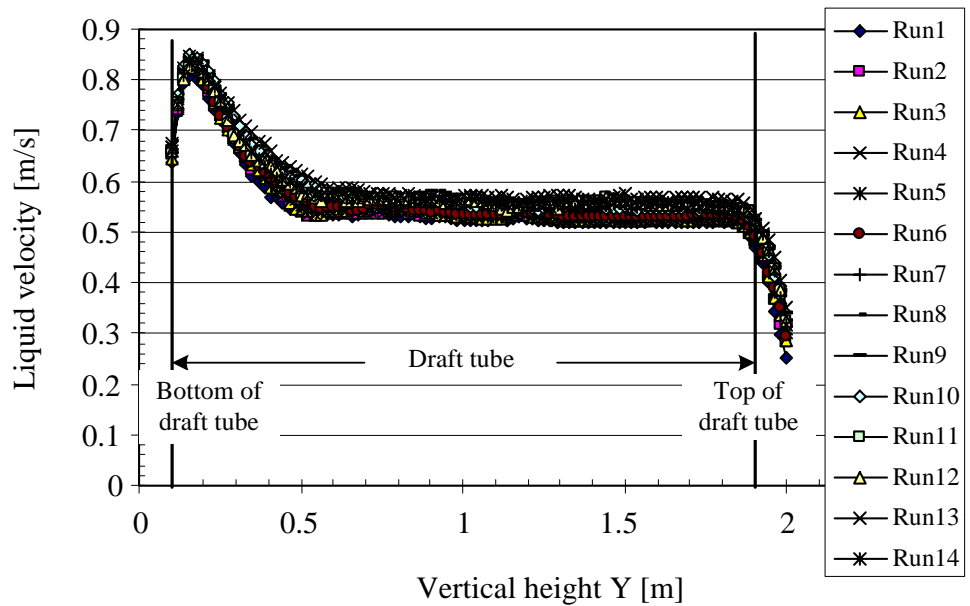


Figure 4.16 Liquid velocity profiles at line 2 with fine mesh around draft tube.

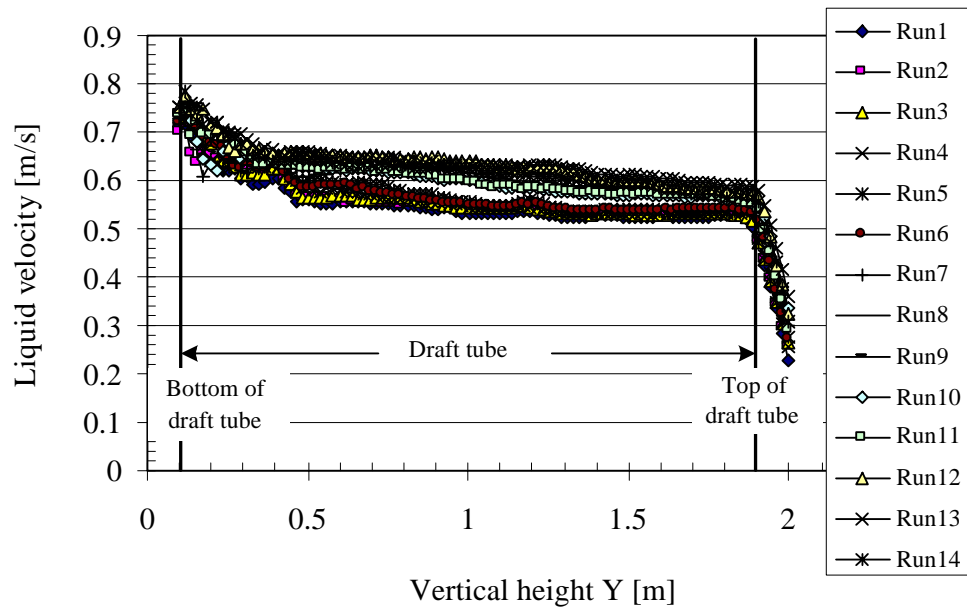


Figure 4.17 Liquid velocity profiles at line 3 with fine mesh around draft tube.

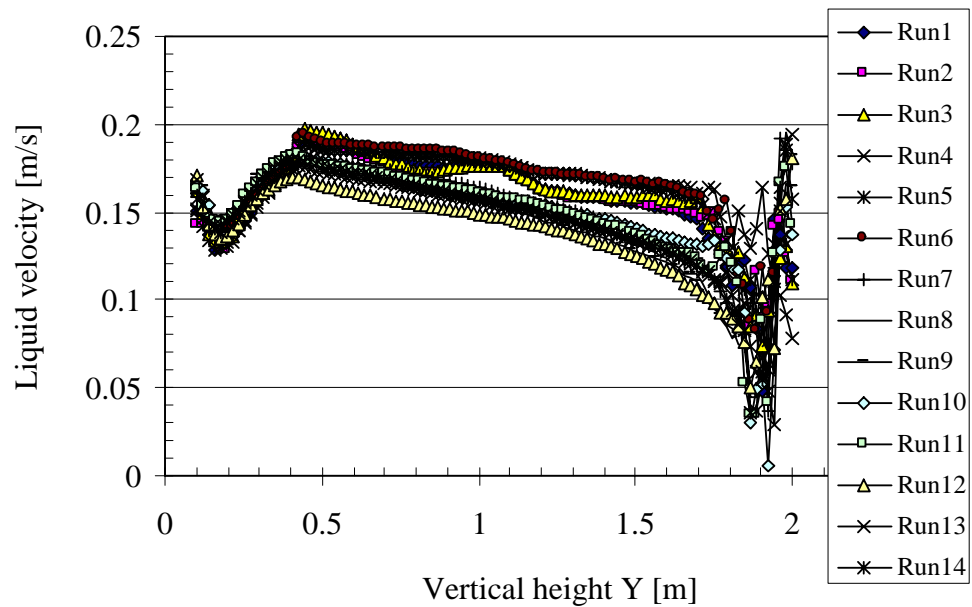


Figure 4.18 Liquid velocity profiles at line 4 with fine mesh around draft tube.

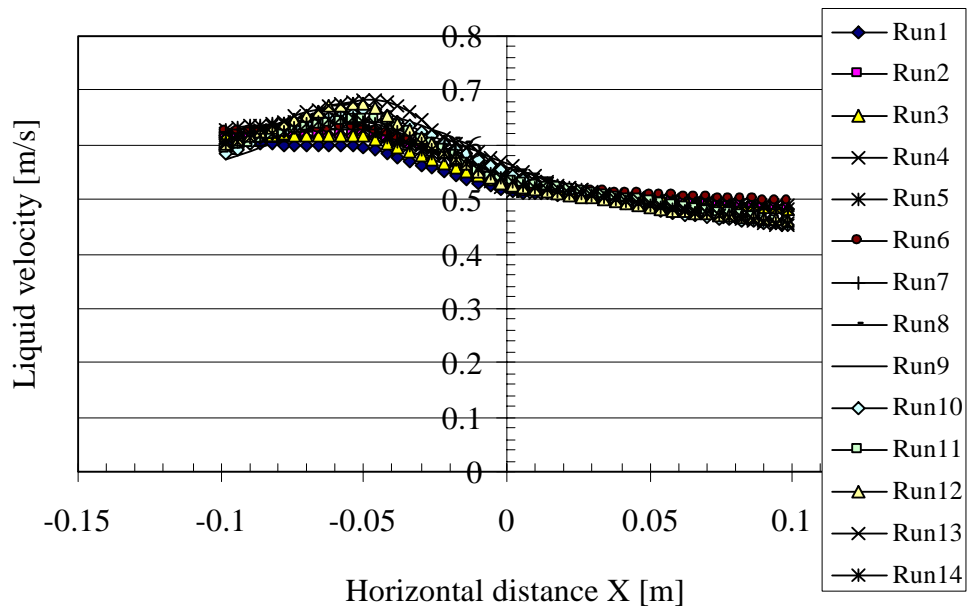


Figure 4.19 Liquid velocity profiles at line 5 with fine mesh around draft tube.

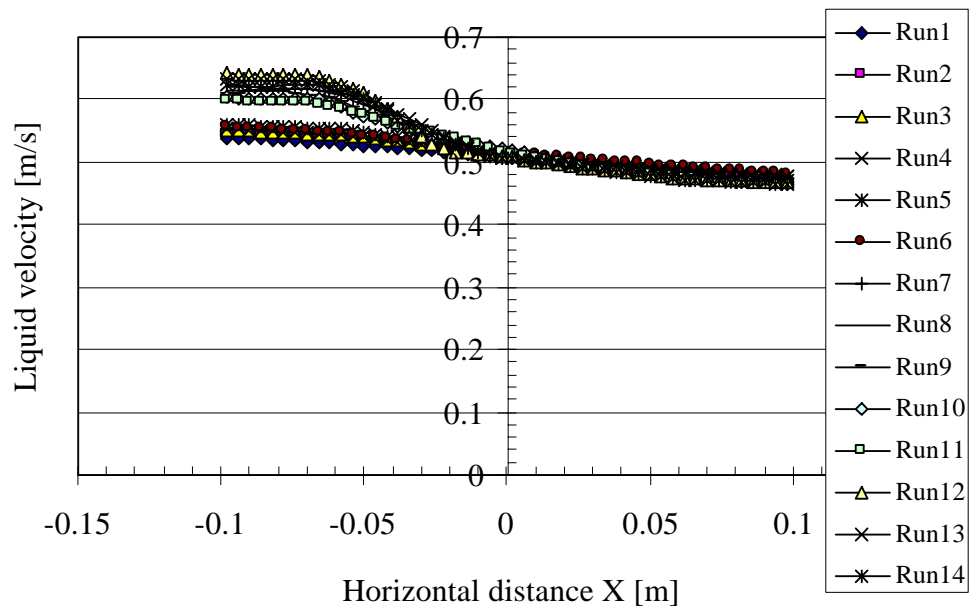


Figure 4.20 Liquid velocity profiles at line 6 with fine mesh around draft tube.

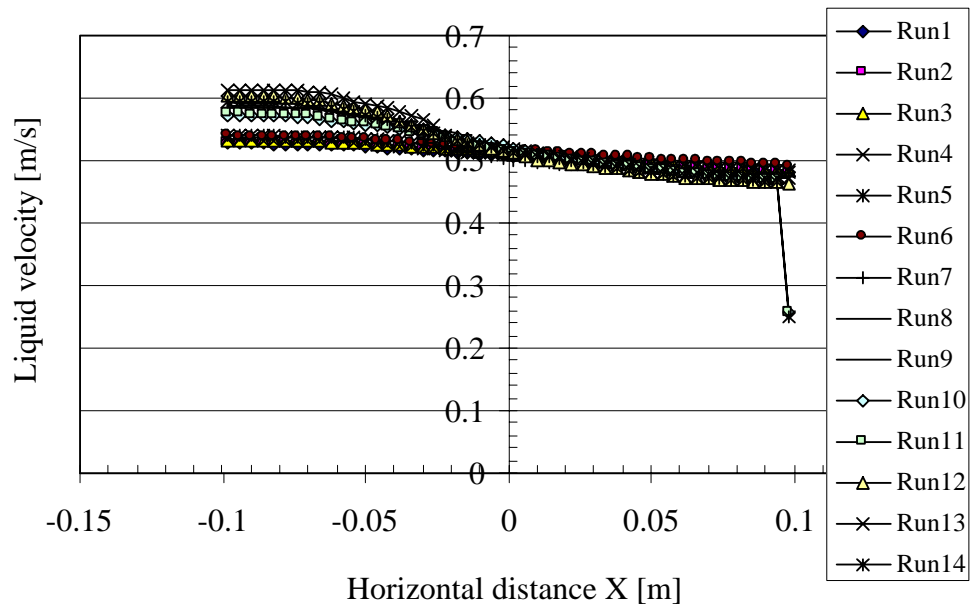


Figure 4.21 Liquid velocity profiles at line 7 with fine mesh around draft tube.

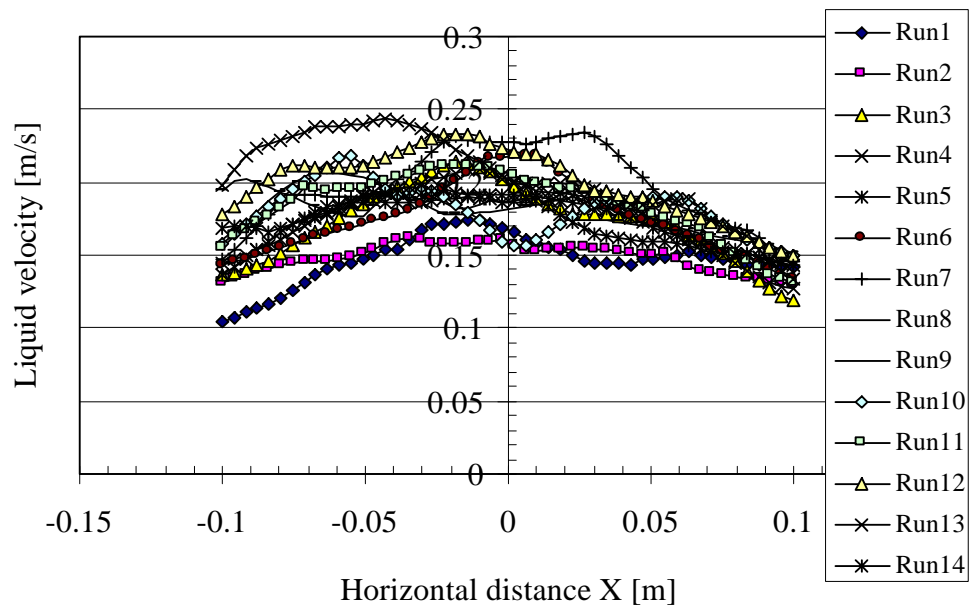


Figure 4.22 Liquid velocity profiles at line 8 with fine mesh around draft tube.

Considering run numbers 8 to 14 in Figure 4.15 to 22, it is seen that the liquid velocity profiles have only small differences so that the mesh size of run number 14 is selected to simulate a DTB crystallizer for all cases studied, because it gives an average value of the velocity profile between the value determined from the maximum and minimum mesh size and the size is small. The mesh of a DTB crystallizer with this mesh size is shown in Figure 4.23. Note that the number of nodes and elements after mesh adaptation is not necessary to equal to the run number in Table 4.4 because it depends on the flow conditions in the system. The number of nodes and elements after mesh adaptation for each case study for the isothermal simulation part (case studies 1-18) is listed in appendix C.

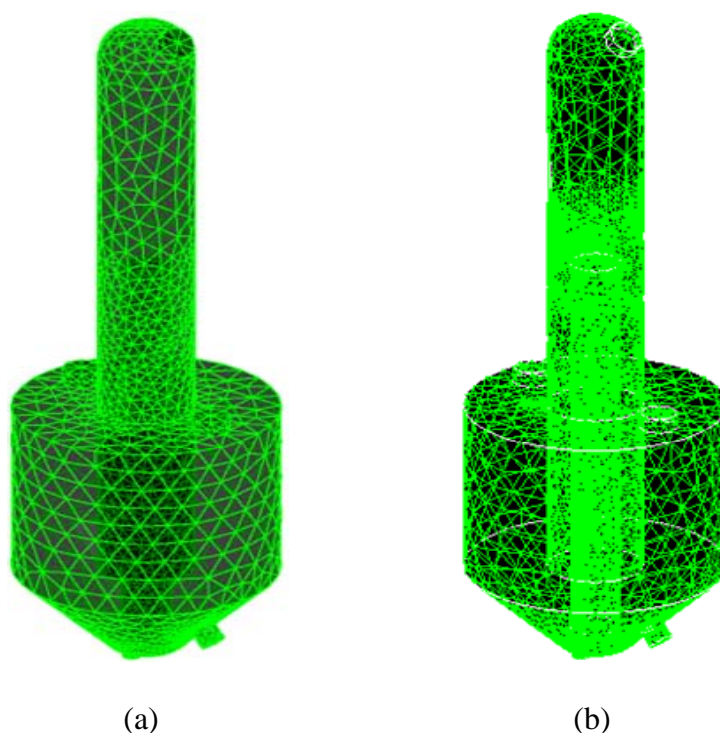


Figure 4.23 Computational mesh of Run14: (a) before mesh adaptation; (b) after mesh adaptation.

For the non-isothermal simulation section of the research no modeling of the area above the liquid free surface (the liquid free surface is at the height of 2.11 m) was performed. The optimum mesh size is of the same magnitude as the isothermal simulation section, so that the mesh of the DTB crystallizer for non-isothermal simulation with this mesh size is shown in Figure 4.24. Note that the number of nodes and elements after mesh adaptation is not necessarily equal to Figure 4.24 because this depends on the flow conditions in the system. The number of nodes and elements after mesh adaptation for each case study for the non-isothermal simulation section (case studies 19-22) are given in appendix C.

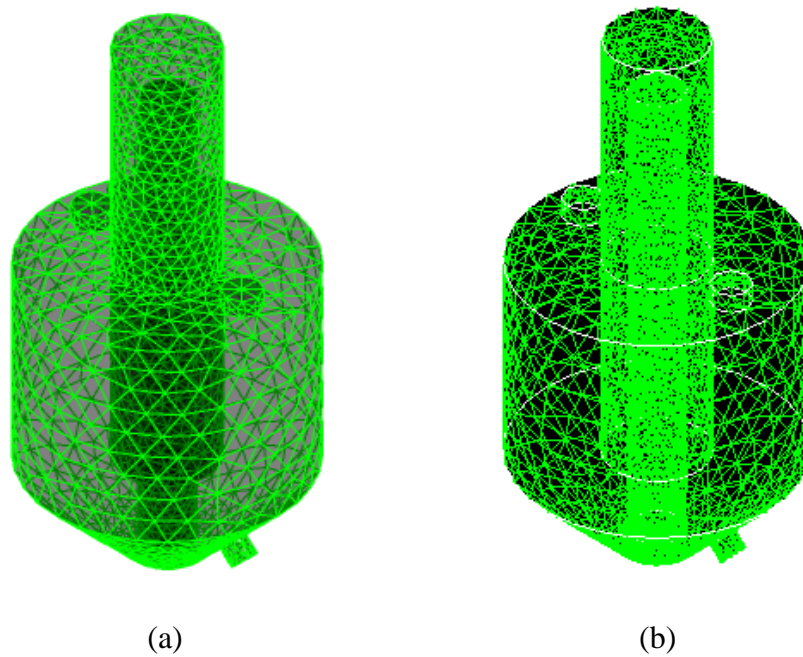


Figure 2.24 Examples of computational mesh of a DTB crystallizer for non-isothermal simulation part: (a) before mesh adaptation; (b) after mesh adaptation.

4.3.3 Physical definition

The physical definition step comprises several definition steps. The mesh files are loaded into the physics pre-processor, CFX-Pre. The physical models which are to be used in the simulation are selected. Fluid properties and boundary conditions are specified.

4.3.3.1 Fluid properties

The physical properties (water solution with 26.66 % NaCl [liquid] and water-vapor [vapor]) are presented in Table 4.5. Note that all properties of water-vapor are available in ANSYS CFX-10.0 and all properties of water solution with 26.66% NaCl at 25 °C were taken from Mullin (2001), with the exception of the specific heat capacity which was taken from Perry and Green (1999). The viscosity of NaCl solution at 106 °C is smaller than used here (about 0.00052 kg/s/m) but simulations run at this condition only varied about 3.5% (as shown in Figures 2.25 and 2.26, which are the results of case study 5) from the lower viscosity value.

4.3.3.2 Flow conditions

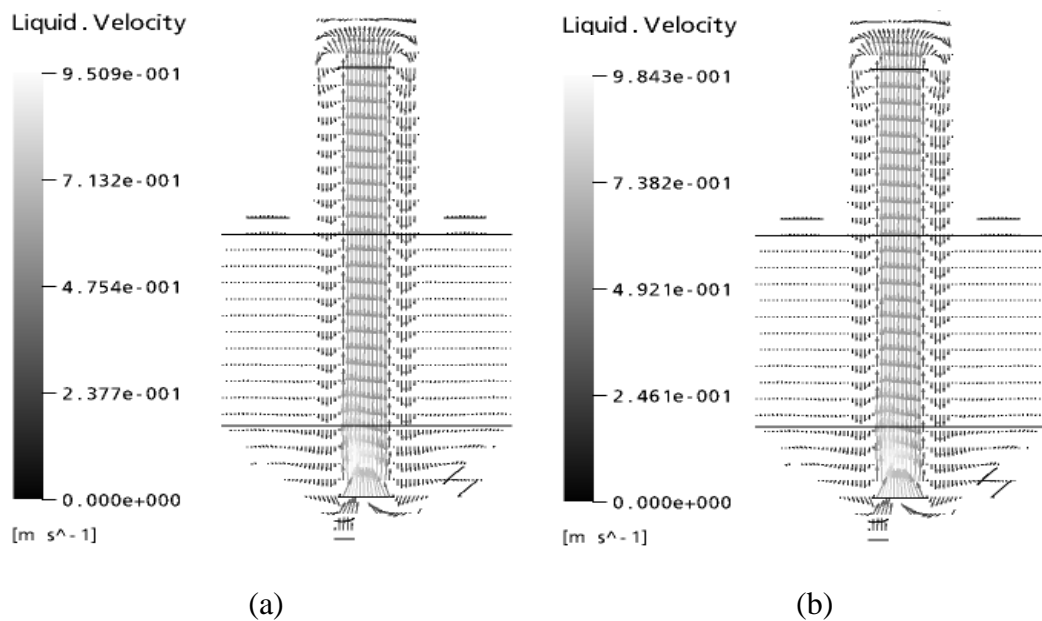
Isothermal simulation

In this part, the following flow conditions were selected:

1. Steady state flow.
2. The reference pressure was set to 0 Pa.
3. The buoyancy reference density was set to the density of the least dense fluid (vapor phase), that is 0.59 kg/m³.
4. The multiphase option was set to the inhomogeneous free surface flow.

Table 4.5 Physical properties of vapor and liquid.

Physical property	Phase	
	Liquid	Vapor
Density ($\text{kg} \cdot \text{m}^{-3}$)	1198.00	0.59
Viscosity ($\text{kg} \cdot \text{s}^{-1} \cdot \text{m}^{-1}$)	0.00152	0.0000124
Thermal conductivity ($\text{W} \cdot \text{m}^{-1} \cdot \text{K}^{-1}$)	0.57	0.025
Boiling temperature ($^{\circ}\text{C}$)	107.6	-
Specific heat capacity ($\text{J} \cdot \text{kg}^{-1} \cdot \text{K}^{-1}$)	3336.85	2080.10
Surface tension ($\text{N} \cdot \text{m}^{-1}$)	0.077	-

**Figure 2.25** Liquid velocity vectors for the simulation results from the viscosity values of (a) 0.00152 kg/s/m; (b) 0.00052 kg/s/m.

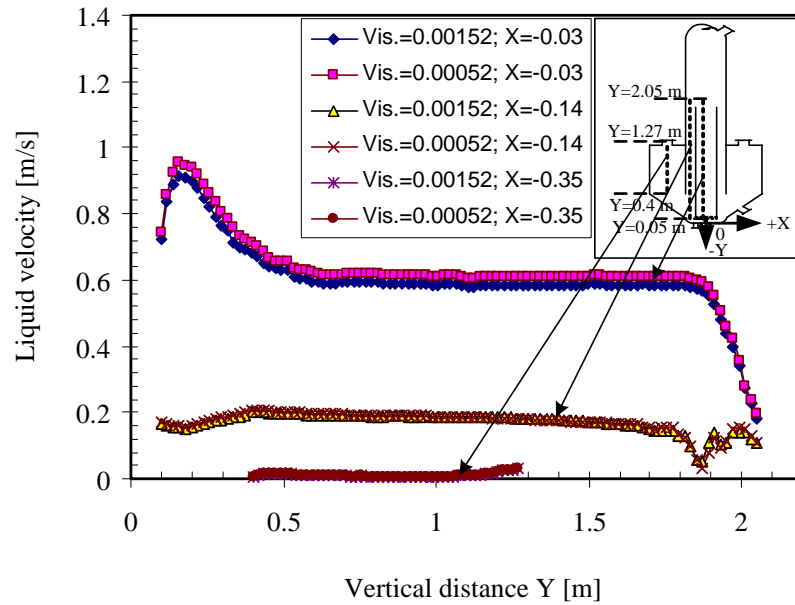


Figure 2.26 Liquid velocity profiles comparing the results from the viscosity values of 0.00152 and 0.00052 kg/s/m.

5. Turbulence was set to the homogeneous model with the $k - \varepsilon$ model. The turbulent wall function was set to the scalable wall function. There are more details of this model in chapter 3.

6. The liquid phase was set as the continuous phase. The vapor phase was defined as a dispersed fluid phase with a mean diameter of 2 mm (Lance *et al.*, 1996). The fluid buoyancy model was set to the density difference model for both fluids

7. For the interphase transfer model, the interphase transfer model was set to the particle model, the drag force was set to the Ishii and Zuber model, the turbulent dispersion force was to the Lopez de Bertodano model with a

dispersion coefficient of 0.3, and the turbulence transfer was set to Sato Enhanced Eddy Viscosity model. More details of these models are provided in chapter 3.

9. The momentum source value was specified directly in the momentum source region (impeller subdomain, see Figure 4.27) and set to the same value for both fluids. The values of each run are shown in Table 4.1 and 4.2.

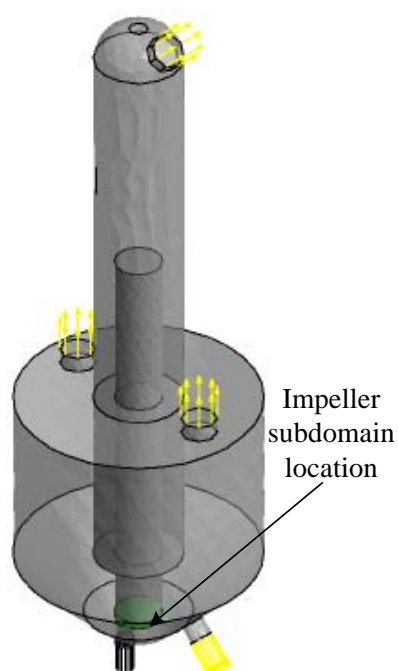


Figure 4.27 Location of impeller subdomain.

Non-isothermal simulation

In this part, the following flow conditions were selected:

1. Steady state flow.
2. The reference pressure was set to 0 Pa.

3. The buoyancy reference density was set to the density of the continuous phase (liquid phase), that is $1,198 \text{ kg/m}^3$.

4. The multiphase option was set to inhomogeneous multiphase flow.

5. Turbulence was set to the inhomogeneous model.

6. The heat transfer model was set to the inhomogeneous interphase heat transfer model with fluid dependent heat transfer.

7. For the liquid phase, the liquid phase was set as the continuous phase, the heat transfer was set to the thermal energy heat transfer model, the turbulence model was set to the $k - \varepsilon$ model, the turbulent wall function was set to the Scalable model, and the fluid buoyancy model was set to the density difference model. More details of these models are shown in chapter 3.

8. For the vapor phase, the vapor phase was set to the dispersed fluid phase with a mean diameter of 2 mm (Lance *et al.*, 1996), the heat transfer was set to an isothermal heat transfer model (at a constant saturation temperature of $107.6 \text{ }^\circ\text{C}$), the turbulence was set to the Dispersed Phase Zero equation model, and the fluid buoyancy model was set to the density difference model. More details of these models are in chapter 3.

9. For the interphase transfer model, the interphase transfer model was set to the particle model, the drag force was set to the Ishii and Zuber model, the turbulent dispersion force was set to the Lopez de Bertodano model with a dispersion coefficient of 0.3, the turbulence transfer was set to Sato Enhanced Eddy Viscosity model, the heat transfer was set to two resistance model with the Hughmark correlation on the liquid phase and Zero Resistance in the vapor phase, and mass

transfer was set to the thermal phase change model with the saturation temperature of 107.6 °C. More details of these models can be seen in chapter 3.

10. The momentum source value was specified directly in the momentum source region (the impeller subdomain, see Figure 4.27) and set to the same value for both fluids. The heat source value was specified directly to impeller subdomain too, and set only in the liquid phase. The values of each run are shown in Table 4.1 and 4.2.

4.3.3.3 Initial and boundary conditions

Boundary conditions

Boundary conditions are specifications of properties or conditions on the surface of domains and are required to fully define the flow simulation. The following fluid boundary condition types are available in ANSYS CFX-10.0 (ANSYS Canada Ltd., 2005):

1. *Inlet*: Fluid is constrained to flow into the domain only.
2. *Outlet*: Fluid is constrained to flow out of the domain only.
3. *Opening*: Fluid can simultaneously flow both in and out of the domain. This is not available for domains with more than one fluid present.
4. *Wall*: Impenetrable boundary to fluid flow
5. *Symmetry plane*: A plane of both geometric and flow symmetry.

The following boundary conditions were used in this work (Figures 4.28 and 4.29):

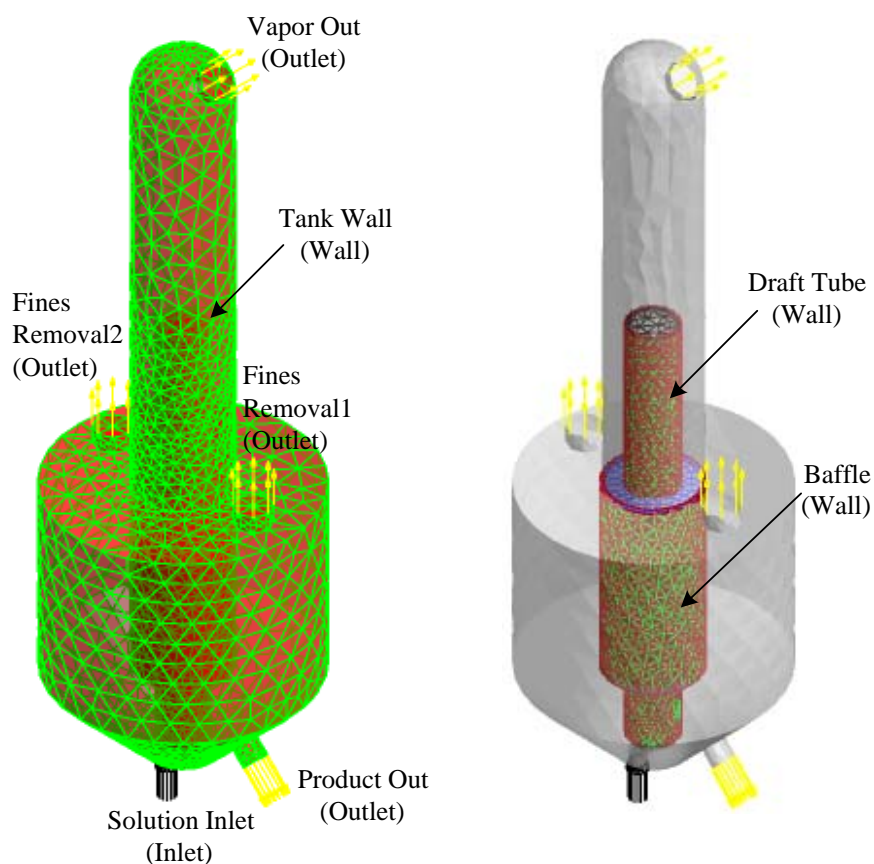


Figure 4.28 The boundary conditions of the DTB crystallizer for isothermal simulation.

1. *Inlet*: The cross-sectional surface area at the solution inlet tube was set to the inlet boundary condition and called “Solution Inlet”. For this boundary, the flow direction is perpendicular to the surface. For the isothermal simulation, the mass flow rates of each phase were specified directly, the volume fraction of vapor was set to 0.1, and the volume fraction of liquid was set to 0.9. For non-isothermal simulation, the bulk mass of the liquid flow rate was specified directly, and the volume fraction of liquid and vapor respectively set to 1.0 and 0.0, and the bulk liquid temperature was set to 106 °C. The values of the mass flow rate of each phase and

bulk mass flow rates of each run are shown in Table 4.1 and 4.2. The turbulence option was set to medium (intensity = 5%).

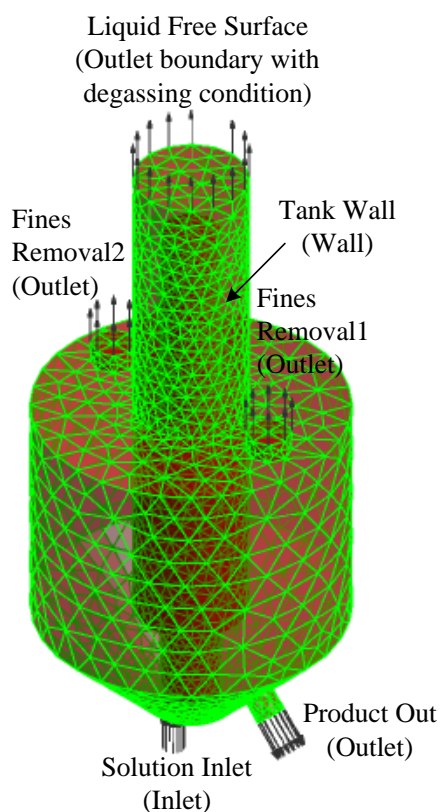


Figure 2.29 The boundary conditions of the DTB crystallizer for non-isothermal simulation.

2. *Outlet*: For this boundary, the flow direction is perpendicular to the given surface. In this work, the boundaries are separated into four locations:

- The cross-sectional surface area at the outlet of the product outlet tube, which is called “Product Out”. For this boundary, the mass flow rate of each phase was specified directly. The values of each run are shown in Table 4.1 and 4.2.

- The cross-sectional surface area at the two outlet fines removal tubes, which are called “Fines Removal1” and “Fines Removal2”, respectively. At these boundaries, the bulk mass flow rate was specified directly. The values of each run are shown in Table 4.1 and 4.2.
- The cross-sectional surface area at the vapor outlet tube, which is called “Vapor Out” (this is only a boundary condition for isothermal simulation part). For this boundary, the mass flow rate of each phase was specified directly. The values of each run are shown in Table 4.1.
- The cross-sectional surface area at the liquid free surface is an outlet boundary with a degassing condition (this is only a boundary condition for non-isothermal simulation part). For this condition, the continuous phase sees this boundary as a free-slip wall and does not leave the domain but the dispersed phase sees this boundary as an outlet.

3. *Wall*: The wall of the draft tube, baffle, and tank wall were set to the zero-slip and smooth wall conditions for both simulation parts. Moreover, these walls were together set to an adiabatic wall conditions for non-isothermal simulation part.

Initial conditions

“The initial conditions for a steady-state calculation are used to serve to give the CFX-Solver a flow field from which to start its calculations. Convergence is more rapidly achieved if sensible initial values are provided.

However, converged results should not be affected by the initialization” (ANSYS Canada Ltd., 2005).

The initial and boundary conditions for the pressure field and volume fraction of free surface flow must be consistent (i.e. the pressure field is hydrostatic in the liquid phase and uniform in the vapor phase). This condition was achieved using CEL (the CFX expression language) defining a step function, as shown below:

$$Den = 1198 \text{ [kg m}^{-3}\text{]}$$

$$FH = 2.11 \text{ [m]}$$

$$VFLiquid = \text{step}((FH-y)/1 \text{ [m]})$$

$$VFVapor = 1 - VFLiquid$$

$$Press = Den * g * (FH - y) * VFLiquid$$

where Den is the density of liquid phase, FH is the liquid level or free surface height, $VFVapor$ is the volume fraction of vapor phase, $VFLiquid$ is the volume fraction of liquid phase, and $Press$ is the pressure. These functions are appropriate to initialize the relative pressure field and volume fraction as shown in Figure 4.30.

The initial conditions of this work are shown below:

1. The initial static pressure, volume fraction of liquid phase, and volume fraction of vapor phase were set to; $Press$, $VFLiquid$, and $VFVapor$, respectively for isothermal simulation part; and automatic values, 1.0, and 0.0, respectively for non-isothermal simulation part.

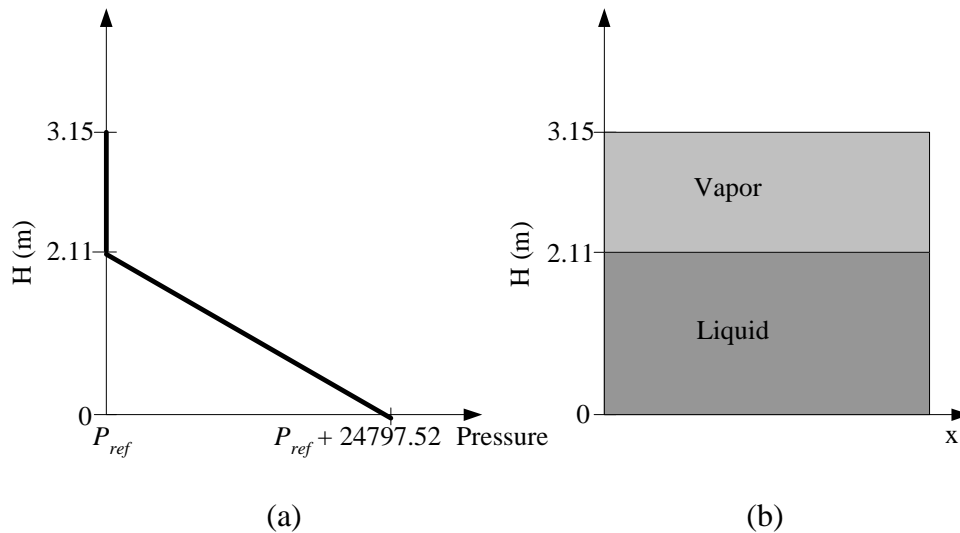


Figure 4.30 Initial conditions: (a) pressure; (b) volume fraction.

2. The velocity of each phase was specified directly with the same with the velocity of the solution inlet.

3. The turbulent kinetic energy and turbulent eddy dissipation were set to automatic values.

4. For the non-isothermal simulation, the static temperature of the liquid was set to 106 °C.

4.3.3.4 Mesh adaptation and solver control

Since the flow is free surface flow, it is necessary to adjust the mesh at the liquid-vapor interface. CFX-Pre has the mode to do this with more detail shown in the 2nd step of section 4.3.2.2.

Solver control is used to set parameters that control the CFX-Solver during the solution stage, and appropriate parameters are essential in order to obtain good convergence of the solution. In this work, the advection scheme was set

to the upwind option. The timescale control was set to auto timescale and the maximum number of iterations was set to 300 for isothermal simulation part (case studies 1-18) and 3,500 for non-isothermal simulation part (case studies 19-22). The RMS (root mean square) residual type was used with a target value of 0.00001.

All sub-sections in section 4.3.3 are the processes in CFX-Pre. CFX-Pre produces a solver (definition) file which is then passed to the CFX-Solver to solve the simulation.

4.3.4 Solver

CFX-Solver solves all variables for the simulation of the problem specification in CFX-Pre by the finite volume method with an unstructured mesh.

CFX-Solver is solved as follows:

1. The partial differential equations (mass, momentum, energy equations and turbulent) are integrated over all the control volumes in the region of interest.
2. These integral equations are converted to a system of algebraic equations by generating a set of approximations for the term in the integral equations.
3. The algebraic equations are solved iteratively until the convergence criteria or maximum iteration is reached.

Exact details of the calculation methods for the software are available in the detailed user notes accompanying the software (ANSYS Canada Ltd., 2005). More details about the finite-volume method (the discretisation of equations and solution strategy) to solve the gas-liquid system are given by Oey (2005).

The solver produces a results file which is then passed to the post-processor.

4.3.5 Post-processing

CFX-Post is the component used to analyze, visualize and present the results interactively.

Examples of some important features of CFX-Post are:

- Visualization of the geometry and control volumes
- Vector plots of the direction and magnitude of the flow
- Virtualization of the variation of scalar variables (variables which have only magnitude, not direction, such as pressure, temperature, speed, etc.) through the domain
- Streamlines of the vapor and liquid
- Charts showing graphical calculations
- Other representations of variables of interest.

The results from CFX-Post of all studies in this research are shown and discussed in chapter 5.

4.4 Conclusions

The study methods to approach each objective shown in chapter 1 and the apparatus used in this work are described in the beginning of this chapter. The complete simulation procedures by ANSYS CFX-10.0 are given, which are split into the following five steps. First step, geometry creation: the DTB crystallizer geometry was created by the program DesignModeler in ANSYS Workbench v.10.0. Second step, mesh creation: the mesh was created by the program CFX-Mesh in ANSYS

Workbench v.10.0 and the mesh were refined step by step until changes in the numerical solution were unnoticeable to achieve mesh independent results. Third step, physical definitions: the mesh files are loaded into the physics pre-processor (CFX-Pre), and then the physical models which are to be used in the simulation are selected and fluid properties and boundary conditions are specified. Fourth step, solver: the solver (definition) file from the CFX-Pre is then passed to the CFX-Solver to solve the simulation, where the CFX-Solver solves all variables for the simulation of the problem specification in CFX-Pre by the finite volume method with an unstructured mesh. Final step, post-processing: the analysis, visualization, and presentation of results are presented by CFX-Post.

CHAPTER V

RESULTS AND DISCUSSION

The numerical results of all case studies listed in Table 4.1 and 4.2 in chapter 4 are presented in this chapter, and these results show the velocity vectors, contours of velocity, contours of vapor volume fraction, contours of pressure, contours of temperature, and streamlines in both graphical and tabular form. These results are shown and discussed for each part of the study mentioned in the previous chapter. In each section of the study, some parameters, such as Reynolds number, power transmitted by the impeller, fines removal cut-size, etc., were calculated to analyze the performance of the crystallizer under different operating conditions. In the final section, the results of the isothermal and non-isothermal simulation are compared to determine whether the heat transfer and boiling in the crystallizer has a significant effect on other parameters in the model, such as the fluid flow fields or the fines cut-size.

5.1 Isothermal Simulation

5.1.1 General characteristics of flow fields and classification of crystals in a DTB crystallizer

In this section, the results of case study number 5 are determined based on the conditions shown in Table 4.1. The power transmitted by the impeller can be estimated by multiplying the momentum source added by two (because

the true 45° pitched blade turbine produces approximately 50% axial flow, but this momentum source specifies 100% axial flow) and then multiplying by the volume of the subdomain (0.0007854 m³) that represents the impeller and the average velocity of the liquid leaving the impeller zone (this zone is represented by the volume defined in Figure 5.1). Note that the velocity must be calculated from the system with no feed only. The power of this case study is 10.21 W (with a momentum source of 10,000 kg/m²/s² and an average liquid velocity of 0.65 m/s).

The results show that the average bubble Reynolds number ($\text{Re}_p = \rho_c |U_d - U_c| d_p / \mu_c$) in the draft tube is 592 with an average vapor velocity (U_d) of 0.9867 m/s and a calculated liquid Reynolds number ($\text{Re} = \rho_c U_c D / \mu_c$) in the draft tube of 96,300 based on an average liquid velocity of 0.611 m/s. These two values of the Reynolds number indicate that the flow in the draft tube (flow in pipe) is turbulent.

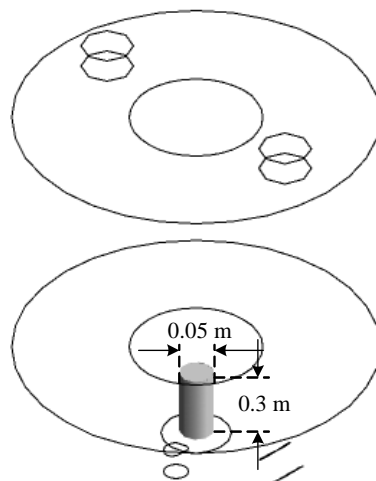


Figure 5.1 The volume defined to calculate the average liquid velocity above the top center of the impeller.

Figure 5.2 show the streamlines inside and outside the draft tube in both 2 and 3 dimensional representations. It can be seen that the flow has to go up and over the draft tube and therefore there is net circulation through the draft tube. It makes sense to have this flow characteristic because it is the function of the draft tube, as was described in chapter 2. This indicates that the impeller can be sufficiently well modeled by an axial momentum source in order to reduce the computational time and model complexity.

Contours of vapor volume fraction are depicted in Figure 5.3. These figures clearly show that only region where vapor is the only phase present (the volume fraction of vapor is 1) is in the upper part of the crystallizer (above the free surface, 2.11 m from the tank bottom) and liquid is the principal phase present (the volume fraction of vapor is small) is in the lower part, below the free surface. This means that the vapor and liquid regions of the crystallizer are separated by a clearly-defined interface (free surface), which occurs at a height of 2.11 m (this is the same as the initial height of the free surface in the simulation). A small amount of vapor (less than 10 % by volume) is in the draft tube because the feed to the crystallizer is 10% volume fraction vapor. The vapor is mostly in the regions near the left side of the draft tube and separates out from the liquid at the top of the draft tube near the left side of the tank (not the center of the tank) because the feed is located under a position between the left side of the draft tube and the tank wall, and the rate of the feed is quite high in this case.

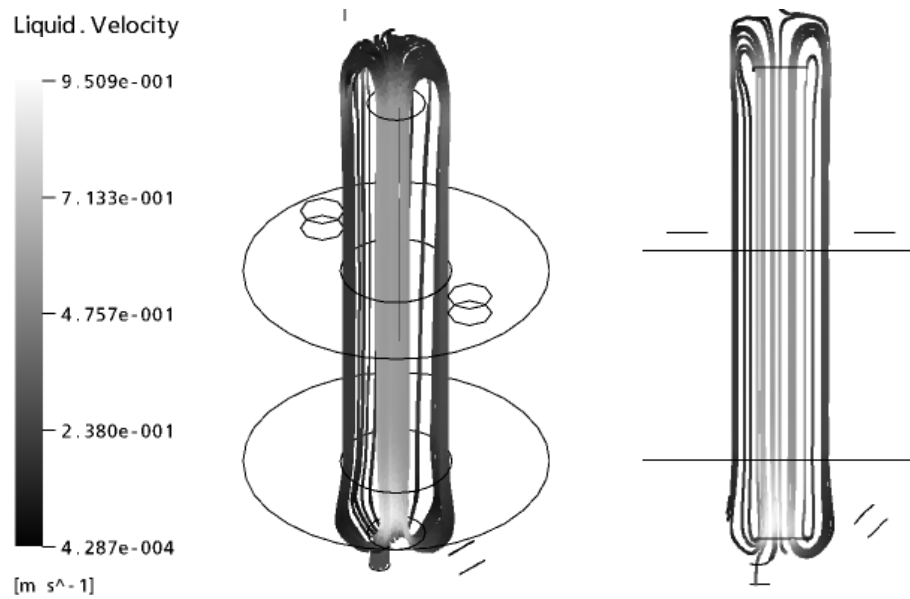


Figure 5.2 Streamlines of liquid flow inside and outside of the draft tube: Case 5.

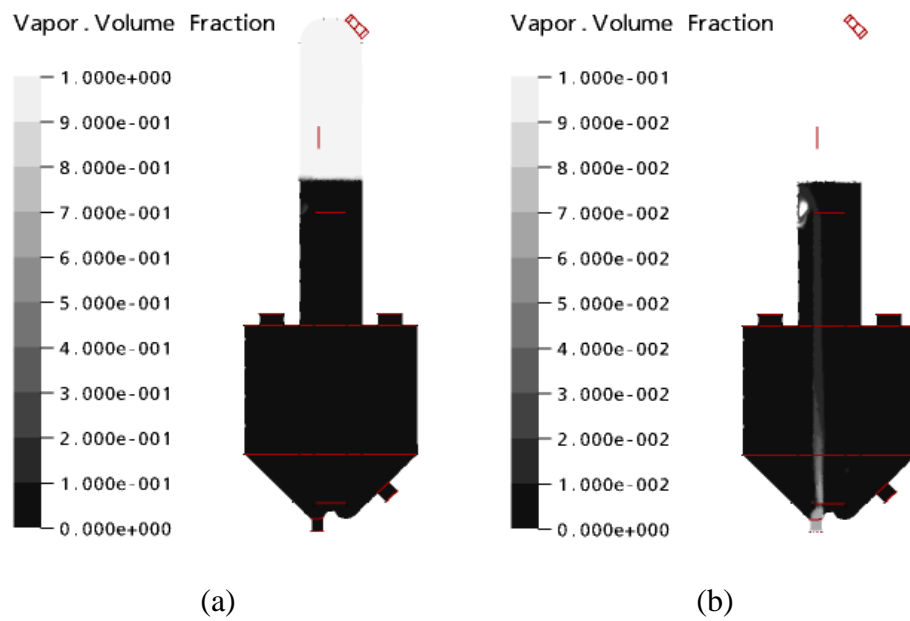


Figure 5.3 Contours of volume fraction of vapor in the vertical center plane: Case 5:
 (a) overall fraction; (b) magnified scale to enable visualization in the draft tube.

Figure 5.4 show the contours of absolute pressure. This figure clearly shows that the pressure has the lowest value (atmospheric pressure) in the top part of the crystallizer (the vapor space above the free surface) and the value is uniform: this makes sense since there is only a light phase (vapor) in this part. Then the pressure increases from the free surface until the maximum value is reached at the bottom of the crystallizer. This means that the hydrostatic pressure is the main part of the pressure value in this section, and this is due to a heavy phase (liquid) being the bulk phase in this region.

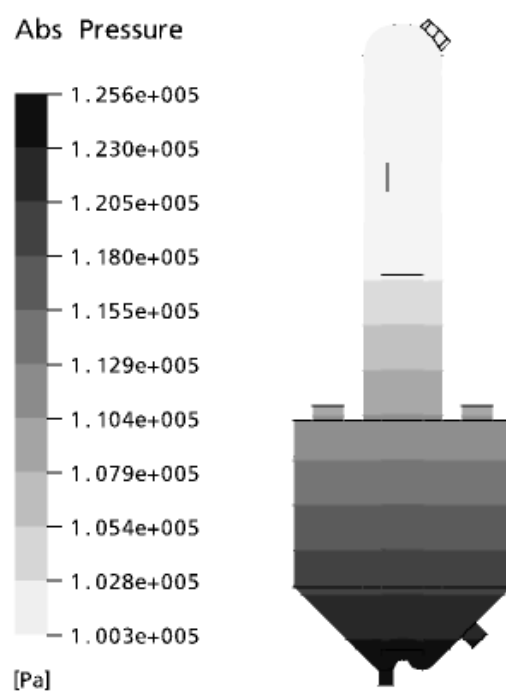


Figure 5.4 Contours of absolute pressure in the vertical center plane: Case 5.

Figure 5.5 represents the velocity vectors and contours for the liquid and vapor velocity in the vertical center plane. It shows that the velocity in the up-flow region (inside the draft tube) is higher than the down flow region (outside the draft tube). This is since the cross sectional area of the up flow region (approximately 0.0314 m^2) is smaller than the down-flow region (approximately 0.0820 m^2). The crystallizer is designed in this way to create a velocity significantly higher than the particle settling velocity in the upward flow to assist in suspension of particles, and this high upward velocity is produced from the momentum added with the impeller. At a larger distance upward from the impeller, the velocity profile becomes more uniform, although averaged velocities in the core remain low (this is far enough from the bottom tube end of the draft tube that the effect of the impeller is less significant), and the velocity is approximately half of the maximum (0.9509 m/s), which occurs at approximately 0.3 m (equal to the 1.5 times the diameter of the draft tube) above the impeller. Figure 5.6 shows a small a recirculation loop occurring under the region where the flow comes over the top of the draft tube. This is more pronounced at the side of the draft tube above the feed, and is undesirable because it will lead to a non-uniform flow. This recirculation does not contribute at all to the desired circulation, and could lead to different crystallization rates for crystals that are trapped there.

The vapor phase is only present in small amounts in the system (Figures 5.5 (c) and (d)), and only in the draft tube, after which it is separated out at the vapor-liquid interface. This interface is at the boiling surface, with some circular flow in the radial direction and non-uniform flow is apparent at this surface (Figure 5.7).

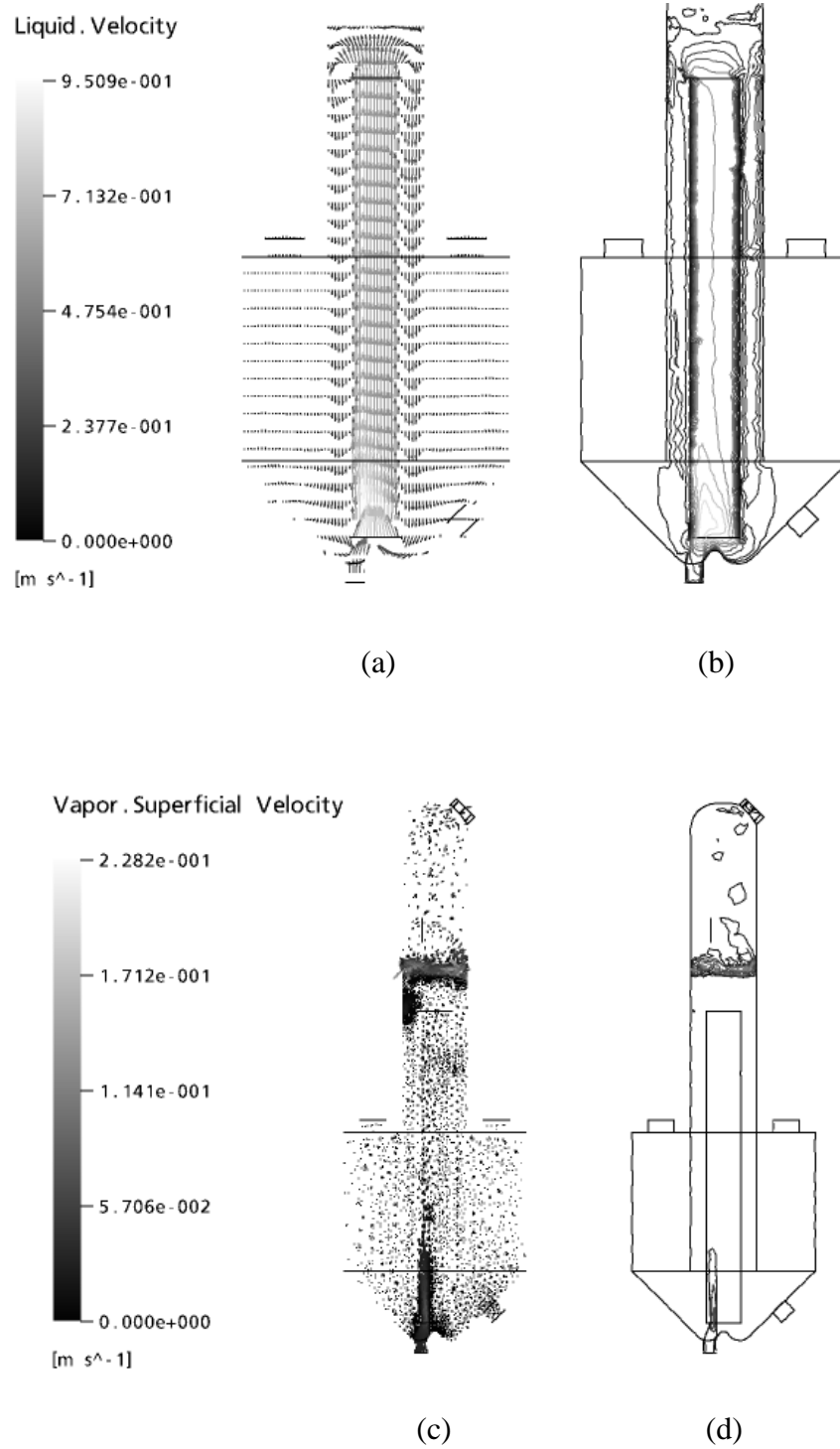


Figure 5.5 Liquid and vapor velocity in the vertical center plane: Case 5; (a) liquid velocity vectors; (b) contours of liquid velocity; (c) vapor velocity vectors; (d) contours of vapor velocity.

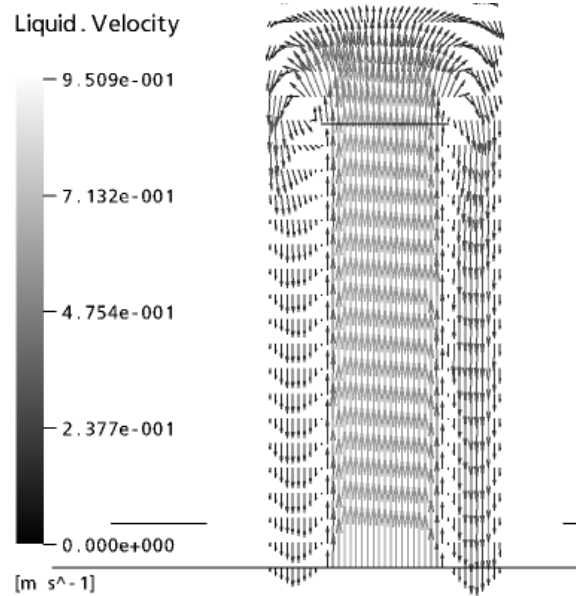


Figure 5.6 Liquid velocity vectors around top of draft tube in the vertical center plane: Case 5.

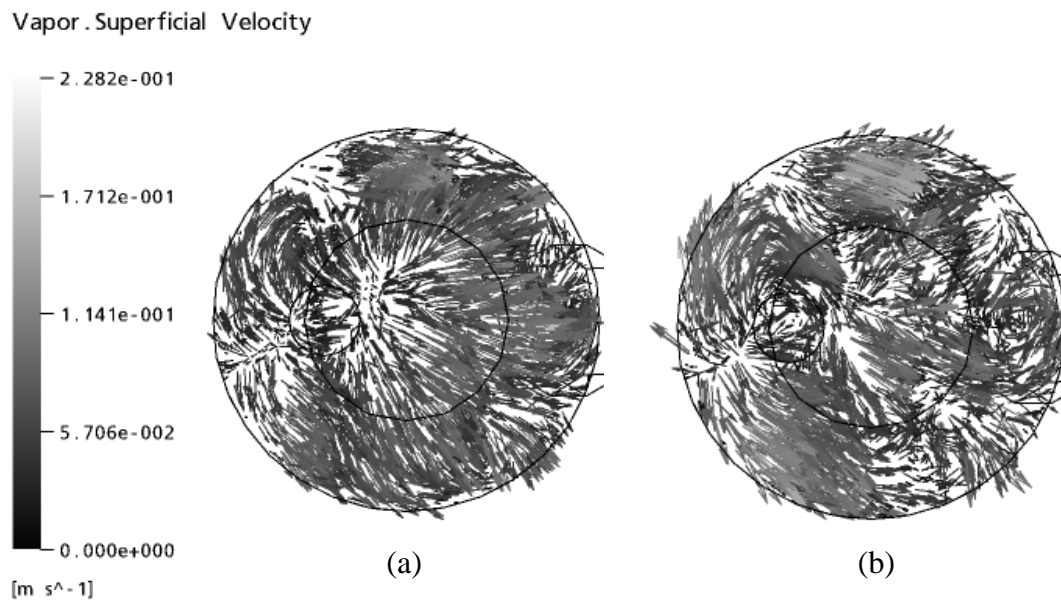


Figure 5.7 Vapor velocity vectors at the vapor-liquid interface in the horizontal plane: Case 5; at the height of (a) 2.11 m; (b) 2.12 m.

The segregation of the upward flow and downward flow parts of the flow loop are clearly confirmed again in Figure 5.8, with a high up flow velocity in the inside of the draft tube (particularly at regions around the draft tube up to 0.4 m above the impeller [see Figure 5.5 (a)]). The upward flow is shown in Figure 5.8, which shows the liquid flow into the center of the base of the draft tube; the liquid then flows upward due to the momentum added by the impeller. For downward flow, Figure 5.8 (f), plotting variables at the height of 2 m, shows the flow turn over the top of the draft tube and Figure 5.8 (e), plotting variables at the height of 1.9 m, the liquid flow down in the annular region outside the draft tube. The largest velocity vectors at the outlet of the impeller are at the centre of the top region of the impeller. This is due to the momentum source in the simulation having a constant amount of momentum added per volume in the region defined, and that there is a zero-slip boundary condition at the walls of the draft tube. In a real impeller the maximum fluid pumping is likely to occur from the largest area of the impeller blades (usually at a distance of approximately $r/2$ from the centre of the impeller) to the tip of the impeller (which has the highest linear speed). However this will have an effect on the flow in the draft tube for only a small height above the impeller, after which the Reynolds number of the flow and the zero-slip boundary condition at the walls will dominate the cause of the flow pattern.

One drawback of many crystallizers is the tendency of the particles to sediment to the bottom of the tank and remain there. The shape of the tank bottom can significantly improve the uniformity of the particle suspension. The rounded tank “corners” and a center peak under the agitator, which is the bottom shape of the DTB crystallizer used in this work, is one of the best designs of the tank bottom

configurations. The rounding of the corners is used to combat settling of particles and the center peak virtually eliminates the stagnation point (dead zone) that would be present at the bottom center of the tank under the agitator (Myerson, 2002). These descriptions can be confirmed by the velocity vectors that are shown in Figure 5.9, which shows that the flow of all fluid packets tends to be into the draft tube.

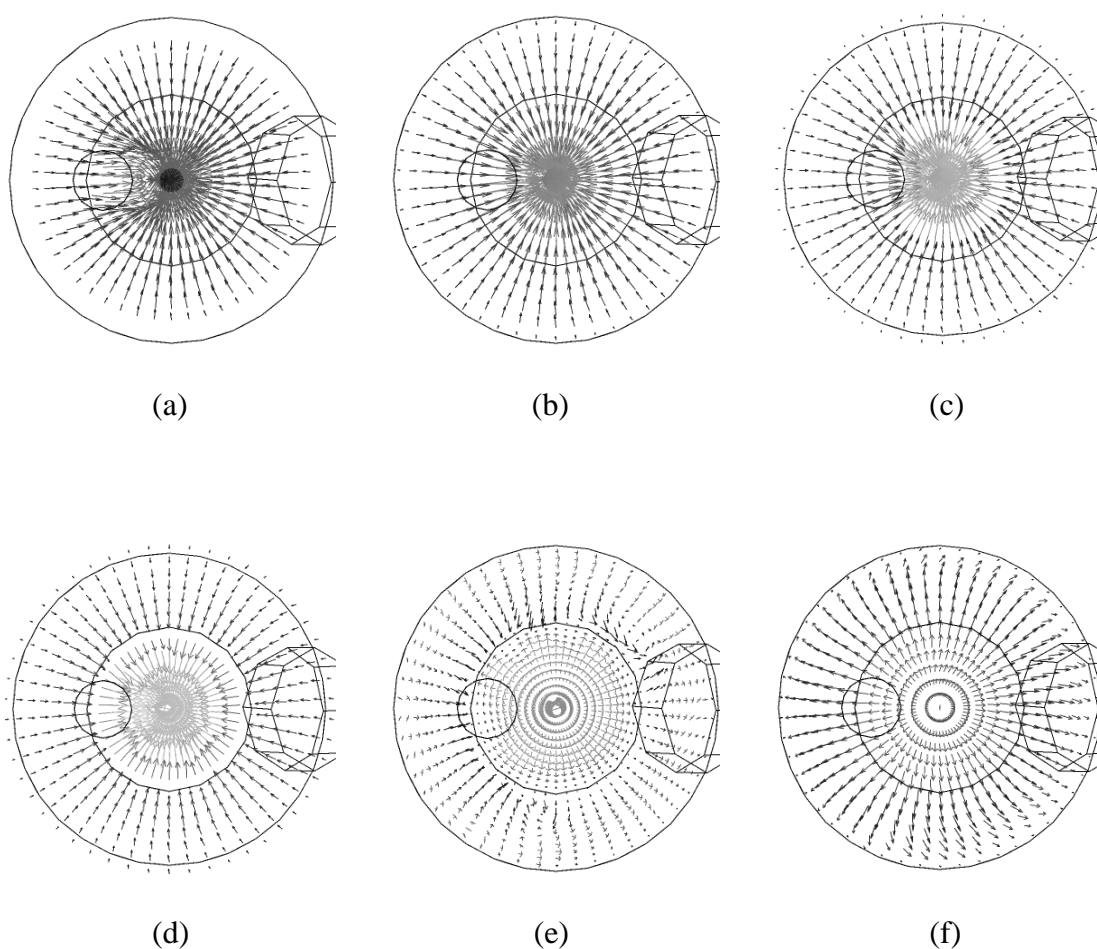


Figure 5.8 Liquid velocity vectors in the horizontal plane: Case 5; at the height of (a) 0.05 m; (b) 0.075 m; (c) 0.0875 m; (d) 0.1 m (the base of the draft tube); (e) 1.9 m; (f) 2 m (the top of the draft tube).

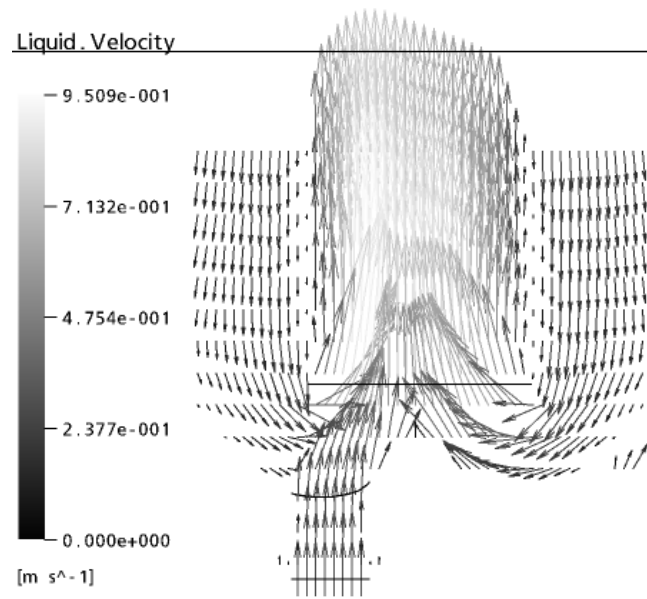


Figure 5.9 Liquid velocity vectors at the tank bottom: Case 5.

Returning to Figure 5.5 again, the flow outside the draft tube is downward and the flow outside the baffle (annular settling zone) is low enough (and sufficiently uniform, [Figure 5.5 (b)]) to confirm the gravitational settling process of the crystals. So the classification of crystals in this work was studied by the fines removal cut-size, which was calculated from the free settling velocity, U_t :

$$U_t = \sqrt{\frac{4g(\rho_p - \rho)d_p}{3C_D\rho}} \quad (2.2)$$

where the density of NaCl crystal is 2,155 kg/m³ (Cheremisinoff, 1986), the C_D of each flow regime is shown Table 2.1 (calculated via the particle Reynolds number), and the settling velocity is the calculated value from the simulation, which is the average value over the volume in Figure 5.10. Calculation of the fines removal cut-

size (d_p) was performed with an iterative calculation, since the value of the Reynolds number determines the flow regime.

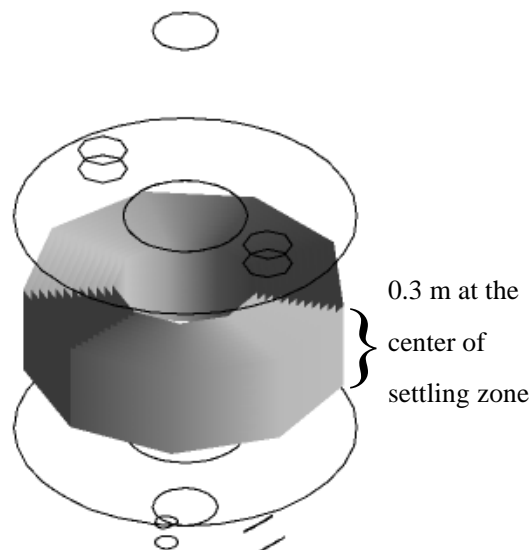


Figure 5.10 The volume defined to calculate the average velocity in the annular settling zone.

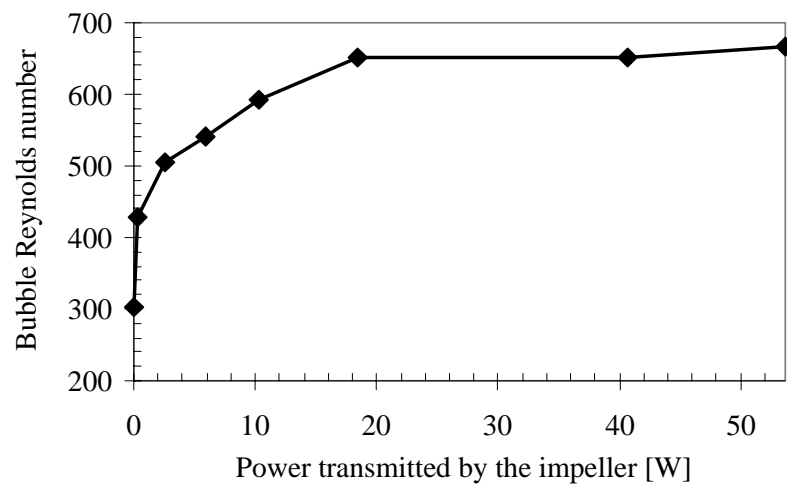
In this case, the particle settling is in the intermediate regime ($0.2 < Re_p < 500$) with a settling velocity of 0.0085 m/s, the calculated fines removal cut-size is 134.94 microns, and the particle Reynolds number is 0.90. The fines removal cut-size of 134.94 microns means that crystals smaller than this size will be removed from the crystallizer; on the other hand, the crystals will settle and leave the crystallizer as product outlet tube if their sizes are equal or larger than 134.94 microns. That means the size of 134.94 microns is the minimum size of the crystal that would be fully settled in the annular settling zone.

5.1.2 Effect of the momentum source

In this section, eight test cases (case studies 1 to 8 in Table 4.1) are performed, using momentum source values of 0, 1,000, 4,000, 7,000, 10,000, 15,000, 25,000, and 30,000 $\text{kg/m}^2/\text{s}^2$. Initially, the power transmitted by the impeller was calculated, as shown in Table 5.1. The average bubble (vapor) Reynolds number inside the draft tube, approximate average liquid Reynolds number inside and outside the draft tube, and approximate liquid Reynolds number in the settling zone of these cases are plotted versus power transmitted by the impeller, and are shown in Figures 5.11 and 5.12, respectively. The large values of the Reynolds number in these figures indicate that turbulent flow occurs inside and outside the draft tube, except for the bubble Reynolds number of the case studies numbers 1 and 2 which are less than 500, indicating transition flow. Furthermore, these figures show that the Reynolds number increases with increasing power transmitted by the impeller (this is equivalent to increasing the momentum source). This is true for both the regions inside and outside of the draft tube, but the Reynolds number inside the draft tube is higher than the Reynolds number outside. This means that the turbulence inside and outside the draft tube is increased with increasing power transmitted by the impeller. The Reynolds numbers in the settling zones are much smaller than those inside the draft tube, and most values are in the transition flow regime ($0.2 < Re_p < 500$) except those at very high values of momentum addition. This indicates that the flow phenomenon in this area is less turbulent than in the other areas, and gravitational settling will occur.

Table 5.1 Values of the power transmitted by the impeller.

Case study number	1	2	3	4	5	6	7	8
Momentum source (kg/m ² /s ²)	0	1,000	4,000	7,000	10,000	15,000	25,000	30,000
Power (W)	0	0.3148	2.560	5.960	10.21	18.48	40.62	53.67

**Figure 5.11** Bubble Reynolds number in the draft tube for case studies 1 to 8 as a function of power transmitted by the impeller.

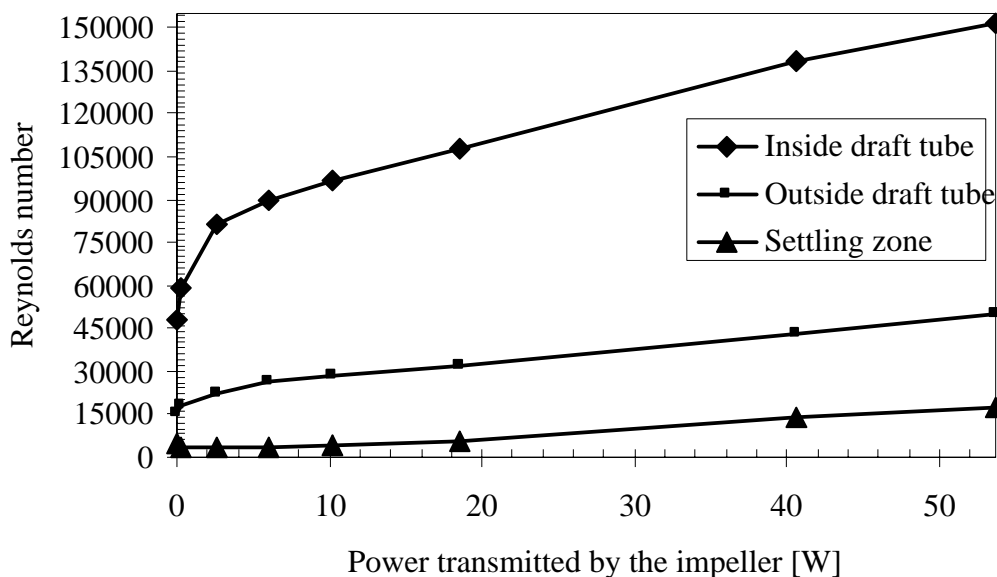


Figure 5.12 Liquid Reynolds number inside and outside the draft tube, and in the settling zone for case studies 1 to 8 as a function of power transmitted by the impeller.

The contours of the vapor fraction for the cases of 0, 1,000, 4,000, 7,000, 10,000, 15,000, 25,000, and 30,000 $\text{kg/m}^2/\text{s}^2$ are shown in Figures 5.13 to 5.20, respectively. The results show that the only region where vapor is the only phase present (the volume fraction of vapor is 1) is in the upper part of the crystallizer (above the free surface) and liquid is the principal phase present (the volume fraction of vapor is small) in the lower part (below the free surface). This is found for all case studies. For the momentum source values of 0 and 1,000 $\text{kg/m}^2/\text{s}^2$, the vapor is in both inside and outside of the draft tube because the momentum source values are very low values, which can not force all the feed solution to flow into the draft tube. On the other hand, momentum source values of 4,000, 7,000, 10,000, 15,000, 25,000, and 30,000 $\text{kg/m}^2/\text{s}^2$ are values that are high enough to assist the inflowing solution to

flow into the draft tube. The residence time for the vapor changes as the momentum source strength changes (as increased momentum source results in increased liquid and vapor velocities in the draft tube), and this causes the vapor volume fraction in the draft tube to decrease as the momentum source strength increases. Moreover, the small circular region with high volume fraction at the top left side of the draft tube increases as the momentum source strength increases, but there is no circulation flow in the top right side of the draft tube because the feed solution is fed under the left side of the draft tube, and the feed solution flow is a strong flow. This indicates that for high values of the momentum source addition, small amounts of the vapor will turn over the top of the draft tube and flow down (i.e. it is not separated out), which disturbs the crystallization kinetics and uniform flow of the liquid in this area. This could result in non-uniformity of particle size in the crystallizer. The vapor-liquid interface changes only a little at the high values of the momentum source addition (see more details later).

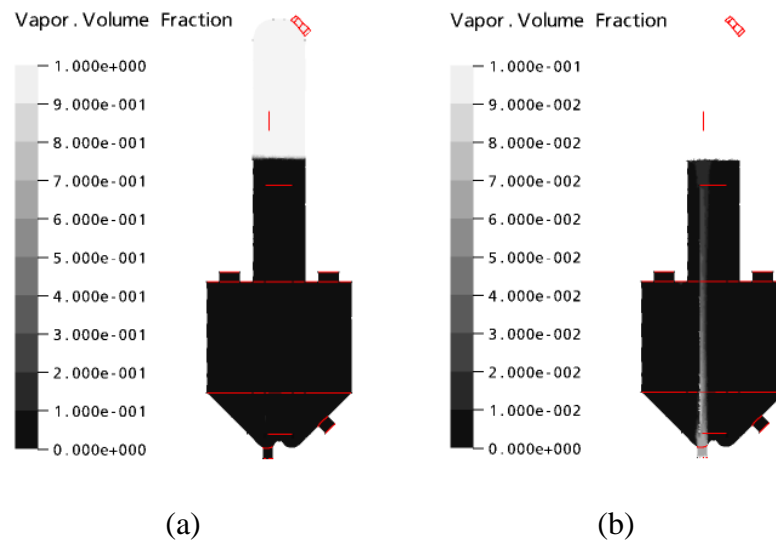


Figure 5.13 Contours of vapor volume fraction in the vertical center plane for no momentum source addition ($0 \text{ kg/m}^2/\text{s}^2$); (a) overall fraction; (b) magnified scale to enable visualization in the draft tube.

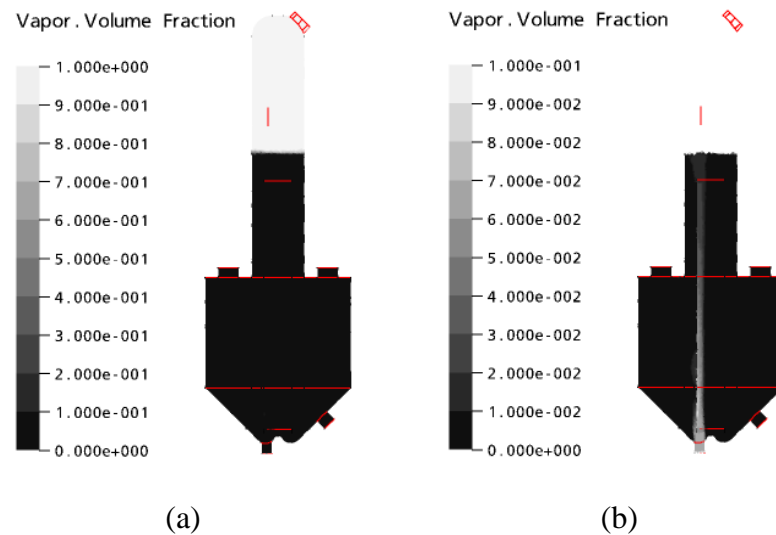


Figure 5.14 Contours of vapor volume fraction in the vertical center plane for momentum source addition of $1,000 \text{ kg/m}^2/\text{s}^2$; (a) overall fraction; (b) magnified scale to enable visualization in the draft tube.

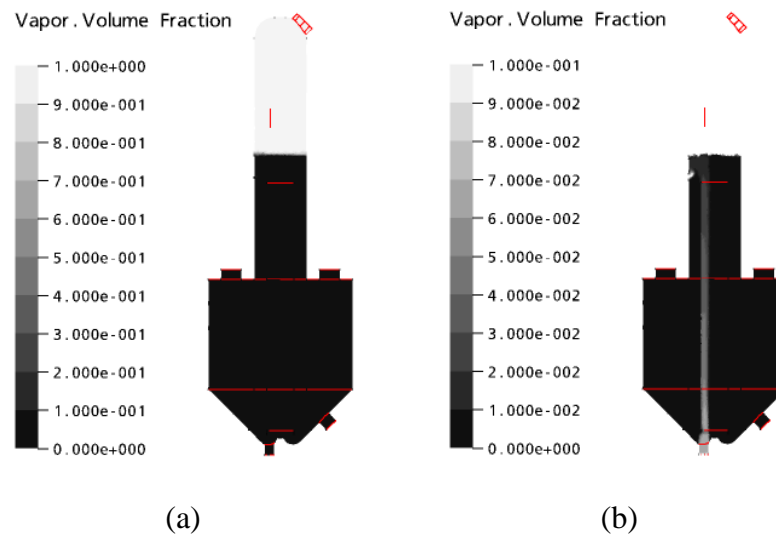


Figure 5.15 Contours of vapor volume fraction in the vertical center plane for momentum source addition of $4,000 \text{ kg/m}^2/\text{s}^2$; (a) overall fraction; (b) magnified scale to enable visualization in the draft tube.

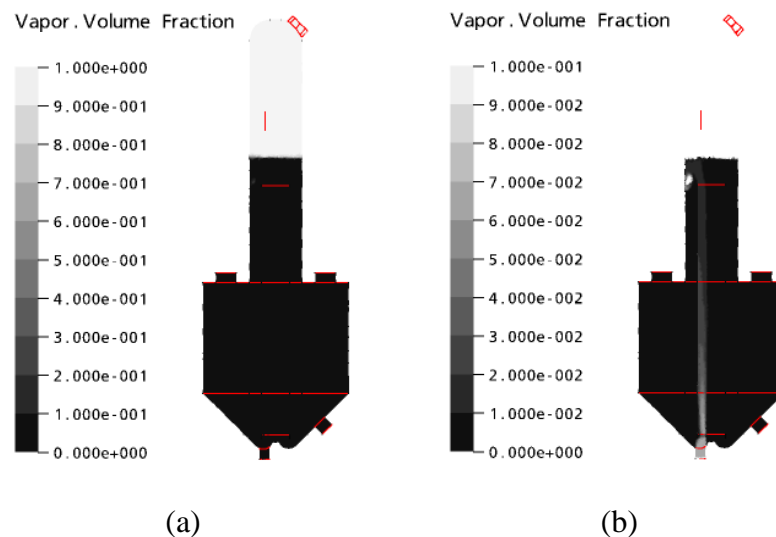


Figure 5.16 Contours of vapor volume fraction in the vertical center plane for momentum source addition of $7,000 \text{ kg/m}^2/\text{s}^2$; (a) overall fraction; (b) magnified scale to enable visualization in the draft tube.

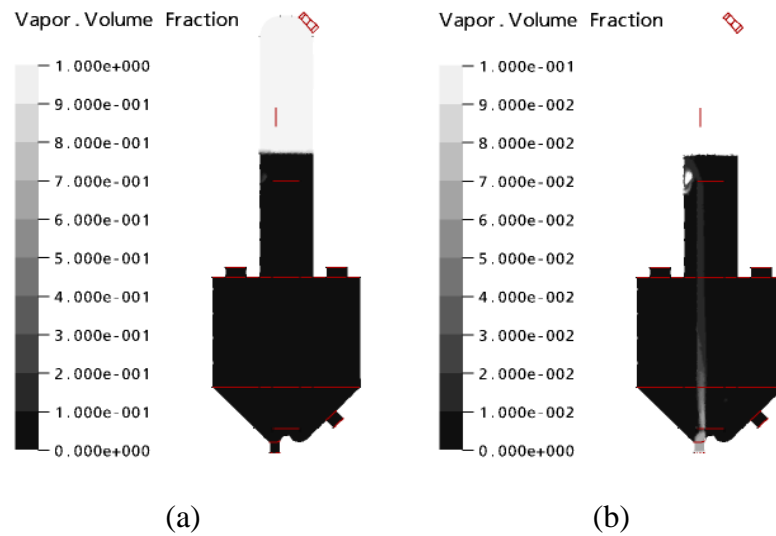


Figure 5.17 Contours of vapor volume fraction in the vertical center plane for momentum source addition of $10,000 \text{ kg/m}^2/\text{s}^2$; (a) overall fraction; (b) magnified scale to enable visualization in the draft tube.

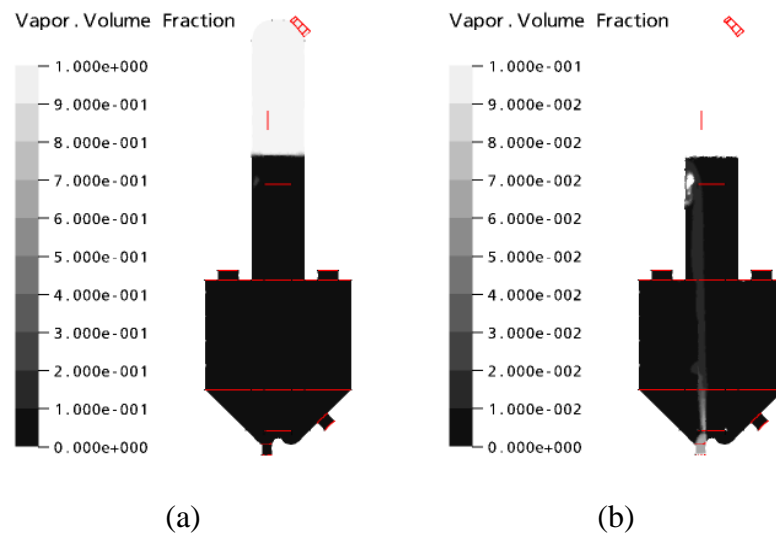


Figure 5.18 Contours of vapor volume fraction in the vertical center plane for momentum source addition of $15,000 \text{ kg/m}^2/\text{s}^2$; (a) overall fraction; (b) magnified scale to enable visualization in the draft tube.

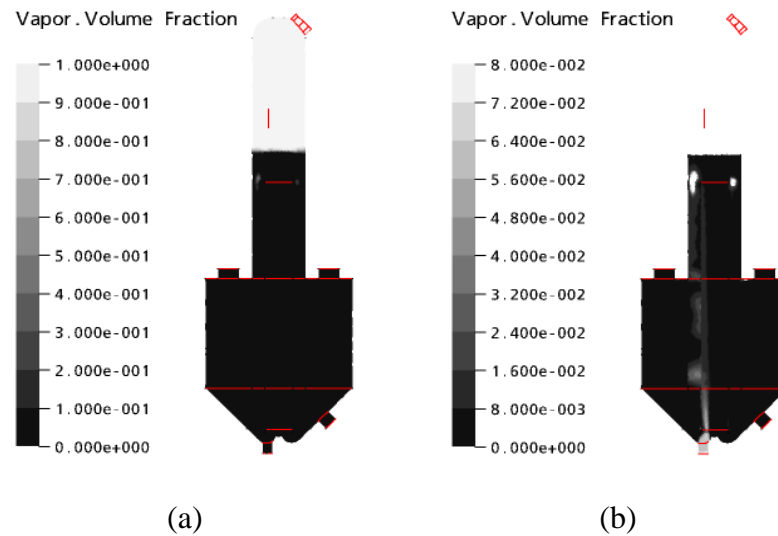


Figure 5.19 Contours of vapor volume fraction in the vertical center plane for momentum source addition of $25,000 \text{ kg/m}^2/\text{s}^2$; (a) overall fraction; (b) magnified scale to enable visualization in the draft tube.

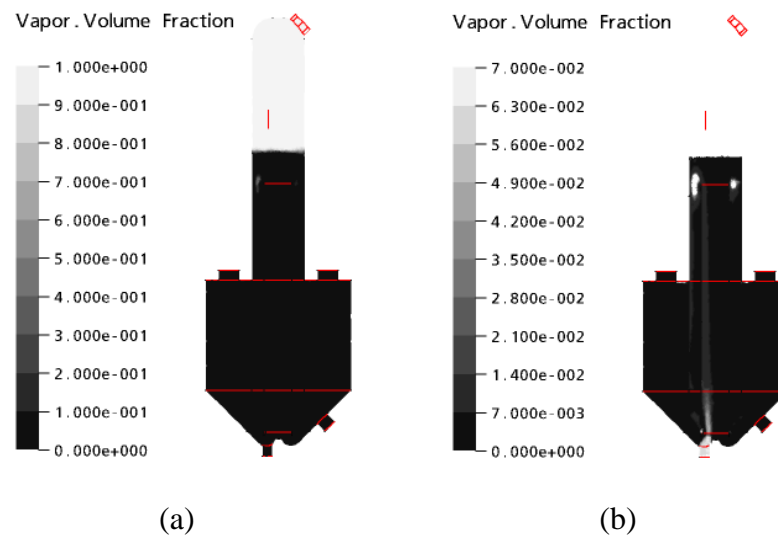


Figure 5.20 Contours of vapor volume fraction in the vertical center plane for momentum source addition of $30,000 \text{ kg/m}^2/\text{s}^2$; (a) overall fraction; (b) magnified scale to enable visualization in the draft tube.

Figures 5.21 to 5.28 show the overall velocity vectors, velocity contours, and 2D streamlines for both phases, respectively (from left to right), for momentum source values of 0, 1,000, 4,000, 7,000, 10,000, 15,000, 25,000, and 30,000 $\text{kg/m}^2/\text{s}^2$. These figures indicate that for the case of no momentum addition (Figure 5.21) and 1,000 $\text{kg/m}^2/\text{s}^2$ of momentum source addition (Figure 5.22) the flows of both liquid and vapor phase are not the general flow field in the DTB crystallizer at the impeller location (that is; for the liquid phase, circulation flow or upward flow inside the draft tube and downward flow outside the draft tube; for the vapor phase, upward flow inside the draft tube and separated out at the vapor-liquid interface), which are described in the previous section. For these two cases, there is upward flow in some part of the outside of the draft tube because the momentum addition through the impeller is not enough to force the feed into the draft tube. The flow features in 3D for both cases are shown in appendix D in Figures D.1 (a) and (b) for the liquid phase and Figures D.4 (a) and (b) for the vapor phase. For the cases of 4,000, 7,000, 10,000, 15,000, 25,000, and 30,000 $\text{kg/m}^2/\text{s}^2$ (Figures 5.23 to 5.28), the flows of both vapor and liquid are the general flow field in the DTB crystallizer, except that a small amount of the vapor will be turned over the top of the draft tube and flow down at high values of the momentum source strength. The flow features in 3D for these cases are shown in appendix D in Figures D.1 (c) to (h) for the liquid and Figures D.4 (c) to (h) for the vapor.

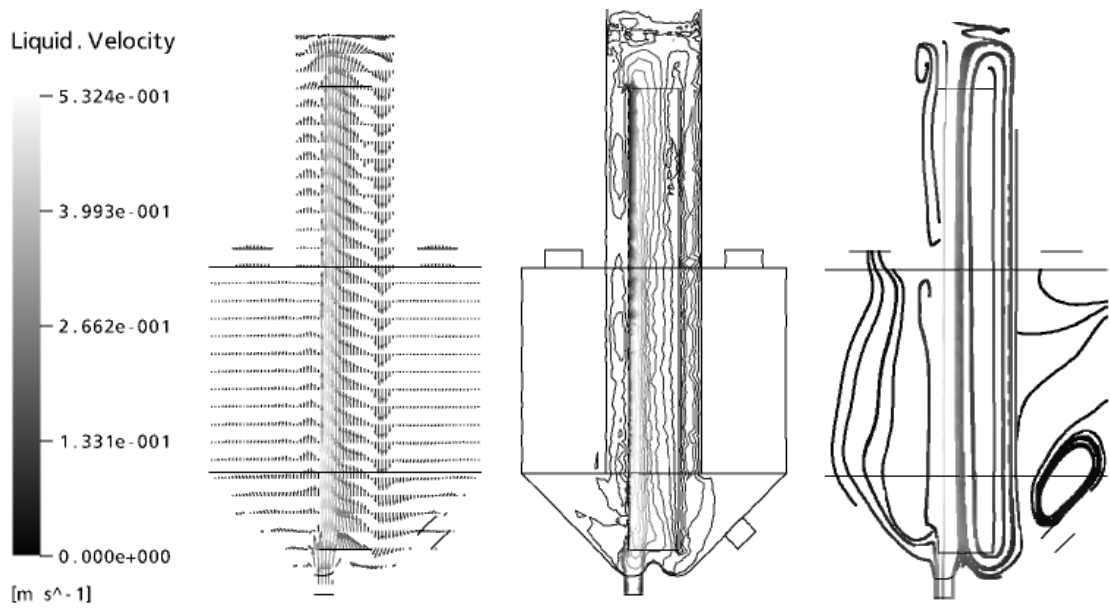
As the momentum added through the impeller increases, the liquid velocity become larger both in the upflow section inside the draft tube and in the downflow area outside the draft tube. This results in a stronger flow (maximum velocity) at the bottom part of the draft tube (near the impeller location), and also a

higher velocity inside the draft tube and lower velocity in the annular space that assists in suspension of particles. For the vapor, the velocity increases with increasing momentum source addition too, but increases to a much smaller degree than the liquid velocity. The overall vapor velocity contours and 2D streamlines have basically the same features without any drastic change in structure, and the other effects of the momentum source addition are the same as described previously.

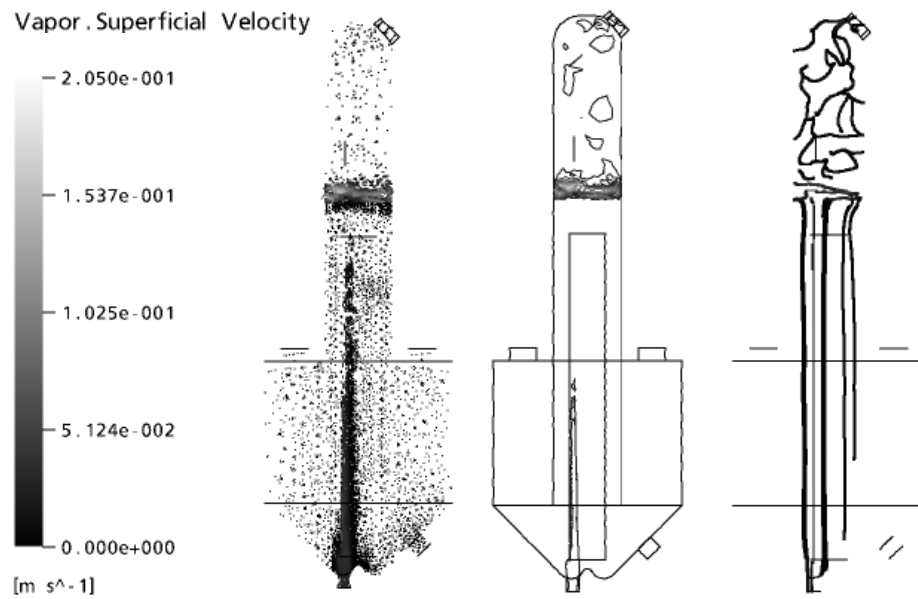
The uniformity of the liquid flow can be clearly depicted by the overall velocity contours (the center picture of Figures 5.21 to 5.28). The results show that full uniformity of the low liquid velocity in the particle settling zone was found for all the case studies; it makes sense to have the uniform flow in this zone. The uniform flow and very low velocity of this zone indicate very low crystallization kinetics (probably entirely mass transfer controlled) in this zone. This is suitable because this zone is designed for the purpose of the particle settling process only. At the point that the liquid flows over the top of the draft tube, and the vapor-liquid interface, the overall flow feature is non-uniform for all case studies. It leads to different crystallization rates, in particular the nucleation rate because the boiling takes place at the liquid surface, which leads to a high level of supersaturation (Mersmann, 2001). This results in a high concentration, which leads to a high nucleation rate. Considering the liquid velocity contours in the draft tube and outside the draft tube, it can be seen that the overall flow features are close to uniform at high values of the momentum source addition. Thus it is evident from Figures 5.25 to 5.28 (for the momentum source values of 10,000, 15,000, 25,000, and 30,000 $\text{kg/m}^2/\text{s}^2$, respectively) that full uniformity is found at the momentum source values of 25,000, and 30,000 $\text{kg/m}^2/\text{s}^2$. This uniform flow occurs from the height of 0.4 m (above the maximum velocity) to

1.9 m (the top of the draft tube), and would assist in producing a narrow crystal size distribution (a more uniform crystal size). Uniform flow can lead to the same crystallization rate, in particular a uniform crystal growth rate because the level of supersaturation in these areas is constant. Note that this does not ensure a completely uniform particle size, because there is still a wide distribution of residence times for both the liquid and the crystals in the crystallizer. In addition the residence time distribution of the liquid and the crystals are different because nucleation does not necessarily occur immediately on entering the crystallizer.

Vorticity at the bottom of the settling zone is found for all the case studies. The results indicate vorticity close to the sides of the outside wall. This vorticity seems to originate in the region where the flow up to the fines removal tube meets tangentially the downwards flow into the product outlet tube and the circuited flow into the draft tube by the impeller effect. Another region of vorticity originates in the region where the flow up to the fines removal tube meets tangentially the circulated flow into the draft tube by the impeller effect and the flow of feed solution. Moreover, at high values of momentum addition, a small vorticity occurs near the mouth of the fines removal tube. This occurs because the flow in the settling zone is higher than the flow of the fines removal. These vorticities do not occur in the main crystallization regions (the inside and outside of the draft tube, the top of the draft tube, and the vapor-liquid interface) and the velocity in the settling zone is very low, so the crystallization kinetics are not significant in this zone (see more details in above paragraph).

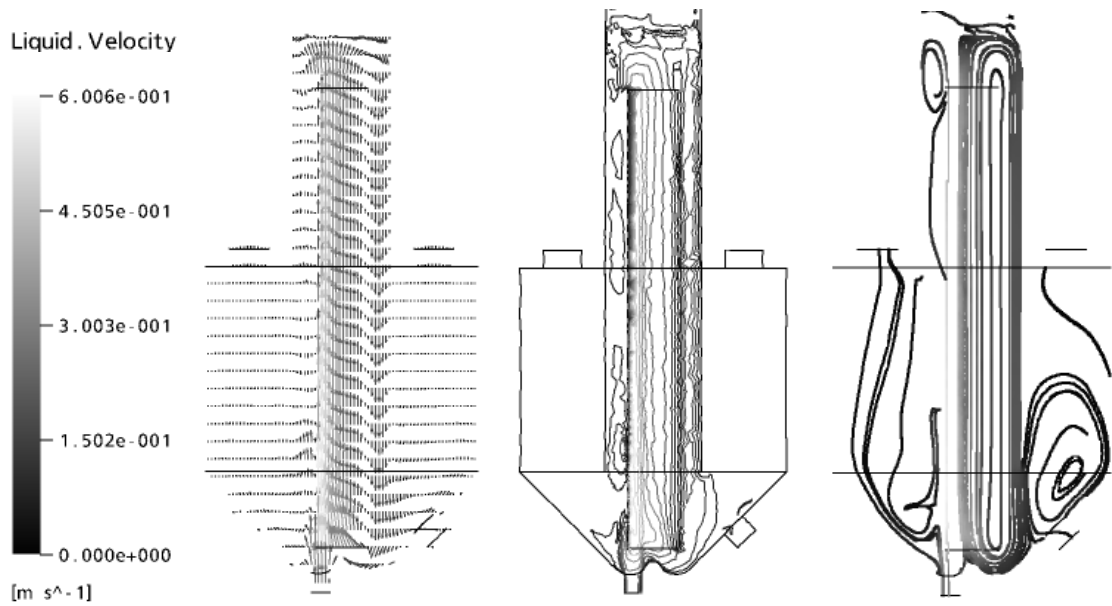


(a)

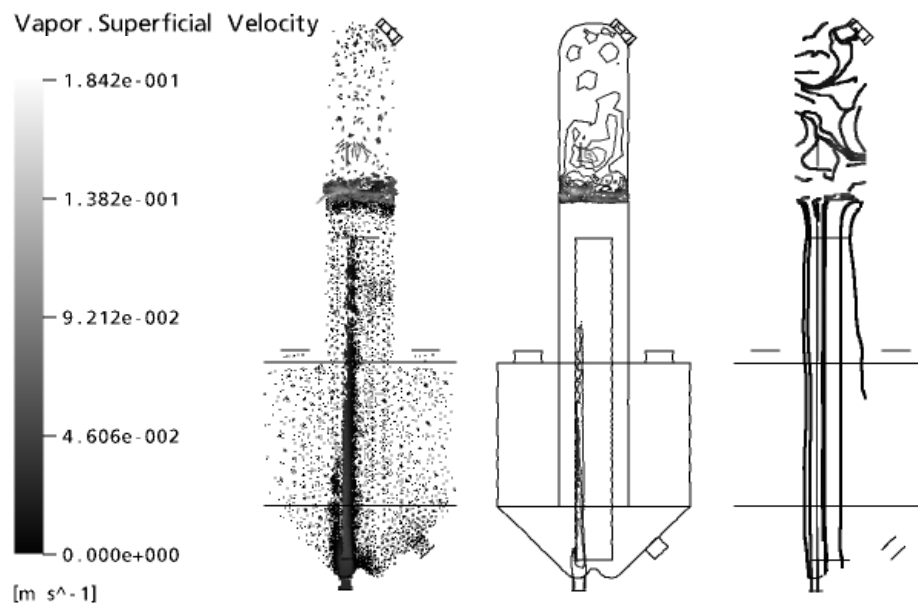


(b)

Figure 5.21 Velocity vectors, contours, and streamlines of liquid (a) and vapor (b) in the vertical center plane for momentum source of $0 \text{ kg/m}^2/\text{s}^2$.



(a)



(b)

Figure 5.22 Velocity vectors, contours, and streamlines of liquid (a) and vapor (b) in the vertical center plane for momentum source of $1,000 \text{ kg/m}^2/\text{s}^2$.

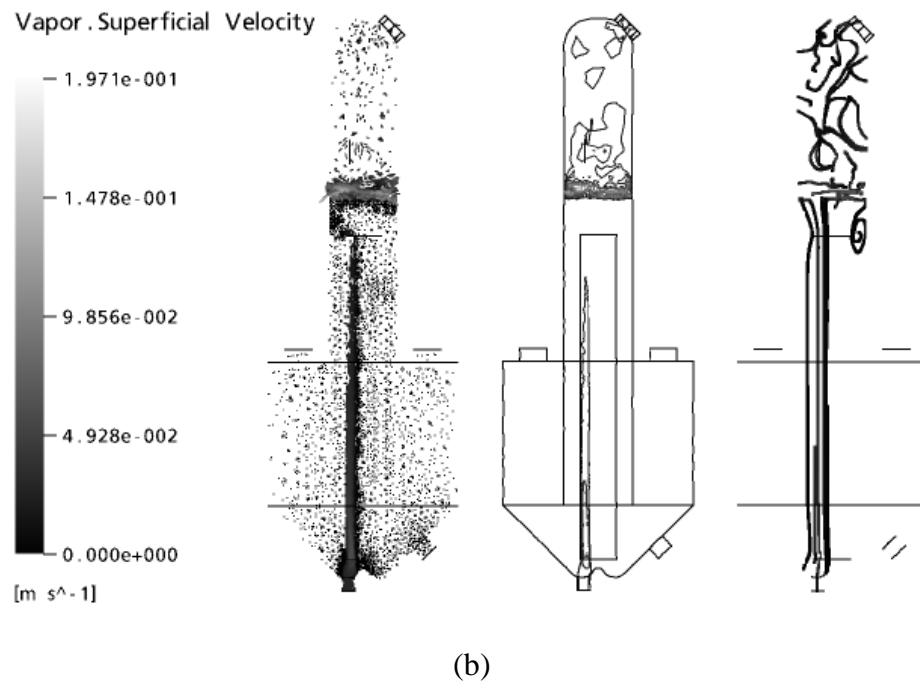
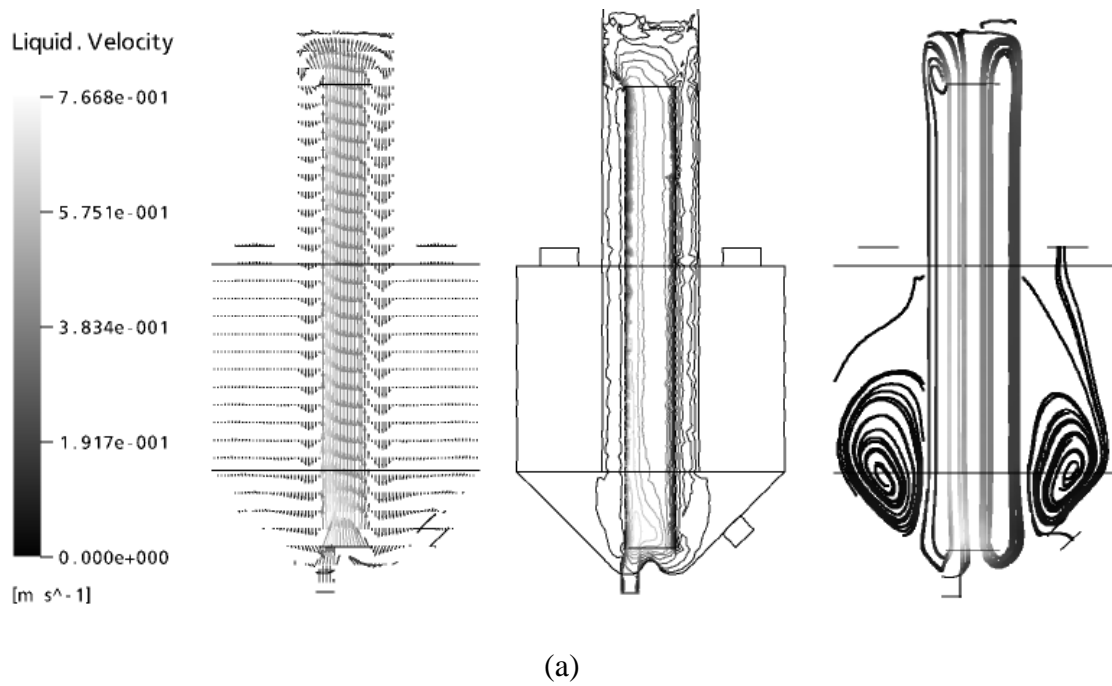
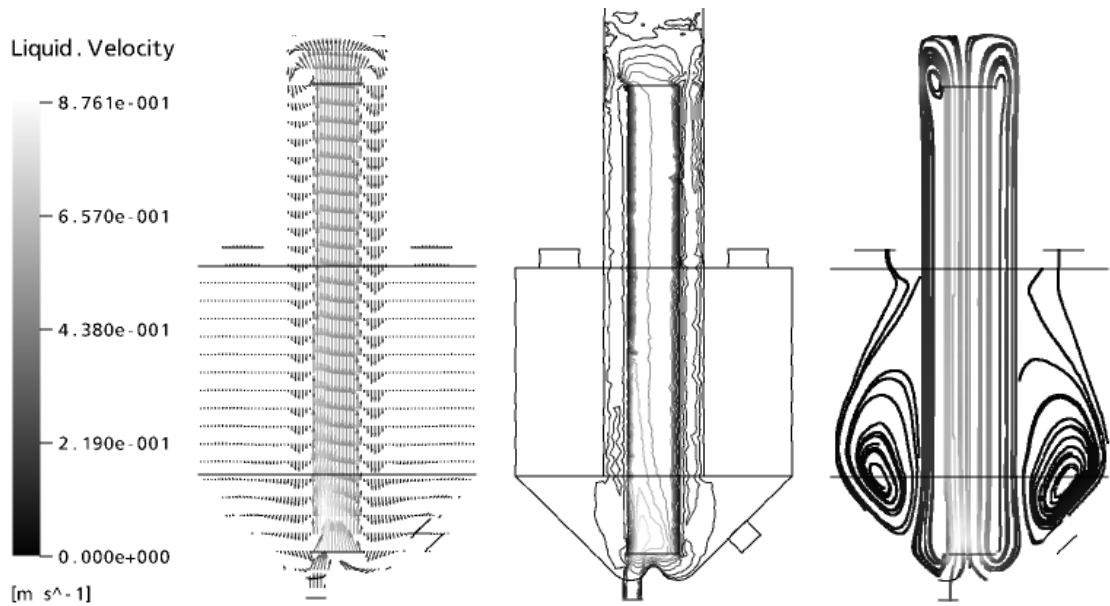
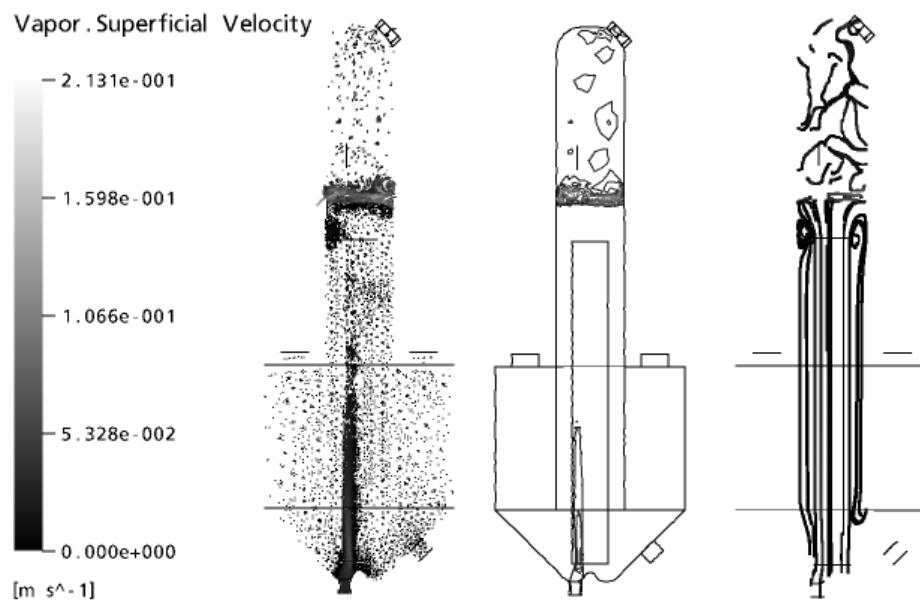


Figure 5.23 Velocity vectors, contours, and streamlines of liquid (a) and vapor (b) in the vertical center plane for momentum source of $4,000 \text{ kg/m}^2/\text{s}^2$.

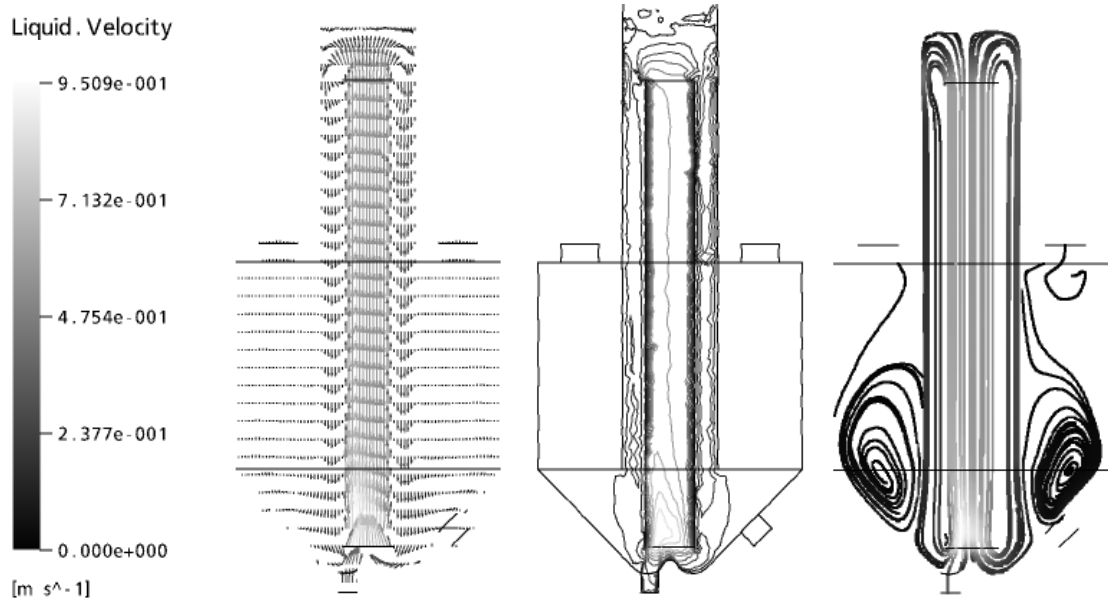


(a)

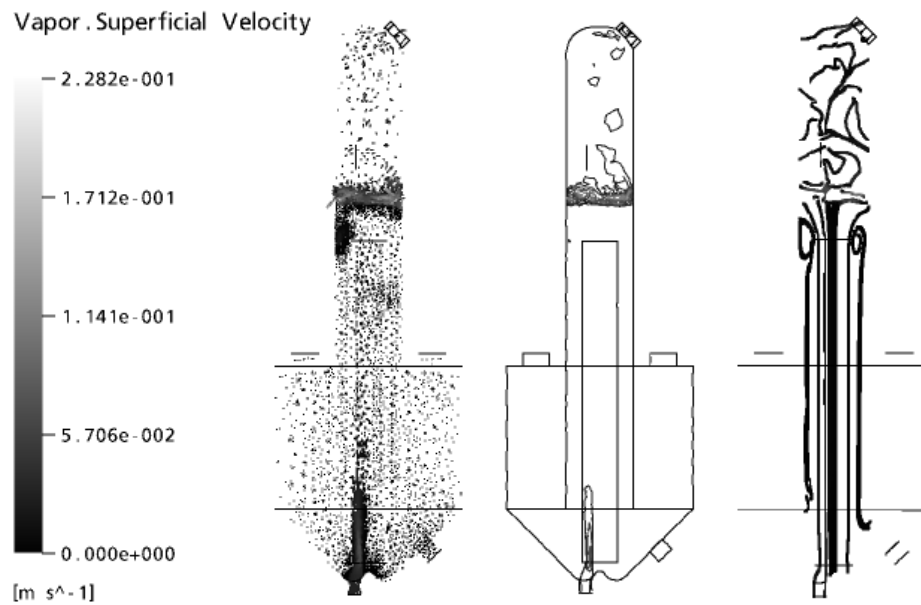


(b)

Figure 5.24 Velocity vectors, contours, and streamlines of liquid (a) and vapor (b) in the vertical center plane for momentum source of $7,000 \text{ kg/m}^2/\text{s}^2$.



(a)



(b)

Figure 5.25 Velocity vectors, contours, and streamlines of liquid (a) and vapor (b) in the vertical center plane for momentum source of $10,000 \text{ kg/m}^2/\text{s}^2$.

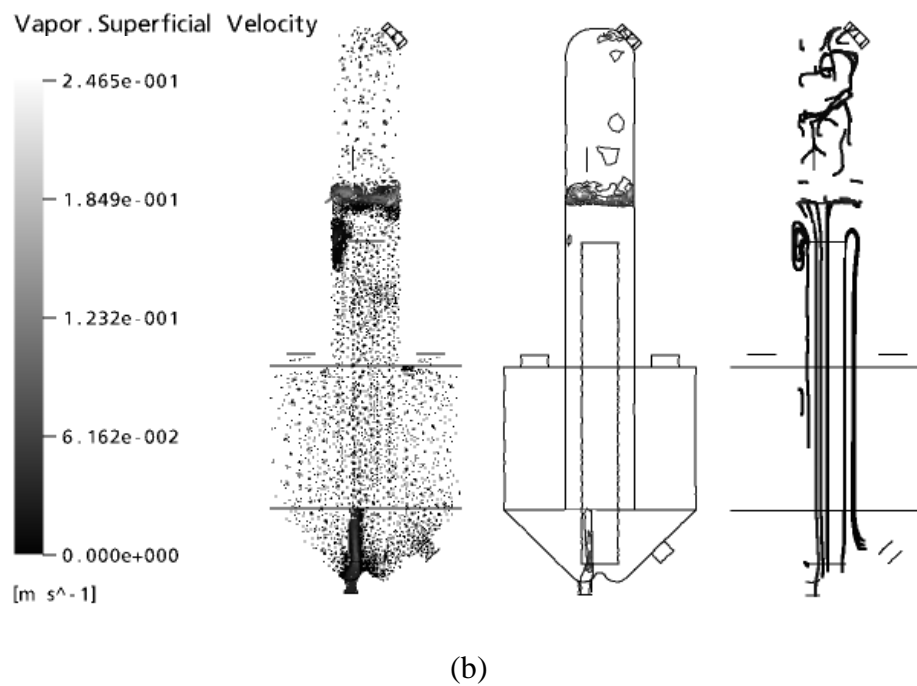
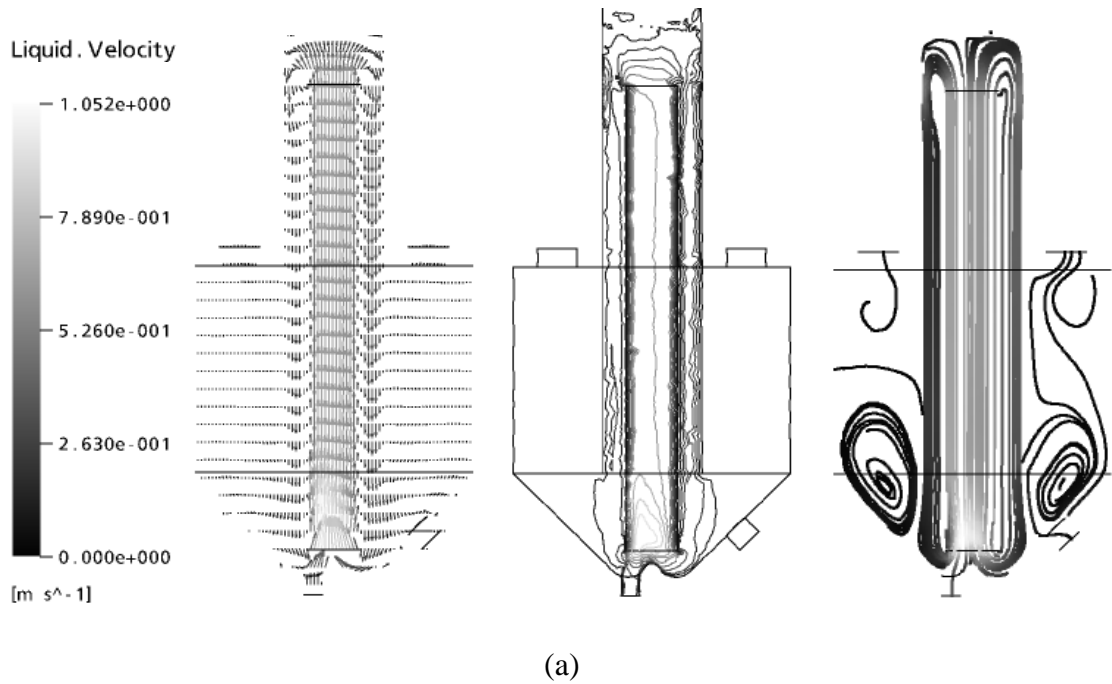
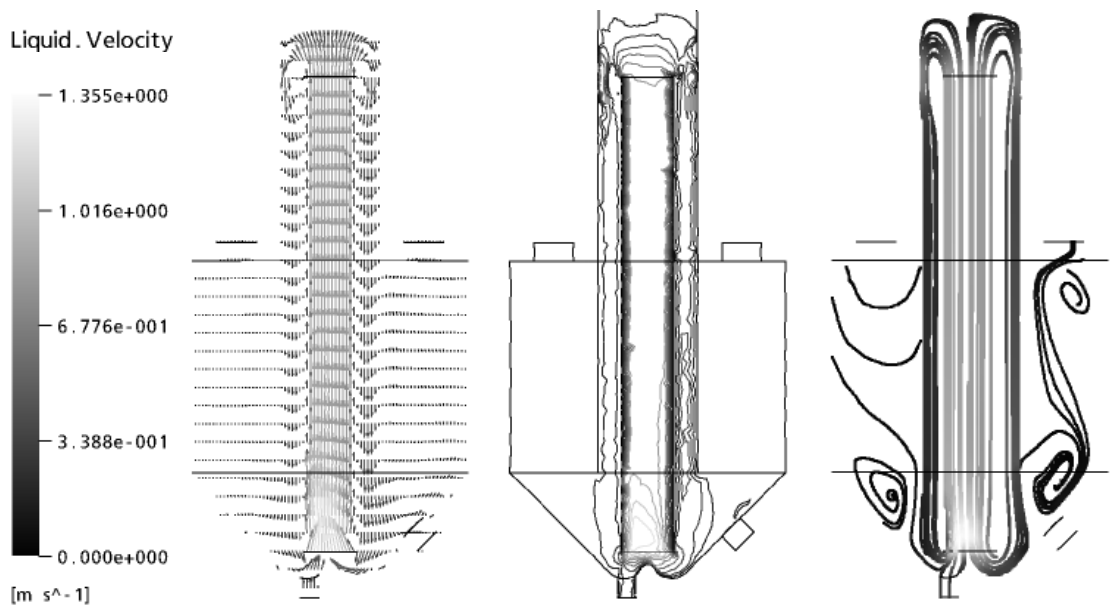
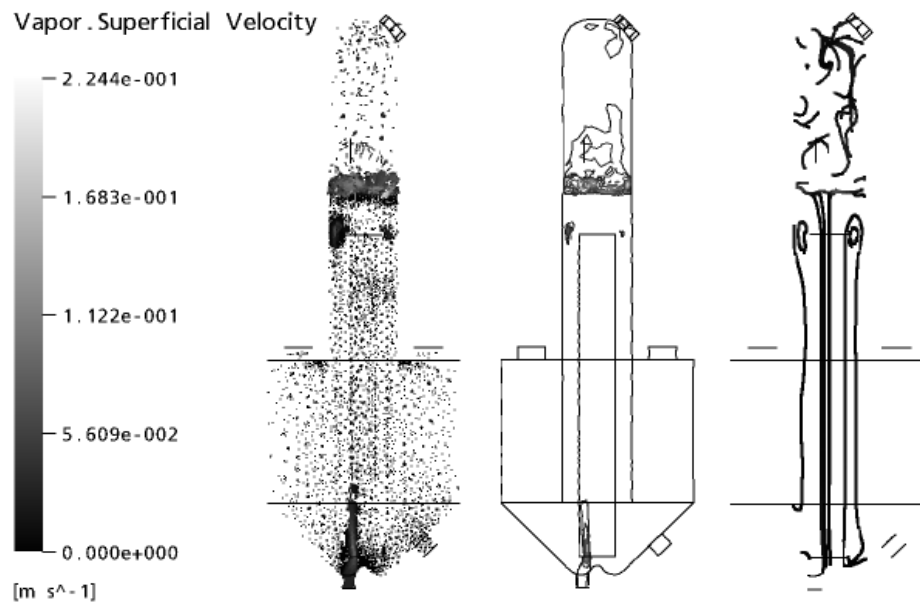


Figure 5.26 Velocity vectors, contours, and streamlines of liquid (a) and vapor (b) in the vertical center plane for momentum source of $15,000 \text{ kg/m}^2/\text{s}^2$.



(a)



(b)

Figure 5.27 Velocity vectors, contours, and streamlines of liquid (a) and vapor (b) in the vertical center plane for momentum source of $25,000 \text{ kg/m}^2/\text{s}^2$.

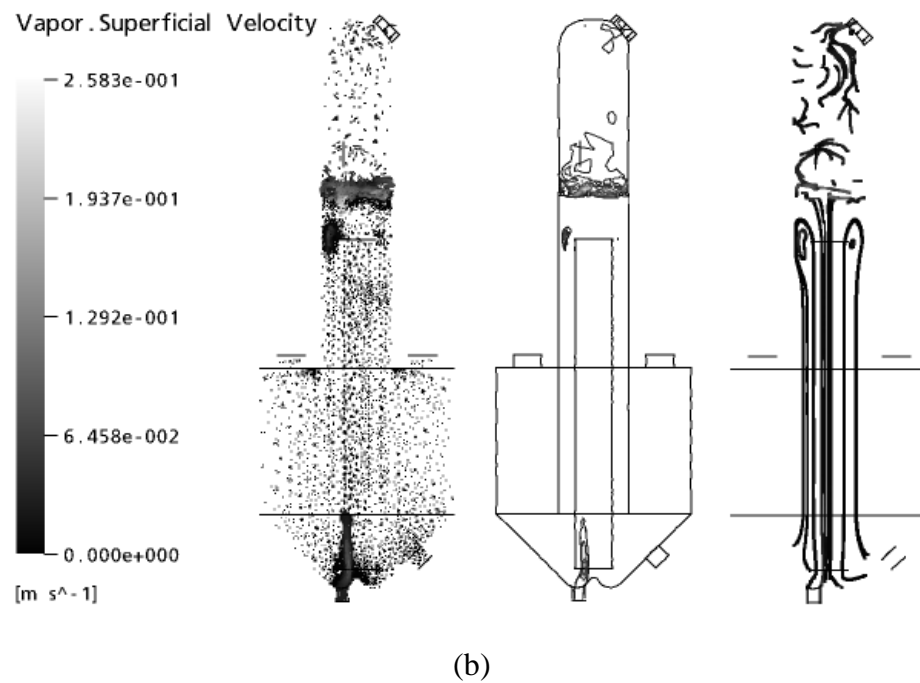
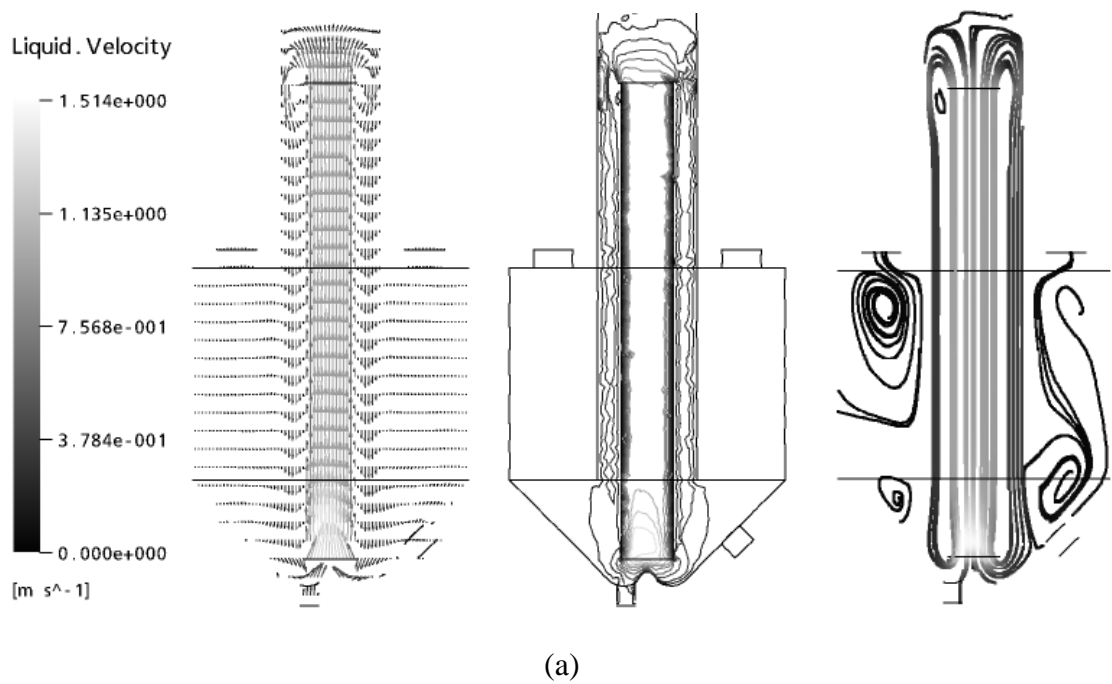


Figure 5.28 Velocity vectors, contours, and streamlines of liquid (a) and vapor (b) in the vertical center plane for momentum source of $30,000 \text{ kg/m}^2/\text{s}^2$.

Figure 5.29 represents the vapor velocity in the horizontal plane at the vapor-liquid interface. It shows that the height of the vapor-liquid interface does not change (constant at the initial height of 2.11 m) when the momentum source increases from 4,000 to 10,000 $\text{kg/m}^2/\text{s}^2$ (Figures 5.29 (a) to (c)), but as the momentum source increases from 15,000 to 30,000 $\text{kg/m}^2/\text{s}^2$ the height of the vapor-liquid interface increases as the momentum source strength increases, as shown in Figures 5.29 (d) to (f). The height of the vapor-liquid interface for momentum source additions of 15,000, 25,000, and 30,000 $\text{kg/m}^2/\text{s}^2$ are 2.118, 2.132, and 2.138 m, respectively.

At the vapor-liquid interface, it is seen that at low momentum source addition (momentum source additions of 4,000, 7,000, and 10,000 $\text{kg/m}^2/\text{s}^2$), the vapor will be separated out from the liquid phase at the center continuing to the left side wall of the tank (in the direction of the feed location), as shown in Figure 5.29 (a) to (c). This means that the momentum source values of 4,000, 7,000, and 10,000 $\text{kg/m}^2/\text{s}^2$ are not enough to cancel the effect of the feed to the flow field in the DTB crystallizer. As the momentum source addition increases from 15,000 to 30,000 $\text{kg/m}^2/\text{s}^2$ (Figures 5.29 (d) to (e)), most vapor will be separated out from the liquid phase at the center of the tank; in particular for the momentum source additions of 25,000 and 30,000 $\text{kg/m}^2/\text{s}^2$ all vapor will be separated out only at the center of the tank. This indicates that the momentum source values of 25,000 $\text{kg/m}^2/\text{s}^2$ and larger are able to completely cancel the effect of the feed solution flow field in the DTB crystallizer. These are correct for the feed solution flow of approximately 1 kg/s, which was used in these case studies. This leads to a uniformity of liquid flow.

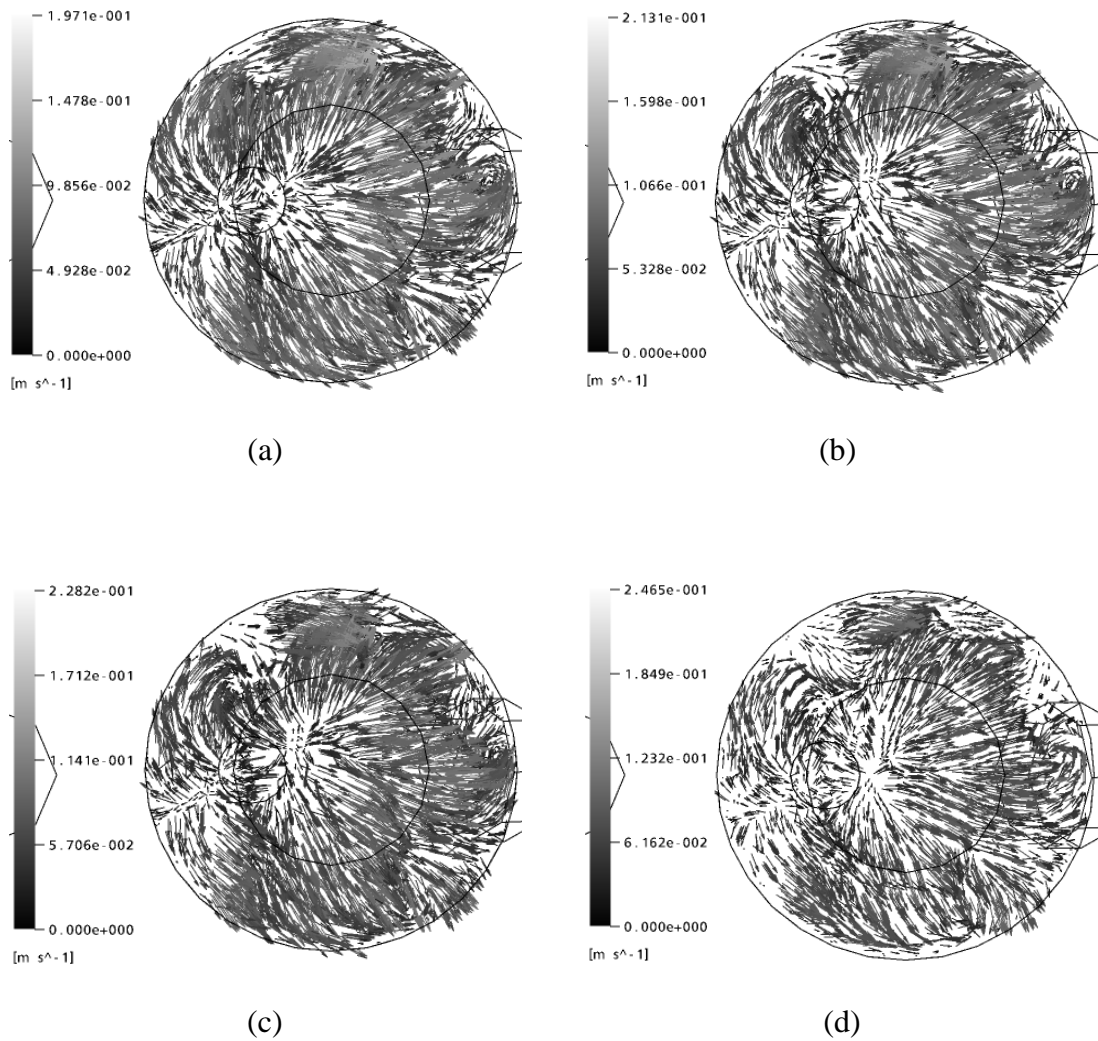


Figure 5.29 Vapor velocity vectors in the horizontal plane at the vapor-liquid interface for momentum source additions of (a) $4,000 \text{ kg/m}^2/\text{s}^2$ (at the height of 2.11 m); (b) $7,000 \text{ kg/m}^2/\text{s}^2$ (at the height of 2.11 m); (c) $10,000 \text{ kg/m}^2/\text{s}^2$ (at the height of 2.11 m); (d) $15,000 \text{ kg/m}^2/\text{s}^2$ (at the height of 2.118 m); (*continued*)

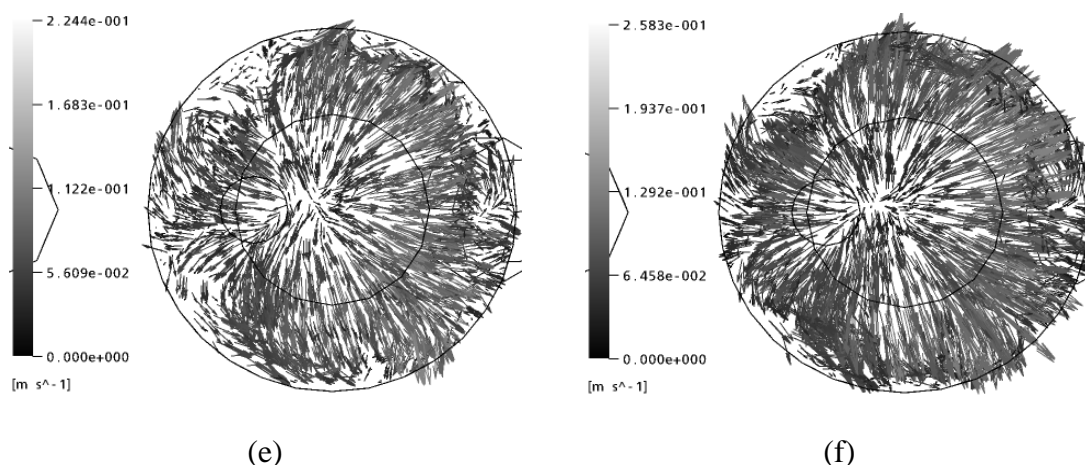


Figure 5.29 (continued) (e) 25,000 kg/m²/s² (at the height of 2.132 m); (f) 30,000 kg/m²/s² (at the height of 2.138 m).

The liquid at the bottom of the tank tends to flow into the draft tube, which is similar to the previous description in section 5.1.1. This is found for all the case studies and means that there is no stagnation point at the bottom of the tank. The liquid velocity vectors at the bottom of the tank for momentum source additions of 4,000, 7,000, 10,000, 15,000, 25,000, and 30,000 kg/m²/s² are shown in appendix D in Figure D.7.

Figure 5.30 represents the contours of the absolute pressure in the vertical center plane. It shows that the pressure has the lowest value in the top part of the tank (the vapor space above the free surface) and the pressure increases continuously when the height of the tank is lower until the maximum value is reached at the bottom of the crystallizer. This is found for all the case studies. This result is mainly due to the static pressure due to the height of liquid above the point the pressure is measured at. As the momentum source added through the impeller

increases the overall magnitude of the pressure will increase only by a small amount. Because the tank is very high, the force effect is less than the hydrostatic effect (weight of the liquid) which leads to a small change in the pressure as the momentum source increases.

As described previously, the flow in the annular settling zone is uniform and the velocity is low enough to confirm the process of the gravitational settling of the particles. The terminal velocity and the fines removal cut-size can be calculated using the method described previously in the section 5.1.1. The results are shown in Figures 5.31 and 5.32. These figures show that as the power transmitted by the impeller increases (equivalent to increasing of the momentum source addition) the terminal velocity increases (Figure 5.32). This indicates that the fines removal cut-size increases with increasing power transmitted by the impeller because the terminal velocity increases approximately linearly with increasing particle size (Figure 5.31), which was suggested by Lapple (1951) and available only for the flow in the transition regime. This means the mean product crystal size increases with increasing momentum source. This result makes sense since the varying upflow velocities in the fines removal section due to the varying momentum source alter the size at which particles are carried out in the fines removal stream. This will strongly affect the product crystal size distribution. Moreover in Figure 5.32, the particle Reynolds numbers increase with increasing power transmitted by the impeller and all of the values of the Reynolds number are in the range of 0.2 to 500, which indicates the particle flow is in the transition regime.

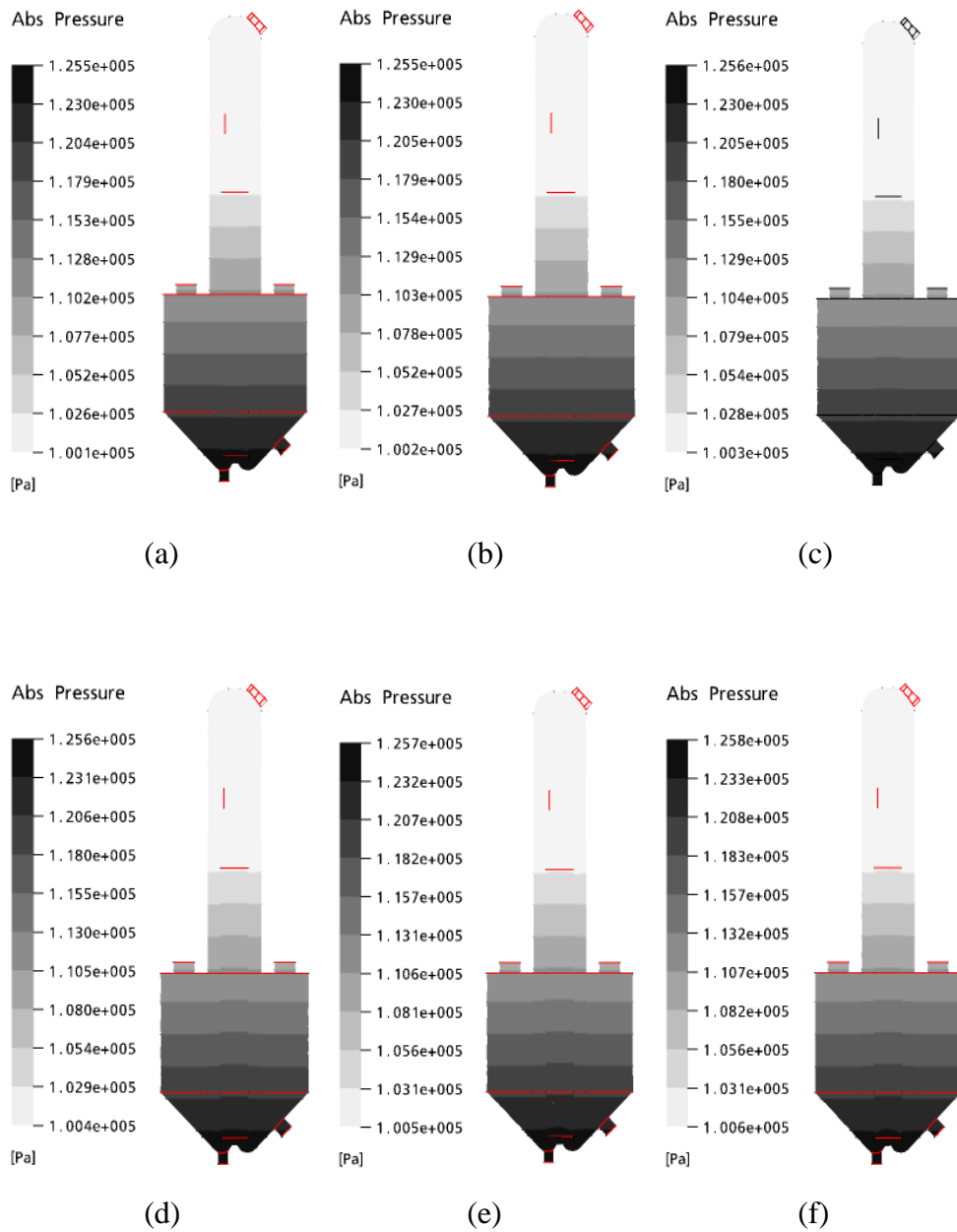


Figure 5.30 Contours of the absolute pressure in the vertical center plane for momentum source additions of (a) 4,000 kg/m²/s²; (b) 7,000 kg/m²/s²; (c) 10,000 kg/m²/s²; (d) 15,000 kg/m²/s²; (e) 25,000 kg/m²/s²; (f) 30,000 kg/m²/s².

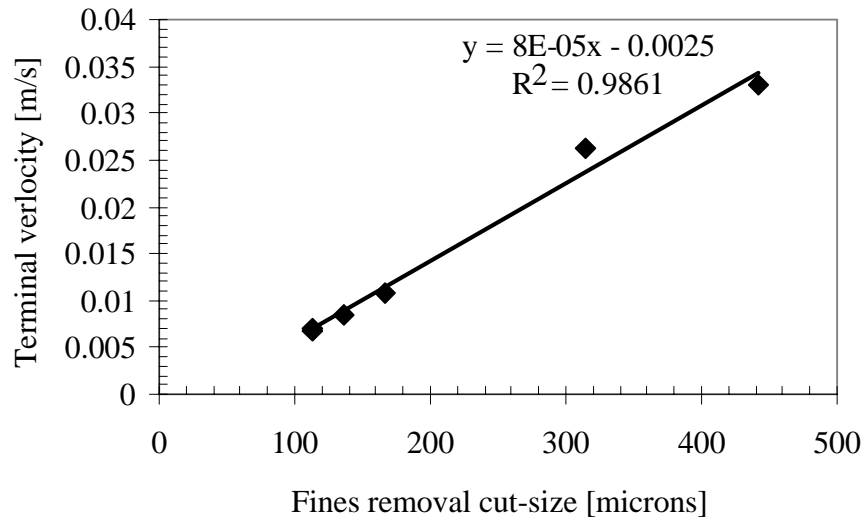


Figure 5.31 Terminal velocity for case studies 3 to 8 as a function of fines removal cut-size.

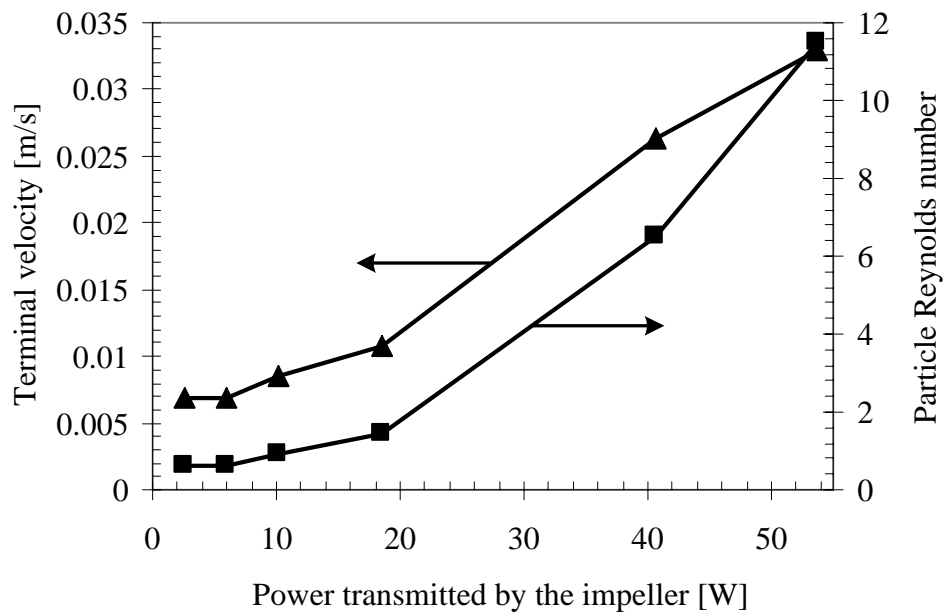


Figure 5.32 Terminal velocity and particle Reynolds number for case studies 3 to 8 as a function of power transmitted by the impeller.

5.1.3 Effect of the fines removal flow rate

In this section, five test cases are performed, using a constant momentum source addition of $10,000 \text{ kg/m}^2/\text{s}^2$ and a constant product crystal suspension flow of 0.1797 kg/s , with the fines removal flow varied at 0.4672 , 1.0063 , 1.5454 , 2.3002 , and 3.594 kg/s , as shown in case studies 9 to 13 of Table 4.1 in chapter 4. The results showed that all values of the Reynolds number indicate that the flow inside and outside of the draft tube are turbulent flow, and the flow in the settling zone is transition flow. Moreover, changes in the fines removal flow have little effect on the bubble Reynolds number (Figure 5.33), and liquid Reynolds numbers inside and outside the draft tube and in settling zone (Figure 5.34). These mean that the turbulence inside and outside the draft tube only slightly increases with increasing fines removal flow (or feed solution flow, which is the result of the material balance).

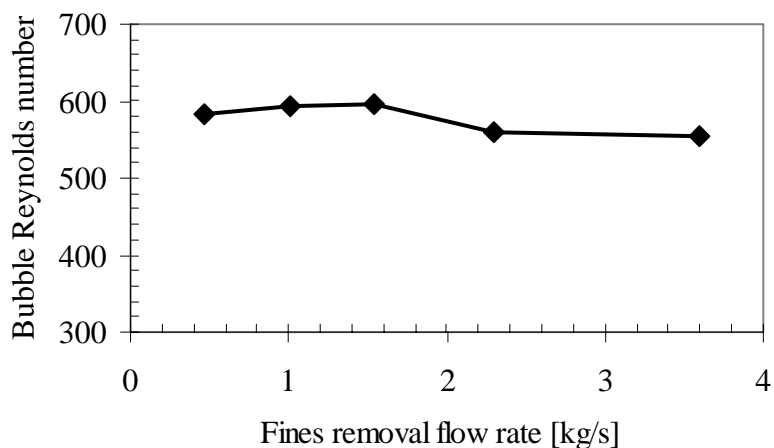


Figure 5.33 Bubble Reynolds number inside the draft tube for case studies 9 to 13 as a function of fines removal flow.

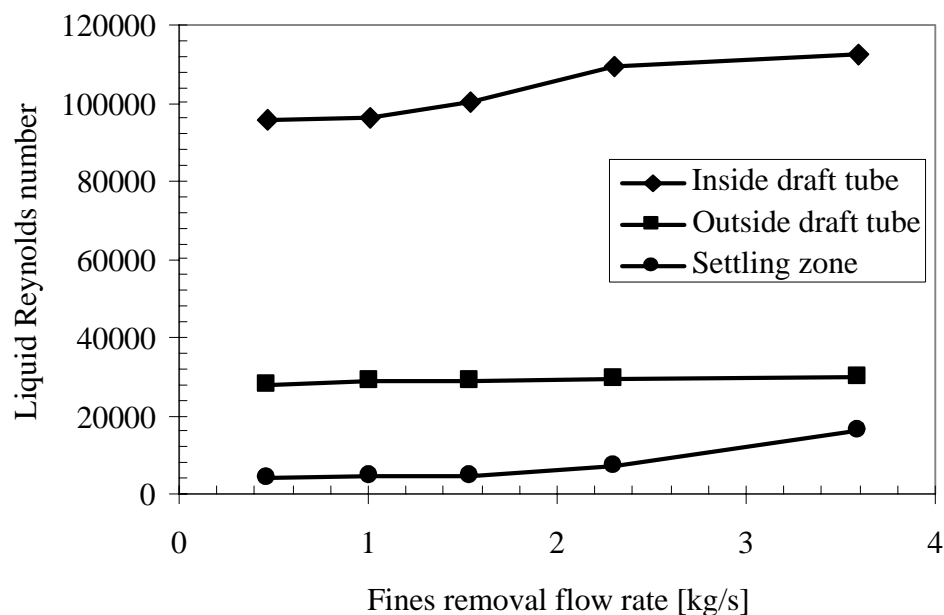


Figure 5.34 Liquid Reynolds number inside and outside the draft tube, and in the settling zone for case studies 9 to 13 as a function of fines removal flow.

The overall contours for volume fractions of vapor in the effect of the fines removal case studies are similar to the effect of the momentum source addition (Figures 5.35 (a), 5.36 (a), 5.37 (a), 5.38 (a), and 5.39 (a)), except the volume fraction of vapor in the draft tube increases with increasing fines removal flow (Figures 5.35 (b), 5.36 (b), 5.37 (b), 5.38 (b), and 5.39 (b)). This is because increasing the fines removal flow necessitates increasing the feed solution (because the product flow is maintained constant) resulting in the amount of vapor in the feed increasing. As described in a previous section, small amounts of vapor will turn over the top of the draft tube and flow down (i.e., is not separated out). This is found in the fines removal flow case studies too.

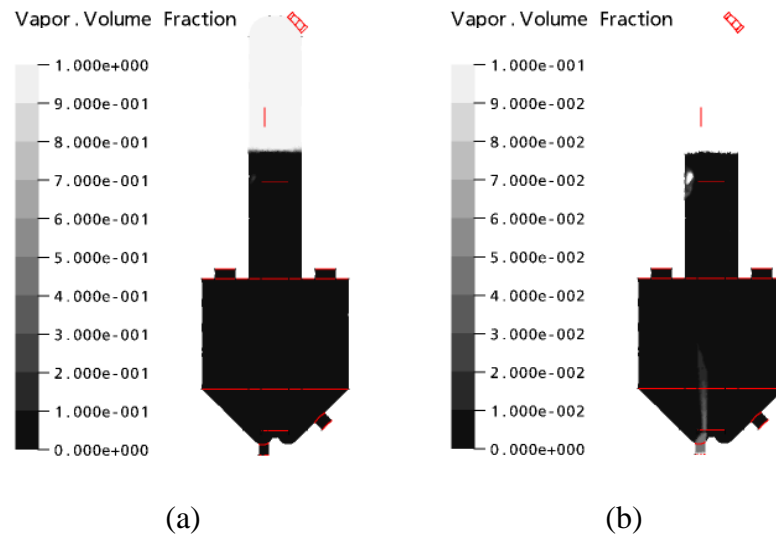


Figure 5.35 Contours of vapor volume fraction in the vertical center plane for fines removal flow of 0.4672 kg/s; (a) overall fraction; (b) magnified scale to enable visualization in the draft tube.

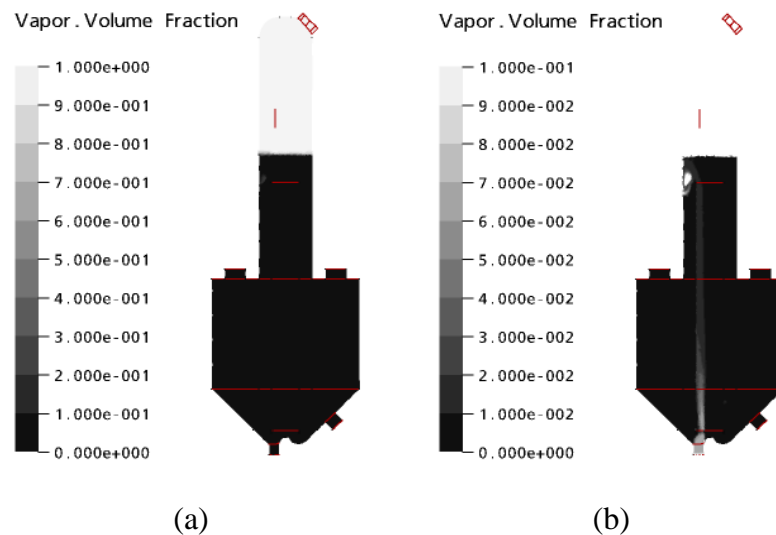


Figure 5.36 Contours of vapor volume fraction in the vertical center plane for fines removal flow of 1.0063 kg/s; (a) overall fraction; (b) magnified scale to enable visualization in the draft tube.

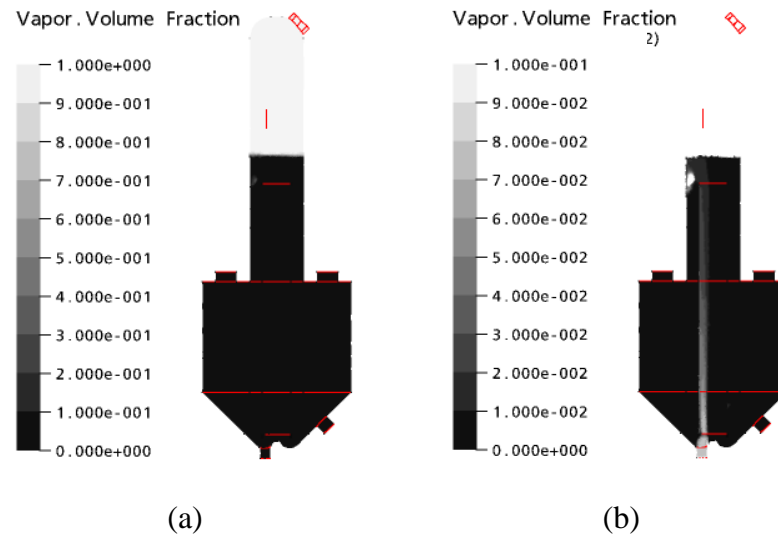


Figure 5.37 Contours of vapor volume fraction in the vertical center plane for fines removal flow of 1.5454 kg/s; (a) overall fraction; (b) magnified scale to enable visualization in the draft tube.

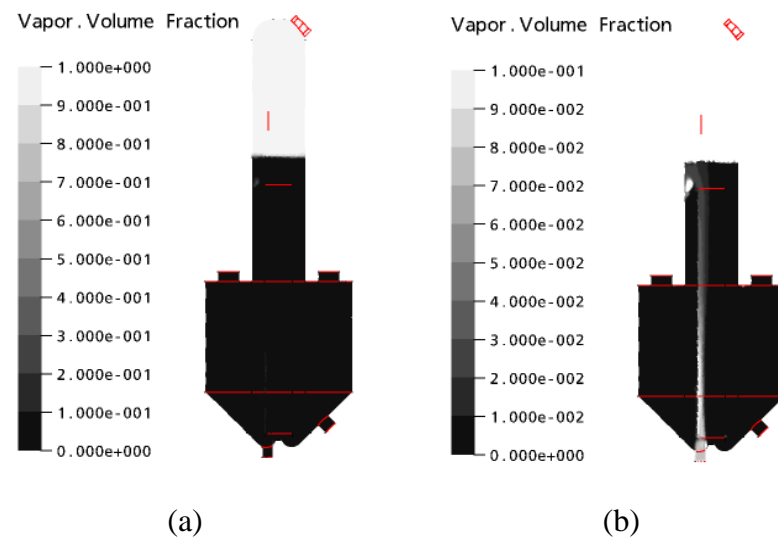


Figure 5.38 Contours of vapor volume fraction in the vertical center plane for fines removal flow of 2.3002 kg/s; (a) overall fraction; (b) magnified scale to enable visualization in the draft tube.

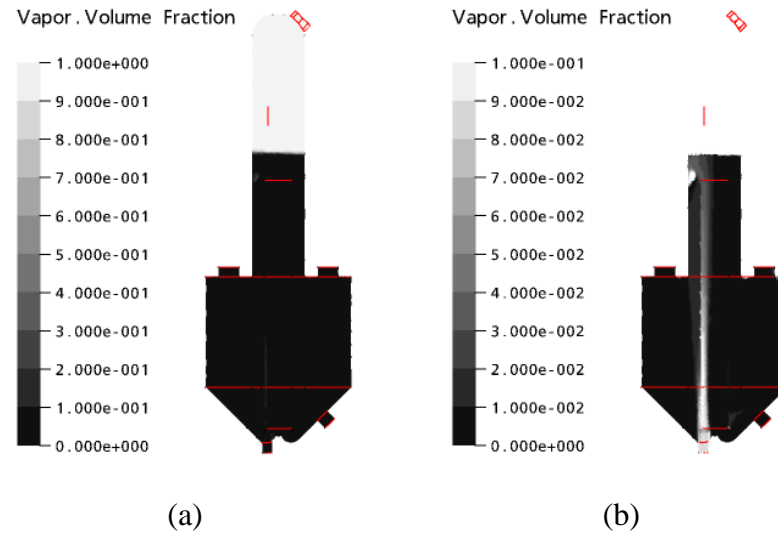


Figure 5.39 Contours of vapor volume fraction in the vertical center plane for fines removal flow of 3.594 kg/s; (a) overall fraction; (b) magnified scale to enable visualization in the draft tube.

Figures 5.40 to 5.44 show the overall velocity vectors, velocity contours, and 2D streamlines (from left to right) for both phases for the fines removal flows of 0.4672, 1.0063, 1.5454, 2.3002, and 3.594 kg/s. These figures indicate that for the cases of fines removal flows of 0.4672, 1.0063, 1.5454, and 2.3002 kg/s the flows of both liquid and vapor phase are the general flow field in the DTB crystallizer, which are described in a previous section. The flow features in 3D of these cases are shown in appendix D in Figures D.2 (a), (b), (c), and (d) for the liquid phase and Figures D.5 (a), (b), (c), and (d) for the vapor phase. For the case of 3.594 kg/s the flow fields are not the general flow fields in the DTB crystallizer (Figures 5.44, D.2 (e), and D.5 (e)) because the momentum source addition of $10,000 \text{ kg/m}^2/\text{s}^2$ is not enough to assist the

feed solution to flow into the draft tube (or is not enough to cancel the effect of the feed solution flow).

As the fines removal flow increases the liquid velocity slightly increases, both in the upflow section inside the draft tube, and in the downflow area in the annular space (outside the draft tube). For the vapor, the velocity increases if the fines removal flow increases from 2.3002 to 3.594 kg/s, but increases by a proportion that is less than the liquid velocity, and as the fines removal flow increases from 0.4672 to 1.5454 kg/s the velocity decreases a little. The overall vapor velocity contours and 2D streamlines are basically of the same feature without any drastic change in structure, which are the same as described previously.

In most fines removal case studies the liquid flow is not uniform, except the fines removal flow of 0.4672 kg/s (which is likely to be uniform flow). This is since at this fines removal flow the feed solution flow is very low so the momentum source addition ($10,000 \text{ kg/m}^2/\text{s}^2$) can completely cancel the effect of the feed flow, but at the higher fines removal flow the momentum source addition is not high enough to cancel this effect. The vorticity at the bottom of the settling zone, as described previous section, is found for all the case studies.

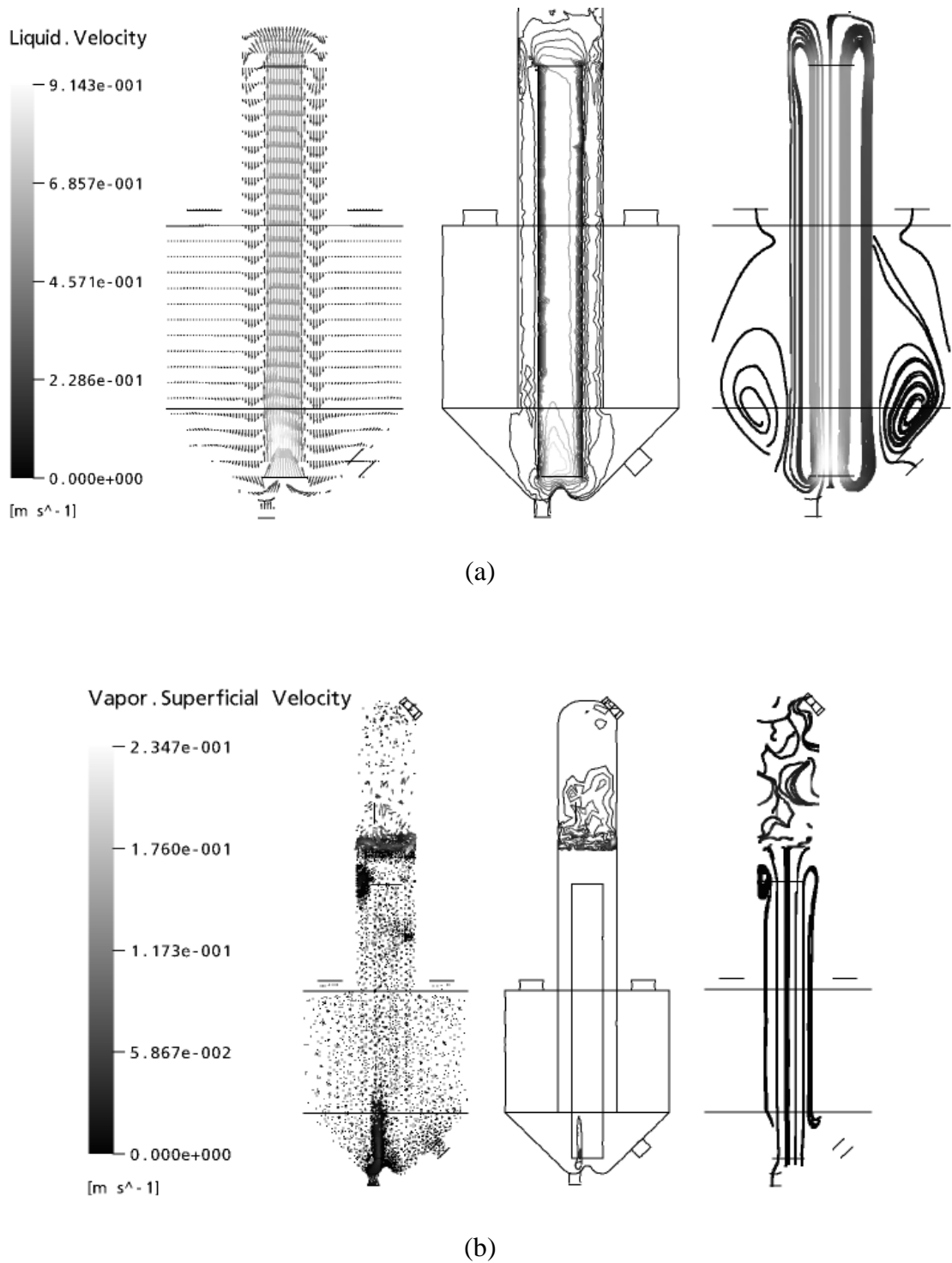
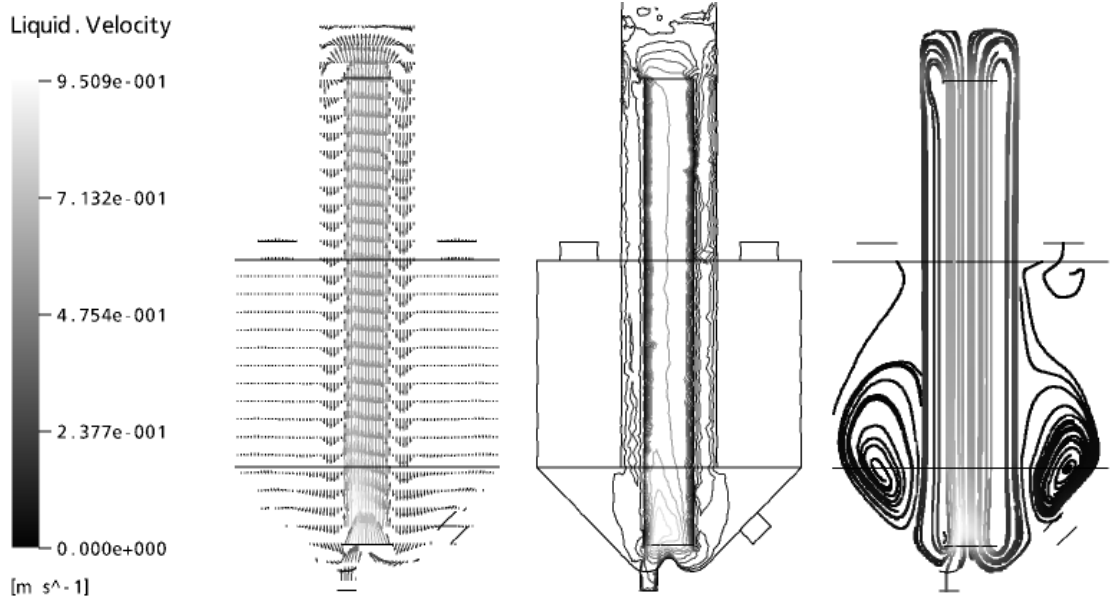
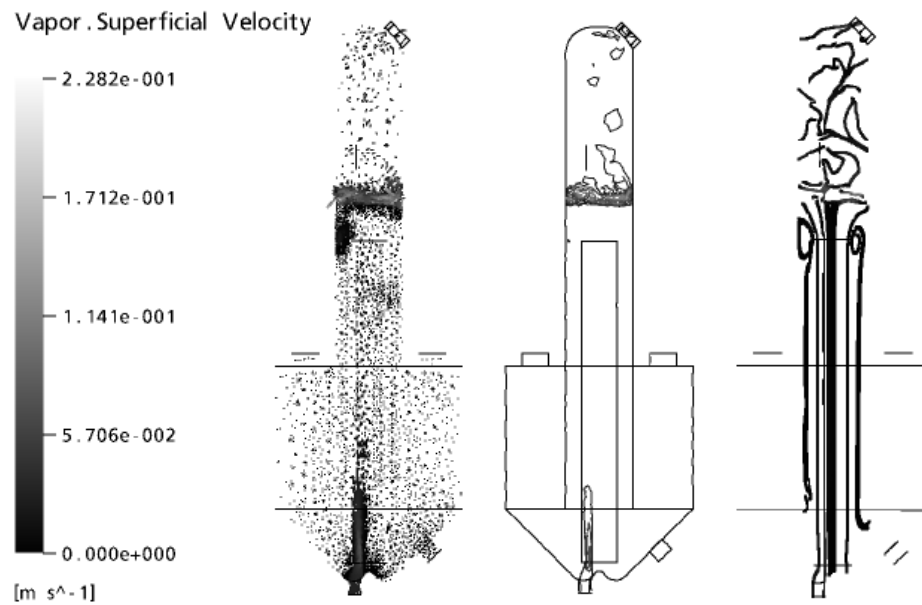


Figure 5.40 Velocity vectors, contours, and streamlines of liquid (a) and vapor (b) in the vertical center plane for fines removal flow of 0.4672 kg/s.

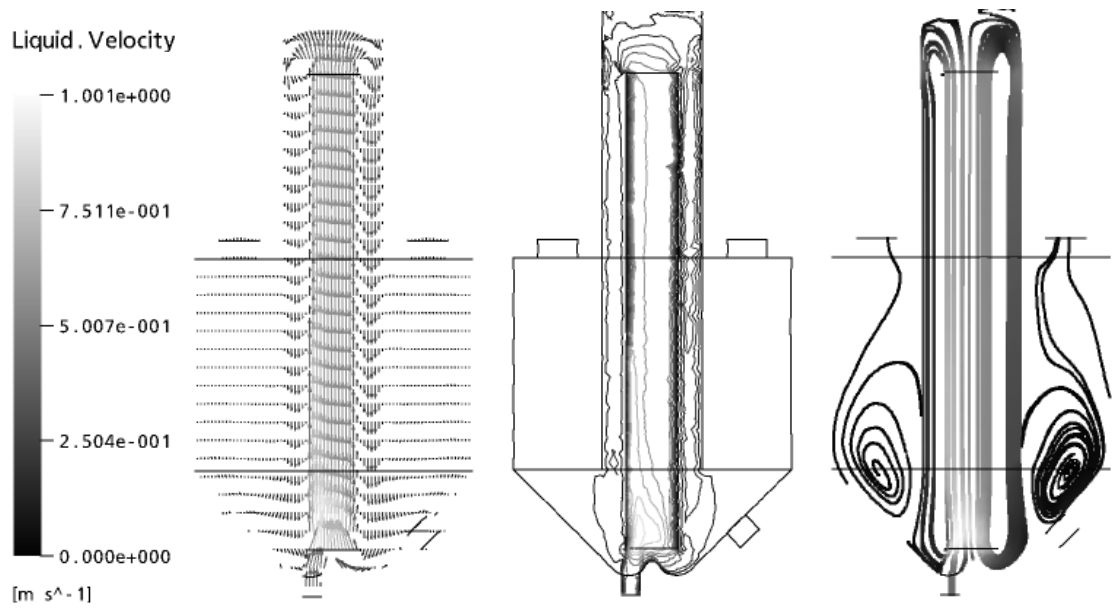


(a)

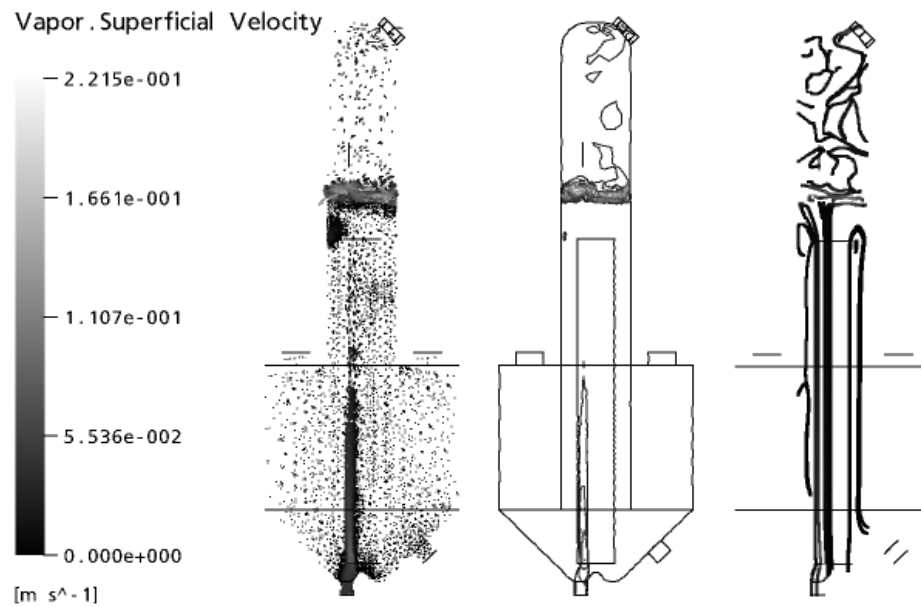


(b)

Figure 5.41 Velocity vectors, contours, and streamlines of liquid (a) and vapor (b) in the vertical center plane for fines removal flow of 1.0063 kg/s.



(a)



(b)

Figure 5.42 Velocity vectors, contours, and streamlines of liquid (a) and vapor (b) in the vertical center plane for fines removal flow of 1.5454 kg/s.

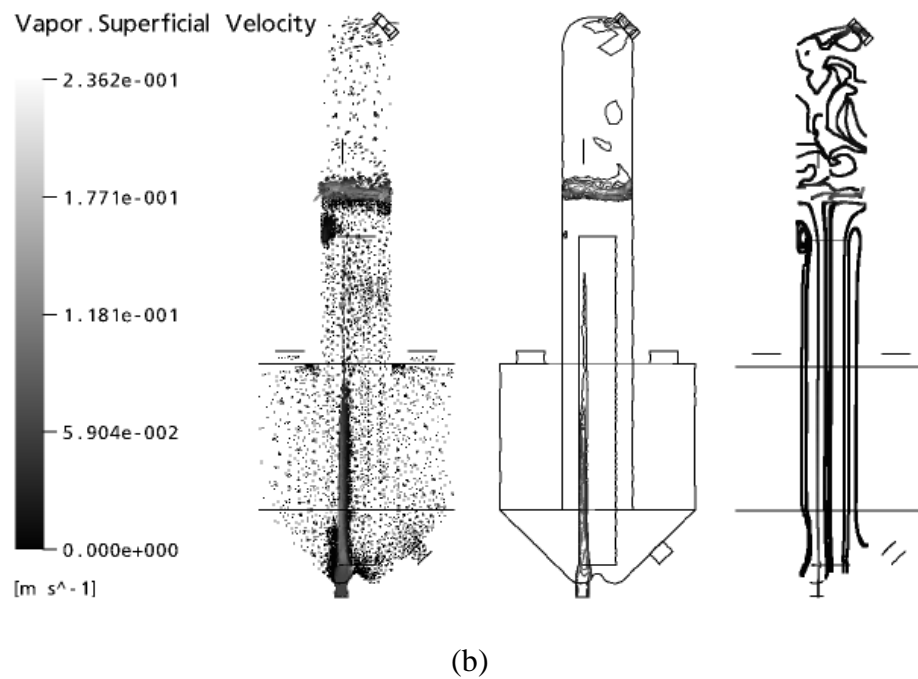
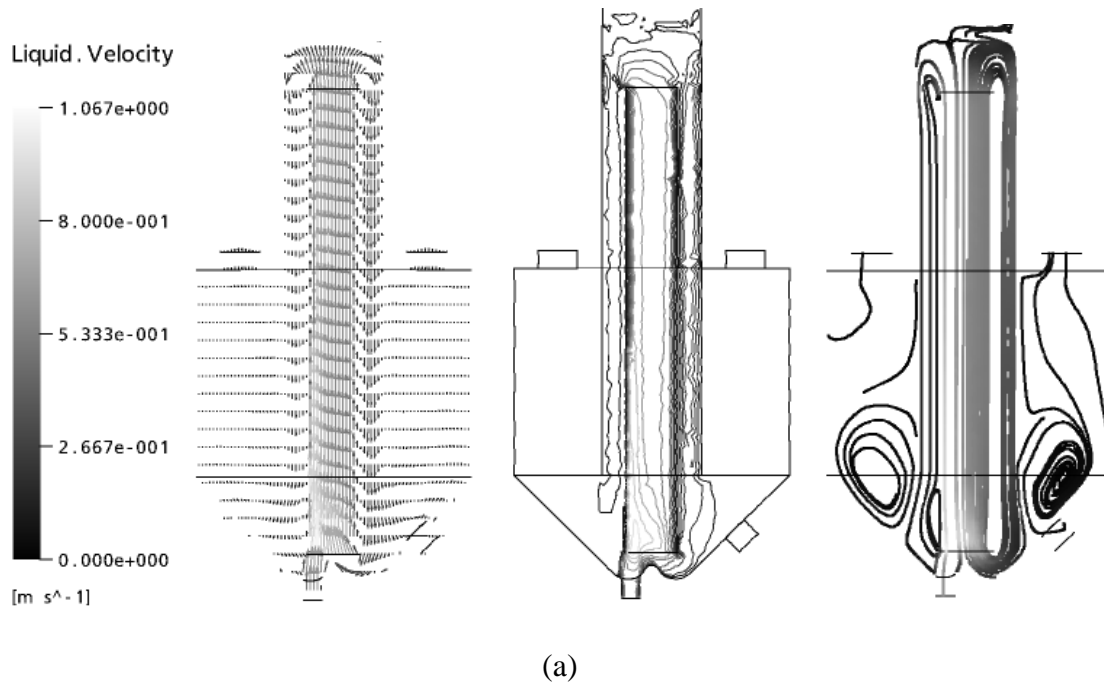


Figure 5.43 Velocity vectors, contours, and streamlines of liquid (a) and vapor (b) in the vertical center plane for fines removal flow of 2.3002 kg/s.

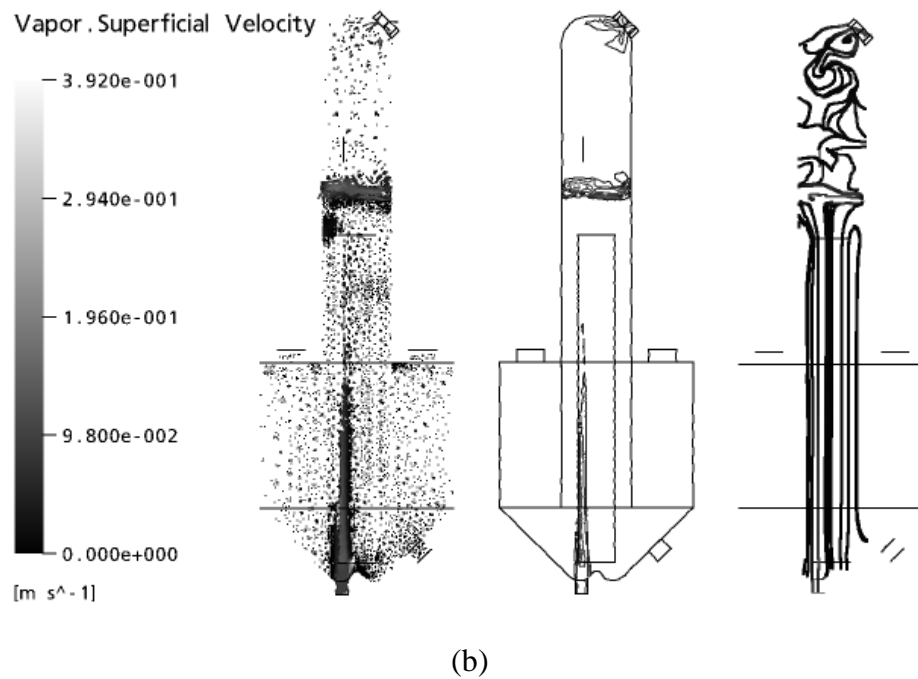
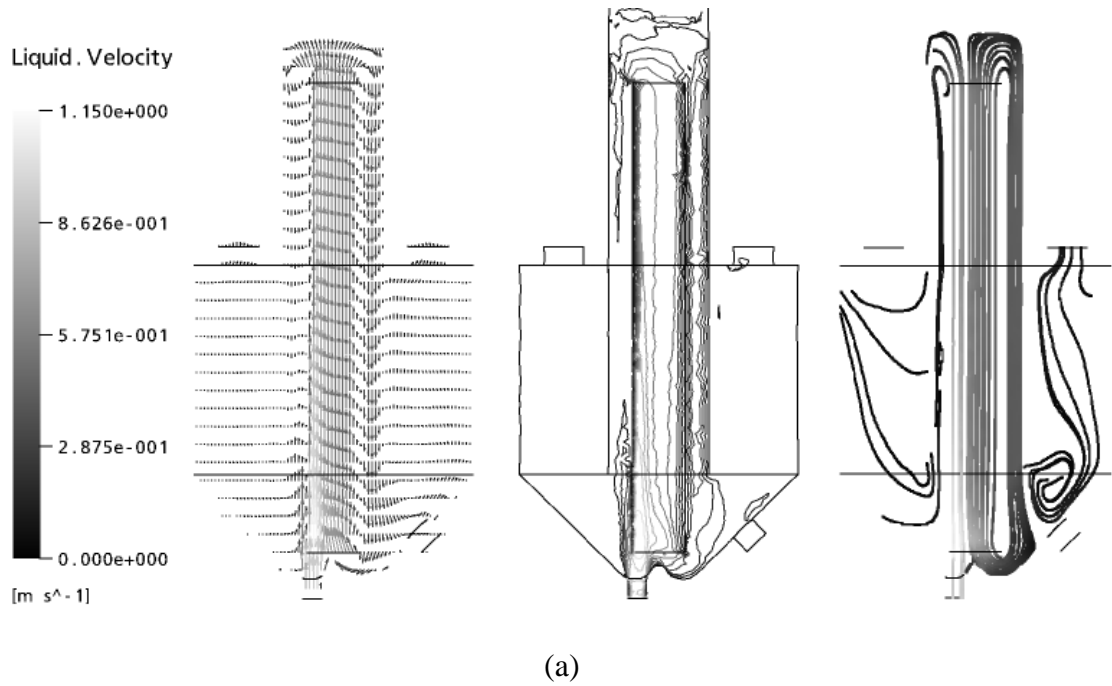


Figure 5.44 Velocity vectors, contours, and streamlines of liquid (a) and vapor (b) in the vertical center plane for fines removal flow of 3.594 kg/s.

Figure 5.45 represents the vapor velocity in the horizontal plane at the vapor-liquid interface. It shows that the height of the vapor-liquid interface does not change (it is constant at the initial height of 2.11 m) when the fines removal flow increases from 1.0063 to 3.594 kg/s (Figures 5.45 (b) to (e)), but at the lowest fines removal flow (0.4672 kg/s) the height of vapor-liquid interface will increase to a height of 2.128 m (Figure 5.45 (a)).

For the flow feature at the vapor-liquid interface, it is seen that at fines removal flows of 1.0063, 1.5454, 2.3002, and 3.594 kg/s, the vapor will be separated out from the liquid phase at the center continuing to the left side wall of the tank (in the direction of the feed location); this is shown in Figures 5.45 (b) to (e). This means that the momentum source value of $10,000 \text{ kg/m}^2/\text{s}^2$ is not enough to cancel the effect of the feed to the flow field in the DTB crystallizer. At the fines removal flow of 0.4672 kg/s (feed equals 0.6470 kg/s), most vapor will be separated out from the liquid phase at the center of the tank (Figure 5.45 (a)). This indicates that the momentum source value of $10,000 \text{ kg/m}^2/\text{s}^2$ completely cancels the effect of the feed solution flow of 0.6470 or lower to the flow field in the DTB crystallizer.

The liquid at the bottom of the tank tends to flow into the draft tube, which is similar to the previous description in section 5.1.1. This is found for all the fines removal case studies and means that there is no stagnation point at the bottom of the tank. The liquid velocity vectors at the bottom of the tank for fines removal flows of 0.4672, 1.0063, 1.5454, 2.3002, and 3.594 kg/s are shown in appendix D in Figure D.8.

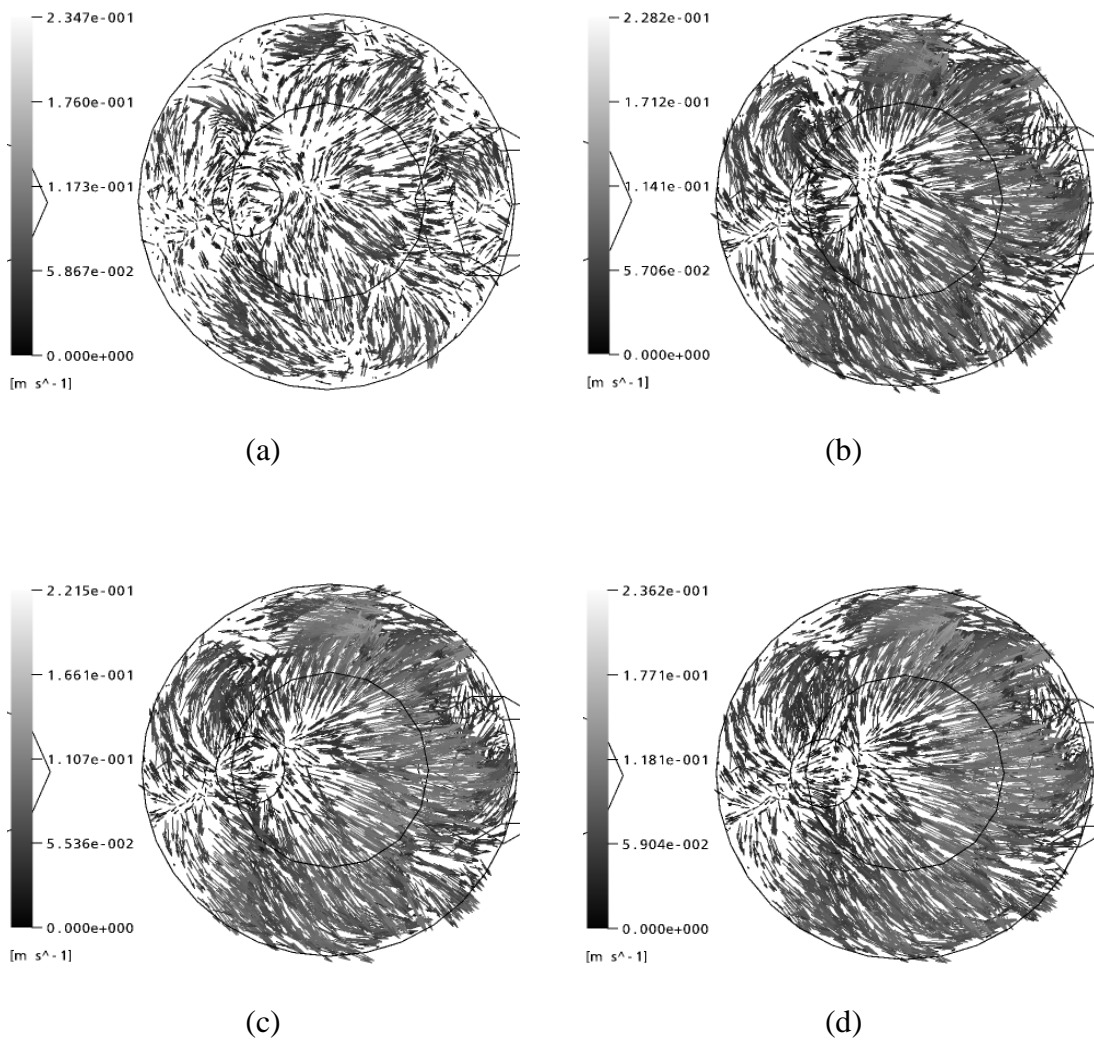


Figure 5.45 Vapor velocity vectors in the horizontal plane at the vapor-liquid interface for fines removal flows of (a) 0.4672 kg/s (at the height of 2.128 m); (b) 1.0063 kg/s (at the height of 2.11 m); (c) 1.5454 kg/s (at the height of 2.11 m); (d) 2.3002 kg/s (at the height of 2.11 m); *(continued)*

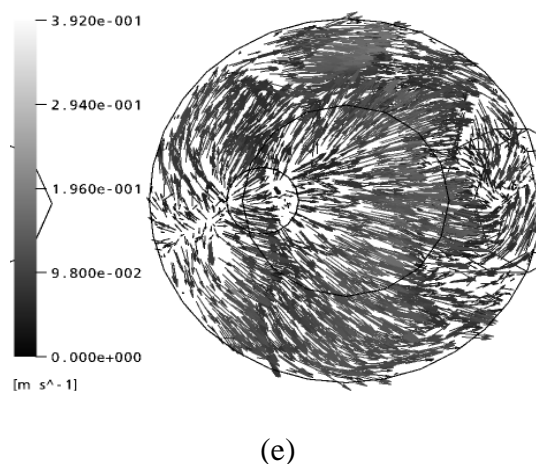


Figure 5.45 (*continued*) (e) 3.594 kg/s (at the height of 2.11 m).

Figure 5.46 represents the contours of the absolute pressure in the vertical center plane. It shows that, as in the section described previously, the lowest pressure is found at the top part of the tank and the pressure increases continuously when the height of the tank is lower until the maximum value is reached at the bottom of the tank. This is found for all the case studies. As the fines removal flow increases the overall magnitude of the pressure will change by only a very small amount. This is due to the force effect from the low values of momentum source addition ($10,000 \text{ kg/m}^2/\text{s}^2$) and all values of feed contribute an effect that is slightly less than the hydrostatic effect (weight of the liquid).

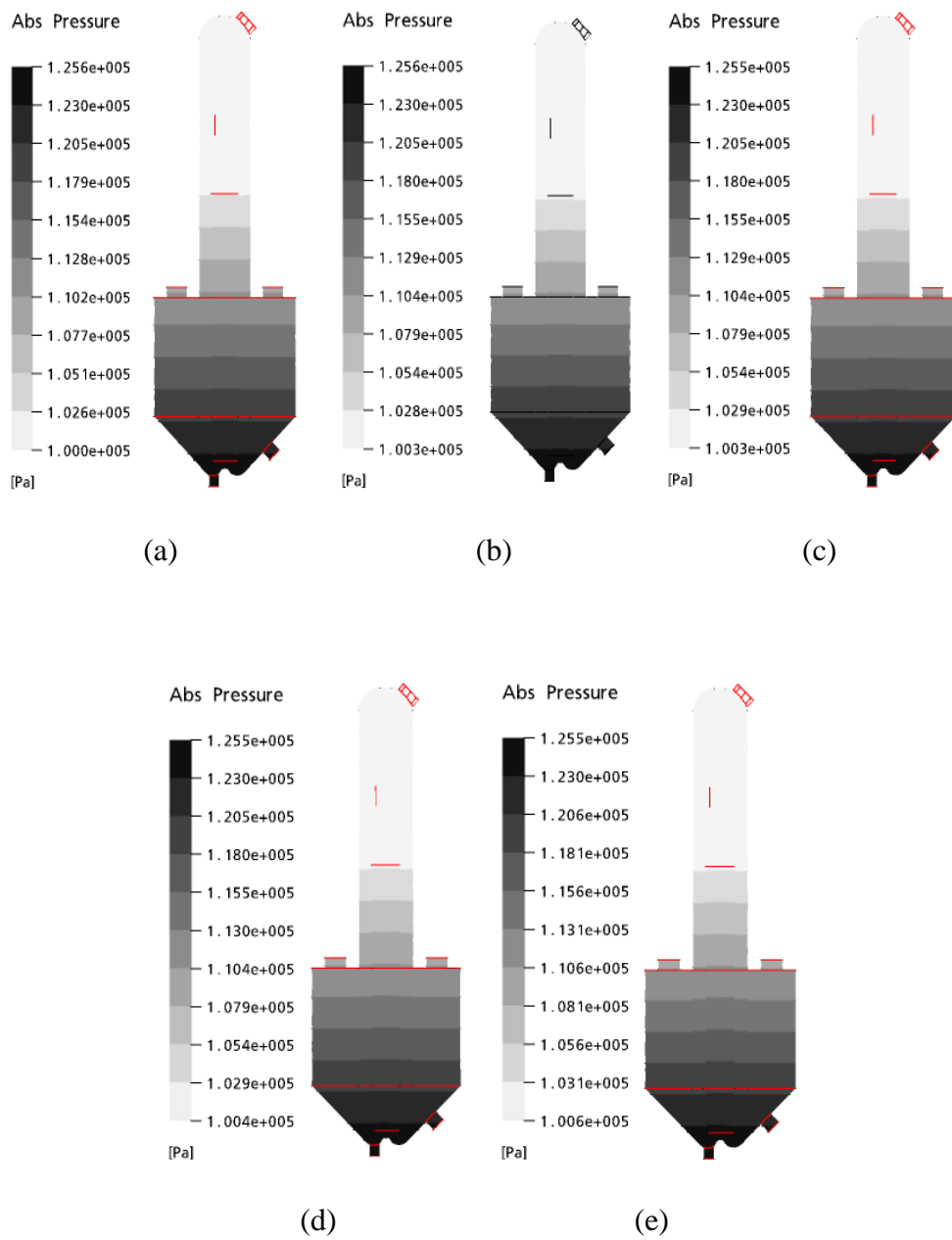


Figure 5.46 Contours of the absolute pressure in the vertical center plane for fines removal flows of (a) 0.4672 kg/s; (b) 1.0063 kg/s; (c) 1.5454 kg/s; (d) 2.3002 kg/s; (e) 3.594 kg/s.

As described previously, the terminal velocity increases approximately linearly with increasing particle size. This is confirmed again in Figure 5.47 (this figure is the result of the fines removal flow effect). Figures 5.31 and 5.47 show the linear equations are the same and R-square approaches unity; this means that the regression approaches a perfect fit. Note that it is necessary to consider this fit again in the next section (effect of product crystal suspension flow) to find the best linear equation for the relationship between particle size and terminal velocity. Figure 5.48 shows that as the fines removal flow increases (this is equivalent to increasing the feed solution flow because the product flow is held constant) the terminal velocity increases. This indicates that the fines removal cut-size increases with increasing fines removal flow too, because the terminal velocity increases linearly with increasing particle size. This indicates the mean product crystal size increases with increasing fines removal flow. Moreover in Figure 5.48, the particle Reynolds number increases with increasing fines removal flow, and all values of the Reynolds number are in the range of 0.2 to 500, which indicates the particle flow is in the transition regime.

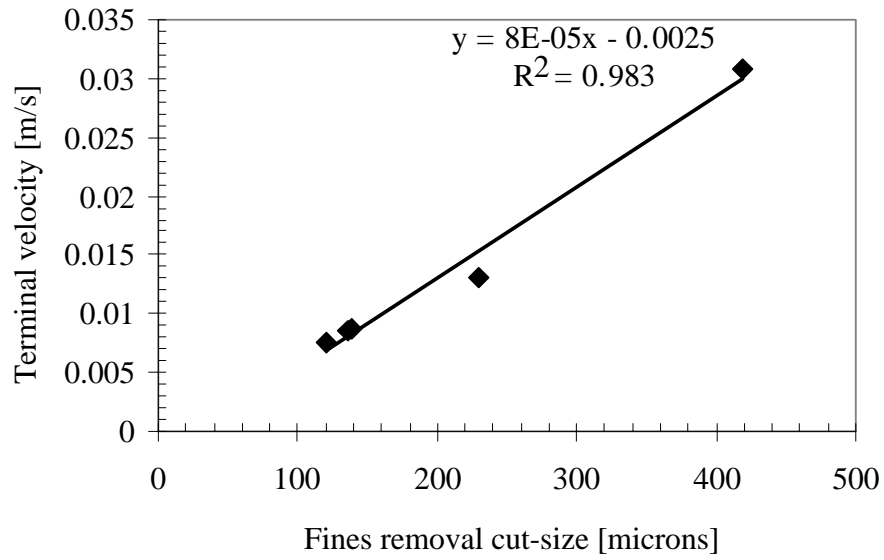


Figure 5.47 Terminal velocity for case studies 9 to 13 as a function of fines removal cut-size.

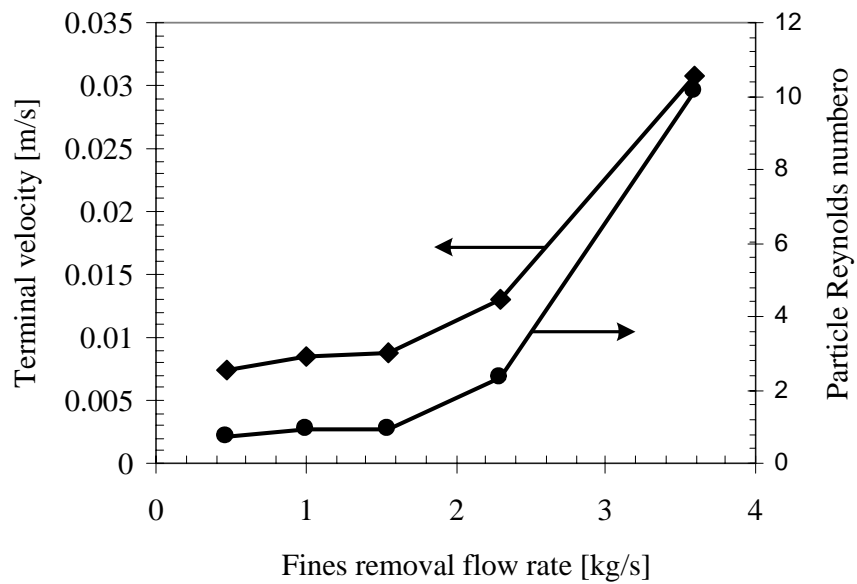


Figure 5.48 Terminal velocity and particle Reynolds number for case studies 9 to 13 as a function of fines removal flow.

5.1.4 Effect of the product crystal suspension flow rate

In this section, five test cases are performed, using a constant momentum source addition of $10,000 \text{ kg/m}^2/\text{s}^2$, a constant fines removal flow of 1.0063 kg/s and feed solution flow of approximately 1 kg/s , with the product crystal suspension flow varied at 0.0599 , 0.1198 , 0.1797 , 0.2636 , and 0.4672 kg/s , as shown in case studies 14 to 18 of Table 4.1 in chapter 4. The results showed that all values of the Reynolds number indicate that the flow inside and outside of the draft tube are turbulent flow, and the flow in the settling zone is transition flow (Figures 5.49 and 5.50). Moreover, increasing product crystal suspension flow has no effect (or only a very small effect) on the bubble Reynolds number (Figure 5.49), liquid Reynolds numbers inside and outside the draft tube, and in the settling zone (Figure 5.50).

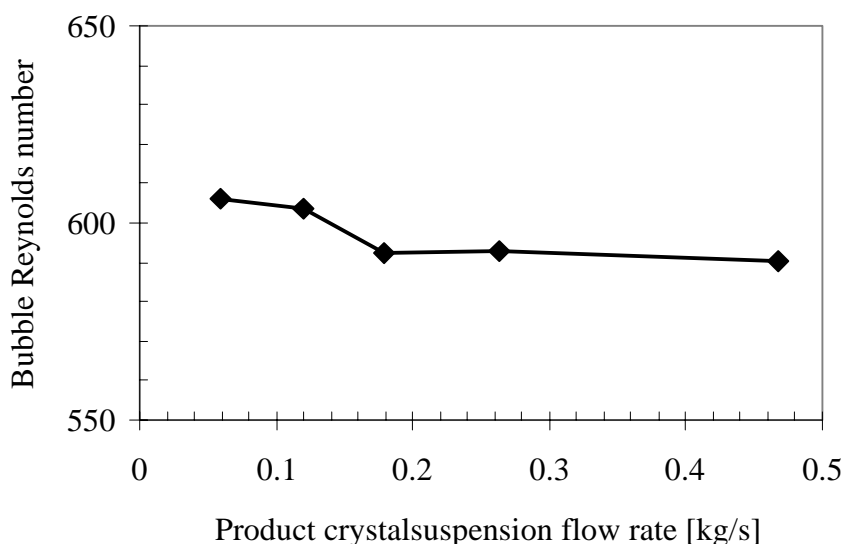


Figure 5.49 Bubble Reynolds number inside the draft tube for case studies 14 to 18 as a function of product crystal suspension flow rate.

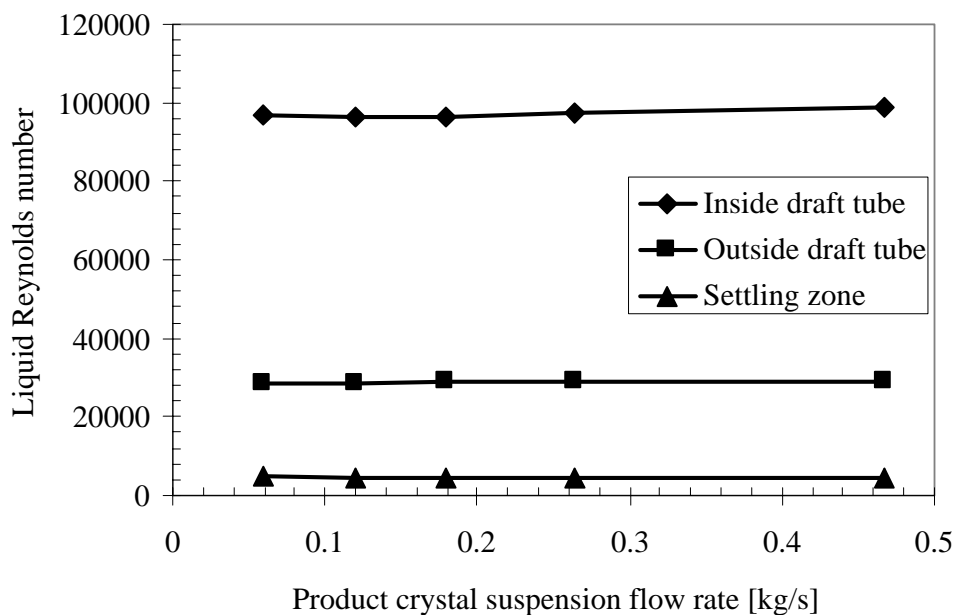


Figure 5.50 Liquid Reynolds number inside and outside the draft tube, and in the settling zone for case studies 14 to 18 as a function of product crystal suspension flow rate.

The overall contours of vapor volume fractions for the effect of the product crystal suspension flow case studies are similar to the previous section (Figures 5.51 (a), 5.52 (a), 5.53 (a), 5.54 (a), and 5.55 (a)), except the volume fraction of vapor in the draft tube increases with increasing product crystal suspension flow (Figures 5.51 (b), 5.52 (b), 5.53 (b), 5.54 (b), and 5.55 (b)). This is because increasing the product crystal suspension flow is equivalent to increasing the feed solution flow (because constant fines removal flow is assumed) resulting in an increased amount of vapor in the feed solution. As described previously, small amounts of the vapor will turn over the top of the draft tube and flow down (i.e. will not be separated out). This is found in the product crystal suspension flow case studies too.

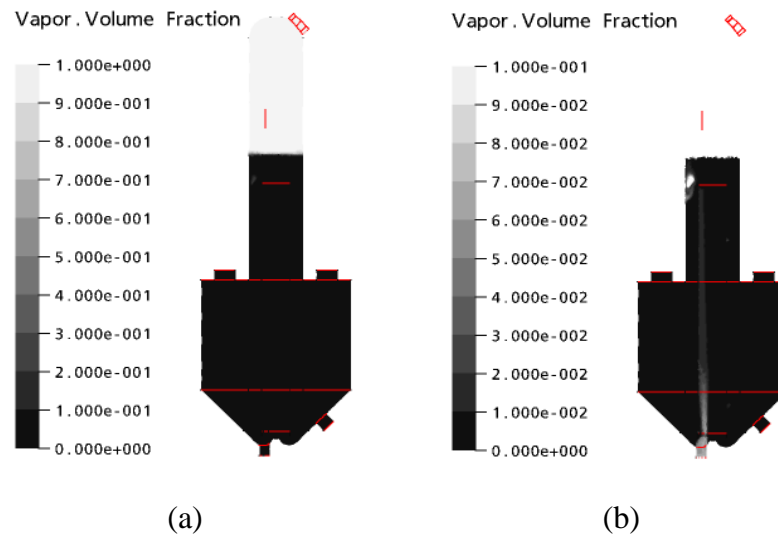


Figure 5.51 Contours of vapor volume fraction in the vertical center plane for product crystal suspension flow of 0.0599 kg/s; (a) overall fraction; (b) magnified scale to enable visualization in the draft tube.

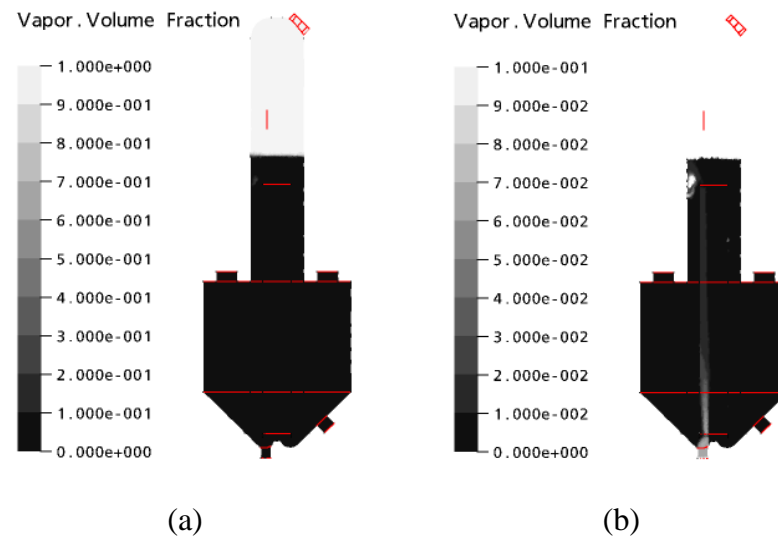


Figure 5.52 Contours of vapor volume fraction in the vertical center plane for product crystal suspension flow of 0.1198 kg/s; (a) overall fraction; (b) magnified scale to enable visualization in the draft tube.

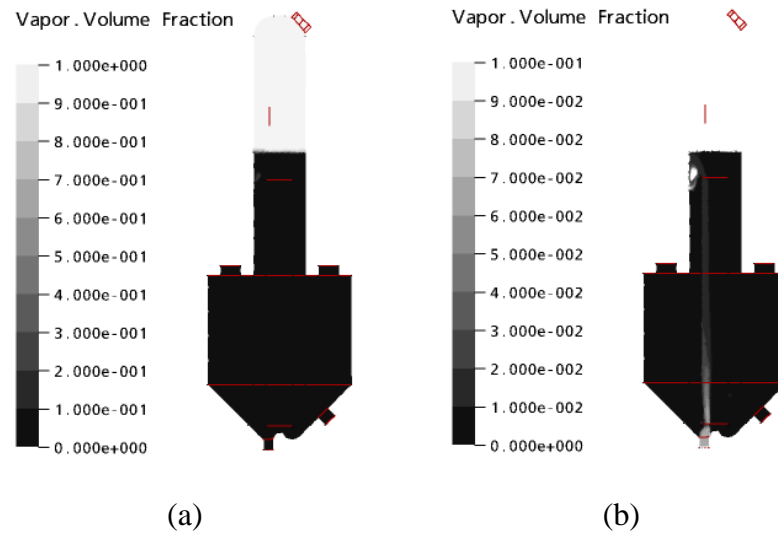


Figure 5.53 Contours of vapor volume fraction in the vertical center plane for product crystal suspension flow of 0.1797 kg/s; (a) overall fraction; (b) magnified scale to enable visualization in the draft tube.

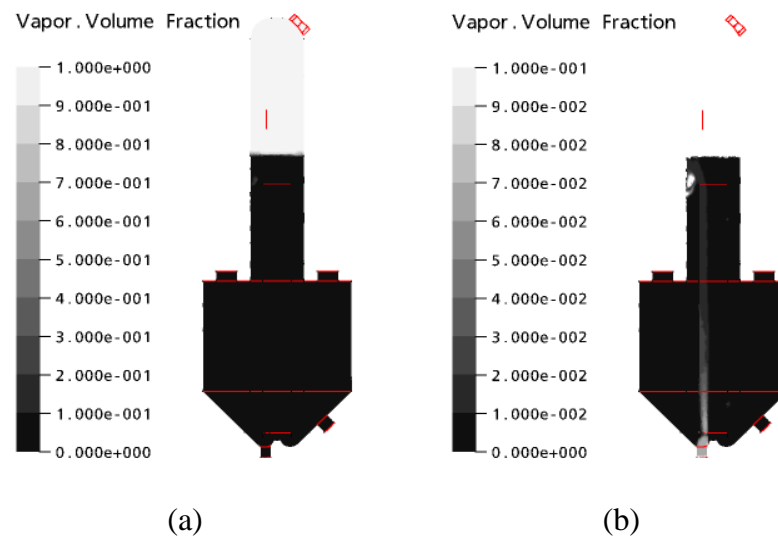


Figure 5.54 Contours of vapor volume fraction in the vertical center plane for product crystal suspension flow of 0.2636 kg/s; (a) overall fraction; (b) magnified scale to enable visualization in the draft tube.

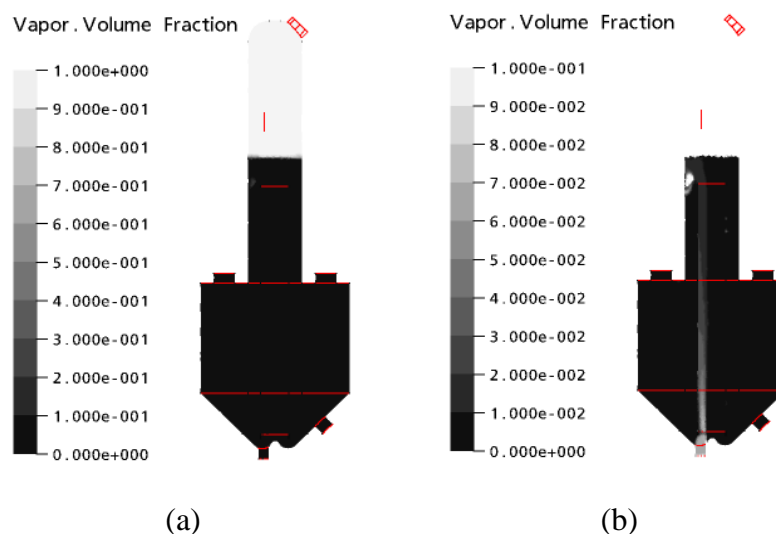


Figure 5.55 Contours of vapor volume fraction in the vertical center plane for product crystal suspension flow of 0.4672 kg/s; (a) overall fraction; (b) magnified scale to enable visualization in the draft tube.

Figures 5.56 to 5.60 show the overall velocity vectors, velocity contours, and 2D streamlines (from left to right) for both phases, for product crystal suspension flows of 0.0599, 0.1198, 0.1797, 0.2636, and 0.4672 kg/s. These figures indicate that for all values of the product crystal suspension flow, the flows of both the liquid and vapor phases are the general flow fields in the DTB crystallizer, which are described in previous sections. The flow features in 3D of these cases are shown in appendix D in Figure D.3 for the liquid phase and Figure D.6 for the vapor phase.

As the product crystal suspension flow increases the liquid velocity slightly increases but this only slightly influences the overall flow pattern. This is true for both the upflow section inside the draft tube, and the downflow area in the annular space (outside the draft tube). For the vapor, the product crystal suspension flow only

slightly influences the vapor velocity and overall flow pattern. The overall vapor velocity contours and 2D streamlines have essentially the same features without any drastic change in structure, similar to that described previously.

For all product crystal suspension flow case studies the liquid flow is not uniform. The vorticity at the bottom of the settling zone, as described previous section, is found for all the case studies.

Figure 5.61 represents the vapor velocity in the horizontal plane at the height of 2.11 m, which is the initial height of the vapor-liquid interface. It shows that the height of the vapor-liquid interface does not change (constant at the height of 2.11 m) as the product crystal suspension flow increases from 0.0599 to 0.46722 kg/s (Figures 5.61 (a) to (e)).

For the flow features at the vapor-liquid interface, it is seen that for all the product crystal suspension flow rates the vapor will be separated out from the liquid phase at the center continuing to the left side wall of the tank (in the direction of the feed location); this is investigated by the Figures 5.61 (a) to (e). This means that momentum source values less than $10,000 \text{ kg/m}^2/\text{s}^2$ are not enough to cancel the effect of the feed (approximately 1 kg/s) on the flow fields in the DTB crystallizer.

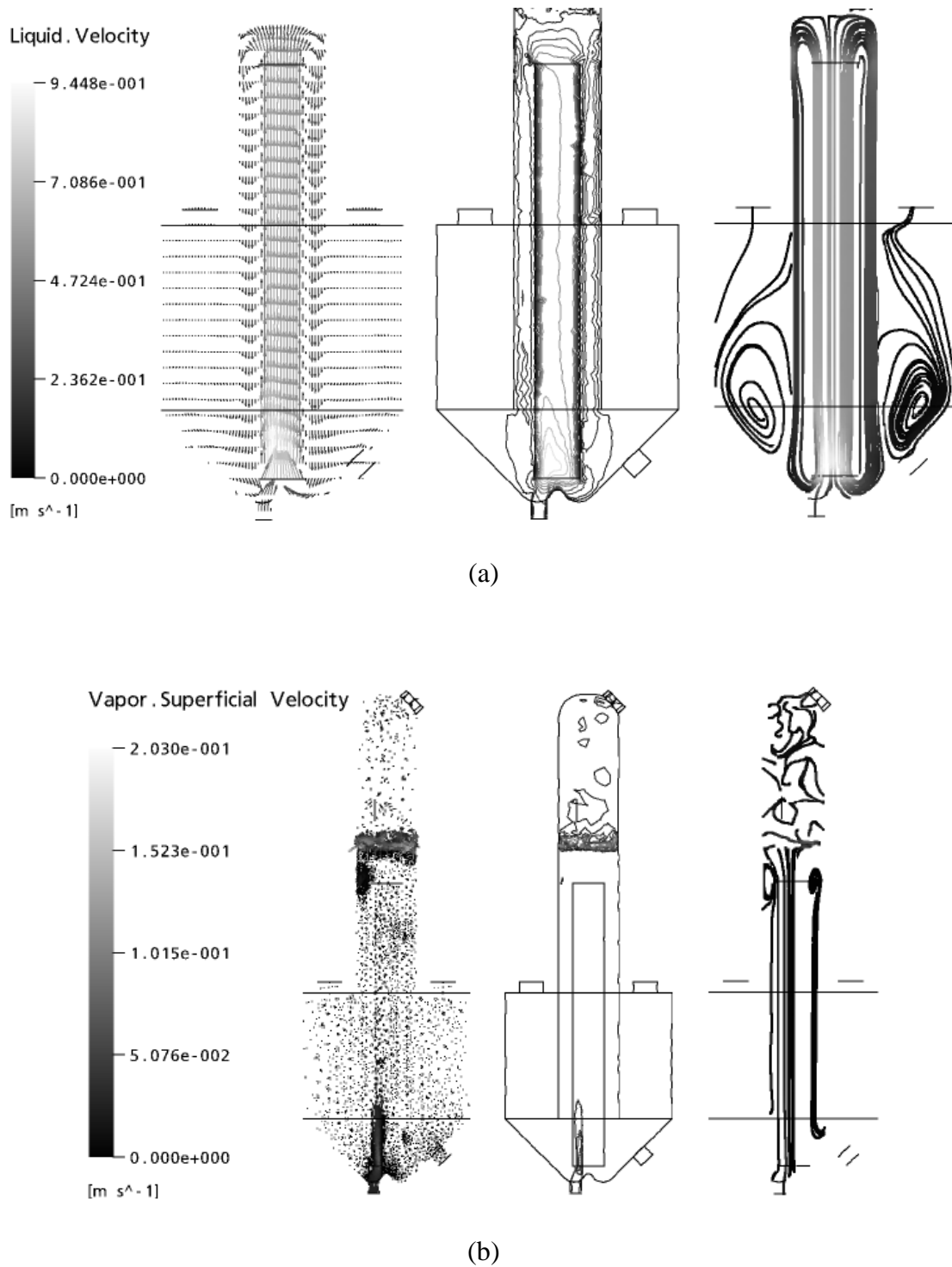
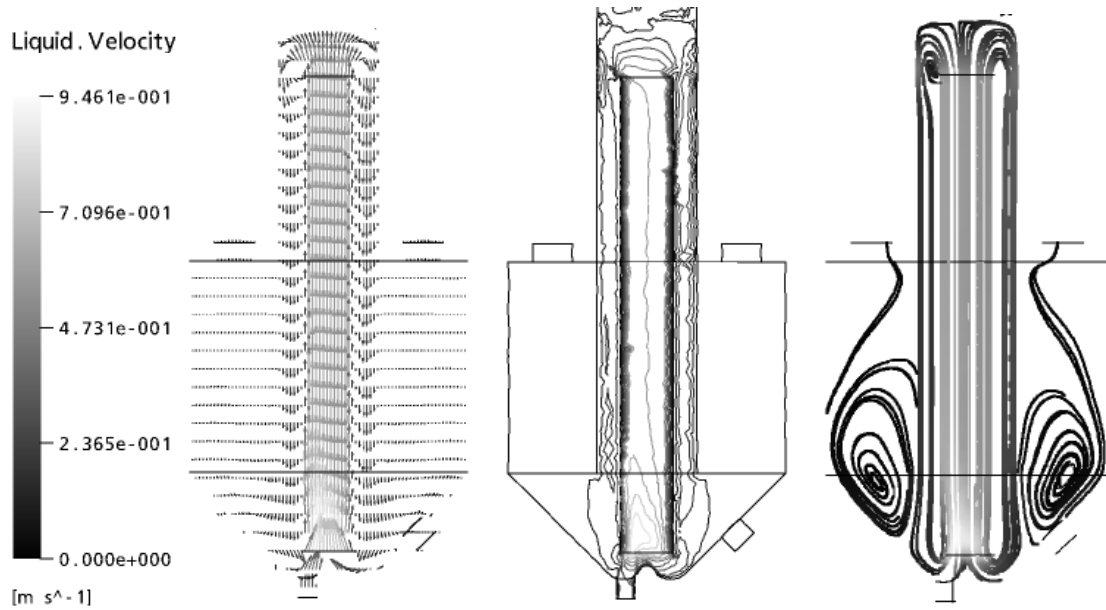
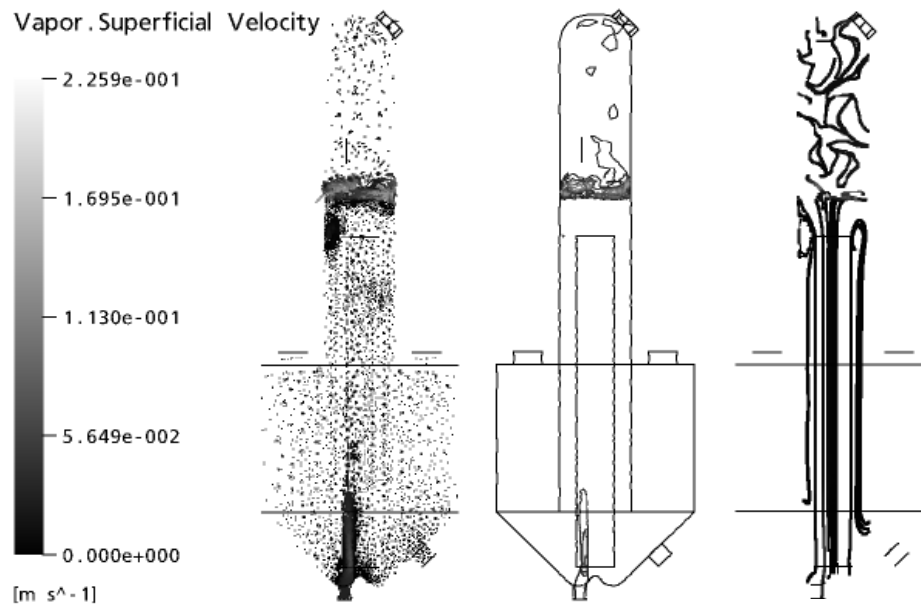


Figure 5.56 Velocity vectors, contours, and streamlines of liquid (a) and vapor (b) in the vertical center plane for product crystal suspension flow of 0.0599 kg/s.



(a)



(b)

Figure 5.57 Velocity vectors, contours, and streamlines of liquid (a) and vapor (b) in the vertical center plane for product crystal suspension flow of 0.1198 kg/s.

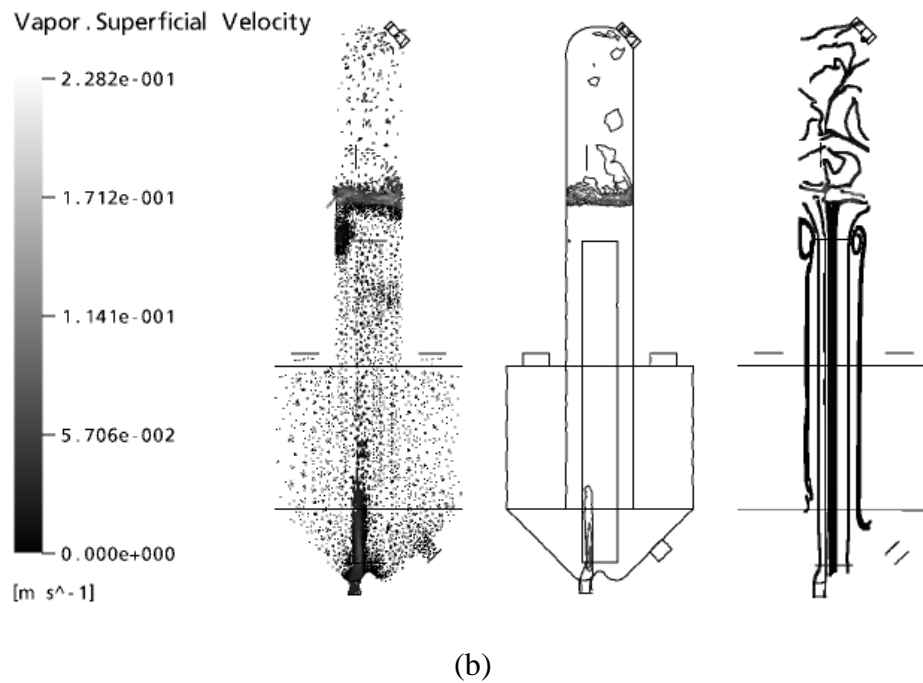
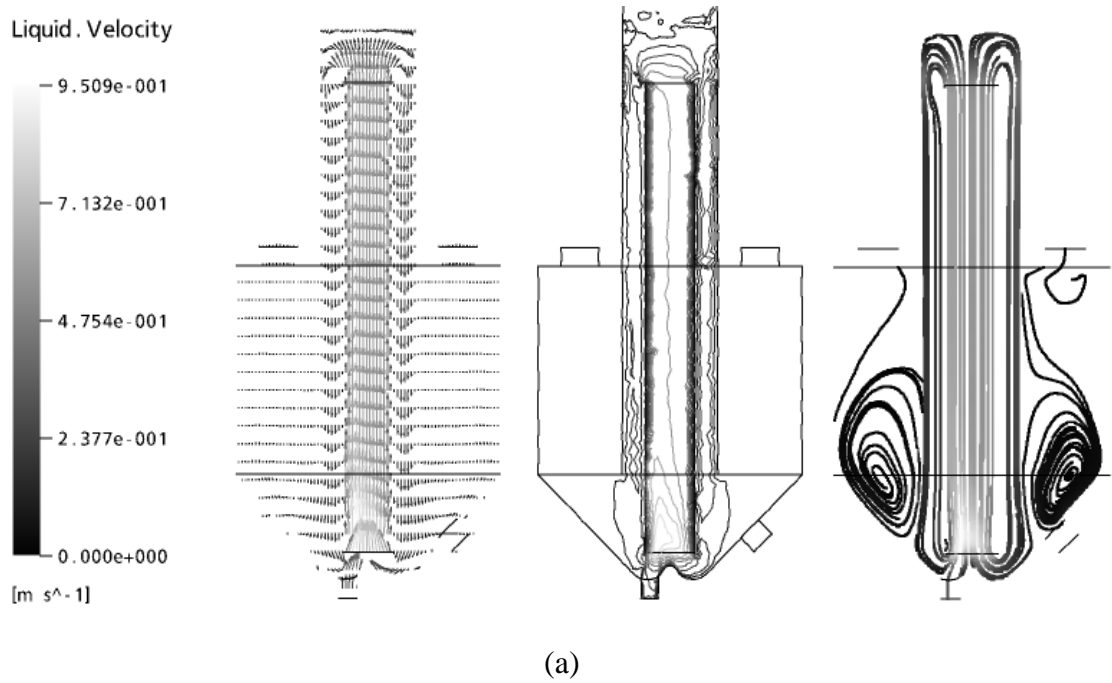


Figure 5.58 Velocity vectors, contours, and streamlines of liquid (a) and vapor (b) in the vertical center plane for product crystal suspension flow of 0.1797 kg/s.

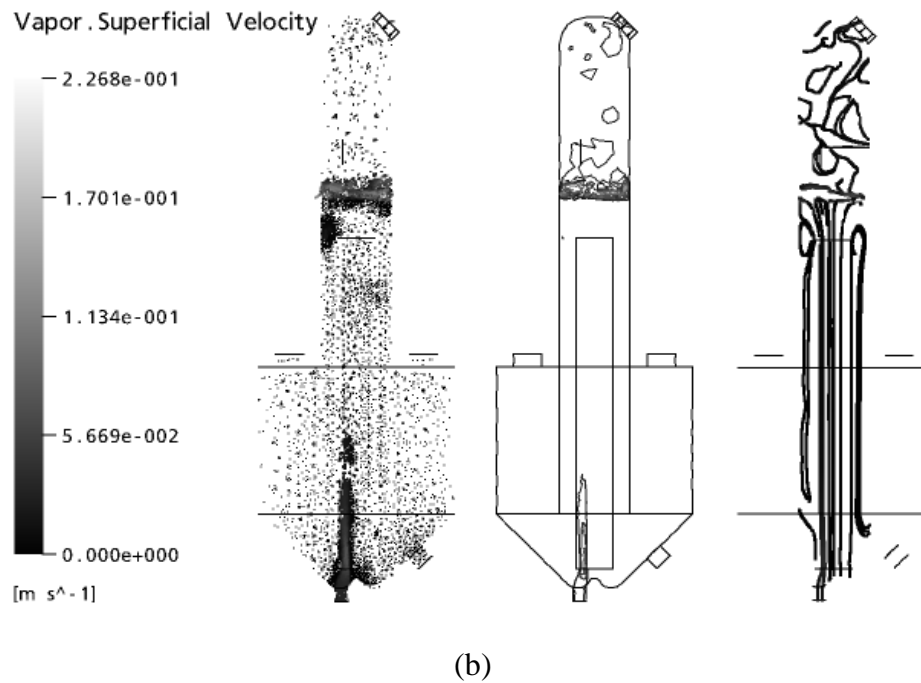
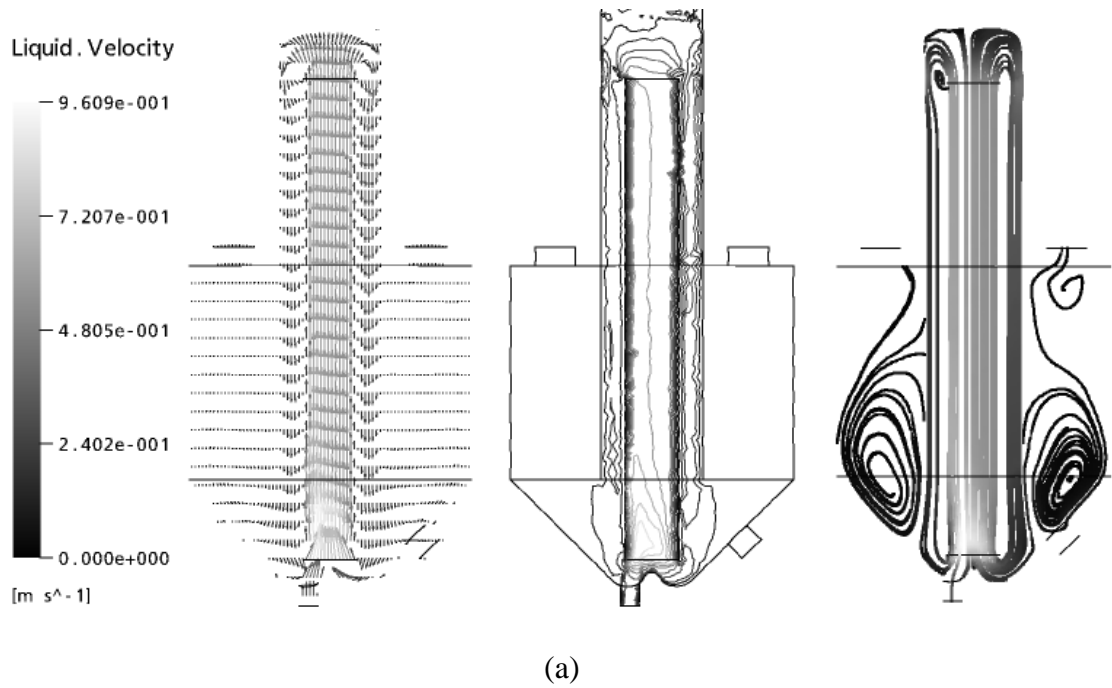


Figure 5.59 Velocity vectors, contours, and streamlines of liquid (a) and vapor (b) in the vertical center plane for product crystal suspension flow of 0.2636 kg/s.

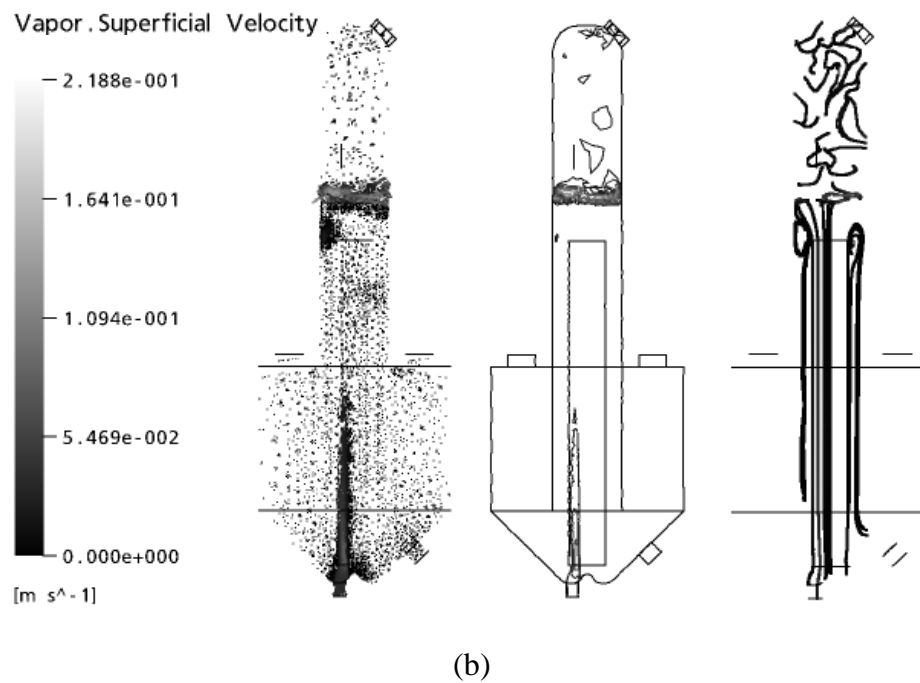
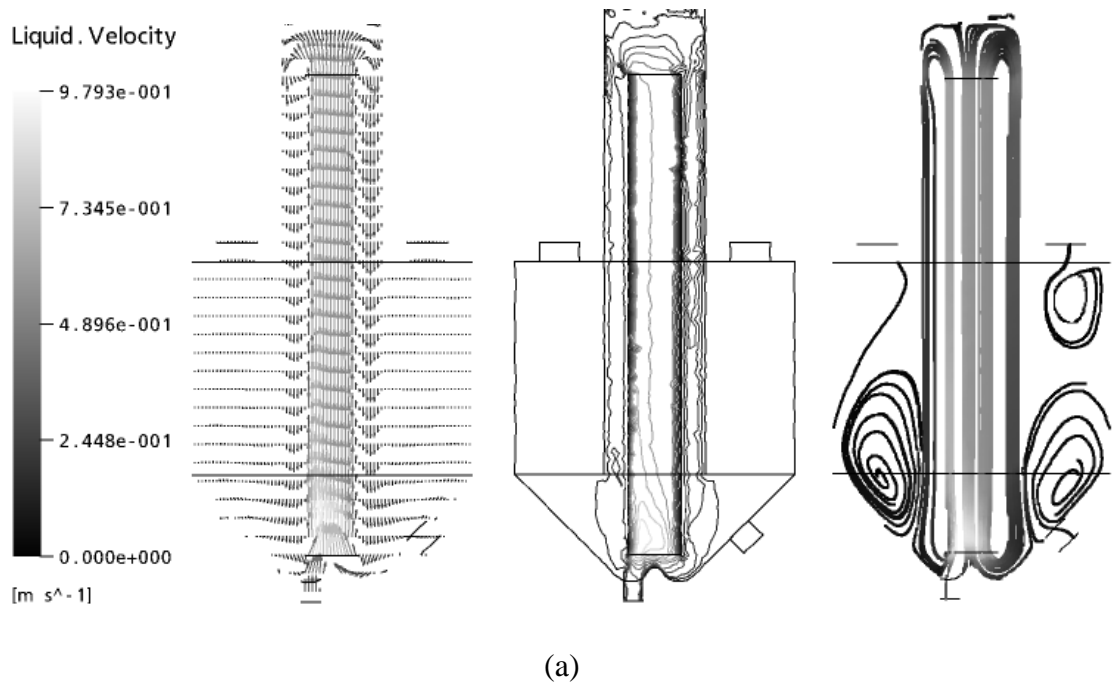


Figure 5.60 Velocity vectors, contours, and streamlines of liquid (a) and vapor (b) in the vertical center plane for product crystal suspension flow of 0.4672 kg/s.

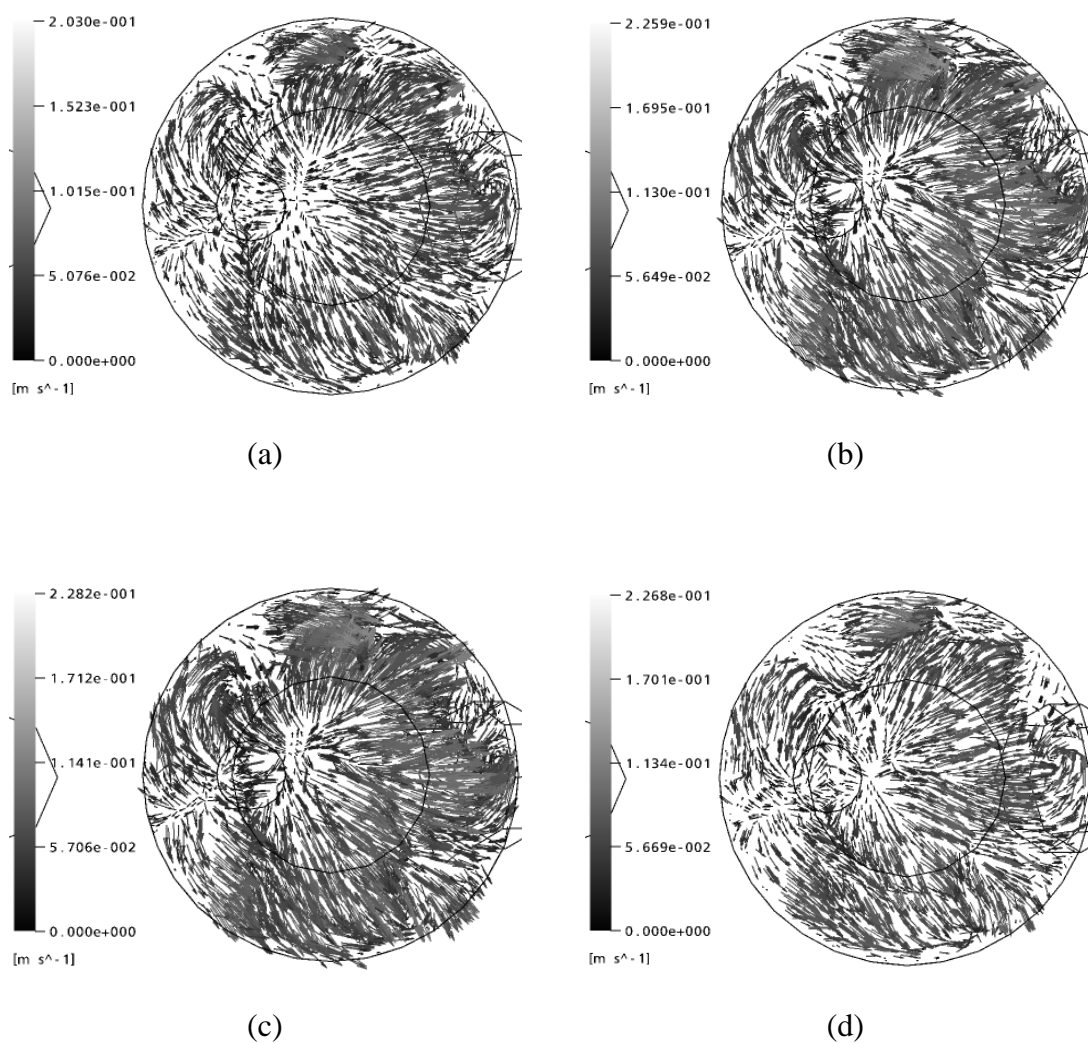


Figure 5.61 Vapor velocity vectors in the horizontal plane at the height of 2.11 m (initial height of vapor-liquid interface) for product crystal suspension flows of (a) 0.0599 kg/s; (b) 0.1198 kg/s; (c) 0.1797 kg/s; (d) 0.2636; (continued)

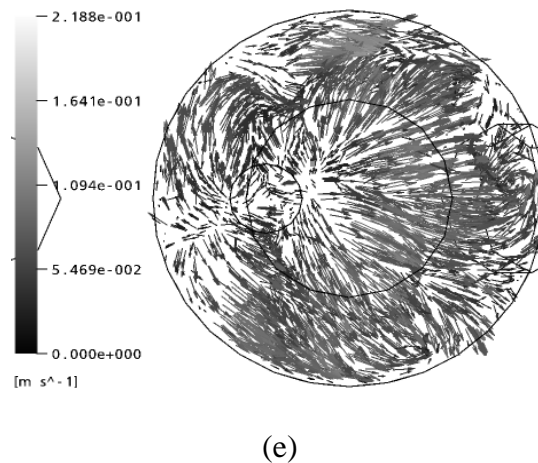


Figure 5.61 (*continued*) (e) 0.4672 kg/s.

The liquid at the bottom of the tank tends to flow into the draft tube, which is similar to the previous description in section 5.1.1. This is found for all the product crystal suspension flow case studies and means that there is no stagnation point at the bottom of the tank. The liquid velocity vectors at the bottom of the tank for product crystal suspension flows of 0.0599, 0.1198, 0.1797, 0.2636, and 0.4672 kg/s are shown in appendix D in Figure D.9.

Figure 5.62 represents the contours of the absolute pressure in the vertical center plane. It shows that, as described in previous sections, the lowest pressure was found at the top part of the tank and the pressure increases continuously when the height of the tank is lower until reached the maximum value at the bottom of the tank. This is found for all the case studies. As the product crystal suspension flow increases the overall magnitude of the pressure will change only by a small amount. This is since the force effect from the low values of momentum source addition

(10,000 kg/m²/s²) and approximately 1 kg/s of feed is slightly less than the hydrostatic effect (weight of the liquid).

As described previously, the particle terminal velocity increases approximately linearly with increasing particle size. It is confirmed again by Figure 5.63 (this figure is the result of the product crystal suspension flow effect). Figures 5.31 and 5.47 show the same linear equation and the R-square approaches unity for both lines; Figure 5.63 shows the R-square is unity, but the linear equation is not the same as in Figures 5.31 and 5.47. The best fit linear equation for the relationship between particle size and terminal velocity should be the linear equation of Figures 5.31 and 5.47 because they are the same equation, but give approximately 14.3 % error in the slope compared to the slope of Figure 5.63. Figure 5.64 shows that as the product crystal suspension flow increases the terminal velocity decreases. This indicates that the fines removal cut-size decreases with increasing product flow because the terminal velocity increases linearly with increasing particle size. This means the mean product crystals size decreases with increasing product crystal suspension flow. Moreover in Figure 5.64, the particle Reynolds number decreases with increasing product crystal suspension flow, and all of the values of the Reynolds number are in the range of 0.2 to 500, which indicates the particle flow is in the transition regime.

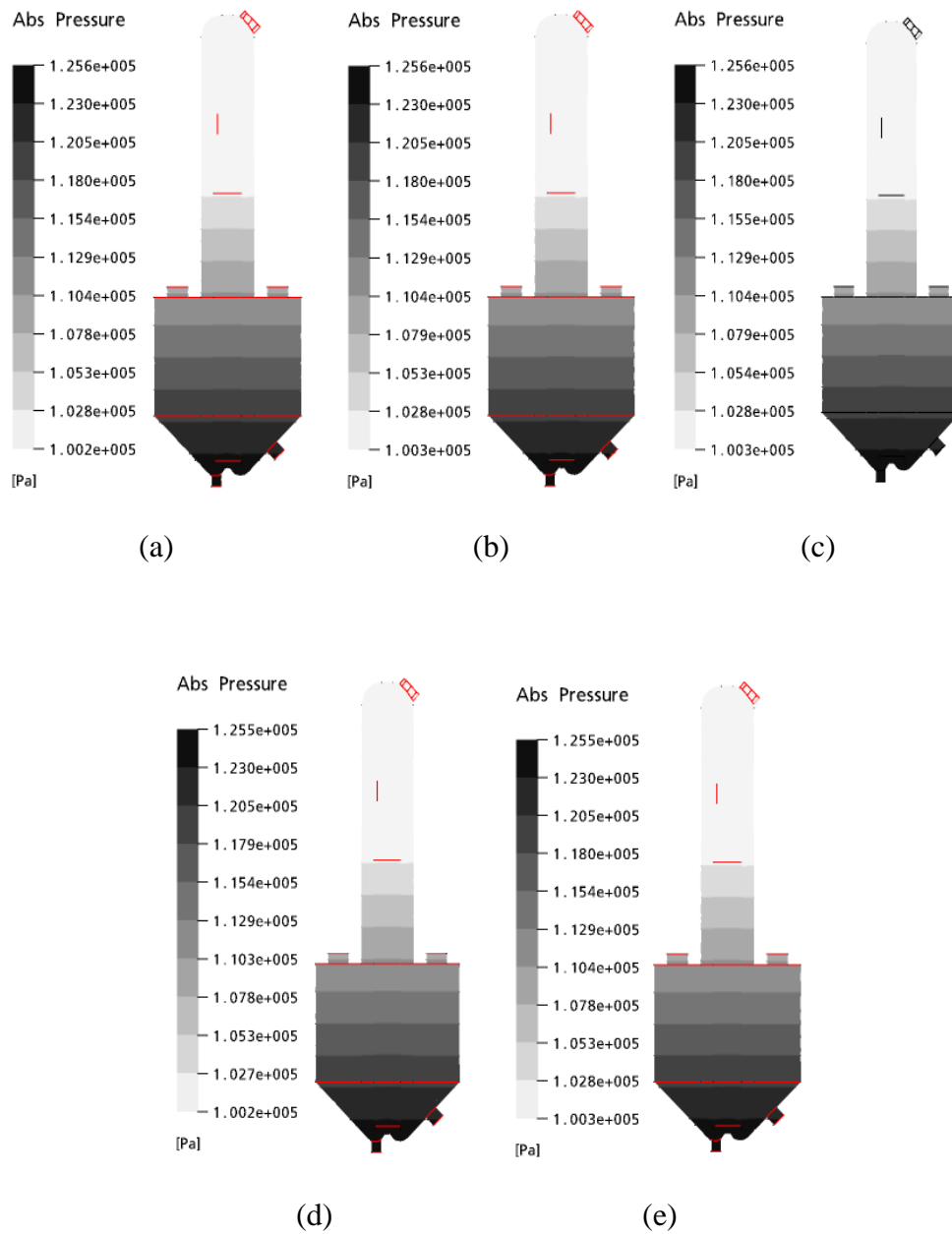


Figure 5.62 Contours of the absolute pressure in the vertical center plane for fines removal flows of (a) 0.0599 kg/s; (b) 0.1198 kg/s; (c) 0.1797 kg/s; (d) 0.2636 kg/s; (e) 0.4672 kg/s.

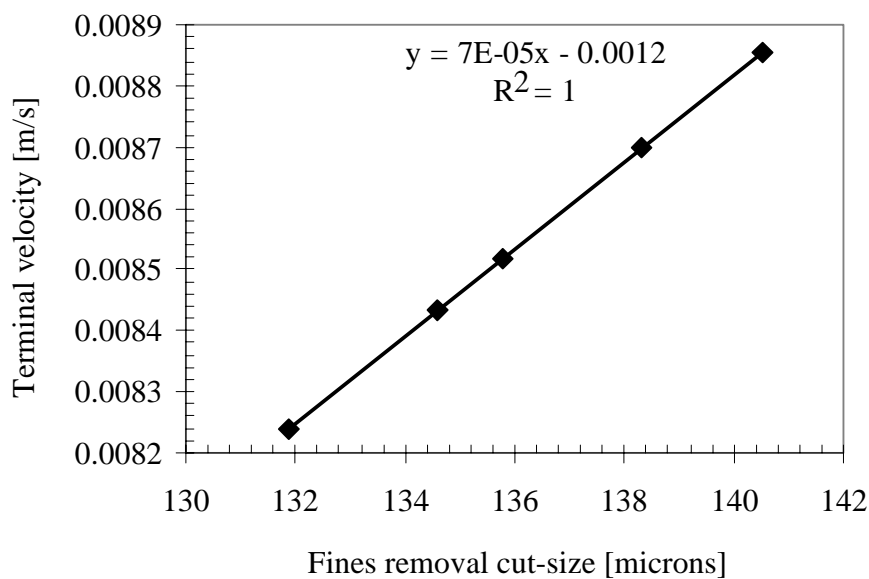


Figure 5.63 Terminal velocity for case studies 14 to 18 as a function of fines removal cut-size.

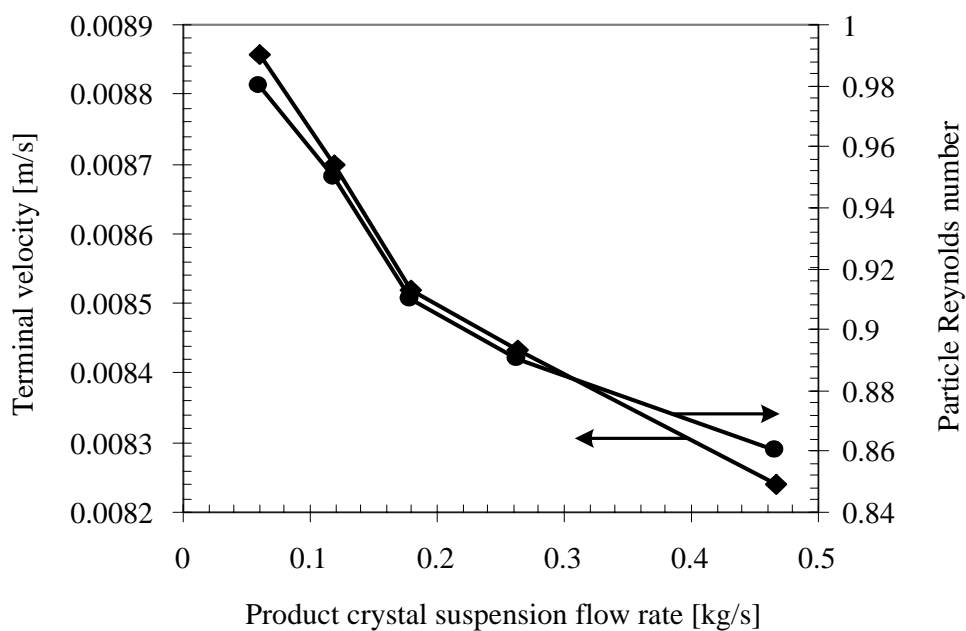


Figure 5.64 Terminal velocity and particle Reynolds number for case studies 14 to 18 as a function of product crystal suspension flow.

5.2 Non-isothermal Simulation

5.2.1 Validation of the degassing condition at the free surface

A study of the liquid velocity of case study number 5 was conducted to compare the free surface flow model (which simulates the whole crystallizer tank) and the degassing condition at the free surface (which simulates only the area under an (assumed) flat free surface). For the second simulation, the simulation methods are the same as for the isothermal simulation (case study number 5), but have no modeling of the area above the free surface, and assume a degassing condition at the free surface, which is an open boundary condition for the gas phase.

The liquid velocity vectors for both simulations are shown in Figure 5.65. This figure shows that the overall flow pattern for both case studies have similar features, but the flow inside and outside the draft tube for the degassing condition is a little more uniform than for the free surface flow model. For the overall magnitudes of velocity, the velocity for the degassing condition is 2.83% higher than the free surface flow model. The liquid velocity at any point in the vertical plane ($z = 0$) for both cases are shown in Figures 5.66 to 5.74. Figures 5.66 to 5.72 show that the velocity at any point in the draft tube for the degassing condition agrees well with the free surface flow model (most average percent errors are less than 10%). Figures 5.73 to 5.74 show that the velocity at any point above the draft tube to the free surface for the degassing condition is significantly different to the free surface flow model (the average percent errors are larger than 20%, which is a quite large percent error). The percent error increases greatly in the region very close to the free surface, due to differences in the assumed boundary conditions. This is since the boiling and the separation of the vapor from the mixture (the mixture of vapor and liquid) occur at the

free surface, and these processes produce complex and oscillating velocity profiles, but the degassing condition produces smoother velocity profiles based on the flat and frictionless free surface assumptions.

Therefore, it can be concluded that the two simulations are very similar, except at the space above the draft tube, but below the free surface. This is because the boundary condition changes significantly at the free surface. However it is suitable to specify the degassing condition to the free surface to reduce the model complexity.

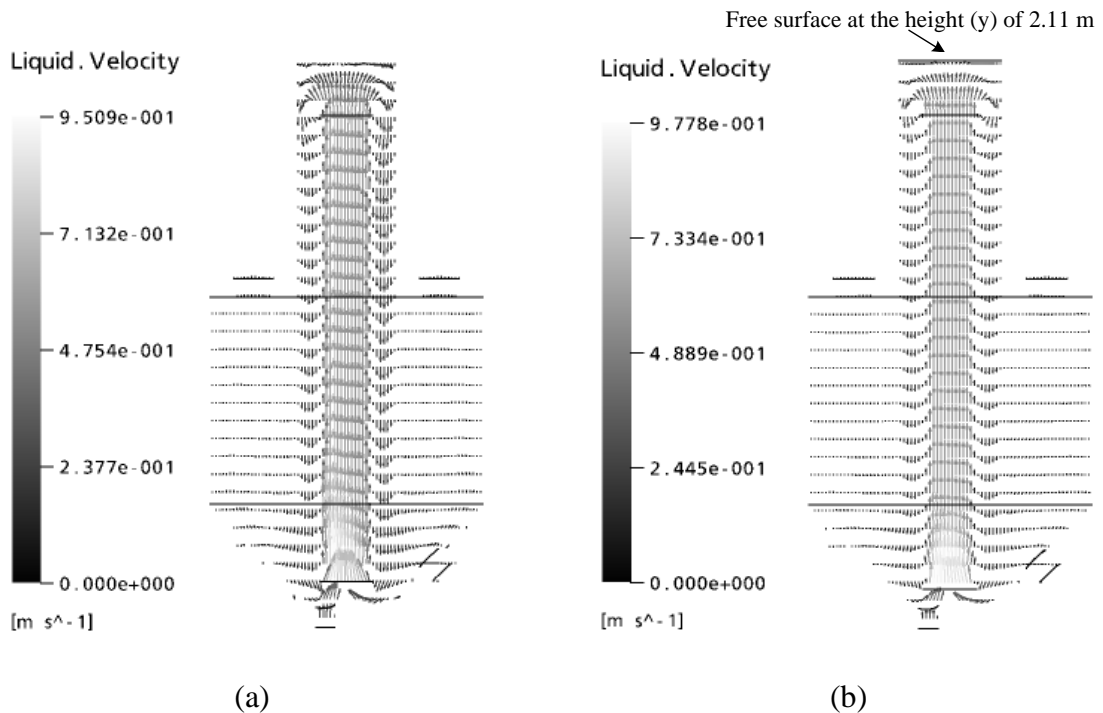


Figure 5.65 Liquid velocity vectors of isothermal simulation (case study 5) for (a) free surface flow model; (b) degassing condition at the liquid surface.

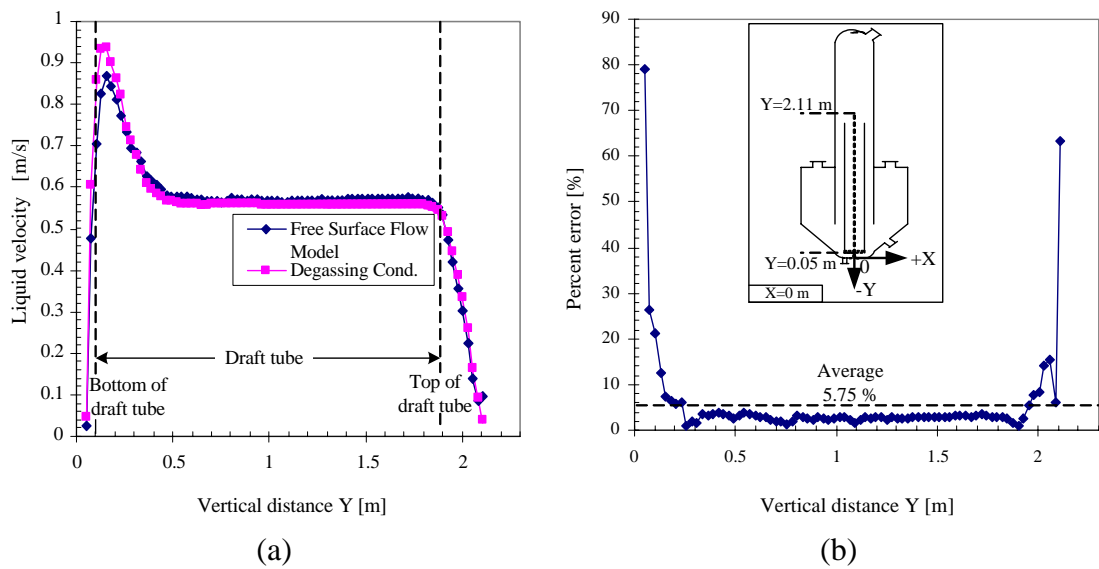


Figure 5.66 (a) liquid velocity at the center of draft tube; (b) percent error of liquid velocity of degassing condition from free surface flow model.

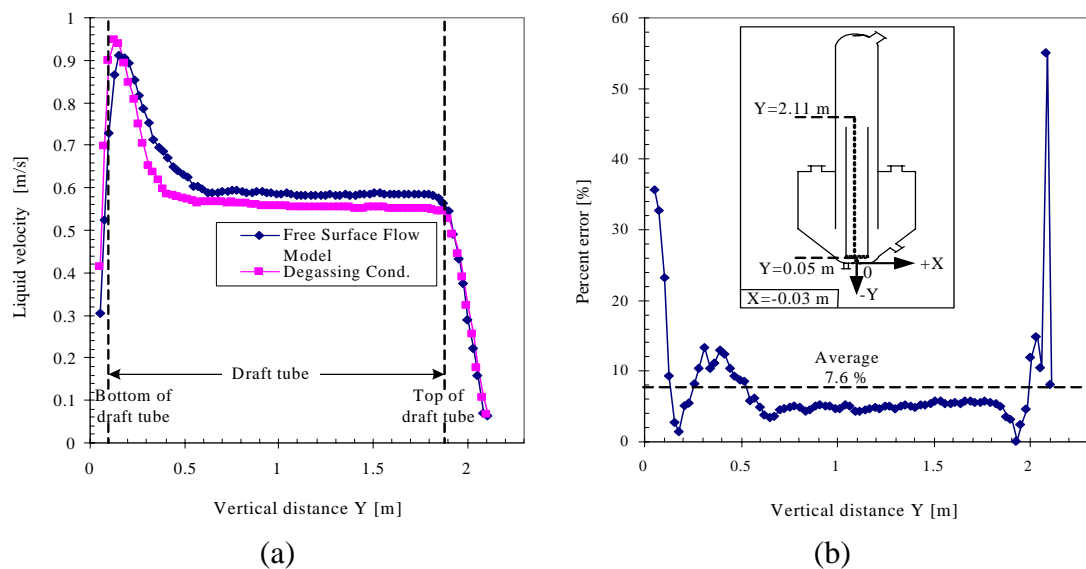


Figure 5.67 (a) liquid velocity at $X = -0.03$ m; (b) percent error of liquid velocity of degassing condition from free surface flow model.

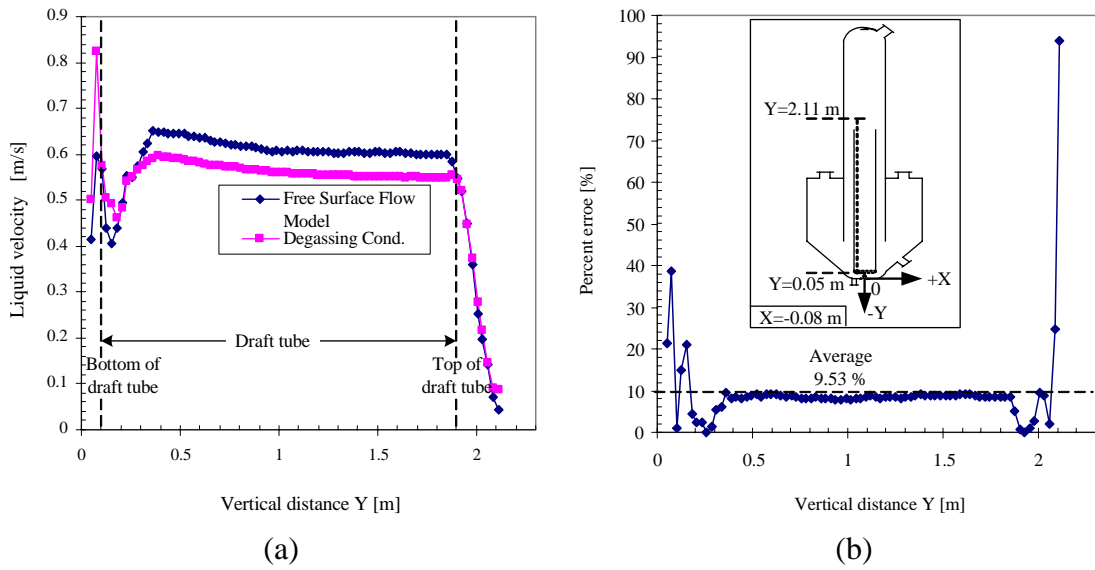


Figure 5.68 (a) liquid velocity at $X = -0.08$ m; (b) percent error of liquid velocity of degassing condition from free surface flow model.

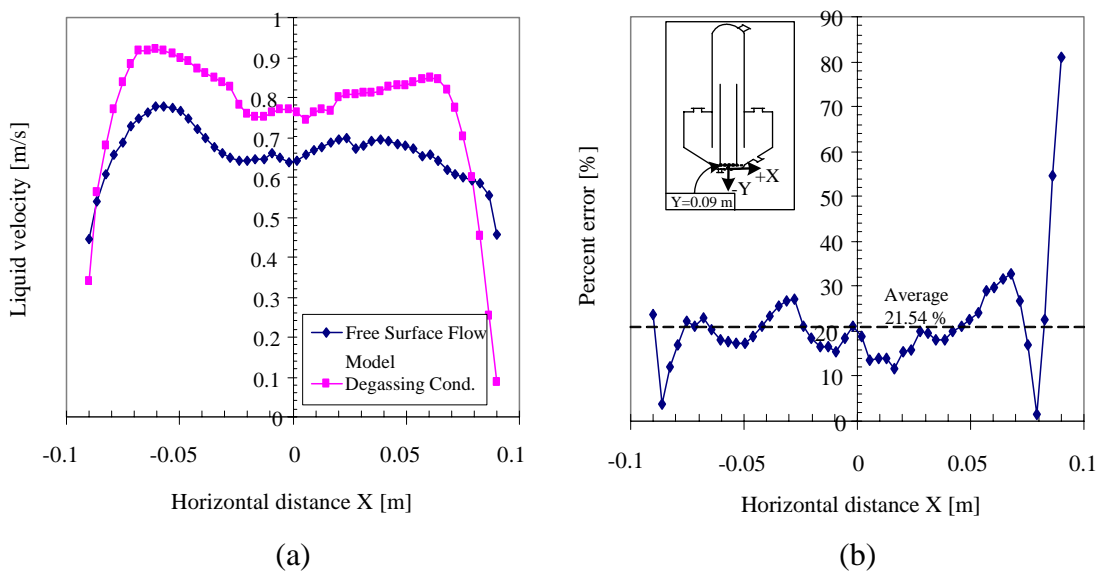


Figure 5.69 (a) liquid velocity at $Y = 0.09$ m; (b) percent error of liquid velocity of degassing condition from free surface flow model.

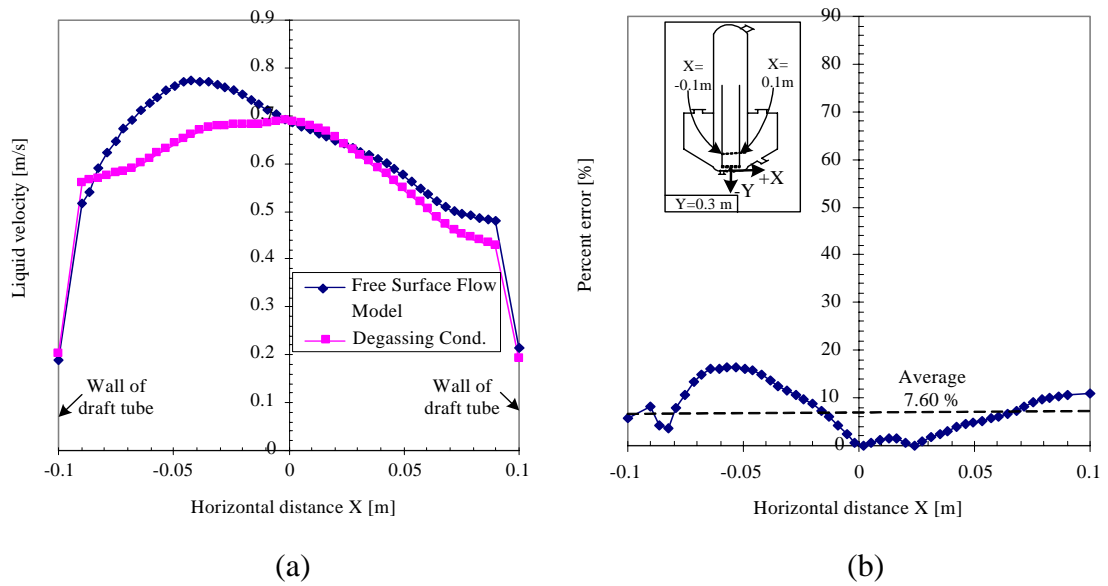


Figure 5.70 (a) liquid velocity at $Y = 0.3 \text{ m}$; (b) percent error of liquid velocity of degassing condition from free surface flow model.

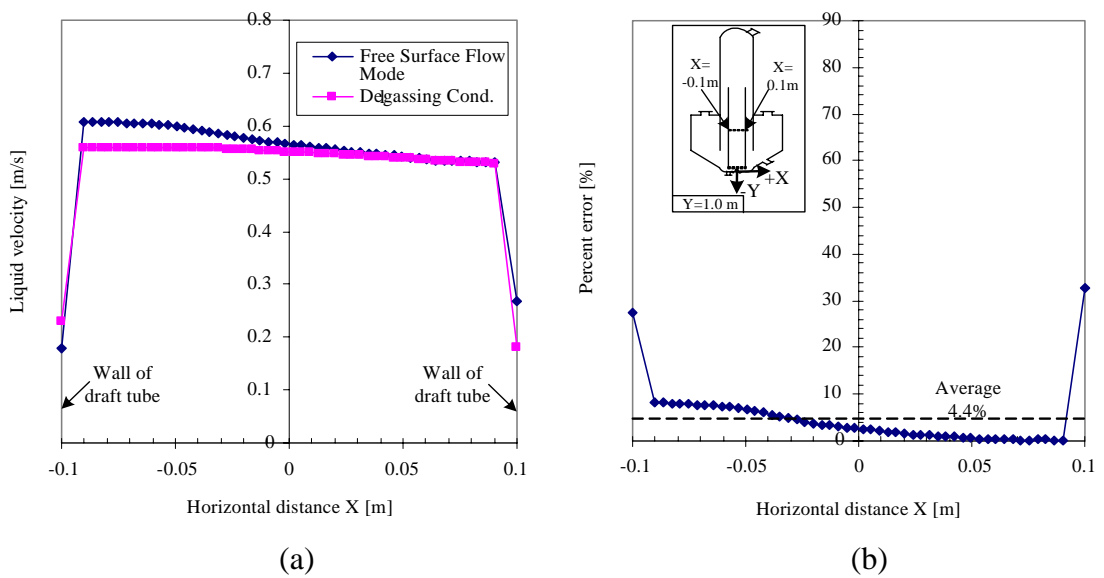


Figure 5.71 (a) liquid velocity at $Y = 1.0 \text{ m}$; (b) percent error of liquid velocity of degassing condition from free surface flow model.

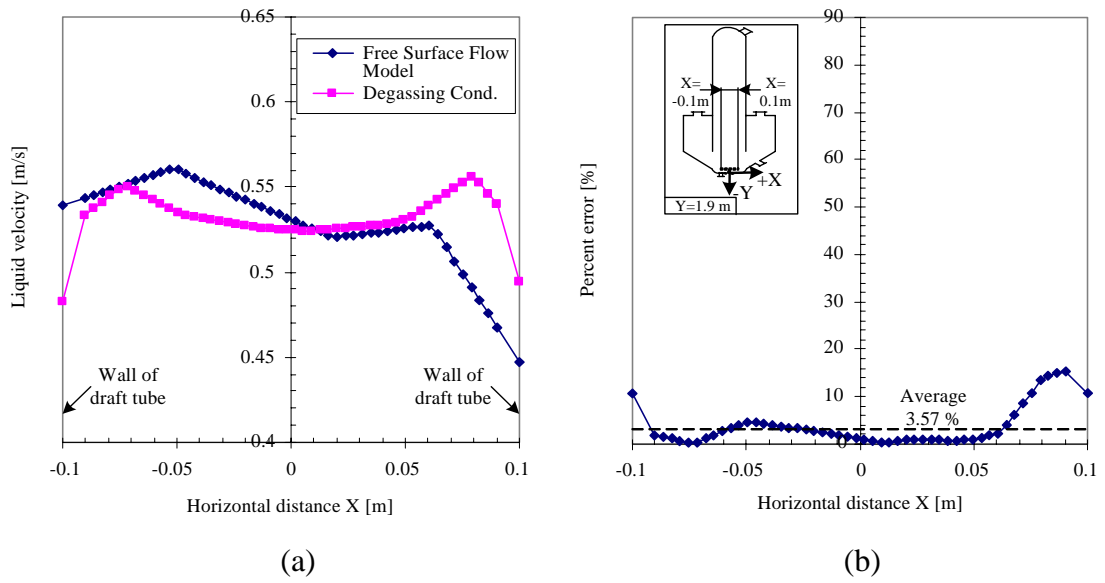


Figure 5.72 (a) liquid velocity at $Y = 1.9$ m; (b) percent error of liquid velocity of degassing condition from free surface flow model.

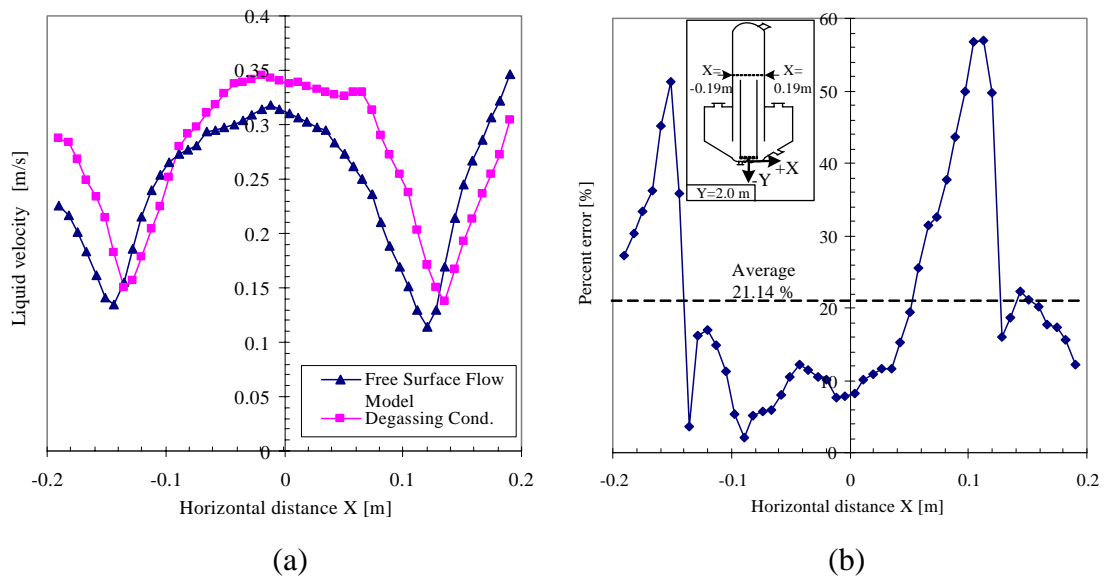


Figure 5.73 (a) liquid velocity at $Y = 2.0$ m; (b) percent error of liquid velocity of degassing condition from free surface flow model.

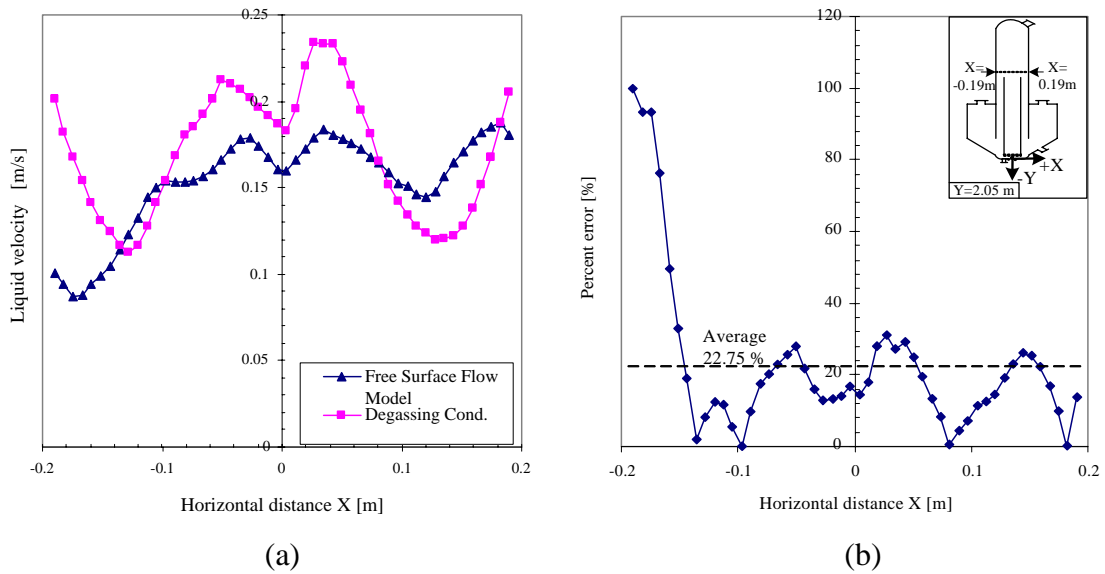


Figure 5.74 (a) liquid velocity at $Y = 2.05$ m; (b) percent error of liquid velocity of degassing condition from free surface flow model.

5.2.2 Effect of the heat source

From the previous section, which shows that the degassing condition available in the program specifies a free surface with degassing, and that this reduces the complexity of the non-isothermal simulation of an evaporative-DTB crystallizer (where only the volume below the free surface is simulated) without changing the key features of the solution, it was decided to simulate the non-isothermal crystallizer using the degassing condition.

In this study, four test cases are performed, using a constant momentum source addition of $10,000 \text{ kg/m}^2/\text{s}^2$, feed solution flow of 1.1861 kg/s and product crystal suspension flow of 0.1797 kg/s , with the heat source value varying at $11,000$, $12,000$, $13,000$, and $13,500 \text{ kW/m}^3$. Note that the heat source is the heat input per unit volume (volume of the impeller sub-domain, which equals 0.0007854 m^3) so that the

heat input values of these heat source values are 8.64, 9.42, 10.21, and 10.60 kW, respectively.

The CFD results showed that the vapor formed increases linearly with increasing heat input (Figure 5.75). This can be shown to be true analytically, and can be investigated by an energy balance around the crystallizer as shown below:

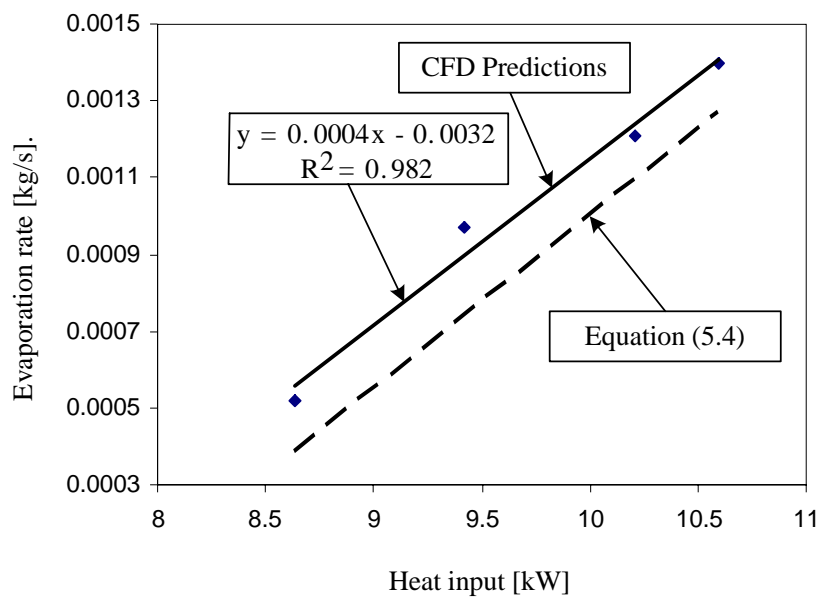


Figure 5.75 Evaporation rate for case studies 19 to 22 as a function of heat input.

Figure 5.76 shows a crystallizer where a mass flow \dot{m}_F of the solution flows in and a mass flow \dot{m}_{Fines} of fines removal stream flows out. In an evaporative-DTB crystallizer, a heat flow \dot{Q}_{to} (heat input by the heat exchanger) is added to the system. A mass flow \dot{m}_v of the evaporated solvent, which has an enthalpy $H^{sat,vap}$, leaves the crystallizer. The mass flow \dot{m}_p of the product crystal suspension leaves the crystallizer and the heat of this stream is the enthalpy of the suspension, which is

mainly a liquid phase, so the enthalpy of the suspensions is replaced by the enthalpy H_p of the saturated solution leaving the crystallizer. In the later case, the energy is added, \dot{W}_{to} , via a circulating device. For the crystallizer operated in the steady-state mode, the following energy balance is obtained around the crystallizer:

$$\dot{m}_F H_F + \dot{Q}_{to} + \dot{W}_{to} = \dot{m}_{Fines} H_{Fines} + \dot{m}_p H_p + \dot{m}_v H^{sat.vap}. \quad (5.1)$$

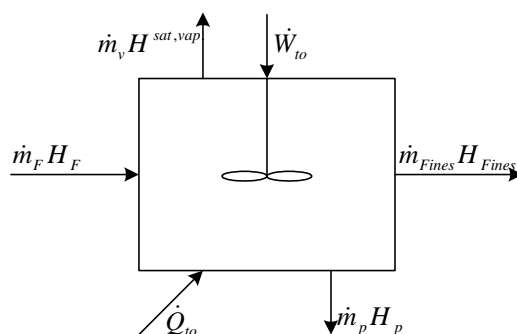


Figure 5.76 Energy balance of a continuously operated crystallizer.

In this work, the temperature of the feed solution is 106 °C, which is near the boiling point of the solution (107.6 °C) and the heat added to the system is used to evaporate a relatively small fraction of the solution to induce crystallization, so the temperature of the solution at the fines removal outlet and product crystal suspension outlet are constant at the boiling temperature (the saturation temperature, 107.6 °C) (Figure 5.77), which leads to $H_{Fines} = H_p = H^{sat.sol.}$ and hence equation (5.1) becomes

$$\dot{m}_F H_F + \dot{Q}_{to} + \dot{W}_{to} = \dot{m}_F H^{sat.sol.} + (H^{sat.vap.} - H^{sat.sol.}) \dot{m}_v \quad (5.2)$$

The enthalpy difference $H^{sat.vap.} - H^{sat.sol.} = L$ (the latent heat), and substitute of this term and rearrangement leads to

$$\dot{m}_v = \frac{\dot{W}_{to} + \dot{m}_F (H_F - H^{sat.sol.})}{L} + \frac{\dot{Q}_{to}}{L} \quad (5.3)$$

Equation (5.3) is linear equation, in which \dot{m}_v is the dependent variable and \dot{Q}_{to} is the independent variable, with a constant work added (power input), feed temperature, and latent heat (constant boiling temperature). Since the enthalpy of a saturated NaCl solution at its boiling point is similar to the enthalpy of water at the boiling point, equation (5.3) can be expressed in terms of the parameters in the system and the properties of water, which are $\dot{W}_{to} = 0.0102$ kJ/s, $\dot{m}_F = 1.1861$ kg/s, H_F (the enthalpy of water at 106 °C) = 444.7 kJ/kg, $H^{sat.sol.}$ (the enthalpy of water at 107.6 °C) = 451.4 kJ/kg, $H^{sat.vap.}$ (the enthalpy of saturated vapor water at 107.6 °C) = 2,687.4 kJ/kg, and $L = 2,236$ kJ/kg. Equation (5.3) becomes

$$\dot{m}_v = 0.00045 \dot{Q}_{to} - 0.0035 \quad (5.4)$$

Equation (5.4) can be plotted as shown in Figure (3.75), and this indicates that the CFD predictions agree well with this equation. The CFD predictions give

approximately 12.5 % difference in the slope compared to equation (5.4), as well as some difference in the intercept.

The liquid temperature profiles (Figure 5.77) in the annular settling zone and area around the product suspension outlet tube are uniform (constant at about the saturated liquid temperature), which shows that the assumptions in equation (5.3) are correct. Figure 5.77 shows that the heat source added (heat input) at the base of the draft tube slightly influences the overall liquid temperature profile; this is since the heat is added at a small value to evaporate the liquid, and the solution can not become superheated, so the liquid does not go over saturated temperature. The subcooled liquid feed to the crystallizer has only a small effect since it is a small amount compared to the recirculated liquid in the crystallizer. Furthermore, Figure 5.77 shows that the liquid temperature near the right wall of the draft tube is higher than at the left wall. This is since the feed is to the left, and the feed is colder than the bulk fluid in the crystallizer. At the right wall, liquid is recirculated from the crystallizer, which is at the boiling point, and at the left side the feed solution (which is a lower temperature) is mixed with recirculated solution. Note that the vapor temperature is not shown in this report because the vapor phase was assumed to be an isothermal phase (based on the simulation model) so the vapor temperature is constant at the boiling temperature (saturated vapor temperature, 107.6 °C). This is quite realistic: the evaporation produces a saturated vapor, and this will not undergo significant cooling before leaving the body of the crystallizer.

Normally, the boiling action is concentrated mostly in the center of the vessel and is well distributed across the surface (free surface) by the vertical draft tube inlet (Myerson, 2002); the simulation results of all case studies (Figure 5.78) of this

work agree well with this conclusion. This is since the boiling point of the solution is a function of pressure, and so boiling tends to take place at the surface of the liquid (the free surface) where there is a lower pressure, which can lead to high levels of supersaturation (Mersmann, 2001). This results in a high concentration, which leads to a high nucleation rate. Figure 5.79 shows that the simulation results of all case studies have lower pressure values at the area above the top of the draft tube up to the liquid surface, due to lower levels of the static pressure.

Figure 5.78 shows that as the heat source added at the base of the draft tube increases, the amount of vapor formed becomes higher; the relationship of the heat source with vapor formed (the evaporation rate) is discussed at the beginning of this section (see Figure 5.75). The pressure profiles in the crystallizer in Figure 5.79 are the same as the isothermal simulation results and the heat source only slightly influences the pressure.

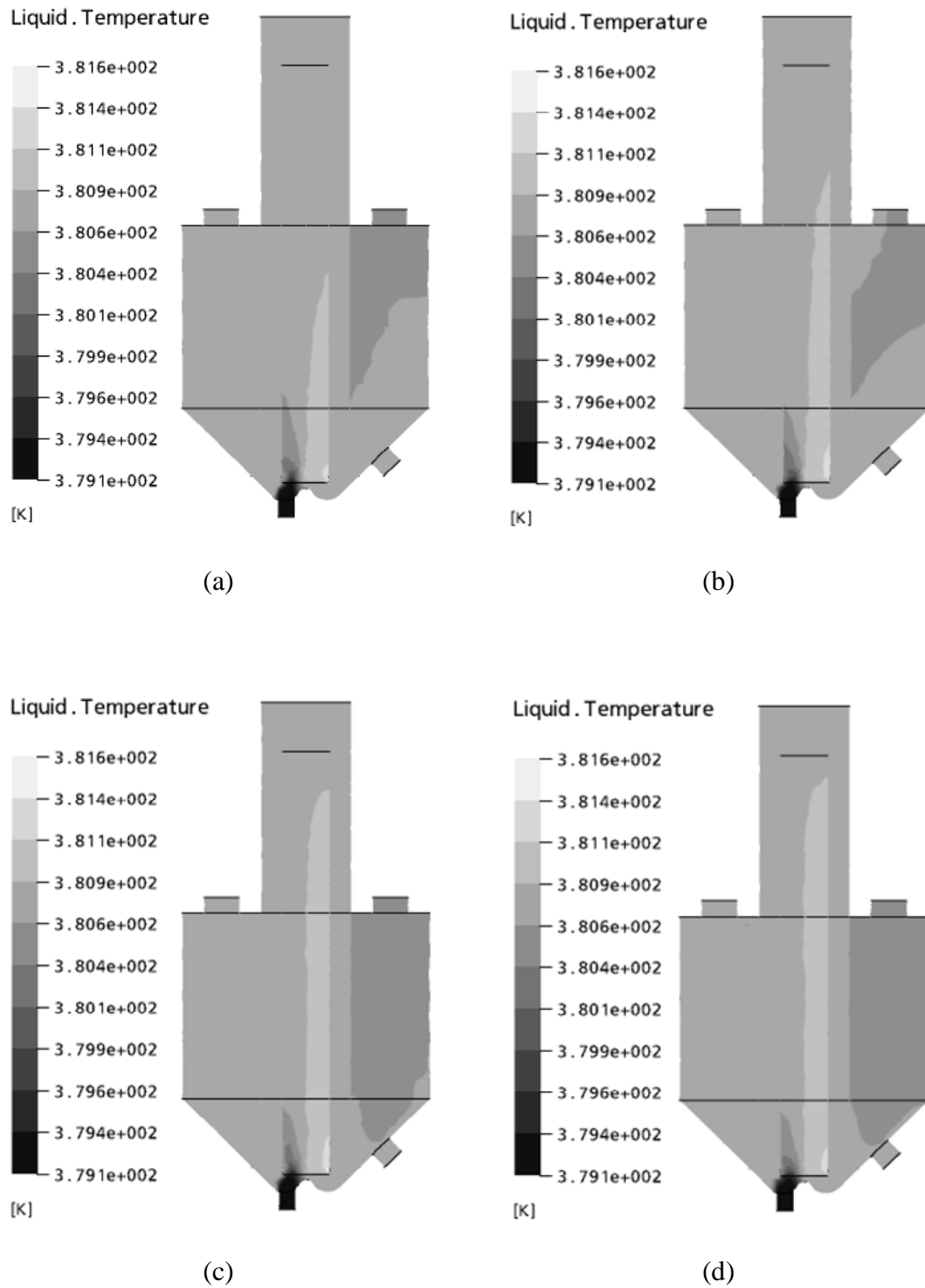


Figure 5.77 Contours of liquid temperature for heat source additions of (a) 11,000 kW/m³; (b) 12,000 kW/m³; (c) 13,000 kW/m³; (d) 13,500 kW/m³.

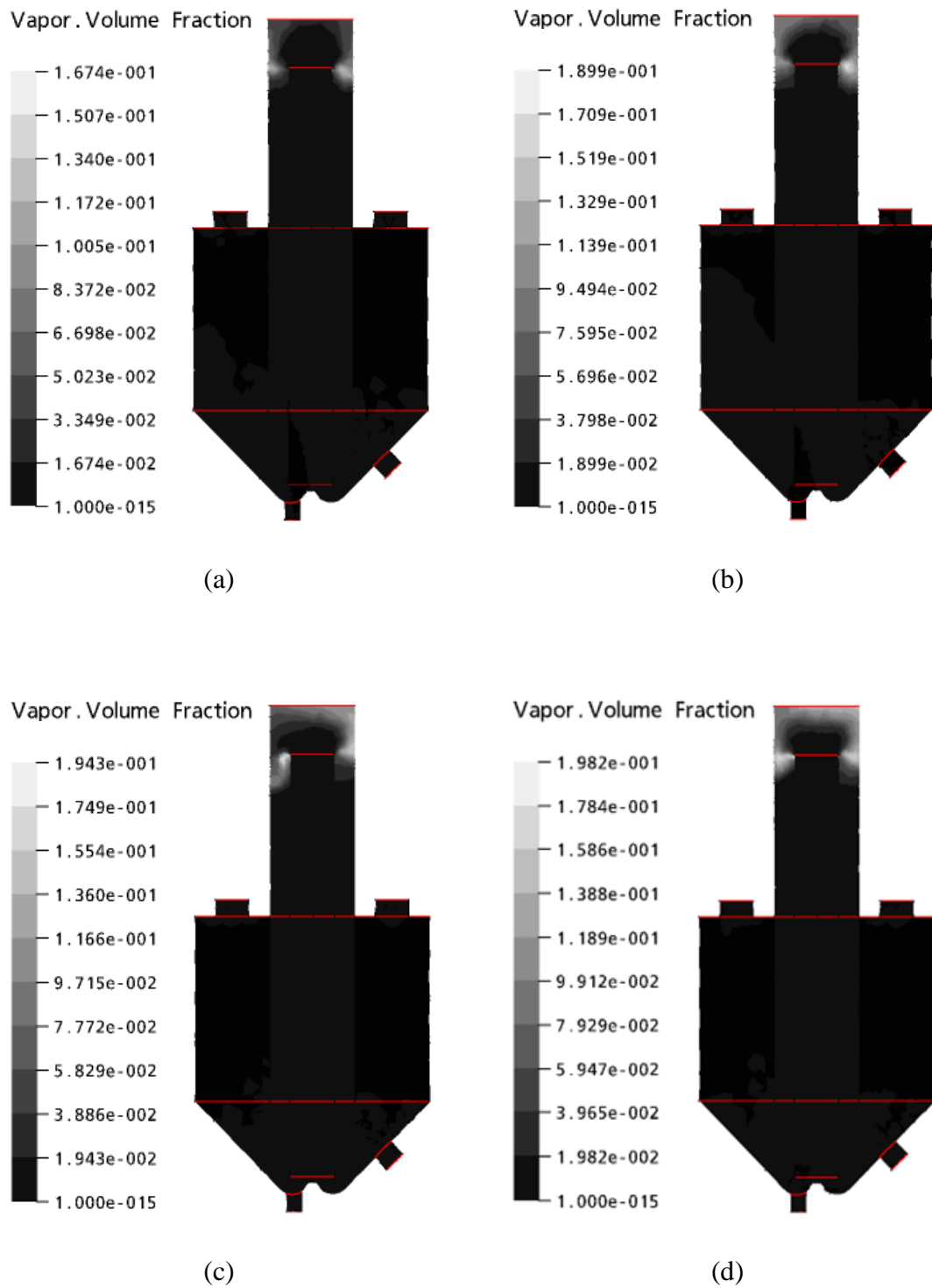


Figure 5.78 Contours of vapor volume fraction for heat source additions of (a) $11,000 \text{ kW/m}^3$; (b) $12,000 \text{ kW/m}^3$; (c) $13,000 \text{ kW/m}^3$; (d) $13,500 \text{ kW/m}^3$.

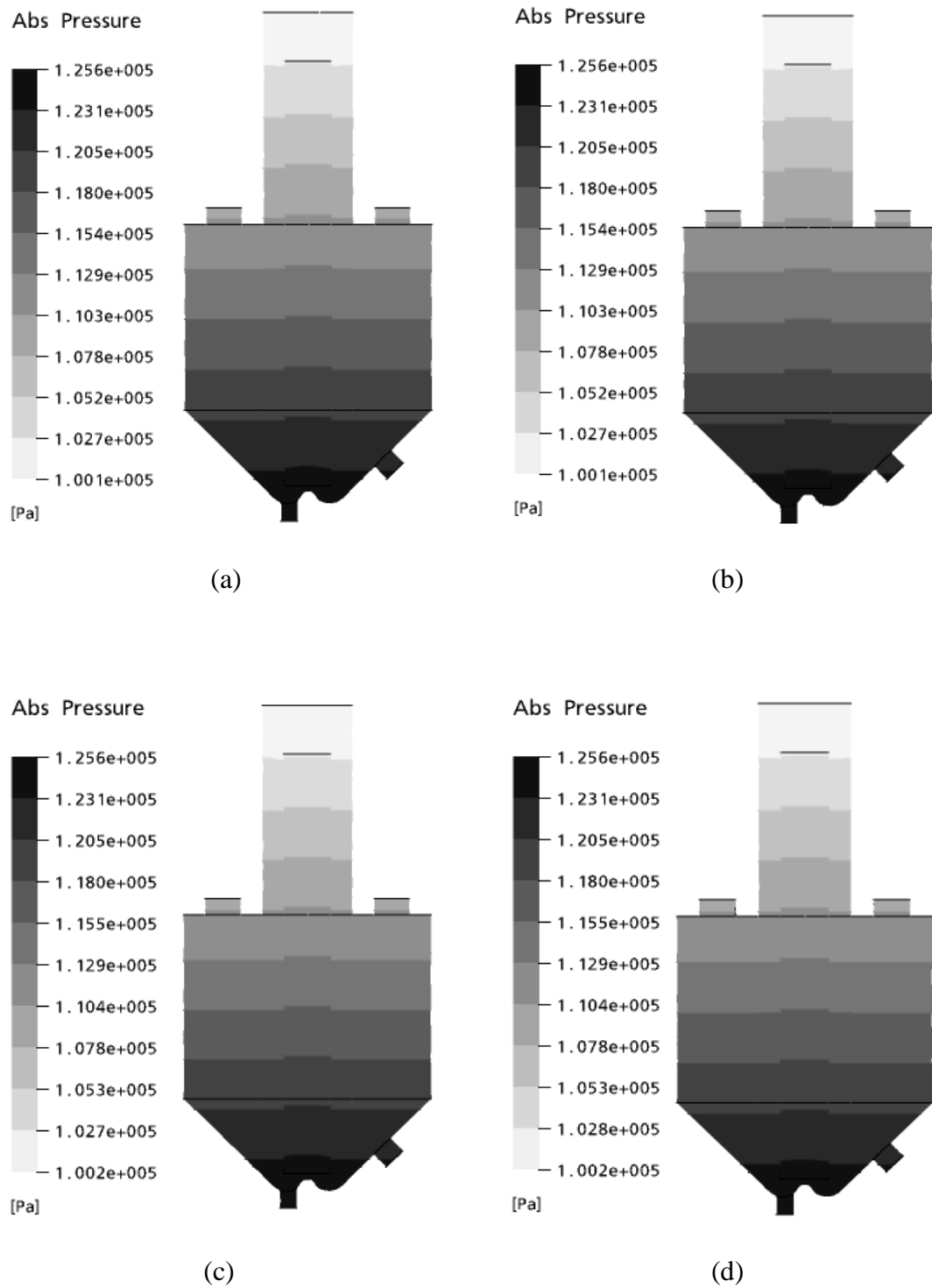


Figure 5.79 Contours of pressure for heat source additions of (a) 11,000 kW/m³; (b) 12,000 kW/m³; (c) 13,000 kW/m³; (d) 13,500 kW/m³.

Figures 5.80 to 5.83 show the overall velocity vectors, contours, and 2D streamlines for both phases, for the heat source values of 11,000, 12,000, 13,000, and 13,500 kW/m³ respectively (from left to right). These figures indicate that the flow of both the liquid and the vapor phase are the general flow fields in the DTB crystallizer (see more details in the isothermal simulation results). The flow features in 3D for these cases are shown in appendix D in Figure D.10 for the liquid phase and Figure D.11 for the vapor phase. The heat source slightly influences the overall velocity for both phases. Furthermore, the vapor velocity appears only in the area above the draft tube because the vapor is formed in this area, and essentially all leaves via the free surface without recirculating into the body of the crystallizer.

The uniformity of the liquid flow can be clearly depicted by the overall velocity contours (the center picture of Figures 5.80 to 5.83). The results show that, as described previously in the isothermal simulation results (section 5.1.2), full uniformity of the low liquid velocity in the particle settling zone, non-uniform flow at the point that the liquid flows over the top of the draft tube and the vapor-liquid interface were found for all the case studies. However, the overall flow features in the draft tube and outside the draft tube are close to uniform. Vorticity at the bottom of the settling zone is found in all the case studies, as described previously for the isothermal simulations (section 5.1.2).

It is important to consider the liquid and vapor velocity vectors in the area around the top of the draft tube in Figure 5.84. Two circulation loops of liquid flow occur in the area above the draft tube (near the free surface); one occurs near the left wall of the tank and another one occurs near the right wall of the tank; these occur since most of the vapor is formed in these areas (Figure 5.78), and then flows up to

the free surface to separate out, while the liquid will flow up together with the vapor to the free surface but it is not separated out. This causes the liquid to flow down until it comes in contact with the bulk of the liquid that flows over the draft tube, and then both liquid streams flow together down the outside of the draft tube; this creates strong recirculation loops. The strength of the loop increases with increasing heat source since the amount of vapor formed increases with increasing heat source. Two circulation loops of liquid flow occur at the top of the draft tube (near the outside wall of the draft tube) too. These circulation loops occur because the vapor tries to flow up while the liquid tries to flow down. The strength of these loops also increases with increasing heat source for the same reason as stated previously. Moreover, in Figure 5.84, the liquid velocity at the free surface is not zero because the simulation method assumes that the surface is frictionless. This is likely in the real system, where the vapor is separated out at this surface so that the velocity is not zero.

The liquid at the bottom of the tank tends to flow into the draft tube, which is similar to the previous description in section 5.1.1. This is found for all the heat source case studies and means that there is no stagnation point at the bottom of the tank. The liquid velocity vectors at the bottom of the tank for heat source additions of 11,000, 12,000, 13,000, and 13,500 kW/m³ are shown in appendix D in Figure D.12.

The liquid flow in the draft tube, as described previously in the isothermal simulation section, is turbulent, and the Reynolds number essentially constant with an average value of 41,000. Full uniformity of the low liquid velocity in the particle settling zone was found for all the case studies, and the average fines removal cut-size was 77 microns, with the average particle Reynolds number of 0.27.

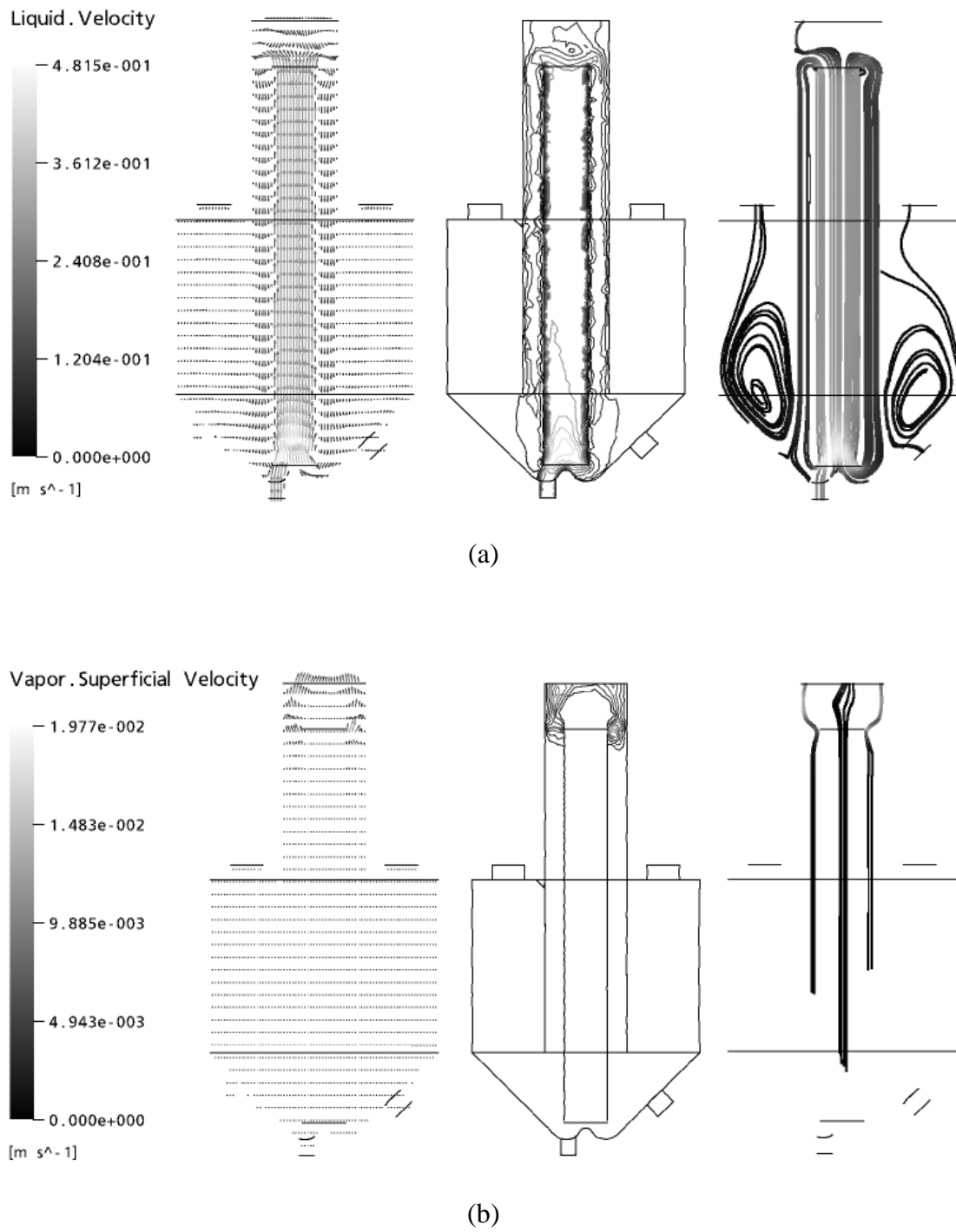


Figure 5.80 Velocity vectors, contours, and streamlines of liquid (a) and vapor (b) in the vertical center plane for a heat source of $11,000 \text{ kW/m}^3$.

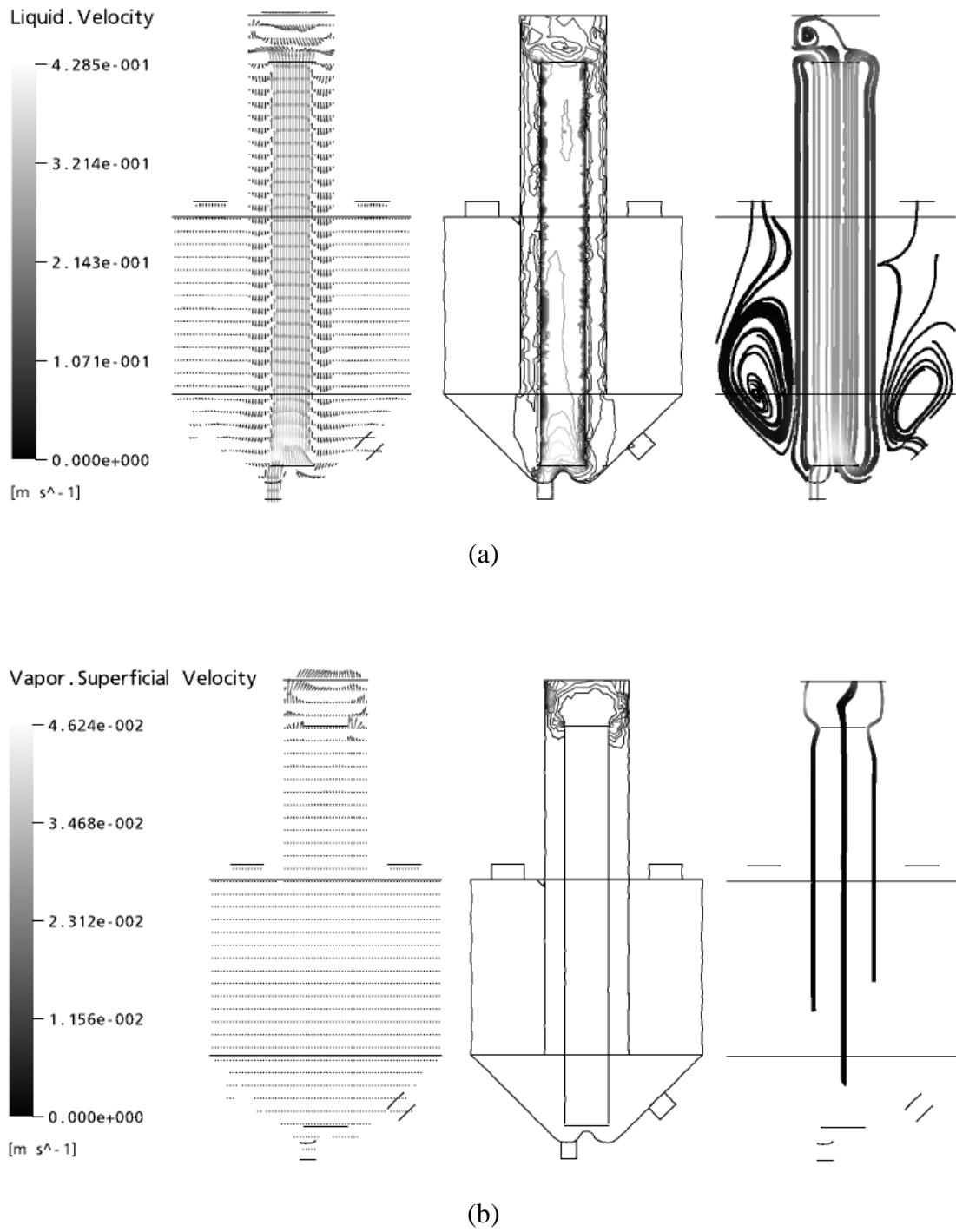


Figure 5.81 Velocity vectors, contours, and streamlines of liquid (a) and vapor (b) in the vertical center plane for a heat source of $12,000 \text{ kW/m}^3$.

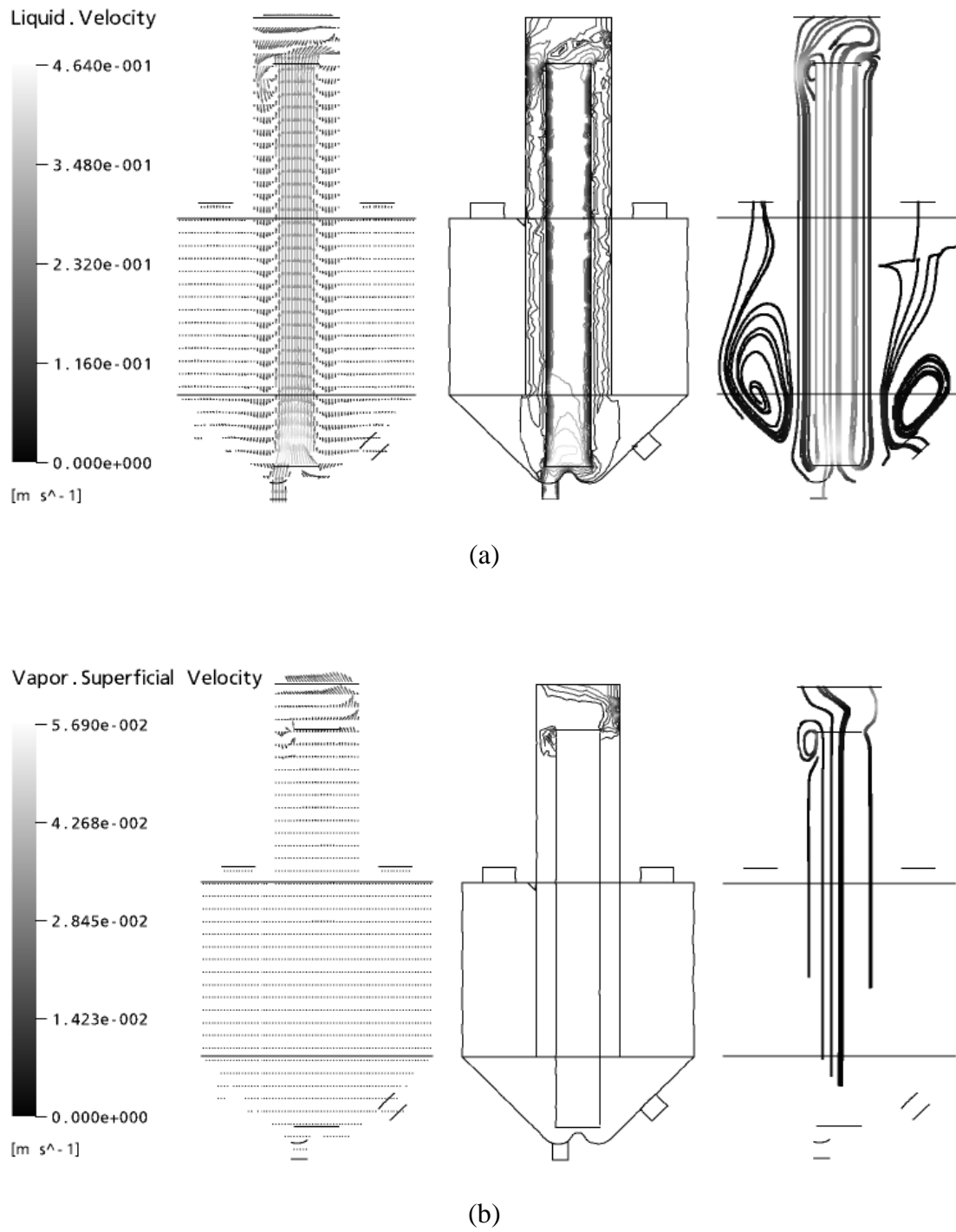


Figure 5.82 Velocity vectors, contours, and streamlines of liquid (a) and vapor (b) in the vertical center plane for a heat source of $13,000 \text{ kW/m}^3$.

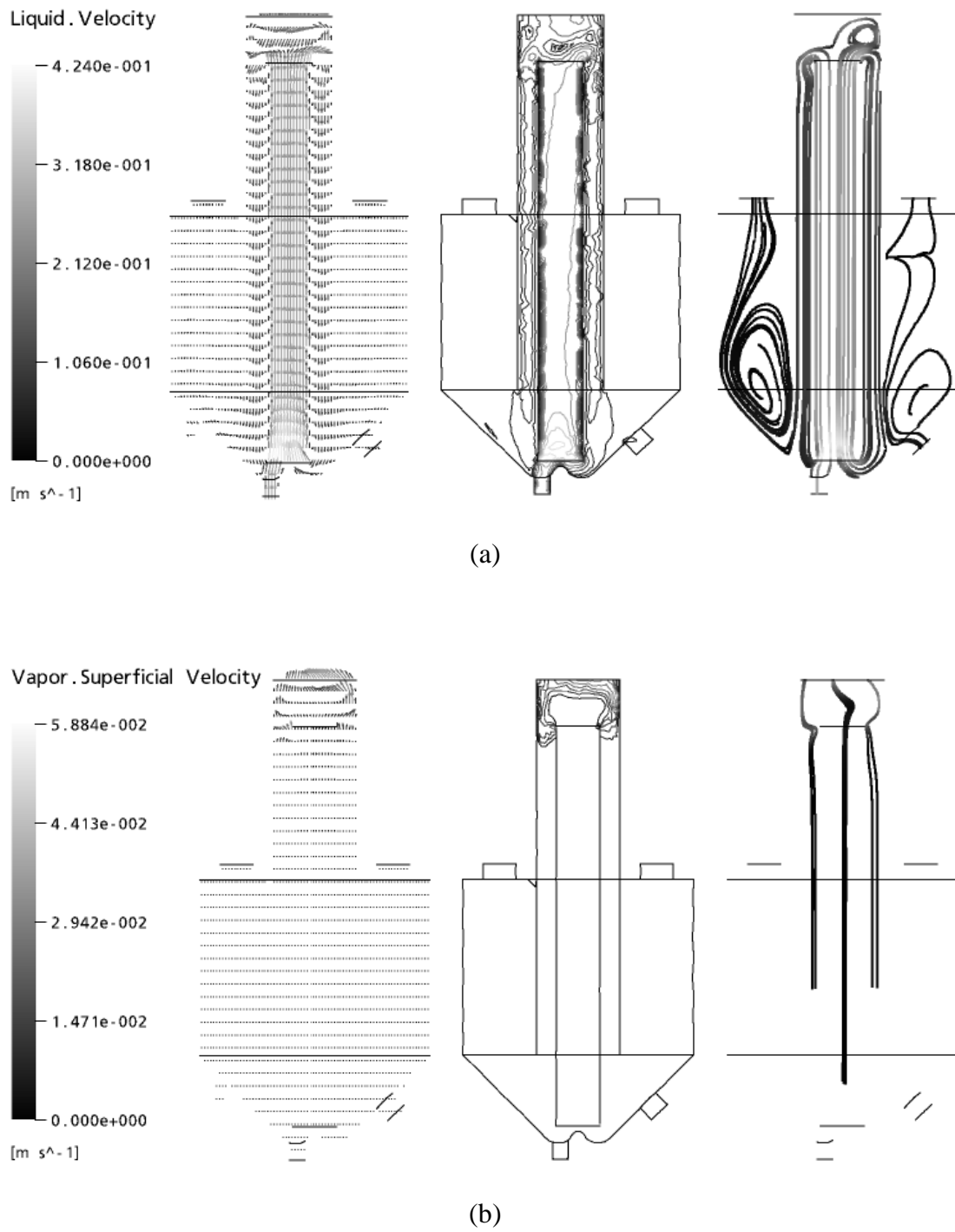


Figure 5.83 Velocity vectors, contours, and streamlines of liquid (a) and vapor (b) in the vertical center plane for a heat source of $13,500 \text{ kW/m}^3$.

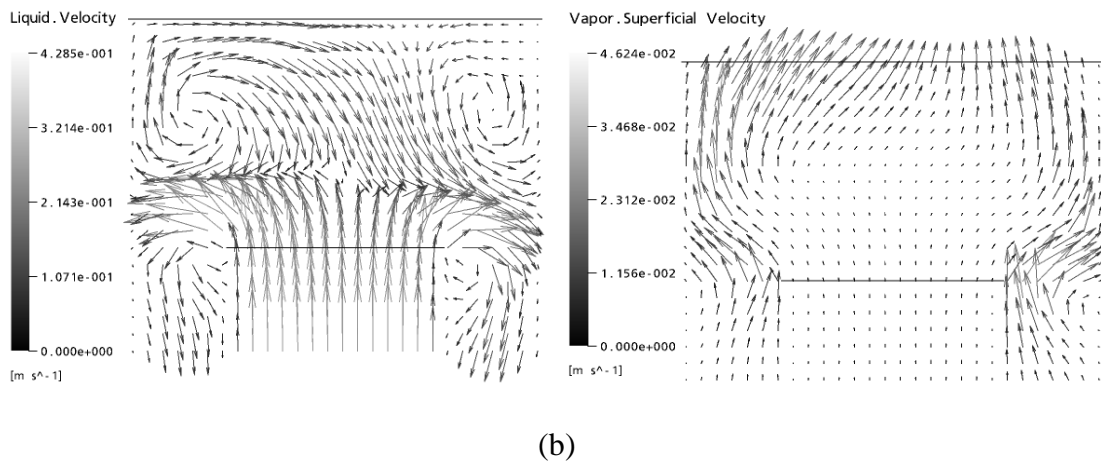
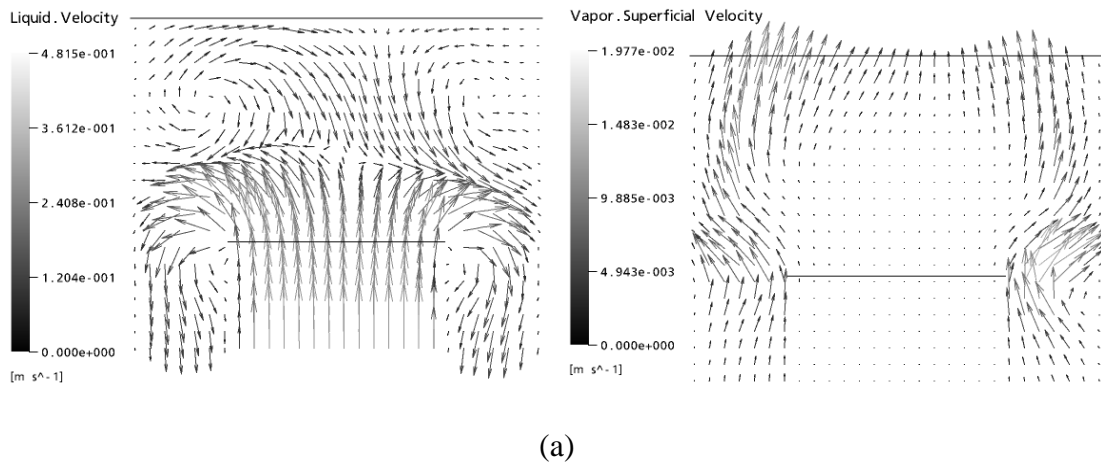


Figure 5.84 Liquid and vapor velocity vector at the top of draft tube for heat source additions of (a) 11,000 kW/m³; (b) 12,000 kW/m³; (*continued*)

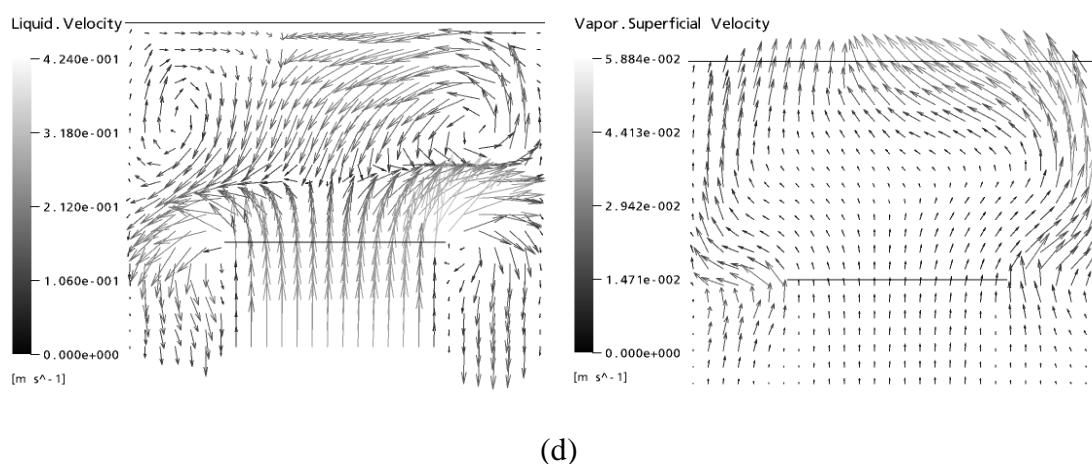
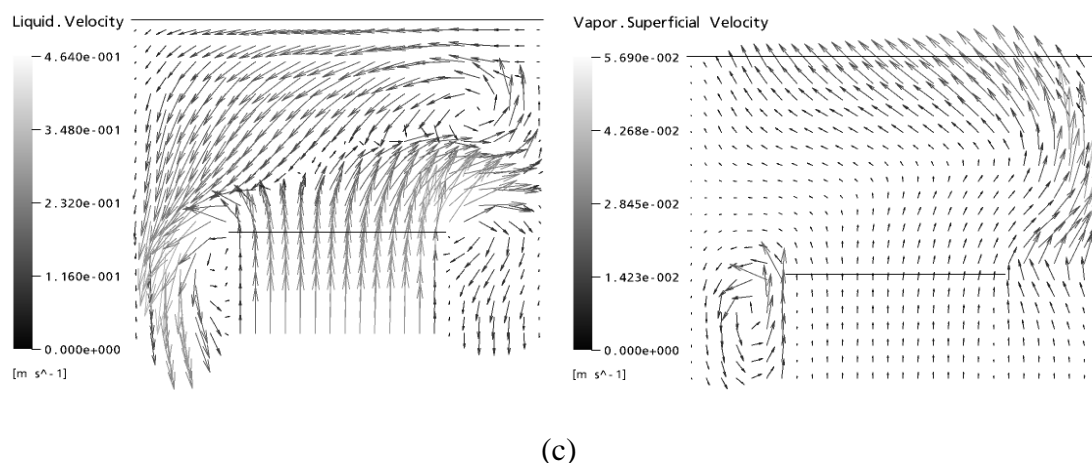


Figure 5.84 (*continued*) (c) 13,000 kW/m³; (d) 13,500 kW/m³.

5.3 Conclusions

The simulation results show that the overall flow features are the general flow fields expected in DTB crystallizer. The effect of the momentum source (power input), fines removal flow, product crystal suspension flow, and heat source to the flow characteristics and the crystals classification agree well with the literature and the original theories for industrial crystallization processes.

The overall velocities of the liquid for non-isothermal simulation are not the same as (usually lower than) the isothermal simulation, because the simulations are for slightly different systems. For the isothermal simulation, the vapor formed before entering the crystallizer so that it is easy to assume an isothermal process. For the non-isothermal simulation, the vapor formed in the crystallizer so an isothermal process should not be assumed, and the velocity should be lower than the isothermal process. This is because in the isothermal simulation the vapor is present in the feed, and the vapor bubbles have some buoyancy force, which encourages their flow up to the free surface. The vapor bubbles flow up under the buoyancy force, and they carry the liquid phase with them to some extent, thus increasing the liquid velocity. The non-isothermal simulation has the vapor formed at the free surface, so the liquid flow does not have the benefit of the buoyant vapor flow. Nevertheless, the overall flow feature in the DTB crystallizer for both simulations is similar.

CHAPTER VI

CONCLUSIONS AND RECOMMENDATIONS

6.1 Conclusions

The proposed computational study to obtain flow fields and to study the classification of crystals within the model DTB crystallizer with fines removal appears to be a successful endeavor, and the results obtained are a reasonable representation of what would occur in a real crystallizer. The following conclusions can be made for each simulation part.

6.1.1 Isothermal simulation

6.1.1.1 The overall flow patterns for both phases (vapor and liquid) are the general characteristics of the flow in the DTB crystallizer for the momentum source values greater than or equal to $4,000 \text{ kg/m}^2/\text{s}^2$ (at a product crystal suspension flow rate of 0.1797 kg/s and a fines removal flow rate of approximately 1 kg/s), fines removal flow rates lower than or approximately equal to 2.3 kg/s (at a momentum source value of $10,000 \text{ kg/m}^2/\text{s}^2$ and product crystal suspension flow rate of 0.1797 kg/s), and the product crystal suspension flow rates of 0.06 to 0.5 kg/s (at a momentum source value of $10,000 \text{ kg/m}^2/\text{s}^2$ and fines removal flow rate of approximately of 1 kg/s).

6.1.1.2 The overall magnitude of the liquid velocity within the crystallizer can be strongly increased by increasing the axial momentum source but

only slightly increased by the product crystal suspension and fines removal flow rate. For the vapor phase, the overall magnitude of the velocity can be slightly increased by the axial momentum source and only slightly influenced by the product crystal suspension and fines removal flow rates.

6.1.1.3 In all the test cases studied, a stronger flow (the maximum velocity) is found at the bottom part of the draft tube (near the impeller location), and a higher velocity is also found inside the draft tube. A lower velocity is found in the annular space, and this assists in the settling of the particles which are sufficiently large that they should not appear in the fines removal.

6.1.1.4 The effect of the feed solution flow on the flow characteristics in the DTB crystallizer can be cancelled by momentum source values equal to or higher than $25,000 \text{ kg/m}^2/\text{s}^2$ for a feed solution lower than 1.2 kg/s . The liquid flow is found to be uniform in the main body of the crystallizer with this condition also.

6.1.1.5 Momentum source strengths, and fines removal and product crystal suspension flow rates also have a significant effect on the fines removal cut-size due to varying upflow velocities in the fines removal section altering the size at which particles are carried out in the fines removal stream. This will strongly affect the product crystal size distribution, because the fines cut size has a strong effect on the product crystal size distribution. The fines removal cut-size increases with increasing momentum source (or power transmitted by impeller) and fines removal flow rate, and decreases with increasing product crystals flow rate.

6.1.1.6 In the settling zone, the flow of the particles is in the transition flow regime and the terminal velocity of the particle increases linearly with increasing particle size.

6.1.2 Non-isothermal simulation

6.1.2.1 The amount of vapor formed in the crystallizer increases linearly with increasing heat source strength (heat input).

6.1.2.2 The boiling action is concentrated mostly in the center of the top of the vessel and is well distributed across the free surface by the vertical draft tube inlet. This leads to high levels of supersaturation (high concentration) at the free surface, and will result in a high nucleation rate (high rate of birth of new crystals) in this area. The flow of the vapor and liquid in the boiling zone (above the top of the draft tube) is highly complex, which leads to this section probably having different crystallization kinetics than the other regions of the crystallizer.

6.1.2.3 The heat source slightly influences the overall velocity for both phases (liquid and vapor).

Moreover, rounded tank “corners” and a center peak under the agitator, which is the bottom shape of the DTB crystallizer used in this work, is used to combat settling of particles, and the center peak virtually eliminates the stagnation point (dead zone) that would be present at the bottom center of the tank under the agitator.

CFD tools can be used for new efforts to improve the design, operation, and upgrade of industrial crystallizers, and give results that should well predict the true situation in the crystallizer. This tool provides a cost-effective approach to process optimization, thus enabling analysis of the design equipment before committing to a final configuration.

6.2 Recommendations

6.2.1 As this work proposed the effect of the momentum source (this is the representation of the impeller) to the flow characteristics and the classification of crystals, further work should study the effect of the impeller speed by modeling a real impeller to ensure that the result is same. Furthermore, further studies should study the effect of the type of the impeller also.

6.2.2 A more exact description of particle flowlines should be considered and it is possible to do this using the two-phase simulation results or using a Lagrangian model for the particles.

6.2.3 The real size of the heat exchanger should be considered and modeled by a solid heat source.

6.2.4 Different size of crystallizers should be considered to determine the effect of process scale on the results.

REFERENCES

- Angst, R. and Kraume, M. (2005). **Experiment investigations of the particle distribution in three differently sized stirred solid/liquid systems** [Online]. Available: <http://www.verfahrenstechnik.tu-berlin.de/mitarbeiter/>.
- ANSYS Canada Ltd. (2005). **ANSYS CFX-10.0 Manual**.
- Åslund, B. and Rasmuson, Å. C. (1992). Semibatch reaction crystallization of benzoic acid. **AIChE Journal**. 38: 328-342.
- Bakker, A., Fasano, J. B., and Myers, K. J. (1998). **Effect of flow pattern on the solids distribution in a stirred tank** [On-line]. Available: <http://www.bakker.org/cfm>.
- Barresi, A. and Baldi, G. (1987). Solid dispersion in an agitated vessel. **Chemical Engineering Science**. 42(12): 2949-2956.
- Bird, R. B., Stewart, W. E., and Lightfoot, E. N. (2002). **Transport phenomena** (2nd ed.). New York: John Wiley and Sons.
- Brucato, A., Micale, G., Montante, G., and Scuzzarella, A. (2002). **Experimental investigation and CFD simulation of dense solid-liquid suspensions in a fully baffled mechanically stirred tank** [On-line]. Available: <http://www.waterloo.ansys.com/cfxcommunity/technotes/techpapers/default.asp>.
- Burigou, M. and Greaves, M. (1992). Bubble-size distribution in a mechanically agitated gas-liquid contactor. **Chemical Engineering**. 47(8): 2009-2025.

- Chen, Z. D. and Chen J. J. J. (2000). A study of agitated gas-liquid reactors with concave impellers. **Mixing and Crystallization** (pp. 43-56). Netherland: Kluwer Academic Publishers.
- Cheremisinoff, N. P. (1986). **Handbook of heat and mass transfer; V2: Mass transfer and reactor design**. Honston, Texas: Gulf publishing company.
- Chung, T. J. (2002). **Computational fluid dynamics**. Cambridge, United Kingdom: Cambridge University Press.
- Deen, N. G., Solberg, T., and Hjertager, B. H. (2002). Flow generated by an aerated Rushton impeller: Two-phase PIV experiments and numerical simulation. **The Canadian Journal of Chemical Engineering**. 80: 1-15.
- Dixon, T., Mann, A., Hobson, P., Plaza, F., Pennisi, S., and Steindl, R. (2003). Application of CFD in the sugar industry. **Proceeding of Third International Conference on CFD in the Minerals and Process Industries** (pp. 77-86). Melbourne, Australia: CSIRO.
- Drewer, G. R., Ahmed, N., and Jameson, G. J. (2000). An optimum concentration for suspension of solids in stirred vessels. **Mixing and Crystallization** (pp. 83-94). Netherland: Kluwer Academic Publishers.
- Eek, R. A., Dijkstra, S., and van Rosmalen, G. M. (1995). Dynamic modeling of suspension crystallizers, using experimental process data. **AIChE Journal**. 44(3): 571-584.
- Essemiani, K., Traversay, C. D., and Gallot, J. C. (2004). Computational fluid dynamics (CFD) modeling of an industrial crystallizer: application to the forced-circulation reactor. **Biotechnology and Applied Biochemistry**. 40: 235-241.

- Fakatselis, T.E. (2006). A review of crystallization theory applied to the draft tube baffle crystallizer [Online]. Available: http://www.niroinc.com/html/evaporator/crystallization_theory_intro.htm.
- Farkas, B., Blickle, T., Ulbert, Zs., and Hasznos-Nezdei, M. (1996). Characterization of mixing of suspension in mechanically stirred precipitation system. **Journal of Crystal Growth**. 166: 1064-1067.
- Flood, A. E. (2003). **Crystallization and modeling**. School of Chemical Engineering, Suranaree University of Technology. (Unpublished manuscript).
- Franke, J. and Mersmann, A. (1995). The influence of the operation conditions on the precipitation process. **Chemical Engineering Science**. 50(11): 1737-1753.
- Genck, W. J. (2004). **Guidelines for crystallizer selection and operation** [On-line]. Available: <http://www.cepmagazine.org>.
- Guiraud, P., Costes, J., and Bertrand, J. (1997). Local measurement of fluid particle velocities in a stirred suspension. **Chemical Engineering Journal**. 68: 75-86.
- Hughmark, G. (1967). Mass and heat transfer from rigid sphere. **AIChE Journal**. 13: 1219-1221.
- Ishii, M. and Zuber, N. (1979). Drag coefficient and relative velocity in bubbly, droplets or particulate flows. **AIChE Journal**. 25(5): 843-855.
- Jakobsen, H. A., Sannaes, B. H., Grevskott, S., and Svendsen, H. F. (1997). Modeling of vertical bubble-driven flows. **Industrial Engineering Chemistry and Research**. 36: 4052-4074.

- Jaworski, Z. and Nienow, A. W. (2003). CFD modeling of continuous precipitation of barium sulphate in a stirred tank. **Chemical Engineering Journal**. 91: 167-174.
- Kleinstreuer, C. (2003). **Two-phase flow: Theory and application**. New York: Taylor and Francis.
- Kramer, H. J. M., Dijkstra, J. W., Neumann, A. M., Meadhra, R. Ó., and van Rosmalen, G. M. (1996). Modeling of industrial crystallizers, a compartmental approach using a dynamic flow-sheeting tool. **Journal of Crystal Growth**. 166: 1084-1088.
- Kramer, H. J. M., Dijkstra, J. W., Verheijen, P. J. T., and van Rosmalen, G. M. (2000). Modeling of industrial crystallizers for control and design purposes. **Powder Technology**. 108: 185-197.
- Lance, M., Marie, J. L., Moursali, E., Bataille, J., Suzanne, C., Roig, V., Bel'Fdhla, R., and Masbernat, L. (1996). Experimental study of turbulent bubbly shear flow. **Chemical Engineering Communication**. 141: 51-70.
- Lapple, C. E. (1951). **Fluid and particle mechanics**. Delaware: University of Delaware Press.
- Liiri, M., Koironen, T., and Aittamaa, J. (2002). Secondary nucleation due to crystal-impeller and crystal-vessel collisions by population balances in CFD modelling. **Journal of Crystal Growth**. 237-239: 2188-2193.
- Lung-Somarriba, B. L. M., Moscosa-Santillan, M., Porte, C., and Delacroix, A. (2002). Stirring optimization and scale-up of crystallization by CFD simulation. **Chemical Engineering Transaction**. 1: 1221-1226.

- Lopez de Bertodano, M. (1991). **Turbulent bubbly flow in triangular duct**. Ph.D. Thesis, Rensselare Polytechnic Institute, Troy New York.
- Maggoris, D., Goulas, A., Alexopoulos, A. H., Chatzi, E. G., and Kiparissides, C. (1998). Use of CFD in prediction of particle size distribution in suspension polymer reactors. **An International Journal of Computer Applications in Chemical Engineering**. 22: 315-322.
- Mandare, P. N. and Pargarkar, V. G. (2003). Semibatch reactive crystallization of sodium perborate tetrahydrate: effect of mixing parameters on crystal size. **Chemical Engineering Science**. 58(7): 1125-1133.
- Maqableh, A., Simmons, K., Hibberd, S., Power, H., and Young, C. (2003). CFD modelling of three-component air/oil flow and heat transfer in rotating annulus. **Proceeding of Eleventh Annual Conference of the CFD society of Canada**. Tenue á Vaconner, Canada.
- Maude (1958). **Cited in Chemical engineers' handbook**, Perry, R. H. and Green, D., McGraw-Hill, New York, 1984, pp. 5-66.
- McCabe, W. L., Smith, J. C., and Harriott, P. (2001). **Unit operations of chemical engineering** (6th ed.). Singapore: McGraw-Hill.
- Mersmann, A. (2001). **Crystallization technology handbook** (2nd ed.). New York: Marcel Dekker.
- Micale, G. and Montante, G. (1999). On the simulation of two-phase solid-liquid stirred vessels. **Proceeding of Fifth CFX International User Conference**. Friedrichshafen, Germany.
- Mullin, J. W. (2001). **Crystallization** (4th ed.). Oxford: Butterworth-Heinemann.

- Myerson, A. E. (2002). **Handbook of industrial crystallization** (2nd ed.). USA: Butterworth-Heinemann.
- Nasr-El-Din, H. A., Mac Taggart, R. S., and Masliyah, J. H. (1996). Local solids concentration measurement in a slurry mixing tank. **Chemical Engineering Science**. 51(8): 1209-1220.
- Oey, R. S. (2005). **Gas-liquid flows in a two-fluid formalism: modeling and validation of closure relations**. Ph.D. Thesis, Delft University of Technology, The Netherlands.
- Oshinowo, L. M. and Bakker, A. (2002). **CFD modeling of solids suspensions in stirred tank** [On-line]. Available: <http://www.bakker.org/cfm>.
- Paul, E. L., Atiemo-Obeng, V. A., and Kresta, S. M. (2004). **Handbook of industrial mixing: Science and practice**. New Jersey: John Wiley & Sons.
- Pennisi, S. N., Liow, J., and Schneider, P. A. (2003). CFD model development for sugar mill evaporators. **Proceeding of Third International Conference on CFD in the Minerals and Process Industries** (pp. 105-110). Melbourne, Australia: CSIRO.
- Pericleous, K. A. and Patel, M. K. (1987). The source-sink approach in the modeling of stirred reactor. **PCH Physiochemical Hydrodynamics**. 9: 279-297.
- Perry, R. H. and Green, D. W. (1997). **Perry's chemical engineers' handbook** (7th ed.). New York: McGraw-Hill.
- Philips, R., Rohani, S., and Baldyga, J. (2000). Micromixing in a single semi-batch precipitation process. **Mixing and Crystallization** (pp. 205-213). Netherland: Kluwer Academic Publishers.

- Randolph, A. D. and Larson, M. A. (1988). **Theory of particulate processes: Analysis and techniques of continuous crystallization** (2nd ed.). California: Academic Press.
- Rein, P. W., Echeverri, L. F., and Acharya, S. (2004). Circulation in vacuum pans. **Journal American Society of Sugar Can Technologists**. 24: 1-17.
- Rielly, C. D. and Marquis, A. J. (2001). A particle's eye view of crystallizer fluid mechanics. **Chemical Engineering Science**. 56: 2475-2493.
- Sadhal, S. S., and Trinh, E. H. (2002). Transport processes during protein crystal growth under microgravity and earth gravity conditions. **Proceeding of the International Symposium on Recent Trends in Heat and Mass Transfer** (pp. 57-80). New Delhi, India: McGraw-Hill.
- Sato, Y. and Sekoguchi, K. (1975). Liquid velocity distribution in two-phase bubble flow. **International Journal of Multiphase Flow**. 2: 79-95.
- Schiller, L. and Naumann, A. (1933). A drag coefficient correlation. **VDI Zeits**. 77: 250-318.
- Sha, Z. and Palosaari, S. (2000a). Size dependent classification function in imperfectly mixed suspension continuous crystallizer. **Mixing and Crystallization** (pp. 133-149). Netherland: Kluwer Academic Publishers.
- Sha, Z., and Palosaari, S. (2000b). Mixing and crystallization in suspensions. **Chemical Engineering Science**. 55(10): 1797-1806.
- Sha, Z., Oinas, P., Louhi-Kultanen, M., Yang, G., and Palosaari, S. (2001). Application of CFD simulation to suspension crystallization factors affecting size-dependent classification. **Powder Technology**. 121: 20-25.

- Sha, Z., Palosaari, S., Oinas, P., and Ogawa, K. (2001). CFD simulation of solid suspension in a stirred tank. **Journal of Chemical Engineering of Japan**. 34(5): 621-626.
- Shamlou, P. A. And Koutsakos, E. (1989). Solid suspension and distribution in liquids under turbulent agitation. **Chemical Engineering Science**. 44(3): 529-542.
- Strickland-Constable, R. F. (1968). **Kinetics and mechanism of crystallization**. London: Academic Press.
- Synowiec, P., Bigda, J., and Wójcik, J. (2002). Comparison of the CFD and experimental data of turbulence field in the MSMR crystallizer. **Chemical Engineering Transaction**. 1: 1191-1196.
- Thompson, T. B. and Kontomaris, K. (1999). **Technology road map for computational fluid dynamics** [On-line]. Available: http://www.eere.energy.gov/industry.chemical/pdfs/cfd_roadmap.pdf.
- Tongtongsakulwong, J. (2003). **Numerical simulation and analysis of flow in crystallization for sugar production**. M.Eng. Thesis, Suranaree University of Technology, Thailand.
- Torbacke, M. and Rasmuson, Å. C. (2001). Influence of different scales of mixing in reaction crystallization. **Chemical Engineering Science**. 56(7): 2459-2473.
- van Leeuwen, M. L. J., Bruinsma, O. S. L., van Rosmalen, G. M., Hounslow, M. J., and Seckler, M. M. (2000) An experimental study to the effects of supersaturation ratio, mpeller speed on agglomeration of aluminum trihydroxide. **Mixing and Crystallization** (pp. 151-161). Netherland: Kluwer Academic Publishers.

- van Leeuwen, M. L. J., Bruinsma, O. S. L., and van Rosmalen, G. M. (1996). Influence of mixing on the product quality in precipitation. **Chemical Engineering Science**. 51(11): 2595-2600.
- Wang, F., Wang, W., Wang, Y., and Mao, Z. (2003). CFD simulation of solid-liquid two-phase flow in baffled stirred vessels with rushton impellers. **Proceeding of Third International Conference on CFD in the Minerals and Process Industries** (pp. 287-292). Melbourne, Australia: CSIRO.
- Wei, H., Zhou, W., and Garside, J. (2001). Computational fluid dynamics modeling of the precipitation process in a semibatch crystallizer. **Industrial Engineering Chemistry and Research**. 40: 5255-5261.
- Yang, W. (2003). **Handbook of fluidization and fluid-particle system**. New York: Marcel Dekker, Inc.
- Yang, G., Louhi-Kultanen, M., and Kallas, J. (2002). The CFD simulation of programmed batch cooling crystallization. **Chemical Engineering Transaction**. 1: 83-88.
- Zauner, R. and Jones, A. G. (2002). On the influence of mixing on crystal precipitation processes-application of the segregated feed model. **Chemical Engineering Science**. 57(5): 821-831.

APPENDIX A

SUMMARY OF THE AGREEMENT BETWEEN

EXPERIMENT RESULTS AND CFD MODELING

IN PREVIOUS STUDY

Table A.1 Summary of the agreement between experiment results and CFD modeling in previous studies.

System/Condition	Researcher (by experiment)	Researcher (by CFD)	Results
Solid suspension in the stirred tank	Shamlou <i>et al.</i> (1989) and Nasr-El-Din <i>et al.</i> (1996)	Sha, Palosaari <i>et al.</i> (2001), Oshinowo and Bakker (2002), and Wang <i>et al.</i> (2003)	The uniformity of the solid distribution in the mixing tank were found to be a function of particle size, impeller speed, and mixing intensity, such as the uniformity increased with increasing impeller speed.
	Barresi and Baldi (1987)	Sha, Palosaari <i>et al.</i> (2001)	<ul style="list-style-type: none"> -The particle free zone at the top of the vessel increased when the impeller speed decreased. -The maximum solid concentration occurred on the centre of the tank bottom, the level gradually decreased from the bottom to the free surface. -The height from the bottom of vessel to the

Table A.1 (continued)

System/Condition	Researcher (by experiment)	Researcher (by CFD)	Results
Solid suspension in the stirred tank			location of maximum solid concentration rose with increasing the impeller speed.
	Brucato <i>et al.</i> (2002) studied both experiment and CFD modeling		Clear liquid layer decreased with increasing agitation speed.
Suspension continuous crystallizer	Sha and Palosaari (2000b)	Sha, Oinas <i>et al.</i> (2001), and Rielly and Marquis (2001)	Confirmed non-ideal MSMPR or imperfectly mixed suspension crystallizer.
	Sha and Palosaari (2000a)	Sha, Oinas <i>et al.</i> (2001)	The product classification depended on the crystal size, product removal location, mixing intensity, and tank geometry, such as it decreased with increasing mixing intensity for the same size particle.

Table A.1 (continued)

System/Condition	Researcher (by experiment)	Researcher (by CFD)	Results
Suspension continuous crystallizer	Franke and Mersmann (1995)	Synowice <i>et al.</i> (2002)	-System without draft tube and flat bottom used the power input was higher than with draft tube and elliptic bottom. -Increasing of stirrer diameter affected on decreasing power input.
Continuous precipitation	Farkas <i>et al.</i> (1996)	Van Leeuwen, Bruinsma, and van Rosmalen (1996)	Mean particle size increased with increasing resident time.
	Jaworski and Nienow (2003) studied both experiment and CFD modeling		The inlet velocity ratio influenced the area mean particle size, the coefficient of variation of CSD and the degree of conversion.

Table A.1 (continued)

System/Condition	Researcher (by experiment)	Researcher (by CFD)	Results
Semibatch precipitation	Philips <i>et al.</i> (2000)	Wei <i>et al.</i> (2001)	-Mean crystal size depended on impeller speed, operating time, and feed location, such as it increased linearly with the operating time. -Reactive precipitation only occurred in an effective zone (such as near the feed point).
	Áslund and Rasmuson (1992)	Zauner and Jones (2002)	The particle size distribution depended on the feed point position, feed rate, feed tube diameter, average and local dissipation, and impeller types and speed
Batch vacuum pan (evaporative crystallizer)	-	Rein <i>et al.</i> (2004)	The circulation was a particularly important factor (see Figure 2.12 in chapter 2)

Table A.1 (continued)

System/Condition	Researcher (by experiment)	Researcher (by CFD)	Results
Continuous vacuum pan (evaporative crystallizer)	Pennisi <i>et al.</i> studied both experiment and CFD modeling		Large amount of mixing was found to occur at the inlet (see Figure 2.13 in chapter 2)
FCC (evaporative crystallizer)	-	Essemiani <i>et al.</i> (2004)	-The system was not perfectly mixed. -Feed rate and crystallizer geometry affected the flow characteristic (see Figure 2.14 in chapter 2).

APPENDIX B

MATHEMATICAL NOTATIONS AND FUNCTIONS

This section describes the basic notations and functions which are used throughout this documentation.

B.1 The Vector Operator ∇ and $\nabla \cdot$

For a Cartesian coordinate system in which \mathbf{i} , \mathbf{j} , and \mathbf{k} are unit vectors in the three coordinate directions, the gradient, ∇ , is defined as:

$$\nabla = \left[\frac{\partial}{\partial x}, \frac{\partial}{\partial y}, \frac{\partial}{\partial z} \right] \quad (\text{B.1})$$

For a scalar function $\phi(x, y, z)$ the gradient of ϕ is defined by

$$\nabla \phi = \frac{\partial \phi}{\partial x} \mathbf{i} + \frac{\partial \phi}{\partial y} \mathbf{j} + \frac{\partial \phi}{\partial z} \mathbf{k} \text{ or } \nabla \phi = \left[\frac{\partial \phi}{\partial x}, \frac{\partial \phi}{\partial y}, \frac{\partial \phi}{\partial z} \right] \quad (\text{B.2})$$

Note that the scalar functions used in this work are h , p , and T .

For a vector function $\mathbf{U}(x, y, z)$ where

$$\mathbf{U} = \begin{bmatrix} U_x \\ U_y \\ U_z \end{bmatrix} \quad (\text{B.3})$$

The divergence of the vector, $\text{div } \mathbf{U}$, is defined by

$$\nabla \cdot \mathbf{U} = \frac{\partial U_x}{\partial x} + \frac{\partial U_y}{\partial y} + \frac{\partial U_z}{\partial z} \quad (\text{B.4})$$

The divergence of the other vector function (\mathbf{g} and \mathbf{S}_M) are defined similarly to the above equation.

B.2 The Dyadic Product

The dyadic product is a tensor product; it is the multiplication of one vector by another.

The tensor product of the two vectors, \mathbf{U} and \mathbf{U} , is defined as:

$$\mathbf{U}\mathbf{U} = \begin{bmatrix} U_x U_x & U_x U_y & U_x U_z \\ U_y U_x & U_y U_y & U_y U_z \\ U_z U_x & U_z U_y & U_z U_z \end{bmatrix} \quad (\text{B.5})$$

The tensor product of two vectors, ∇ and \mathbf{U} , is defined as:

$$\nabla \mathbf{U} = \begin{bmatrix} \frac{\partial U_x}{\partial x} & \frac{\partial U_y}{\partial x} & \frac{\partial U_z}{\partial x} \\ \frac{\partial U_x}{\partial y} & \frac{\partial U_y}{\partial y} & \frac{\partial U_z}{\partial y} \\ \frac{\partial U_x}{\partial z} & \frac{\partial U_y}{\partial z} & \frac{\partial U_z}{\partial z} \end{bmatrix} \quad (\text{B.6})$$

By the definition above the divergence of the vector, $\text{div } \nabla \bullet \rho \mathbf{U} \mathbf{U}$, is represented as:

$$\nabla \bullet \rho \mathbf{U} \mathbf{U} = \begin{bmatrix} \frac{\partial}{\partial x}(\rho U_x U_x) + \frac{\partial}{\partial y}(\rho U_y U_x) + \frac{\partial}{\partial z}(\rho U_z U_x) \\ \frac{\partial}{\partial x}(\rho U_x U_y) + \frac{\partial}{\partial y}(\rho U_y U_y) + \frac{\partial}{\partial z}(\rho U_z U_y) \\ \frac{\partial}{\partial x}(\rho U_x U_z) + \frac{\partial}{\partial y}(\rho U_y U_z) + \frac{\partial}{\partial z}(\rho U_z U_z) \end{bmatrix} \quad (\text{B.7})$$

B.3 Matrix Transposition

The transpose of a matrix is defined by the operator T . For example, the transpose of $\nabla \mathbf{U}$ is defined as:

$$(\nabla \mathbf{U})^T = \begin{bmatrix} \frac{\partial U_x}{\partial x} & \frac{\partial U_x}{\partial y} & \frac{\partial U_x}{\partial z} \\ \frac{\partial U_y}{\partial x} & \frac{\partial U_y}{\partial y} & \frac{\partial U_y}{\partial z} \\ \frac{\partial U_z}{\partial x} & \frac{\partial U_z}{\partial y} & \frac{\partial U_z}{\partial z} \end{bmatrix} \quad (\text{B.8})$$

B.4 Mathematical Functions Used in the Study

- **max**([a], [b]) is the maximum values between [a] and [b].
- **min**([a], [b]) is the minimum values between [a] and [b].
- **step(x)** is 0 for negative x, 1 for positive x and 0.5 for x = 0. x must be dimensionless.

APPENDIX C

THE NUMBER OF NODES AND ELEMENTS

OF EACH CASE STUDY

In this thesis work, the mesh structures depend on the flow conditions of each case study so the number of nodes and elements are not the same numbers. The number of nodes and elements of each case study are shown in the below table.

Table C.1 The number of nodes and elements of each case study.

Case Study Number	Number of Nodes	Number of Elements
1	78,390	392,766
2	78,767	393,690
3	77,029	384,838
4	76,770	384,419
5	76,613	383,409
6	78,383	390,631
7	79,184	393,219
8	79,211	393,108
9	76,053	381,785
10	76,613	383,409
11	78,764	392,646
12	79,786	396,756

Table C.1 (Continued)

Case Study Number	Number of Nodes	Number of Elements
13	81,984	407,244
14	76,260	381,813
15	76,442	382,586
16	76,613	383,409
17	76,360	381,760
18	77,653	387,606
19	63,259	316,734
20	66,892	335,903
21	65,938	334,514
22	63,994	322,192

APPENDIX D
SIMULATION RESULTS

D.1 Isothermal Simulation Results

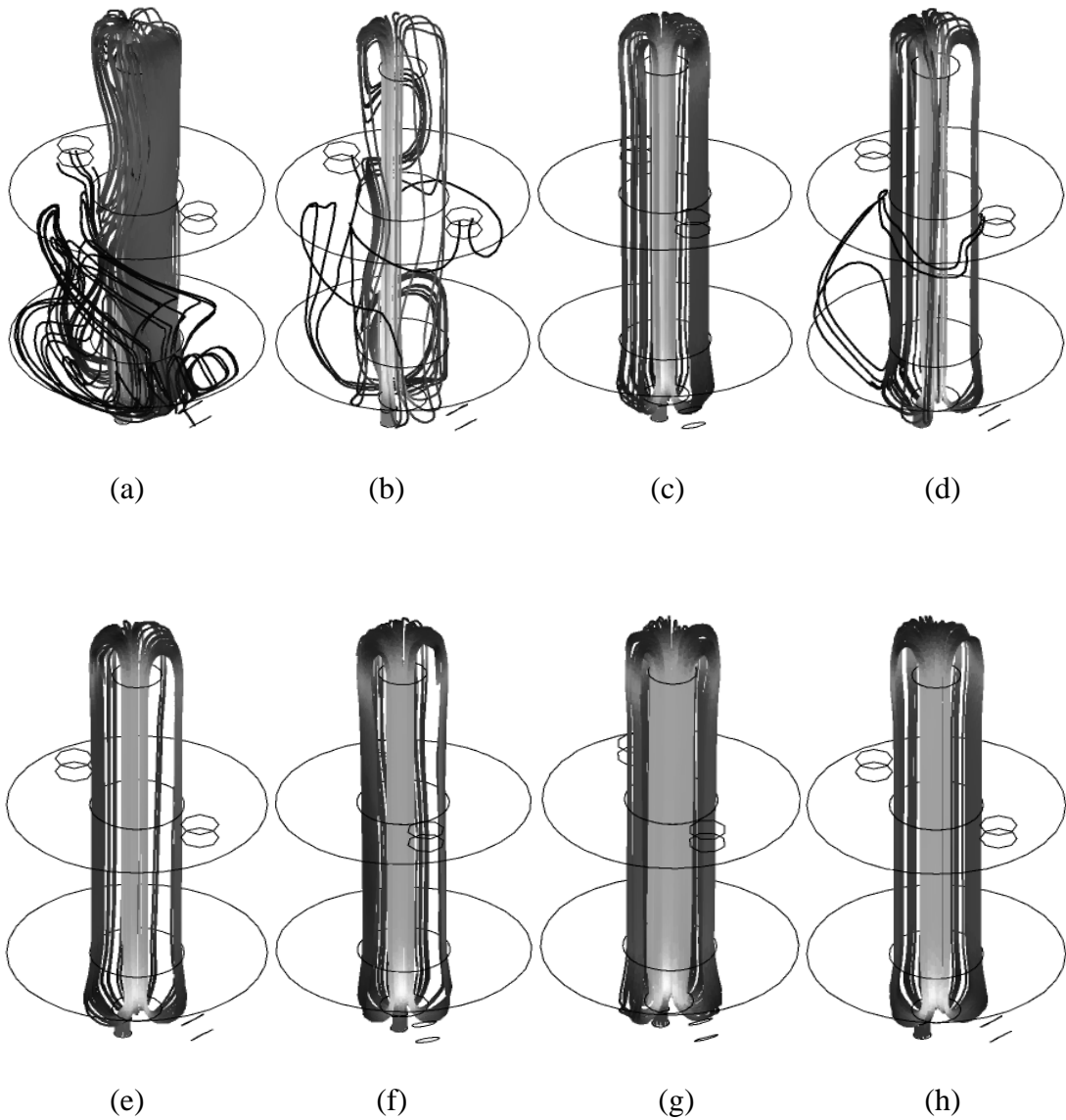


Figure D.1 3D streamlines of liquid velocity in DTB crystallizer for momentum source additions of (a) $0 \text{ kg/m}^2/\text{s}^2$; (b) $1,000 \text{ kg/m}^2/\text{s}^2$; (c) $4,000 \text{ kg/m}^2/\text{s}^2$; (d) $7,000 \text{ kg/m}^2/\text{s}^2$; (e) $10,000 \text{ kg/m}^2/\text{s}^2$; (f) $15,000 \text{ kg/m}^2/\text{s}^2$; (g) $25,000 \text{ kg/m}^2/\text{s}^2$; (h) $30,000 \text{ kg/m}^2/\text{s}^2$.

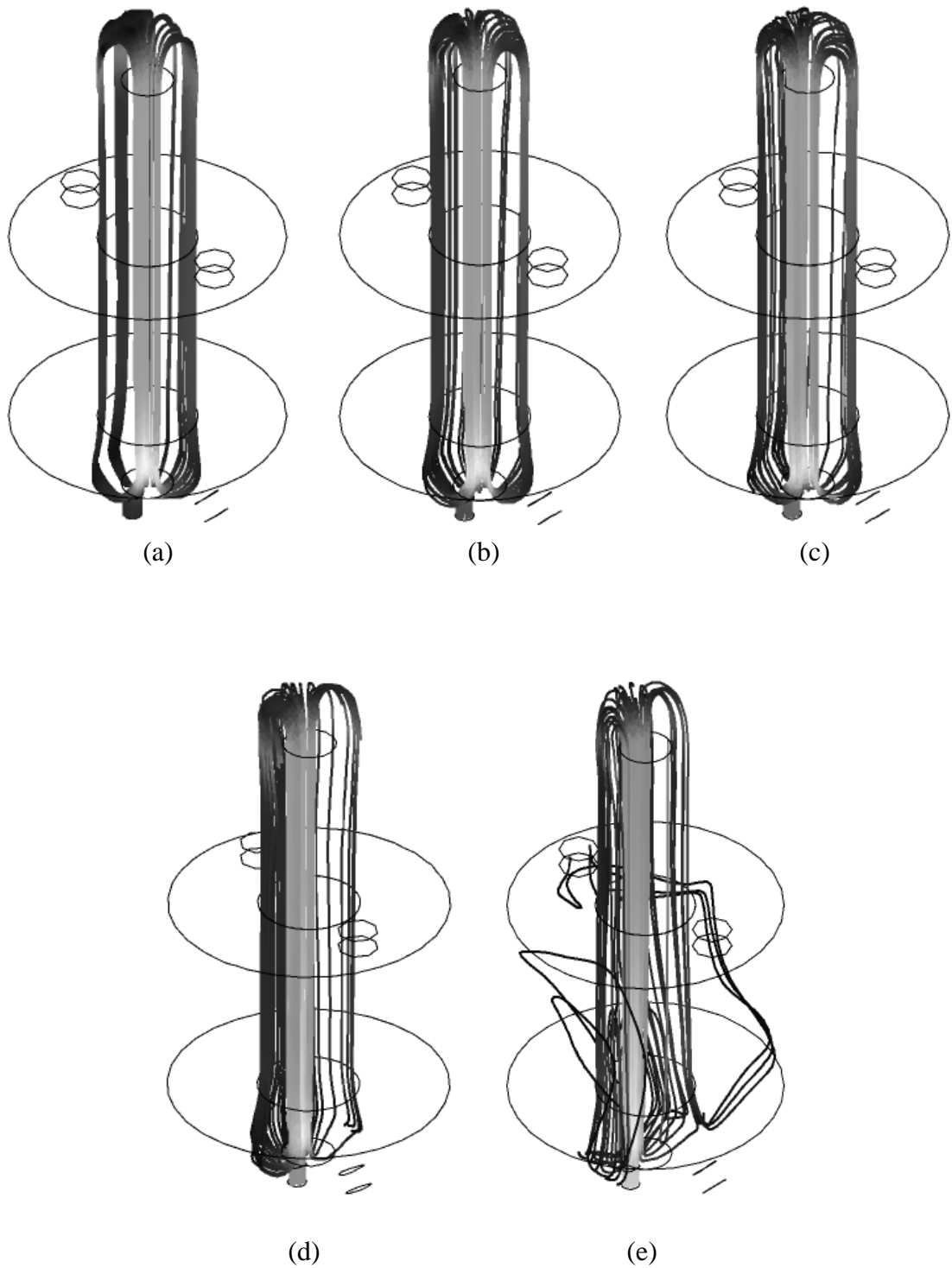


Figure D.2 3D streamlines of liquid velocity in DTB crystallizer for fines removal flows of (a) 0.4672 kg/s; (b) 1.0063 kg/s; (c) 1.5454 kg/s; (d) 2.3002 kg/s; (e) 3.594 kg/s.

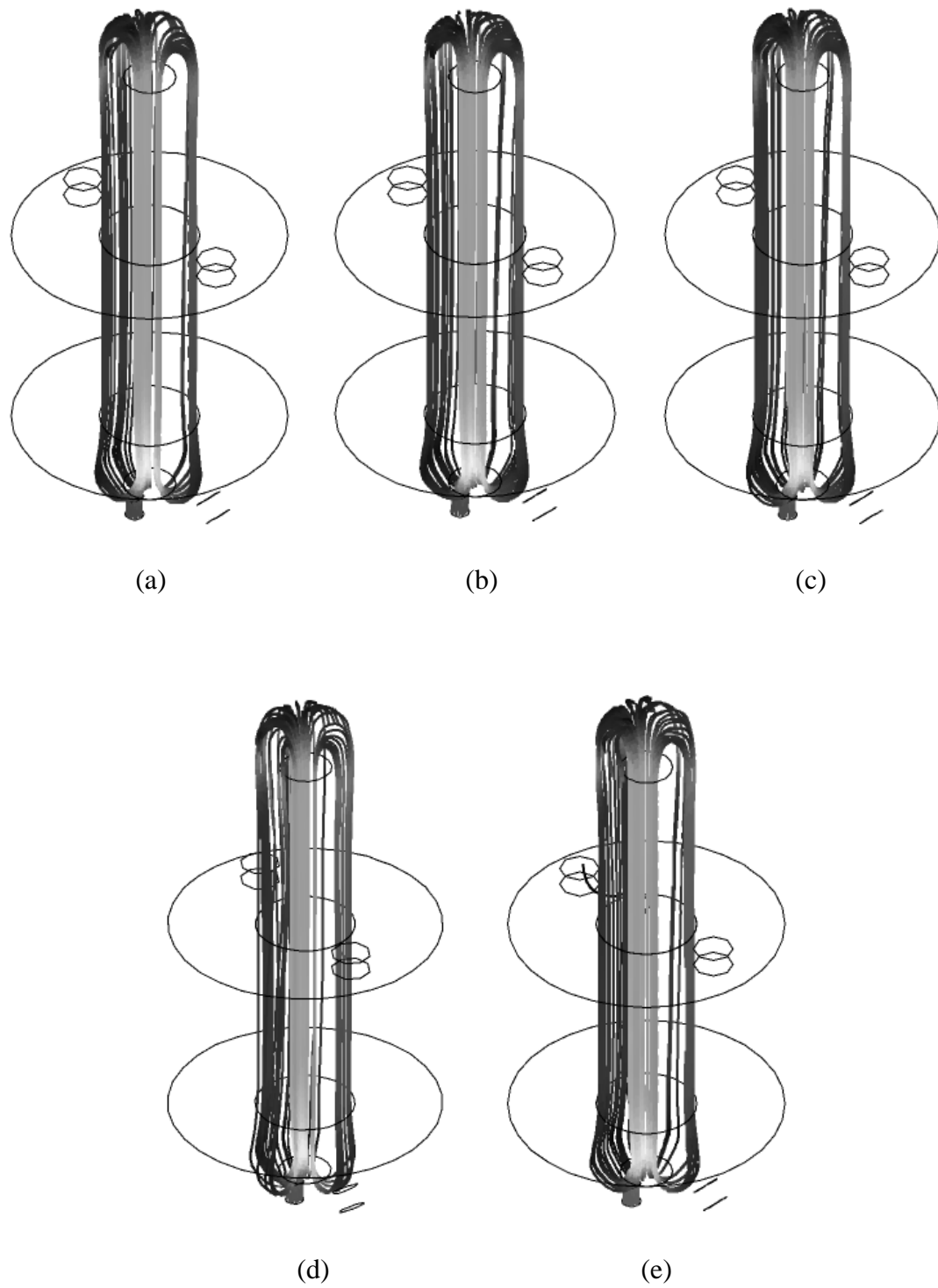


Figure D.3 3D streamlines of liquid velocity in DTB crystallizer for product crystal suspension flows of (a) 0.0599 kg/s; (b) 0.1198 kg/s; (c) 0.1797 kg/s; (d) 0.2636 kg/s; (e) 0.4672kg/s.

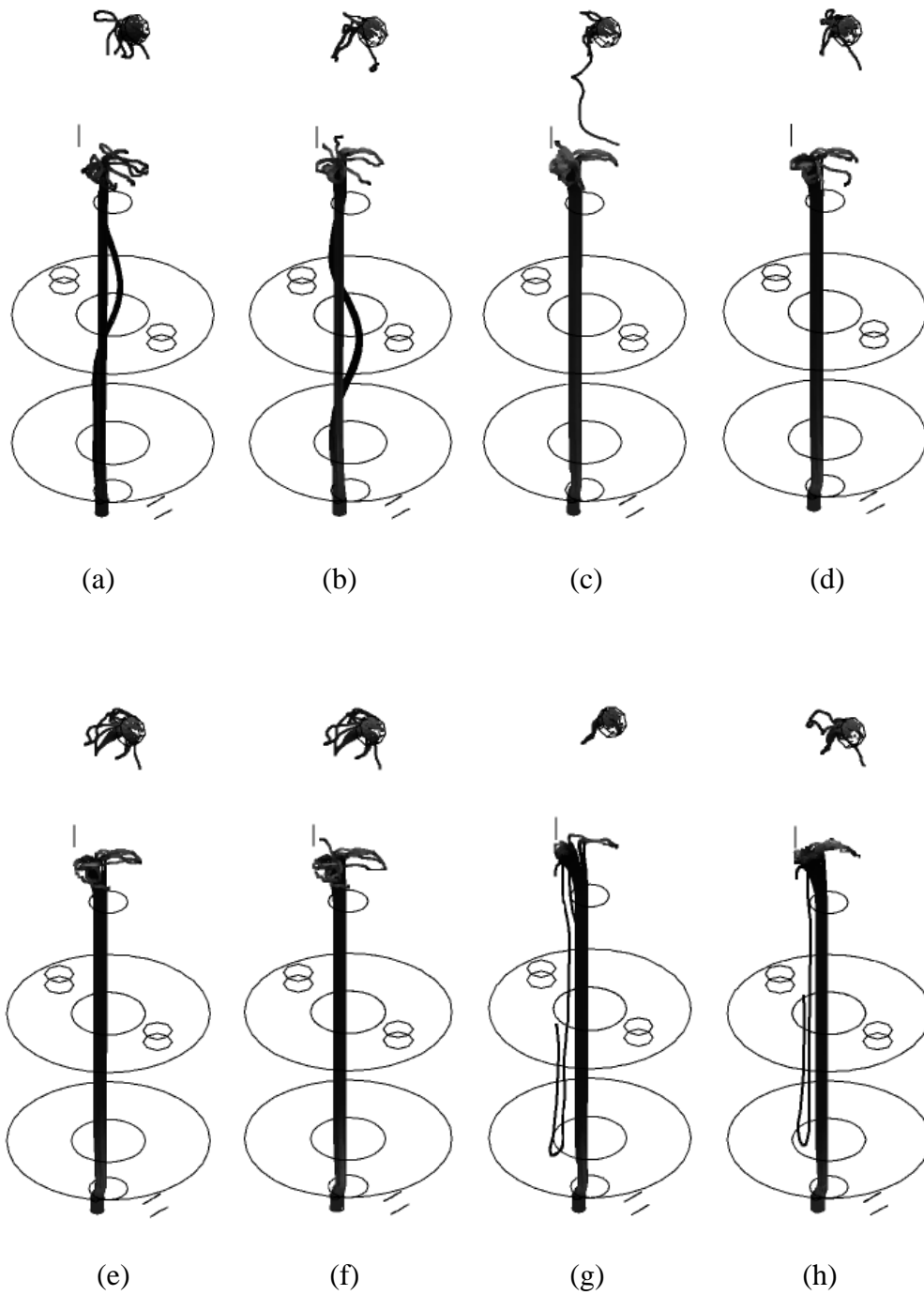


Figure D.4 3D streamlines of vapor velocity in DTB crystallizer for momentum source additions of (a) $0 \text{ kg/m}^2/\text{s}^2$; (b) $1,000 \text{ kg/m}^2/\text{s}^2$; (c) $4,000 \text{ kg/m}^2/\text{s}^2$; (d) $7,000 \text{ kg/m}^2/\text{s}^2$; (e) $10,000 \text{ kg/m}^2/\text{s}^2$; (f) $15,000 \text{ kg/m}^2/\text{s}^2$; (g) $25,000 \text{ kg/m}^2/\text{s}^2$; (h) $30,000 \text{ kg/m}^2/\text{s}^2$.

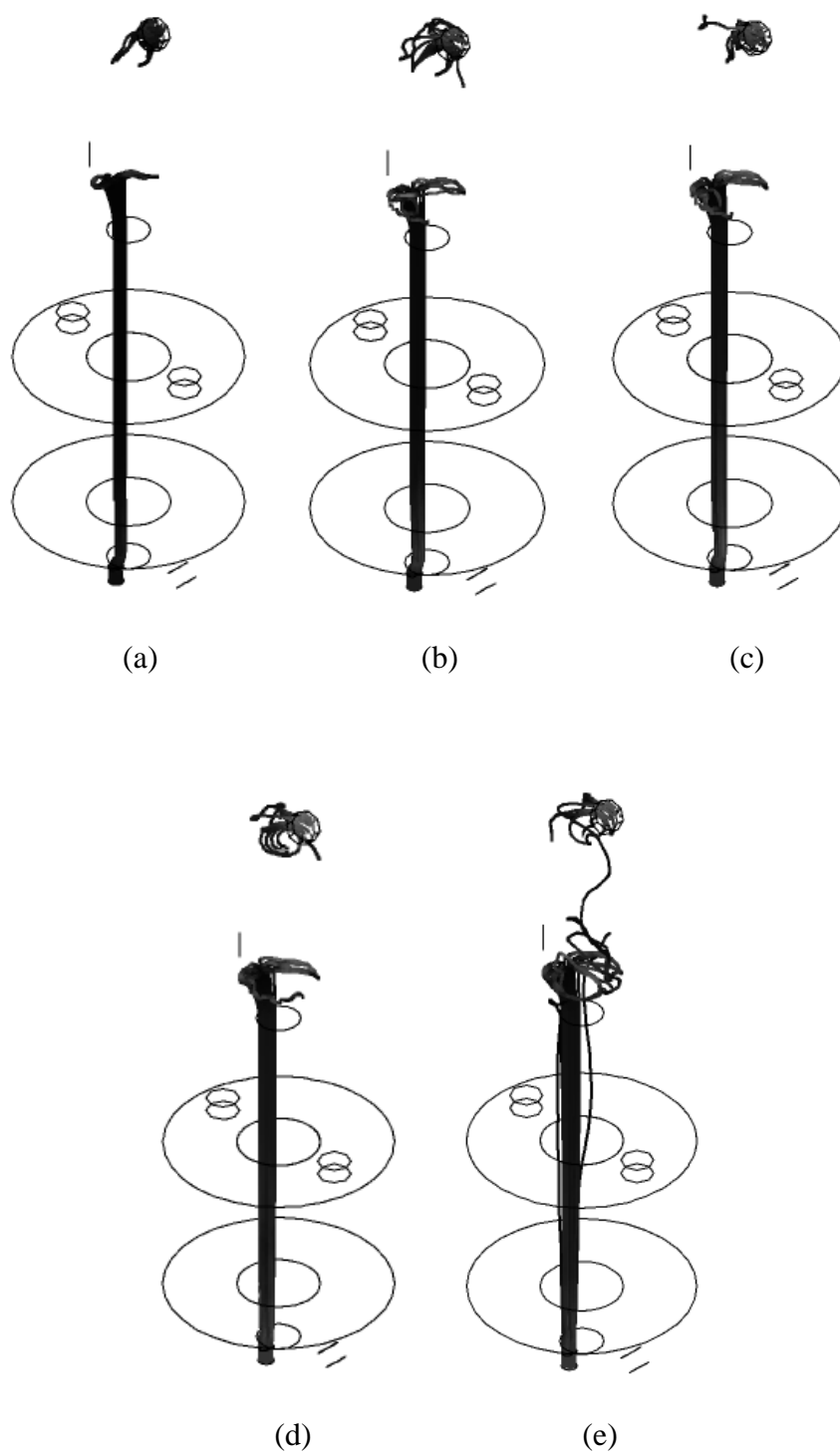


Figure D.5 3D streamlines of vapor velocity in DTB crystallizer for fines removal flows of (a) 0.4672 kg/s; (b) 1.0063 kg/s; (c) 1.5454 kg/s; (d) 2.3002 kg/s; (e) 3.594 kg/s.

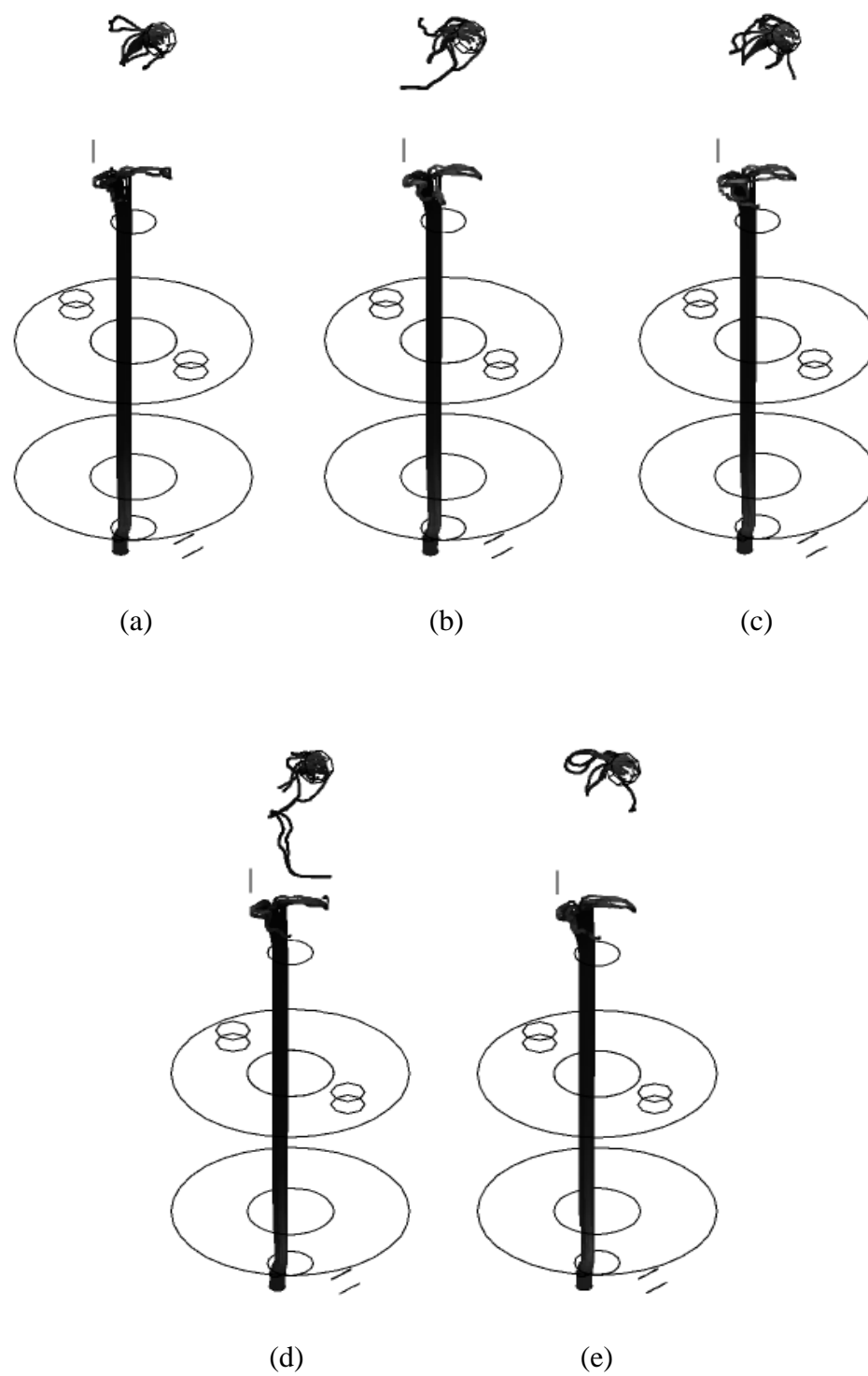


Figure D.6 3D streamlines of vapor velocity in DTB crystallizer for product crystal suspension flows of (a) 0.0599 kg/s; (b) 0.1198 kg/s; (c) 0.1797 kg/s; (d) 0.2636 kg/s; (e) .4672 kg/s.

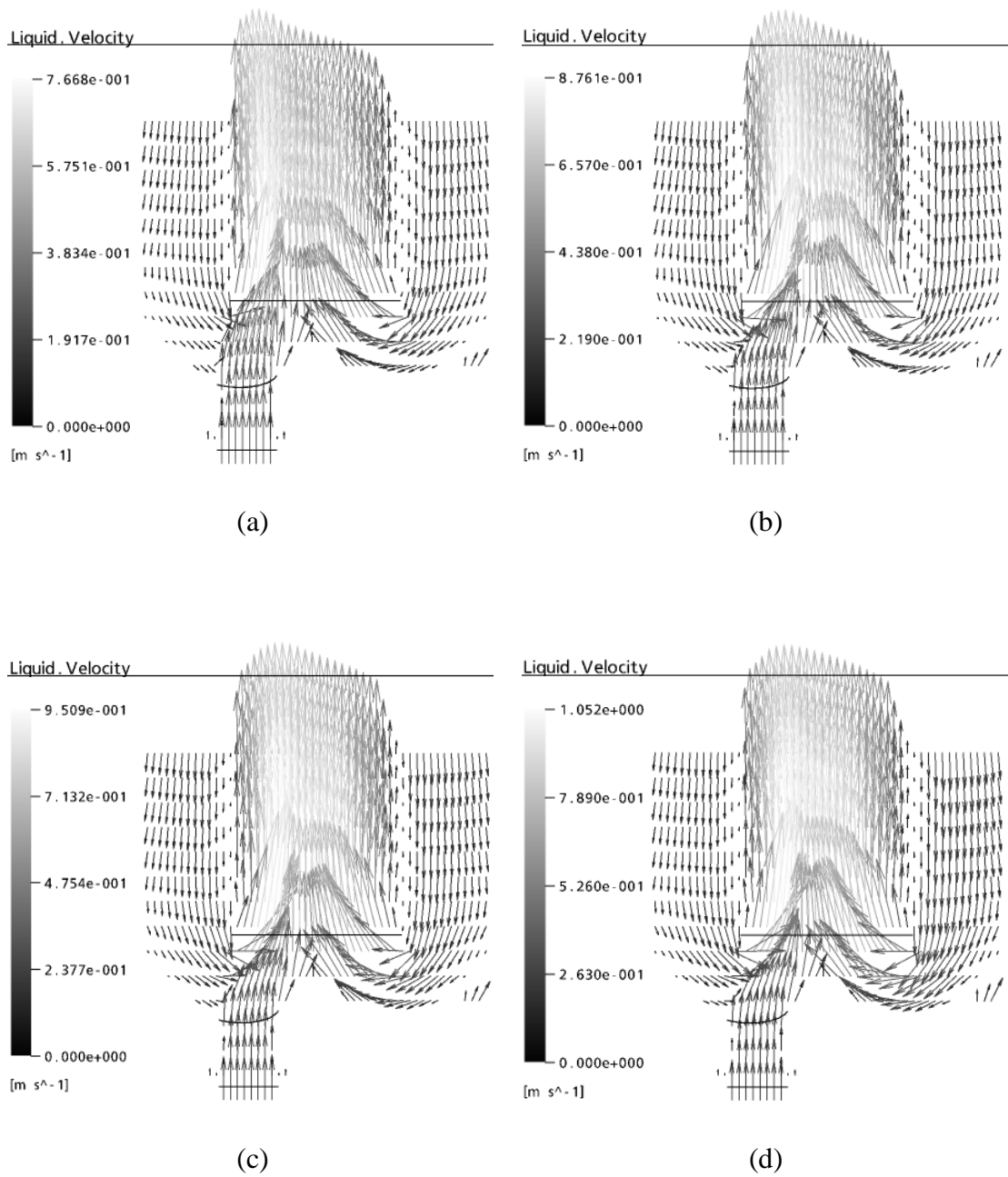


Figure D.7 Liquid velocity vectors at the tank bottom for momentum source additions of (a) $4,000\ kg/m^2/s^2$; (b) $7,000\ kg/m^2/s^2$; (c) $10,000\ kg/m^2/s^2$; (d) $15,000\ kg/m^2/s^2$ (*continued*)

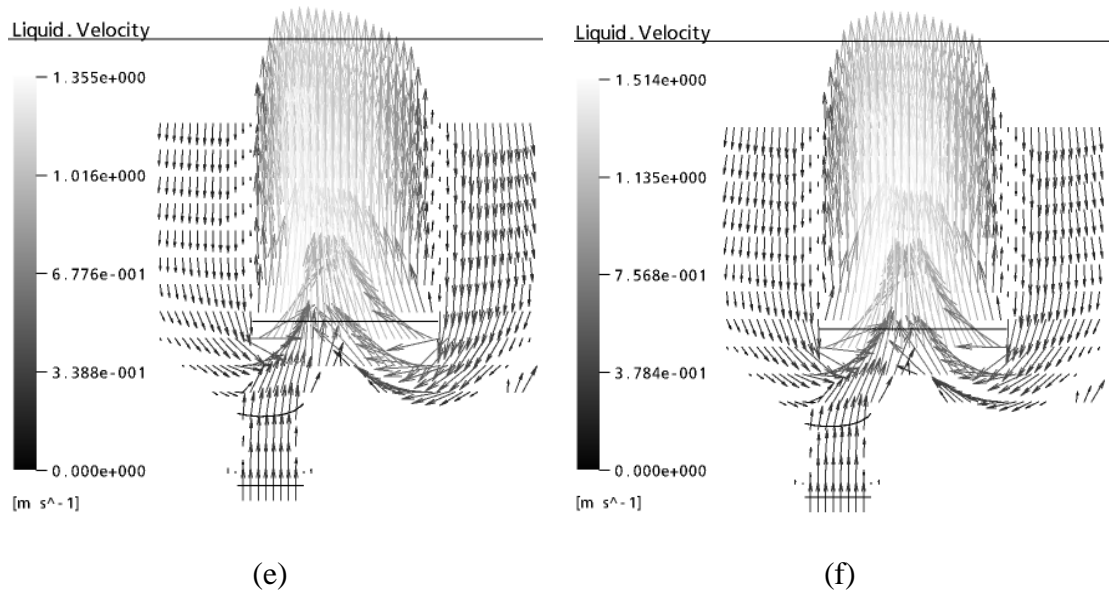


Figure D.7 (continued) (e) $25,000 \text{ kg/m}^2/\text{s}^2$; (f) $30,000 \text{ kg/m}^2/\text{s}^2$.

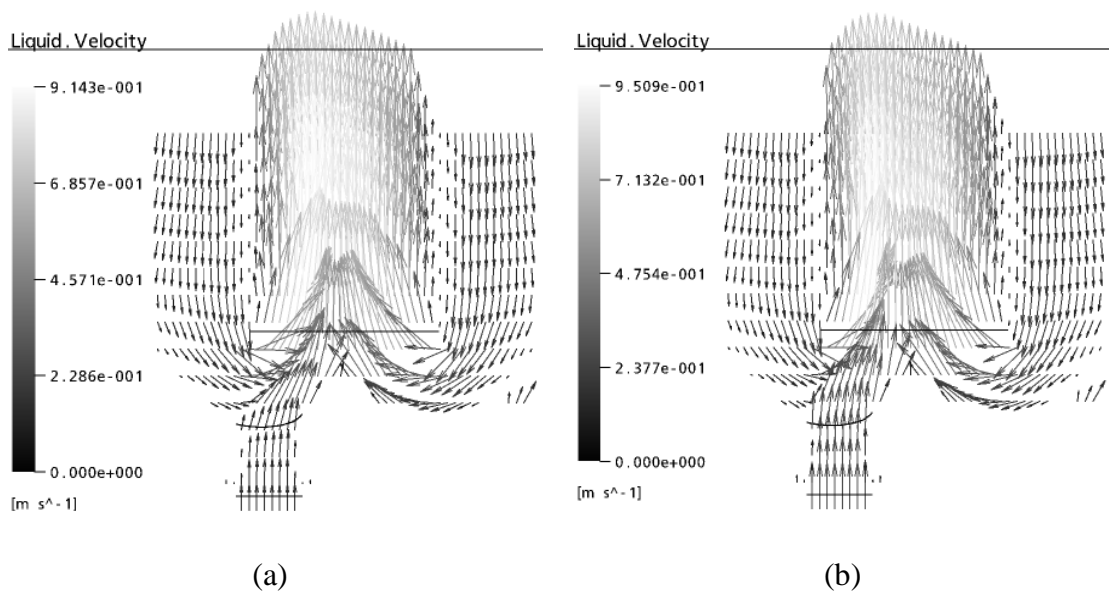


Figure D.8 Liquid velocity vectors at the tank bottom for fines removal flows of (a) 0.4672 kg/s ; (b) 1.0063 kg/s ; (continued)

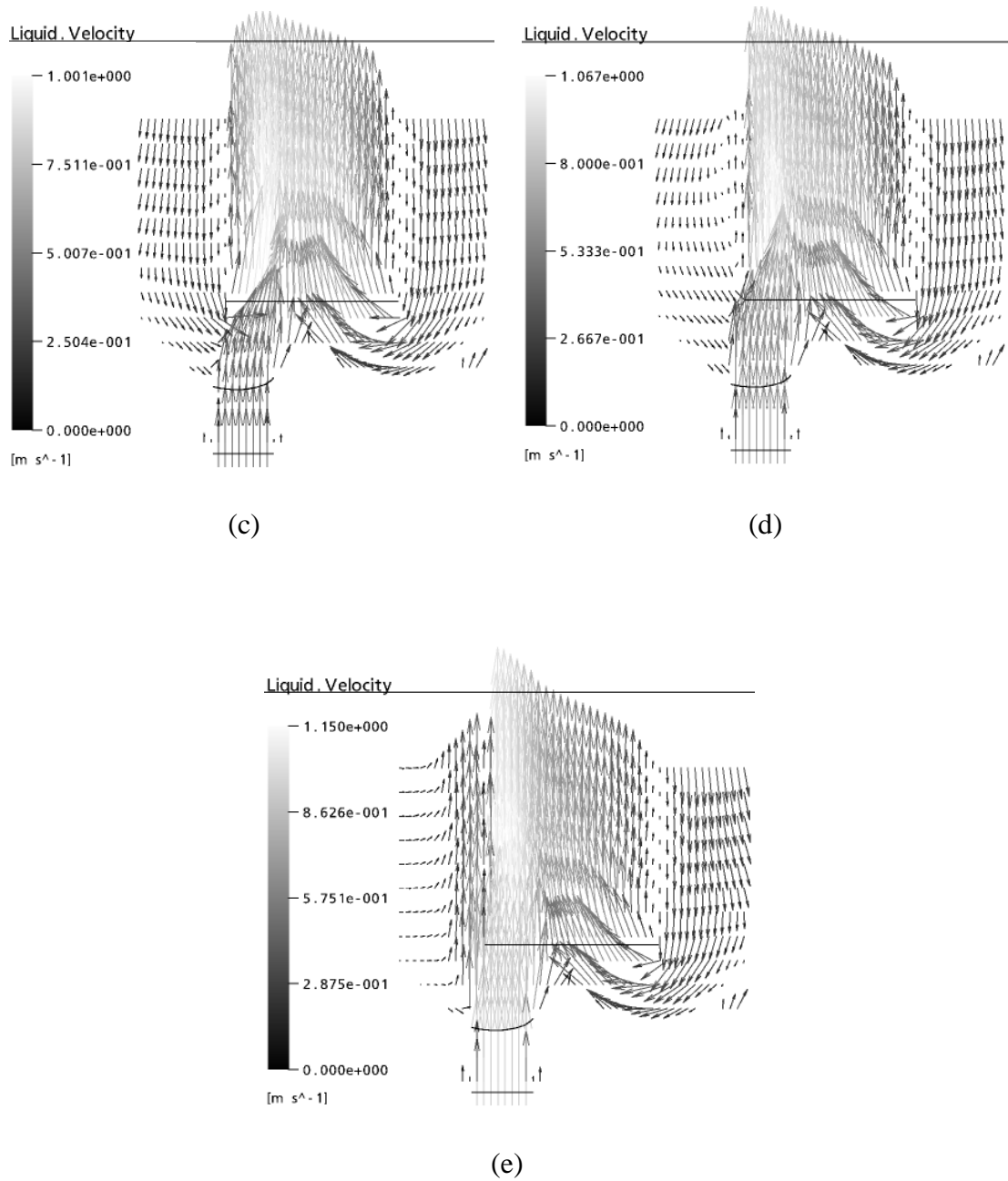


Figure D.8 (continued) (c) 1.5454 kg/s; (d) 2.3002 kg/s; (e) 3.594 kg/s.

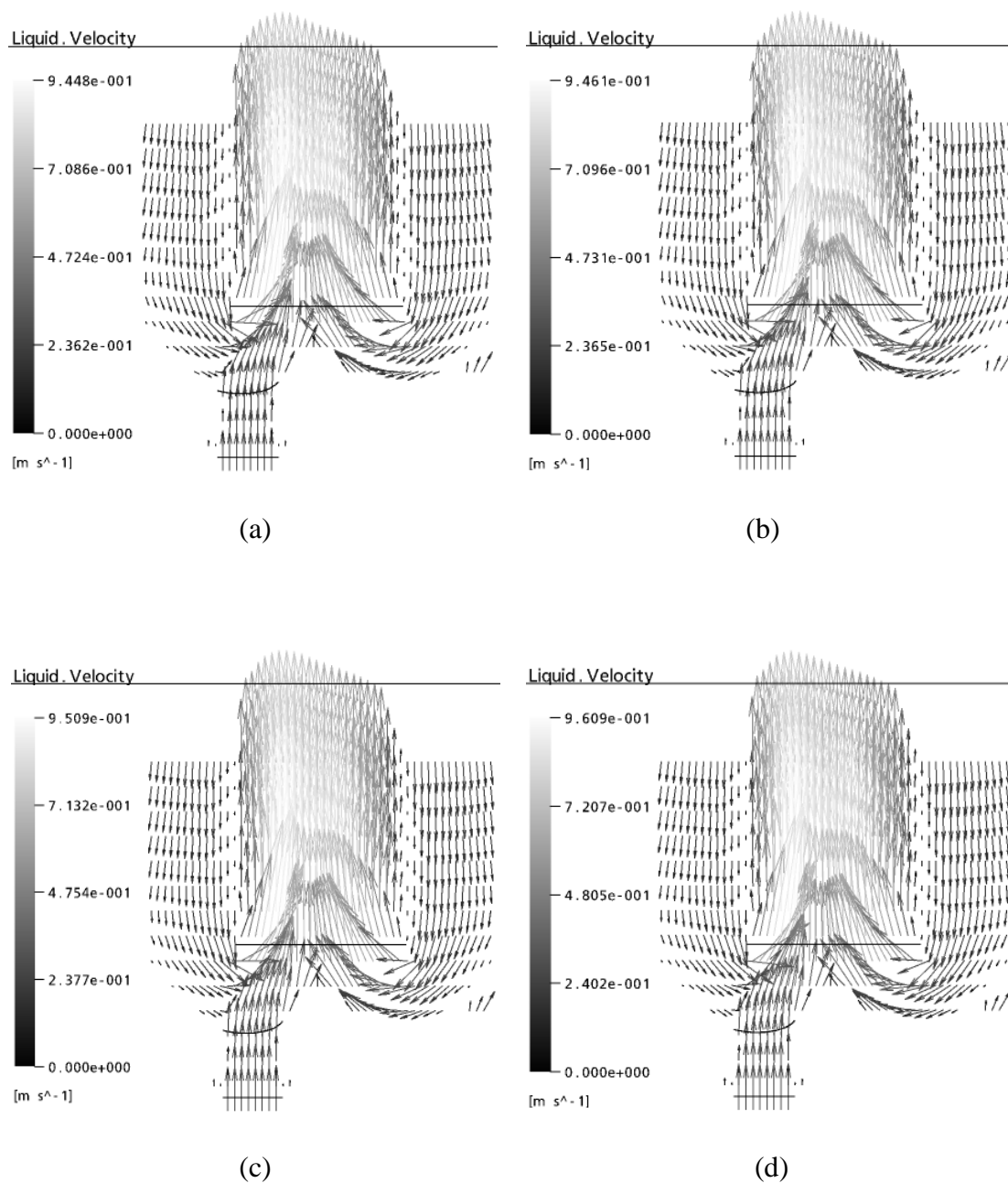
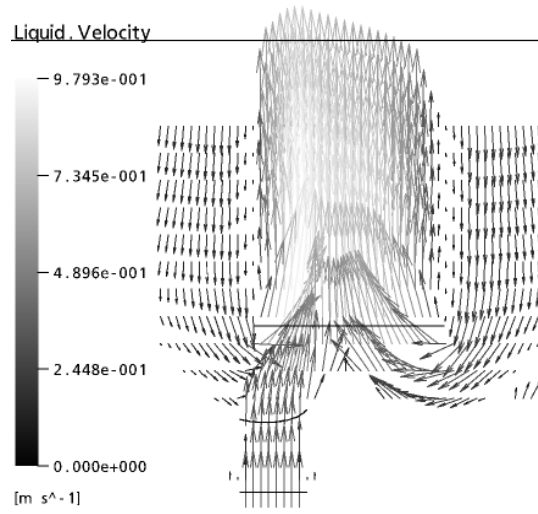


Figure D.9 Liquid velocity vectors at the tank bottom for product crystal suspension flows of (a) 0.0599 kg/s; (b) 0.1198 kg/s; (c) 0.1797 kg/s; (d) 0.2636 kg/s; (*continued*)



(e)

Figure D.9 (continued) (e) 0.4672 kg/s.

D.2 Non-isothermal Simulation Results

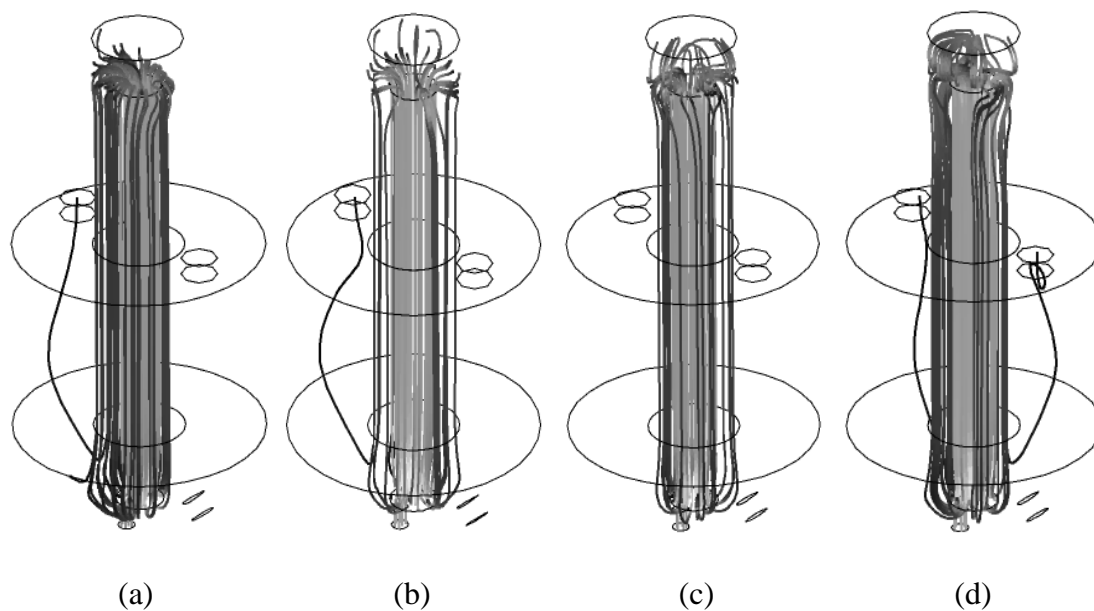


Figure D.10 3D streamlines of liquid velocity in DTB crystallizer for heat source additions of (a) $11,000 \text{ kW/m}^3$; (b) $12,000 \text{ kW/m}^3$; (c) $13,000 \text{ kW/m}^3$; (d) $13,500 \text{ kW/m}^3$.

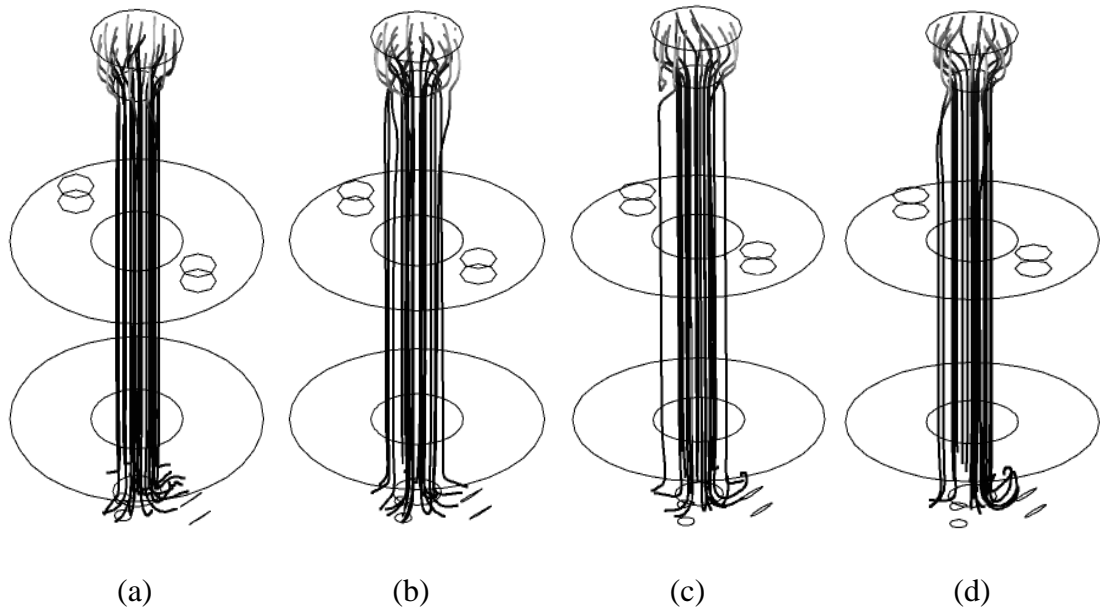


Figure D.11 3D streamlines of vapor velocity in DTB crystallizer for heat source additions of (a) $11,000 \text{ kW/m}^3$; (b) $12,000 \text{ kW/m}^3$; (c) $13,000 \text{ kW/m}^3$; (d) $13,500 \text{ kW/m}^3$.

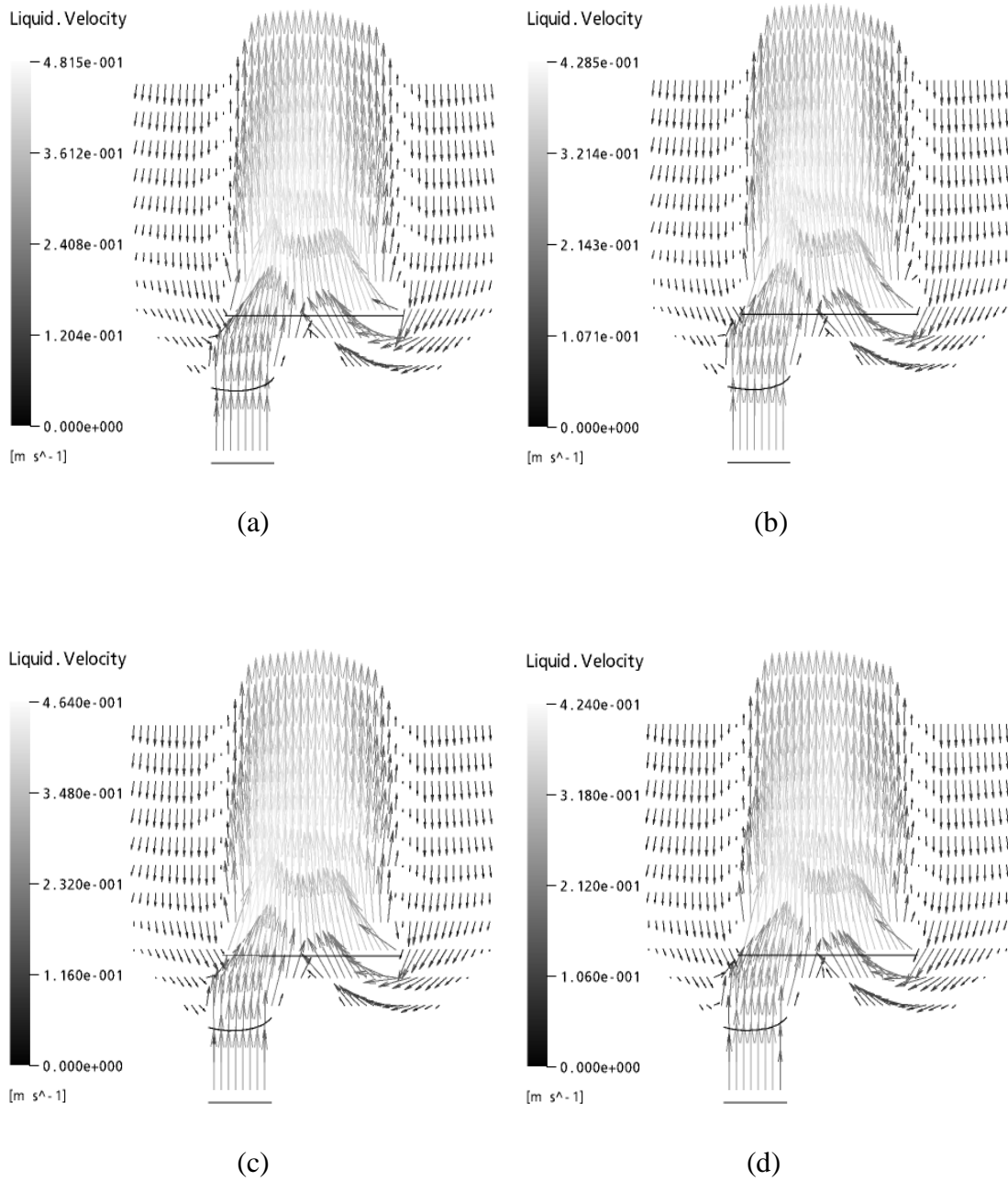


Figure D.12 Liquid velocity vectors at the tank bottom for heat source additions of (a) $11,000 \text{ kW/m}^3$; (b) $12,000 \text{ kW/m}^3$; (c) $13,000 \text{ kW/m}^3$; (d) $13,500 \text{ kW/m}^3$.

APPENDIX E
EXAMPLE OF SOURCE CODES

The source code of case study number 5 (with momentum source addition of $10,000 \text{ kg/m}^2/\text{s}^2$) is shown below:

This run of the CFX-10.0 Solver started at 12:14:10 on 19 Jan 2006 by user Lek on SUT-C7J1H7UTXTQ (intel_p4.sse2_winnt5.1) using the command:

```
"C:\Program Files\Ansys Inc\CFX\CFX-10.0\bin\perl\lib\cfx5solve.pl"  
-stdout-comms -batch -ccl -
```

Setting up CFX-5 Solver run...

```
+-----+  
|               CFX Command Language for Run               |  
+-----+
```

LIBRARY:

CEL:

EXPRESSIONS:

Den = 1198 [kg m⁻³]

FH = 2.11 [m]

VFLiquid = step((FH-y)/1[m])

Press = Den*g*VFLiquid*(FH-y)

VFVapor = 1-VFLiquid

END

END

MATERIAL: Liquid

Material Group = User

Option = Pure Substance

Thermodynamic State = Liquid

PROPERTIES:

Option = General Material

DYNAMIC VISCOSITY:

Dynamic Viscosity = 0.00152 [Pa s]

Option = Value

END

EQUATION OF STATE:

Density = 1198 [kg m⁻³]

Molar Mass = 1.0 [kg kmol⁻¹]

Option = Value

END

THERMAL CONDUCTIVITY:

Option = Value

Thermal Conductivity = 0.57 [W m⁻¹ K⁻¹]

END

END

MATERIAL: Vapor

Material Group = User

Option = Pure Substance

Thermodynamic State = Gas

PROPERTIES:

Option = General Material

DYNAMIC VISCOSITY:

Dynamic Viscosity = 0.0000124 [Pa s]

Option = Value

END

EQUATION OF STATE:

Density = 0.59 [kg m⁻³]

Molar Mass = 1.0 [kg kmol⁻¹]

Option = Value

END

THERMAL CONDUCTIVITY:

Option = Value

Thermal Conductivity = 0.025 [W m⁻¹ K⁻¹]

END

END

END

END

EXECUTION CONTROL:

PARALLEL HOST LIBRARY:

HOST DEFINITION: sutc7j1h7utxtq

Remote Host Name = SUT-C7J1H7UTXTQ

Installation Root = C:\Program Files\Ansys Inc\CFX\CFX-%v

Host Architecture String = intel_p4.sse2_winnt5.1

END

END

PARTITIONER STEP CONTROL:

Multidomain Option = Independent Partitioning

Runtime Priority = Standard

MEMORY CONTROL:

Memory Allocation Factor = 1.0

END

```

PARTITIONING TYPE:
  MeTiS Type = k-way
  Option = MeTiS
  Partition Size Rule = Automatic
END
END
RUN DEFINITION:
  Definition File = D:/CFXworks/IsothermalIDTB/IsoDTB/IsoDTBCase4.def
  Interpolate Initial Values = Off
  Run Mode = Full
END
SOLVER STEP CONTROL:
  Runtime Priority = Standard
EXECUTABLE SELECTION:
  Double Precision = Off
END
MEMORY CONTROL:
  Memory Allocation Factor = 1.0
END
PARALLEL ENVIRONMENT:
  Number of Processes = 1
  Start Method = Serial
END
END
FLOW:
  DOMAIN: IsoDTB
  Coord Frame = Coord 0
  Domain Type = Fluid
  Fluids List = Liquid,Vapor
  Location = Assembly
  BOUNDARY: Solution Inlet
  Boundary Type = INLET
  Location = Solution Inlet
  BOUNDARY CONDITIONS:
  FLOW REGIME:
    Option = Subsonic
  END
  MASS AND MOMENTUM:
    Option = Fluid Velocity
  END
  TURBULENCE:
    Option = Medium Intensity and Eddy Viscosity Ratio

```

```

END
END
FLUID: Liquid
BOUNDARY CONDITIONS:
  FLOW DIRECTION:
    Option = Normal to Boundary Condition
  END
  VELOCITY:
    Mass Flow Rate = 1.18602 [kg s^-1]
    Option = Mass Flow Rate
  END
  VOLUME FRACTION:
    Option = Value
    Volume Fraction = 0.9
  END
END
END
FLUID: Vapor
BOUNDARY CONDITIONS:
  FLOW DIRECTION:
    Option = Normal to Boundary Condition
  END
  VELOCITY:
    Mass Flow Rate = 0.0000649 [kg s^-1]
    Option = Mass Flow Rate
  END
  VOLUME FRACTION:
    Option = Value
    Volume Fraction = 0.1
  END
END
END
BOUNDARY: Product Out
Boundary Type = OUTLET
Location = Product Out
BOUNDARY CONDITIONS:
  FLOW REGIME:
    Option = Subsonic
  END
  MASS AND MOMENTUM:
    Option = Fluid Velocity
  END

```

```

END
FLUID: Liquid
BOUNDARY CONDITIONS:
  VELOCITY:
    Mass Flow Rate = 0.1797 [kg s^-1]
    Option = Mass Flow Rate
  END
END
FLUID: Vapor
BOUNDARY CONDITIONS:
  VELOCITY:
    Mass Flow Rate = 0 [kg s^-1]
    Option = Mass Flow Rate
  END
END
END
BOUNDARY: Vapor Out
Boundary Type = OUTLET
Location = Vapor Out
BOUNDARY CONDITIONS:
  FLOW REGIME:
    Option = Subsonic
  END
  MASS AND MOMENTUM:
    Option = Fluid Velocity
  END
END
FLUID: Liquid
BOUNDARY CONDITIONS:
  VELOCITY:
    Mass Flow Rate = 0 [kg s^-1]
    Option = Mass Flow Rate
  END
END
FLUID: Vapor
BOUNDARY CONDITIONS:
  VELOCITY:
    Mass Flow Rate = 0.0000649 [kg s^-1]
    Option = Mass Flow Rate
  END
END

```

```

END
END
END
BOUNDARY: Fines Removal1
Boundary Type = OUTLET
Location = Fines Removal1
BOUNDARY CONDITIONS:
  FLOW REGIME:
    Option = Subsonic
  END
  MASS AND MOMENTUM:
    Mass Flow Rate = 0.50316 [kg s^-1]
    Option = Bulk Mass Flow Rate
  END
END
END
BOUNDARY: Fines Removal2
Boundary Type = OUTLET
Location = Fines Removal2
BOUNDARY CONDITIONS:
  FLOW REGIME:
    Option = Subsonic
  END
  MASS AND MOMENTUM:
    Mass Flow Rate = 0.50316 [kg s^-1]
    Option = Bulk Mass Flow Rate
  END
END
END
BOUNDARY: Draft Tube
Boundary Type = WALL
Location = Draft Tube
BOUNDARY CONDITIONS:
  WALL INFLUENCE ON FLOW:
    Option = No Slip
  END
  WALL ROUGHNESS:
    Option = Smooth Wall
  END
END
WALL CONTACT MODEL:
  Option = Use Volume Fraction
END

```

```

END
BOUNDARY: Draft Tube Other Side
Boundary Type = WALL
Location = F59.71,F68.69,F65.72
BOUNDARY CONDITIONS:
  WALL INFLUENCE ON FLOW:
    Option = No Slip
  END
  WALL ROUGHNESS:
    Option = Smooth Wall
  END
END
WALL CONTACT MODEL:
  Option = Use Volume Fraction
END
END
BOUNDARY: Baffle
Boundary Type = WALL
Location = Baffle
BOUNDARY CONDITIONS:
  WALL INFLUENCE ON FLOW:
    Option = No Slip
  END
  WALL ROUGHNESS:
    Option = Smooth Wall
  END
END
WALL CONTACT MODEL:
  Option = Use Volume Fraction
END
END
BOUNDARY: Baffle Other Side
Boundary Type = WALL
Location = F57.70
BOUNDARY CONDITIONS:
  WALL INFLUENCE ON FLOW:
    Option = No Slip
  END
  WALL ROUGHNESS:
    Option = Smooth Wall
  END
END
WALL CONTACT MODEL:

```

```

  Option = Use Volume Fraction
END
END
BOUNDARY: Tank Wall
Boundary Type = WALL
Location = Tank Wall
BOUNDARY CONDITIONS:
  WALL INFLUENCE ON FLOW:
    Option = No Slip
  END
  WALL ROUGHNESS:
    Option = Smooth Wall
  END
END
WALL CONTACT MODEL:
  Option = Use Volume Fraction
END
END
DOMAIN MODELS:
BUOYANCY MODEL:
  Buoyancy Reference Density = 0.59 [kg m^-3]
  Gravity X Component = 0 [m s^-2]
  Gravity Y Component = -g
  Gravity Z Component = 0 [m s^-2]
  Option = Buoyant
BUOYANCY REFERENCE LOCATION:
  Option = Automatic
END
END
DOMAIN MOTION:
  Option = Stationary
END
REFERENCE PRESSURE:
  Reference Pressure = 0 [Pa]
END
END
FLUID: Liquid
FLUID MODELS:
  FLUID BUOYANCY MODEL:
    Option = Density Difference
  END
MORPHOLOGY:
  Option = Continuous Fluid

```



```

END
END
END
FLUID: Vapor
FLUID MODELS:
  FLUID BUOYANCY MODEL:
    Option = Density Difference
  END
  MORPHOLOGY:
    Mean Diameter = 2 [mm]
    Option = Dispersed Fluid
  END
END
END
FLUID MODELS:
  COMBUSTION MODEL:
    Option = None
  END
  HEAT TRANSFER MODEL:
    Homogeneous Model = False
    Option = None
  END
  THERMAL RADIATION MODEL:
    Option = None
  END
  TURBULENCE MODEL:
    Homogeneous Model = On
    Option = k epsilon
  BUOYANCY TURBULENCE:
    Dissipation Coefficient = 1.0
    Option = Production and Dissipation
    Turbulent Schmidt Number = 1
  END
END
  TURBULENT WALL FUNCTIONS:
    C Coefficient = 5.2
    Energy Calibration Coefficient = 0.2
    Kappa Coefficient = 0.41
    Minimum Yplus = 11.06
    Near Wall Distance Factor = 0.5
    Option = Scalable
  END
END
END

```

```

FLUID PAIR: Liquid | Vapor
Surface Tension Coefficient = 0.077 [N m^-1]
INTERPHASE TRANSFER MODEL:
  Option = Particle Model
END
MASS TRANSFER:
  Option = None
END
MOMENTUM TRANSFER:
  DRAG FORCE:
    Option = Ishii Zuber
  END
  LIFT FORCE:
    Option = None
  END
  TURBULENT DISPERSION FORCE:
    Option = Lopez de Bertodano
    Turbulent Dispersion Coefficient = 0.3
  END
  VIRTUAL MASS FORCE:
    Option = None
  END
  WALL LUBRICATION FORCE:
    Option = None
  END
END
SURFACE TENSION MODEL:
  Option = None
END
TURBULENCE TRANSFER:
  ENHANCED TURBULENCE PRODUCTION MODEL:
    Option = Sato Enhanced Eddy Viscosity
  END
END
END
MULTIPHASE MODELS:
  Homogeneous Model = False
  FREE SURFACE MODEL:
    Option = Standard
  END
END
SUBDOMAIN: Impeller
Coord Frame = Coord 0

```

```

Location = B27
FLUID: Liquid
SOURCES:
  MOMENTUM SOURCE:
    GENERAL MOMENTUM SOURCE:
      Momentum Source X Component = 0 [kg m^-2 s^-2]
      Momentum Source Y Component = 10000 [kg m^-2 s^-2]
      Momentum Source Z Component = 0 [kg m^-2 s^-2]
      Option = Cartesian Components
    END
  END
END
FLUID: Vapor
SOURCES:
  MOMENTUM SOURCE:
    GENERAL MOMENTUM SOURCE:
      Momentum Source X Component = 0 [kg m^-2 s^-2]
      Momentum Source Y Component = 10000 [kg m^-2 s^-2]
      Momentum Source Z Component = 0 [kg m^-2 s^-2]
      Option = Cartesian Components
    END
  END
END
INITIALISATION:
Option = Automatic
FLUID: Liquid
INITIAL CONDITIONS:
  Velocity Type = Cartesian
  CARTESIAN VELOCITY COMPONENTS:
    Option = Automatic with Value
    U = 0 [m s^-1]
    V = 0.2859 [m s^-1]
    W = 0 [m s^-1]
  END
  VOLUME FRACTION:
    Option = Automatic with Value
    Volume Fraction = VFLiquid
  END
END
FLUID: Vapor
INITIAL CONDITIONS:
  Velocity Type = Cartesian
  CARTESIAN VELOCITY COMPONENTS:
    Option = Automatic with Value
    U = 0 [m s^-1]
    V = 0.2859 [m s^-1]
    W = 0 [m s^-1]
  END
  VOLUME FRACTION:
    Option = Automatic with Value
    Volume Fraction = VVapor
  END
END
INITIAL CONDITIONS:
  EPSILON:
    Option = Automatic
  END
  K:
    Option = Automatic
  END
  STATIC PRESSURE:
    Option = Automatic with Value
    Relative Pressure = Press
  END
END
OUTPUT CONTROL:
  RESULTS:
    File Compression Level = Default
    Option = Standard
  END
SIMULATION TYPE:
  Option = Steady State
  END
SOLUTION UNITS:
  Angle Units = [rad]
  Length Units = [m]
  Mass Units = [kg]
  Solid Angle Units = [sr]

```

```

Temperature Units = [K]
Time Units = [s]
END
SOLVER CONTROL:
ADVECTION SCHEME:
Option = Upwind
END
CONVERGENCE CONTROL:
Length Scale Option = Conservative
Maximum Number of Iterations = 300
Timescale Control = Auto Timescale
END
CONVERGENCE CRITERIA:
Residual Target = 0.00001
Residual Type = RMS
END
DYNAMIC MODEL CONTROL:
Global Dynamic Model Control = On
END
END
END
COMMAND FILE:
Version = 10.0
Results Version = 10.0
END

```

```

+-----+
| Solver |
+-----+
+-----+
| ANSYS CFX Solver 10.0 |
| Version 2005.07.11-10.24 Mon Jul 11 10:26:04 GMTDT 2005 |
| Executable Attributes |
| single-32bit-optimised-supfort-noprof-nospag-lcomp |
| Copyright 1996-2005 ANSYS Europe Ltd. |
+-----+
+-----+

```

```

| Job Information |
+-----+

```

```

Run mode: serial run

Host computer: SUT-C7J1H7UTXTO
Job started: Thu Jan 19 12:14:33 2006

```

```

+-----+
| Memory Allocated for Run (Actual usage may be less) |
+-----+

```

Data Type	Kwords	Words/Node	Words/Elem	Kbytes	Bytes/Node
Real	15246.1	949.44	191.87	59555.0	3797.75
Integer	3079.1	191.75	38.75	12027.8	767.00
Character	2478.2	154.33	31.19	2420.1	154.33
Logical	40.0	2.49	0.50	156.2	9.96
Double	501.3	31.22	6.31	3916.1	249.72

```

+-----+
| Total Number of Nodes, Elements, and Faces |
+-----+

```

```

Domain Name : IsoDTB

Total Number of Nodes = 16058
Total Number of Elements = 79460
Total Number of Tetrahedrons = 79460
Total Number of Faces = 10998

```

```

+-----+
| Reference Pressure Information |
+-----+

```

```

Domain Group: IsoDTB

Pressure has not been set at any boundary conditions.
The pressure will be set to 0.00000E+00 at the following location:
Domain : IsoDTB
Node : 1 (equation 1)

```

Coordinates : (-3.67382E-17, 7.50000E-02, 1.00000E-01).

Domain Group: IsoDTB

Buoyancy has been activated. The absolute pressure will include hydrostatic pressure contribution, using the following reference coordinates: (-3.67382E-17, 7.50000E-02, 1.00000E-01).

```
+-----+
|           Adaption Parameters           |
+-----+
Domains                = IsoDTB
Sub-domains            = B27|B31|B38|B42|B44|B47|B50|B53|B69|B70|B71|B72
Allocation Parameter   = 1.6
Number of Adaption Levels = 2
Number of Adaption Steps = 2
Multiple of Nodes      = 4
Adaption Variables     = Vapor.VolumeFraction
Min Edge Length        = 0.0
Number of Nodes        = MultipleofInitialMesh
Adaption Criteria      = SolutionVariation
Adapting to Geometry  = No
Save Intermediate Files = Yes
Target Residual        = 0.00001
Max Its. per Step      = 200
Type of Residual       = RMSNormforResiduals
```

```
+-----+
|           Average Scale Information       |
+-----+
```

Domain Name : IsoDTB

Global Length	= 1.0152E+00
Minimum Extent	= 1.0500E+00
Maximum Extent	= 3.2013E+00
Liquid.Density	= 1.1980E+03
Liquid.Dynamic Viscosity	= 1.5200E-03
Liquid.Velocity	= 2.8590E-01
Liquid.Advection Time	= 3.5508E+00
Liquid.Reynolds Number	= 2.2875E+05
Liquid.Mass (Conservative)	= 1.1279E+03
Liquid.Mass (Normalised)	= 1.1279E+03
Liquid.Volume	= 9.4147E-01

Liquid.Volume Fraction	= 8.9990E-01
Vapor.Density	= 5.9000E-01
Vapor.Dynamic Viscosity	= 1.2400E-05
Vapor.Velocity	= 2.8590E-01
Vapor.Advection Time	= 3.5508E+00
Vapor.Reynolds Number	= 1.3810E+04
Vapor.Mass (Conservative)	= 6.1785E-02
Vapor.Mass (Normalised)	= 6.1785E-02
Vapor.Volume	= 1.0472E-01
Vapor.Volume Fraction	= 1.0010E-01
Liquid Vapor.Slip Reynolds Number	= 1.5763E-12

```
+-----+
|           Checking for Isolated Fluid Regions           |
+-----+
```

No isolated fluid regions were found.

```
+-----+
|           The Equations Solved in This Calculation       |
+-----+
```

Subsystem : Momentum and Mass

U-Mom-Liquid
V-Mom-Liquid
W-Mom-Liquid
U-Mom-Vapor
V-Mom-Vapor
W-Mom-Vapor
P-Vol

Subsystem : Volume Fractions

Mass-Liquid
Mass-Vapor

Subsystem : TurbKE and Diss.K

K-TurbKE-Bulk
E-Diss.K-Bulk

CFD Solver started: Thu Jan 19 12:14:39 2006

```

+-----+
| Convergence History |
+-----+

```

```

=====
| Timescale Information |
+-----+-----+-----+
| Equation | Type | Timescale |
+-----+-----+-----+
| U-Mom-Liquid | Auto Timescale | 3.21742E-01 |
| V-Mom-Liquid | Auto Timescale | 3.21742E-01 |
| W-Mom-Liquid | Auto Timescale | 3.21742E-01 |
| U-Mom-Vapor | Auto Timescale | 3.21742E-01 |
| V-Mom-Vapor | Auto Timescale | 3.21742E-01 |
| W-Mom-Vapor | Auto Timescale | 3.21742E-01 |
+-----+-----+-----+
| Mass-Liquid | Auto Timescale | 3.21742E-01 |
| Mass-Vapor | Auto Timescale | 3.21742E-01 |
+-----+-----+-----+
| K-TurbKE-Bulk | Auto Timescale | 3.21742E-01 |
| E-Diss.K-Bulk | Auto Timescale | 3.21742E-01 |
+-----+-----+-----+

```

```

=====
OUTER LOOP ITERATION = 1 CPU SECONDS = 4.062E+00

```

```

+-----+-----+-----+-----+-----+
| Equation | Rate | RMS Res | Max Res | Linear Solution |
+-----+-----+-----+-----+-----+
| U-Mom-Liquid | 0.00 | 5.2E-04 | 2.9E-02 | 2.2E-01 ok |
| V-Mom-Liquid | 0.00 | 9.2E-03 | 1.1E-01 | 9.0E-02 OK |
| W-Mom-Liquid | 0.00 | 5.6E-04 | 3.0E-02 | 2.4E-01 ok |
| U-Mom-Vapor | 0.00 | 7.3E-04 | 4.3E-02 | 1.3E-01 ok |
| V-Mom-Vapor | 0.00 | 7.7E-03 | 1.1E-01 | 5.3E-02 OK |
| W-Mom-Vapor | 0.00 | 8.1E-04 | 6.1E-02 | 1.5E-01 ok |
| P-Vol | 0.00 | 5.1E-04 | 6.4E-03 | 8.4 2.3E-02 OK |
+-----+-----+-----+-----+-----+
| Mass-Liquid | 0.00 | 1.1E-02 | 4.1E-01 | 9.8 1.4E-06 OK |
| Mass-Vapor | 0.00 | 9.3E-03 | 4.7E-01 | 10.0 1.5E-03 OK |
+-----+-----+-----+-----+-----+
| K-TurbKE-Bulk | 0.00 | 1.1E-02 | 8.5E-01 | 9.8 1.2E-05 OK |
| E-Diss.K-Bulk | 0.00 | 4.2E-02 | 1.2E+00 | 10.9 1.8E-06 OK |
+-----+-----+-----+-----+-----+

```

```

=====
OUTER LOOP ITERATION = 400 ( 200) CPU SECONDS = 1.294E+04 (8.620E+03)

```

```

+-----+-----+-----+-----+-----+
| Equation | Rate | RMS Res | Max Res | Linear Solution |
+-----+-----+-----+-----+-----+
| U-Mom-Liquid | 1.10 | 3.0E-04 | 1.2E-02 | 9.4E-02 OK |
| V-Mom-Liquid | 0.99 | 3.1E-03 | 8.0E-02 | 1.1E-03 OK |
| W-Mom-Liquid | 0.97 | 2.7E-04 | 8.9E-03 | 9.1E-02 OK |
| U-Mom-Vapor | 0.89 | 1.8E-06 | 6.6E-05 | 5.3E-01 ok |
| V-Mom-Vapor | 0.98 | 7.6E-06 | 1.9E-04 | 6.2E-04 OK |
| W-Mom-Vapor | 0.99 | 1.9E-06 | 8.1E-05 | 5.9E-01 ok |
| P-Vol | 0.98 | 4.4E-07 | 2.4E-05 | 8.4 2.9E-02 OK |
+-----+-----+-----+-----+-----+
| Mass-Liquid | 1.23 | 2.0E-04 | 1.1E-02 | 9.6 9.1E-05 OK |
| Mass-Vapor | 0.96 | 8.9E-04 | 4.8E-02 | 9.7 3.9E-05 OK |
+-----+-----+-----+-----+-----+
| K-TurbKE-Bulk | 0.80 | 3.1E-04 | 1.4E-02 | 9.6 7.9E-05 OK |
| E-Diss.K-Bulk | 0.65 | 8.4E-05 | 5.2E-03 | 7.5 7.1E-04 OK |
+-----+-----+-----+-----+-----+

```

```

+-----+
| Job Information |
+-----+

```

```

Host computer: SUT-C7J1H7UTXTO
Job finished: Thu Jan 19 15:56:42 2006
Total CPU time: 8.665E+03 seconds
or: ( 0: 2: 24: 24.781 )
( Days: Hours: Minutes: Seconds )

Total wall clock time: 8.833E+03 seconds
or: ( 0: 2: 27: 13.000 )
( Days: Hours: Minutes: Seconds )

```

```

End of solution stage.

```

```

+-----+
| Mesh Adaption |
+-----+

```

```

+-----+
| Saving intermediate results file as |
| D:\CFXworks\IsothermalDTB\IsoDTB\IsoDTBCase4_001\mesh2.res|
+-----+

```

Refiner 10.0 [2005.07.08-23.00]

Adaption step 2 of 2.

0 prismatic stacks have been identified in the original mesh.

Marking elements for coarsening and refinement:

```

-----
Number of elements initially marked for coarsening: 124879
Number of elements removed because:
  They appear in the original coarse mesh: -67745
-----
Number of elements actually marked for coarsening: 57134
-----

```

```

Number of elements initially marked for refinement: 126260
Number of elements removed because:
  They already meet the minimum length criteria: 0
  They are in regions not marked for refinement: 0
  They are already in the deepest refinement level: 0
  There are not enough nodes available to refine them: -116007
-----

```

```

Number of elements actually marked for refinement: 10253
-----

```

Target number of nodes at end of step: 64232

Mesh refinement complete:

```

-----
          Nodes  Elements
Mesh before refinement: 46464  228636
Mesh after  refinement: 76613  383409
-----

```

```

+-----+

```

```

+-----+
| Solver |
+-----+

```

```

+-----+
| Reference Pressure Information |
+-----+

```

Domain Group: IsoDTB

Pressure has not been set at any boundary conditions.
The pressure will be set to 0.00000E+00 at the following location:
Domain : IsoDTB
Node : 1 (equation 1)
Coordinates : (-3.67382E-17, 7.50000E-02, 1.00000E-01).

Domain Group: IsoDTB

Buoyancy has been activated. The absolute pressure will include hydrostatic pressure contribution, using the following reference coordinates: (-3.67382E-17, 7.50000E-02, 1.00000E-01).

```

+-----+
| Checking for Isolated Fluid Regions |
+-----+

```

No isolated fluid regions were found.

CFD Solver started: Thu Jan 19 15:57:10 2006

```

+-----+
| Convergence History |
+-----+

```

```

=====
| Timescale Information |
+-----+
| Equation | Type | Timescale |
+-----+
| U-Mom-Liquid | Auto Timescale | 3.21742E-01 |
| V-Mom-Liquid | Auto Timescale | 3.21742E-01 |
| W-Mom-Liquid | Auto Timescale | 3.21742E-01 |
+-----+

```

U-Mom-Vapor	Auto Timescale	2.35030E-01
V-Mom-Vapor	Auto Timescale	2.35030E-01
W-Mom-Vapor	Auto Timescale	2.35030E-01
Mass-Liquid	Auto Timescale	3.21742E-01
Mass-Vapor	Auto Timescale	2.35030E-01
K-TurbKE-Bulk	Auto Timescale	3.21742E-01
E-Diss.K-Bulk	Auto Timescale	3.21742E-01

=====

OUTER LOOP ITERATION = 401 (1) CPU SECONDS = 1.295E+04 (8.562E+00)

Equation	Rate	RMS Res	Max Res	Linear Solution
U-Mom-Liquid	0.00	3.5E-03	1.1E-01	1.3E-02 OK
V-Mom-Liquid	0.00	2.0E-02	1.1E+00	4.3E-03 OK
W-Mom-Liquid	0.00	3.4E-03	1.1E-01	1.4E-02 OK
U-Mom-Vapor	0.00	1.0E-05	3.0E-04	4.0E-02 OK
V-Mom-Vapor	0.00	3.0E-05	2.5E-03	3.0E-03 OK
W-Mom-Vapor	0.00	1.1E-05	3.0E-04	3.9E-02 OK
P-Vol	0.00	6.1E-05	1.8E-03	8.4 8.0E-02 OK
Mass-Liquid	0.00	1.9E-02	4.9E-01	9.6 2.1E-04 OK
Mass-Vapor	0.00	2.1E-02	4.0E-01	9.6 1.7E-04 OK
K-TurbKE-Bulk	0.00	1.4E-02	2.3E-01	9.6 6.1E-05 OK
E-Diss.K-Bulk	0.00	1.5E-02	6.4E-01	12.1 2.0E-05 OK

=====

OUTER LOOP ITERATION = 700 (300) CPU SECONDS = 3.137E+04 (1.842E+04)

Equation	Rate	RMS Res	Max Res	Linear Solution
U-Mom-Liquid	1.09	4.2E-04	1.1E-02	3.9E-02 OK
V-Mom-Liquid	1.07	2.5E-03	8.1E-02	4.4E-03 OK
W-Mom-Liquid	1.04	4.3E-04	1.8E-02	4.0E-02 OK
U-Mom-Vapor	1.07	1.4E-06	7.6E-05	1.4E-01 ok
V-Mom-Vapor	1.15	5.8E-06	1.3E-04	4.1E-03 OK

W-Mom-Vapor	1.13	1.5E-06	6.2E-05	2.1E-01 ok
P-Vol	1.01	2.5E-06	1.1E-04	8.4 2.7E-02 OK

***** Notice *****

A wall has been placed at portion(s) of an OUTLET boundary condition (at 7.7% of the faces, 6.1% of the area) to prevent fluid from flowing into the domain. The boundary condition name is: Product Out. The fluid name is: Liquid. If this situation persists, consider switching to an Opening type boundary condition instead.

***** Notice *****

A wall has been placed at portion(s) of an OUTLET boundary condition (at 19.2% of the faces, 13.8% of the area) to prevent fluid from flowing into the domain. The boundary condition name is: Product Out. The fluid name is: Vapor. If this situation persists, consider switching to an Opening type boundary condition instead.

Mass-Liquid	0.97	3.2E-03	1.4E-01	9.6 2.8E-05 OK
Mass-Vapor	0.98	7.8E-03	3.3E-01	9.6 7.1E-06 OK
K-TurbKE-Bulk	1.17	2.0E-03	7.3E-02	9.6 6.7E-05 OK
E-Diss.K-Bulk	0.94	2.9E-04	4.4E-02	12.1 3.3E-05 OK

CFD Solver finished: Thu Jan 19 21:09:49 2006
 CFD Solver wall clock seconds: 1.8759E+04

Execution terminating: maximum number of time-step iterations, or maximum time has been reached.

=====

Boundary Flow and Total Source Term Summary

=====

U-Mom-Liquid

=====

Boundary	: Baffle	1.3449E+00
Boundary	: Baffle Other Side	-1.8127E+00
Boundary	: Draft Tube	4.7571E+00
Boundary	: Draft Tube Other Side	3.9588E+01
Boundary	: Fines Removal1	3.3621E-04
Boundary	: Fines Removal2	2.0718E-04
Boundary	: Product Out	3.4762E+00
Boundary	: Solution Inlet	-3.8739E-07
Boundary	: Tank Wall	1.2401E+01
Boundary	: Vapor Out	4.1503E-02
Domain	: IsoDTB	-5.9808E+01

Domain Imbalance : -1.2341E-02

Domain Imbalance, in %: -0.0001 %

```
+-----+
|               V-Mom-Liquid               |
+-----+
```

Boundary	: Baffle	3.5241E+00
Boundary	: Baffle Other Side	-3.2930E+00
Boundary	: Draft Tube	-3.7162E+00
Boundary	: Draft Tube Other Side	2.6440E+00
Boundary	: Fines Removal1	2.2176E+02
Boundary	: Fines Removal2	2.2179E+02
Boundary	: Product Out	-3.5982E+00
Boundary	: Solution Inlet	6.6053E+00
Boundary	: Tank Wall	7.9428E+03
Boundary	: Vapor Out	4.1503E-02
Domain	: IsoDTB	-8.3983E+03
Sub-Domain	: Impeller	7.6537E+00

Domain Imbalance : -2.0700E+00

Domain Imbalance, in %: -0.0211 %

```
+-----+
|               W-Mom-Liquid               |
+-----+
```

Boundary	: Baffle	-1.6118E+00
Boundary	: Baffle Other Side	1.4664E+00
Boundary	: Draft Tube	6.9159E+00
Boundary	: Draft Tube Other Side	1.1384E+00

Boundary	: Fines Removal1	-5.2707E-04
Boundary	: Fines Removal2	-6.9514E-05
Boundary	: Product Out	5.0921E-04
Boundary	: Solution Inlet	8.0678E-08
Boundary	: Tank Wall	-1.0126E+01
Boundary	: Vapor Out	1.9396E-10
Domain	: IsoDTB	2.2211E+00

Domain Imbalance : 3.4504E-03

Domain Imbalance, in %: 0.0000 %

```
+-----+
|               U-Mom-Vapor               |
+-----+
```

Boundary	: Baffle	-1.3485E+00
Boundary	: Baffle Other Side	1.7689E+00
Boundary	: Draft Tube	-4.4763E+00
Boundary	: Draft Tube Other Side	-3.9545E+01
Boundary	: Fines Removal1	3.6594E-10
Boundary	: Fines Removal2	3.5908E-11
Boundary	: Product Out	7.6053E-07
Boundary	: Solution Inlet	-2.9713E-10
Boundary	: Tank Wall	-2.8013E+02
Boundary	: Vapor Out	2.6393E+02
Domain	: IsoDTB	5.9808E+01

Domain Imbalance : 8.3923E-05

Domain Imbalance, in %: 0.0000 %

```
+-----+
|               V-Mom-Vapor               |
+-----+
```

Boundary	: Baffle	1.1527E-02
Boundary	: Baffle Other Side	-5.4860E-03
Boundary	: Draft Tube	-1.7506E-02
Boundary	: Draft Tube Other Side	1.1932E-02
Boundary	: Fines Removal1	3.5164E-02
Boundary	: Fines Removal2	3.1101E-03
Boundary	: Product Out	-7.8755E-07
Boundary	: Solution Inlet	4.2244E-01
Boundary	: Tank Wall	2.3643E+03


```

Boundary      : Vapor Out      2.6393E+02
Domain        : IsoDTB        -2.6355E+03
Sub-Domain    : Impeller      7.6537E+00

```

```

-----
Domain Imbalance :      8.2432E-01

```

```

Domain Imbalance, in %:      0.0313 %

```

```

+-----+
|                W-Mom-Vapor                |
+-----+

```

```

Boundary      : Baffle          1.6092E+00
Boundary      : Baffle Other Side -1.3014E+00
Boundary      : Draft Tube      -6.9680E+00
Boundary      : Draft Tube Other Side -1.3135E+00
Boundary      : Fines Removal1  -3.2237E-10
Boundary      : Fines Removal2   6.9790E-12
Boundary      : Product Out      1.3500E-15
Boundary      : Solution Inlet    6.6708E-11
Boundary      : Tank Wall        1.0195E+01
Boundary      : Vapor Out        4.2873E-07
Domain        : IsoDTB         -2.2211E+00

```

```

-----
Domain Imbalance :      2.7061E-04

```

```

Domain Imbalance, in %:      0.0000 %

```

```

+-----+
|                P-Vol                |
+-----+

```

```

Boundary      : Fines Removal1  -5.0316E-01
Boundary      : Fines Removal2  -5.0316E-01
Boundary      : Product Out      -1.7970E-01
Boundary      : Solution Inlet    1.1861E+00
Boundary      : Vapor Out        -6.4902E-05

```

```

-----
Domain Imbalance :     -1.7110E-07

```

```

Domain Imbalance, in %:      0.0000 %

```

```

+-----+
|                Mass-Liquid                |
+-----+

```

```

Boundary      : Fines Removal1  -5.0316E-01
Boundary      : Fines Removal2  -5.0316E-01
Boundary      : Product Out      -1.7970E-01
Boundary      : Solution Inlet    1.1860E+00

```

```

-----
Domain Imbalance :      1.1921E-07

```

```

Domain Imbalance, in %:      0.0000 %

```

```

+-----+
|                Mass-Vapor                |
+-----+

```

```

Boundary      : Fines Removal1  -2.7914E-07
Boundary      : Fines Removal2  -2.6274E-08
Boundary      : Solution Inlet    6.4900E-05
Boundary      : Vapor Out        -6.4902E-05

```

```

-----
Domain Imbalance :     -3.0717E-07

```

```

Domain Imbalance, in %:     -0.4733 %

```

```

=====
                        Wall Force and Moment Summary
=====

```

Note: Pressure integrals exclude the reference pressure. To include it, set the expert parameter 'include pref in forces = t'.

```

+-----+
|                Pressure Force On Walls                |
+-----+

```

```

                        X-Comp.      Y-Comp.      Z-Comp.

```

```

Domain Group: IsoDTB
Baffle          4.4250E-03  -3.5322E+00  2.6016E-03
Baffle Other Side  4.6142E-02  3.5235E+00 -1.6623E-01
Draft Tube      -2.7759E-01  3.9637E+00  5.2032E-02
Draft Tube Other Side -4.2765E-02 -3.9410E+00  1.7681E-01
Tank Wall       2.6792E+02 -1.0312E+04 -6.8121E-02

```

```

-----
Domain Group Totals :  2.6765E+02 -1.0312E+04 -2.9084E-03

```

Viscous Force On Walls			
	X-Comp.	Y-Comp.	Z-Comp.
Domain Group: IsoDTB			
Baffle	1.1629E-04	-5.1189E-03	2.9796E-05
Baffle Other Side	-2.3236E-03	-2.2325E-01	1.1064E-03
Draft Tube	-3.6106E-03	-2.2811E-01	4.4791E-04
Draft Tube Other Side	4.0906E-04	1.2830E+00	-1.6042E-03
Tank Wall	9.6080E-03	-4.2265E-01	-3.5059E-05
Domain Group Totals :	4.1991E-03	4.0389E-01	-5.5159E-05

Pressure Moment On Walls			
	X-Comp.	Y-Comp.	Z-Comp.
Domain Group: IsoDTB			
Baffle	-1.1987E-01	-1.1238E-02	-2.4780E-02
Baffle Other Side	-9.2560E-03	1.1074E-02	2.0318E-02
Draft Tube	-1.3885E-02	4.8265E-04	3.9174E-01
Draft Tube Other Side	1.5263E-01	-4.8776E-04	1.5438E-01
Tank Wall	4.0745E-01	2.7781E-02	-7.7290E+02
Domain Group Totals :	4.1707E-01	2.7612E-02	-7.7235E+02

Viscous Moment On Walls			
	X-Comp.	Y-Comp.	Z-Comp.
Domain Group: IsoDTB			
Baffle	6.6493E-05	7.8269E-06	-3.3112E-05
Baffle Other Side	-2.4673E-03	3.9717E-05	-3.8620E-03
Draft Tube	-3.3106E-03	-2.0203E-05	-8.7320E-04
Draft Tube Other Side	-1.7038E-03	-2.0134E-04	-1.2046E-02
Tank Wall	-2.2191E-03	7.9570E-04	-3.4312E-02
Domain Group Totals :	-9.6344E-03	6.2170E-04	-5.1127E-02

Locations of Maximum Residuals				
Equation	Node #	X	Y	Z
U-Mom-Liquid	14311	-1.105E-01	2.891E+00	-7.092E-02
V-Mom-Liquid	58482	1.264E-01	2.127E+00	9.566E-02
W-Mom-Liquid	59302	-1.258E-01	2.135E+00	1.284E-01
U-Mom-Vapor	13111	-1.474E-01	3.040E+00	6.210E-02
V-Mom-Vapor	58464	-1.345E-01	2.181E+00	1.098E-01
W-Mom-Vapor	25230	-2.457E-02	2.202E+00	1.821E-01
P-Vol	59284	-7.607E-02	2.096E+00	1.225E-01
Mass-Liquid	76369	-4.659E-02	2.111E+00	7.284E-03
Mass-Vapor	67209	-1.190E-01	1.920E+00	-1.039E-01
K-TurbKE-Bulk	59274	-7.840E-02	2.142E+00	1.628E-01
E-Diss.K-Bulk	75605	1.891E-01	2.146E+00	1.789E-02

Peak Values of Residuals			
Equation	Loop #	Peak Residual	Final Residual
U-Mom-Liquid	1	3.52150E-03	4.23016E-04
V-Mom-Liquid	3	2.56263E-02	2.54102E-03
W-Mom-Liquid	3	3.46323E-03	4.31200E-04
U-Mom-Vapor	1	1.04130E-05	1.44136E-06
V-Mom-Vapor	3	5.23075E-05	5.77375E-06
W-Mom-Vapor	1	1.09648E-05	1.48236E-06
P-Vol	1	6.14788E-05	2.54522E-06
Mass-Liquid	1	1.91153E-02	3.19445E-03
Mass-Vapor	1	2.10694E-02	7.79202E-03
K-TurbKE-Bulk	1	1.38593E-02	2.04997E-03
E-Diss.K-Bulk	1	1.47064E-02	2.89999E-04

False Transient Information		
Equation	Type	Elapsed Pseudo-Time
U-Mom-Liquid	Auto	9.65224E+01
V-Mom-Liquid	Auto	9.65224E+01
W-Mom-Liquid	Auto	9.65224E+01
U-Mom-Vapor	Auto	6.01174E+01

V-Mom-Vapor	Auto	6.01174E+01
W-Mom-Vapor	Auto	6.01174E+01
Mass-Liquid	Auto	9.65224E+01
Mass-Vapor	Auto	6.01174E+01
K-TurbKE-Bulk	Auto	9.65224E+01
E-Diss.K-Bulk	Auto	9.65224E+01

Average Scale Information

Domain Name : IsoDTB

Global Length	= 1.0152E+00
Minimum Extent	= 1.0500E+00
Maximum Extent	= 3.2013E+00
Liquid.Density	= 1.1980E+03
Liquid.Dynamic Viscosity	= 1.5200E-03
Liquid.Velocity	= 3.8334E-01
Liquid.Advection Time	= 2.6482E+00
Liquid.Reynolds Number	= 3.0671E+05
Liquid.Mass (Conservative)	= 1.1262E+03
Liquid.Mass (Normalised)	= 1.1262E+03
Liquid.Volume	= 9.4008E-01
Liquid.Volume Fraction	= 8.9858E-01
Vapor.Density	= 5.9000E-01
Vapor.Dynamic Viscosity	= 1.2400E-05
Vapor.Velocity	= 2.2069E+01
Vapor.Advection Time	= 4.6000E-02
Vapor.Reynolds Number	= 1.0660E+06
Vapor.Mass (Conservative)	= 6.2602E-02
Vapor.Mass (Normalised)	= 6.2602E-02
Vapor.Volume	= 1.0611E-01
Vapor.Volume Fraction	= 1.0142E-01
Liquid Vapor.Slip Reynolds Number	= 2.3133E+03

Variable Range Information

Domain Name : IsoDTB

Variable Name	min	max
Liquid.Density	1.20E+03	1.20E+03

Liquid.Dynamic Viscosity	1.52E-03	1.52E-03
Vapor.Density	5.90E-01	5.90E-01
Vapor.Dynamic Viscosity	1.24E-05	1.24E-05
Liquid.Velocity u	-3.47E-01	4.27E-01
Liquid.Velocity v	-4.83E-01	9.51E-01
Liquid.Velocity w	-3.24E-01	3.40E-01
Vapor.Velocity u	-3.46E-01	4.47E-01
Vapor.Velocity v	-3.42E-01	7.34E+02
Vapor.Velocity w	-3.24E-01	3.40E-01
Pressure	-2.35E+04	1.78E+03
Liquid.Conservative Volume Fraction	9.51E-05	1.00E+00
Vapor.Conservative Volume Fraction	1.00E-07	1.00E+00
Liquid.Volume Fraction	9.51E-05	1.00E+00
Vapor.Volume Fraction	1.00E-07	1.00E+00
Liquid.Turbulence Kinetic Energy	8.94E-07	6.33E-03
Liquid.Turbulence Eddy Dissipation	1.25E-08	5.05E-01
Liquid.Eddy Viscosity	1.04E-03	3.32E-01
Vapor.Eddy Viscosity	4.80E-07	1.61E-04
Eddy Viscosity	5.64E-05	1.87E-01

CPU Requirements of Numerical Solution

Subsystem Name	Discretization		Linear Solution	
	(secs.)	%total	(secs.)	%total
Momentum and Mass	9.94E+03	53.8 %	1.76E+03	9.5 %
Volume Fractions	1.10E+03	6.0 %	8.24E+02	4.5 %
TurbKE and Diss.K	2.01E+03	10.9 %	9.51E+02	5.1 %
Subsystem Summary	1.31E+04	70.6 %	3.53E+03	19.1 %
Variable Updates	1.51E+03	8.2 %		
Miscellaneous	3.81E+02	2.1 %		
Total	1.85E+04			

Job Information

Host computer: SUT-C7J1H7UTXTQ

Job finished: Thu Jan 19 21:10:12 2006

Total CPU time: 1.850E+04 seconds

or: (0: 5: 8: 21.094)
(Days: Hours: Minutes: Seconds)

Total wall clock time: 1.879E+04 seconds

or: (0: 5: 13: 12.000)
(Days: Hours: Minutes: Seconds)

finished.

End of solution stage.

```
+-----+  
| The results from this run of the CFX-5 solver have been written to |  
| D:\CFXworks\IsothermalDTB\IsoDTB\IsoDTBCase4_001.res |  
+-----+
```

This run of the CFX-5 Solver has

BIOGRAPHY

Mr. Wirapong Wantha was born on October 7, 1980 in Surin Province. He graduated with a bachelor degree in chemical engineering in 2004 from Suranaree University of Technology (SUT). He has received scholarships for students with outstanding academic performance from SUT to study for the master degree in chemical engineering at SUT since 2004. From 2004 - 2006 he was a research assistant at SUT.